Design and Characterization of The Silicon Strip Sensors for The Future Hadron Colliders

THESIS SUBMITTED TO THE
UNIVERSITY OF DELHI FOR THE AWARD OF DEGREE OF
DOCTOR OF PHILOSOPHY IN PHYSICS

BY

GEETIKA JAIN

March, 2019

DEPARTMENT OF PHYSICS & ASTROPHYSICS
UNIVERSITY OF DELHI
DELHI-110 007, INDIA

Declaration

This thesis describes work done by the candidate during her tenure as Ph.D. student at the Department of Physics and Astrophysics, University of Delhi, Delhi, India under the supervision of Dr. Ashutosh Bhardwaj. The work reported in this thesis is original and it has not been submitted earlier for any degree to any university.

Candidate ....

Geetika Jain

Supervisor ....

Dr. Ashutosh Bhardwaj

Head of Department ....

Prof. Brajesh Chandra Choudhary

Department of Physics and Astrophysics

University of Delhi

Delhi-110007, India

Date: ....

Certificate of Originality

The research work embodied in this thesis entitled "**Design and Characterization of The Silicon Strip Sensors for The Future Hadron Colliders**" has been carried out by me at the **Department of Physics and Astrophysics**, University of Delhi, Delhi, India. The manuscript has been subjected to plagiarism check by **Urkund** software. The work submitted for consideration of award of Ph.D. is original.

....

Geetika Jain

Name and Signature of the Candidate

Student Approval Form

Name of the Author	**Geetika Jain**
Department	Department of Physics and Astrophysics
Degree	Doctor of Philosophy
University	University of Delhi
Guide	Dr. Ashutosh Bhardwaj
Thesis Title	Design and Characterization of The Silicon Strip Sensors for The Future Hadron Colliders
Year of Award	

Agreement

1. I hereby certify that if appropriate, I have obtained and attached hereto a written permission/statement from the owner(s) of each third party copyrighted matter to be included in my thesis/dissertation, allowing distribution as specified below.

2. I hereby grant to the university and its agents the non-exclusive license to archive and make accessible, under the conditions specified below, my thesis/dissertation, in whole or in part in all forms of media, now or hereafter known. I retain all other ownership rights to the copyright of the thesis/dissertation. I also retain the right to use in future works (such as articles or books) all or part of this thesis, dissertation, or project report.

Conditions:

1. Release the entire work for access worldwide	
2. Release the entire work for 'My University' only for: 1 Year 2 Year 3 Year and after this time release the work for access worldwide.	
3. Release the entire work for 'My University' only while at the same time releasing the following parts of the work (e.g. because other parts relate to publications) for world-wide access: a) Bibliographic details and Synopsis only b) Bibliographic details, synopsis and the following chapters only c) Preview/Table of Contents/24 page only	
4. View Only (No Downloads) (worldwide)	

....
Signature of the Scholar
Geetika Jain

....
Signature and seal of the Guide
Ashutosh Bhardwaj

Place: ....

Date: ....

Dedicated to My Parents and My Loving Brother & Sister

List of Publications

Publications

1. Articles in Peer Reviewed Journals

1.1: **G. Jain**, C. Jain, A. Bhardwaj, K. Ranjan, A. Dierlamm, F. Hartmann, M. Demarteau: Radiation Tolerance Study on Irradiated AC-coupled, Poly-silicon biased, p-on-n Silicon Strip sensors developed in India. NIM A 913 (2019) 97102.

1.2: **G. Jain**, R. Dalal, A. Bhardwaj, K. Ranjan, A. Dierlamm, F. Hartmann, R. Eber, M. Demarteau: Development of AC-Coupled, Poly-silicon biased, p-on-n Silicon Strip sensors in India for HEP Experiments. NIM A 882 (2018) 1-10.

1.3: R. Dalal, **G. Jain**, A. Bhardwaj, K. Ranjan: TCAD Simulation of Low Gain Avalanche sensors. NIM A 836 (2016) 113-121.

2. Conference Proceedings

2.1: **G. Jain**, C. Jain, A. Kumar, A. Sisodia, S. Sharma, M. Saxena, A. Bhardwaj, K. Ranjan: Development of an automated and programmable characterization system for silicon multi-strip sensors. Accepted by NIM A.

2.2: **G. Jain**, S. Sharma, C. Jain, A. Kumar, A. Bhardwaj, K. Ranjan: Radiation hardness investigation of thin and low resistivity bulk Si sensors. Accepted by NIM A.

2.3: **G. Jain**, C. Jain, R. Dalal, A. Bhardwaj, K. Ranjan: Study of trapping probability in proton irradiated silicon pad sensors using Transient Current Technique simulations. Proceedings of XXII DAE High Energy Physics Symposium (2018), SPPHY, volume 203 293-296. Springer publisher. ISBN 978-3-319-73170-4.

2.4: M. C. Vignali, R. Dalal, M. Gallinaro, B. Harrop, **G. Jain**, C. Lu, M. McClish, K. T. McDonald, M. Moll, F. M. Newcomer, S. O. Ugobonoa, S. White: Characterization of irradiated APDs for picosecond time measurements. JINST 13 (2018) C01041.

2.5: The Tracker Group of the CMS Collaboration (... **G. Jain** ...): P-Type Silicon Strip sensors for the new CMS Tracker at HL-LHC. JINST 12 (2017) P06018.

2.6: **G. Jain**, R. Dalal, A. Bhardwaj, K. Ranjan: Dependence of charge multiplication on different design parameters of LGAD devices. JINST 12 (2017) C03022.

2.7: A. Bhardwaj, **G. Jain**, K. Ranjan: Chapter - Silicon sensors in Experimental High Energy Physics Experiments in Book - Advanced sensors for Nuclear, High Energy and Astroparticle Physics. Proceedings of ADNHEAP (2017), SPPHY, volume 201 3-13. Springer publisher. ISBN 978-981-10-7665-7.

2.8: K. Lalwani, **G. Jain**, R. Dalal, A. Bhardwaj, K. Ranjan: Study the radiation damage effects in Si microstrip sensors for future HEP experiments. NIM B 379 (2016) 262-264.

2.9: **G. Jain**, A. Bhardwaj, R. Dalal, R. Eber, T. Eichorn, M. Fernandez, K. Lalwani, A. Messineo, F. R. Palomo, T. Peltola, M. Printz, K. Ranjan, I. Villa, S. Hidalgo: Design Optimization of Pixel sensors using Device Simulations for the Phase-II CMS Tracker Upgrade. NIM A 824 (2016) 413-416.

2.10: **G. Jain**, K. Lalwani, R. Dalal, A. Bhardwaj, K. Ranjan: Characterization of Silicon sensors Through TCT at Delhi University. NIM A 824 (2016) 411-412.

2.11: K. Lalwani, **G. Jain**, R. Dalal, A. Bhardwaj, K. Ranjan: Design, Fabrication and Characterization of multi-guard-ring furnished p+n-n+ Silicon Strip sensors for future HEP experiments. NIM A 824 (2016) 428-431.

2.12: P. Kumari, **G. Jain**, K. Lalwani, R. Dalal, A. Bhardwaj, K. Ranjan: Development of Silicon Sensor Characterization System for Future High Energy Physics Experiments. Journal of Nuclear Physics, Material Sciences, Radiation and Applications 3, No. 1 (2015)

25-29.

2.13: **G. Jain**, K. Lalwani, R. Dalal, A. Bhardwaj, K. Ranjan: Development and Characterization of AC-coupled Si strip sensors for Nuclear & High Energy Physics Applications. Proceedings of the DAE Symp. on Nucl. Phys. 59 (2014) 954-955.

Conferences, Workshops and Schools - Talks & Posters

1. Conferences

1.1: XXIII DAE-BRNS High Energy Physics Symposium, IIT Madras, Chennai, India (2016). **Talk** on: Transient Current Technique (TCT) Measurements & Simulations at the University of Delhi.

1.2: Frontier sensors For Frontier Physics 14th Pisa Meeting on Advanced sensors (Elba Conference), La Biodala, Isola d'Elba, Italy (2018). **Poster** on: Radiation hardness investigation of thin and low resistivity bulk Si sensors.

1.3: Frontier sensors For Frontier Physics 14th Pisa Meeting on Advanced sensors (Elba Conference), La Biodala, Isola d'Elba, Italy (2018). **Poster** on: Development of an automated and programmable characterization system for silicon multi-strip sensors.

1.4: XXII DAE-BRNS High Energy Physics Symposium, DU, Delhi, India (2016). **Talk** on: Study of trapping probability in proton irradiated silicon pad sensors using Transient Current Technique simulations.

1.5: 14th Topical Seminar on Innovative Particle and Radiation sensors (IPRD16), Siena, Italy (2016). **Talk** on: Dependence of charge multiplication on different design parameters of LGAD devices.

1.6: Frontier sensors For Frontier Physics 13th Pisa Meeting on Advanced sensors (Elba Conference), La Biodala, Isola d'Elba, Italy (2015). **Poster** on: Design Optimization of Pixel sensors using Device Simulations for the Phase-II CMS Tracker Upgrade.

1.7: Frontier sensors For Frontier Physics 13th Pisa Meeting on Advanced sensors (Elba Conference), La Biodala, Isola d'Elba, Italy (2015). **Poster** on: Characterization of Silicon sensors Through TCT at Delhi University.

1.8: 59th DAE Symposium on Nuclear Physics, BHU, Banaras, India (2014). **Poster** on: Characterization of ac-coupled Si strip sensors for Nuclear & High Energy Physics Applications.

2. Workshops

2.1: 27th International Workshop on Vertex sensors, Chennai, India (2018). **Invited Talk** on: Radiation Damage Modelling: TCAD Simulation.

2.2: Sensor QA Workshop - II, Perugia, Italy (2018). **Talk** on: Update on the development of SQC at Delhi University.

2.3: Sensor QA Workshop - I, HEPHY, Vienna, Austria (2017). **Talk** on: Update on the development of the 'Sensor Qualification Centre' at Delhi University in India.

2.4: 27th RD50 Workshop, CERN, Geneva, Switzerland (2015). **Talk** on: TCAD 2D Simulations for Phase II Pixel Sensor Design.

2.5: Workshop on Contemporary Trends in High-Energy Physics and Experimentation. Department of Physics, Panjab University, Chandigarh, India (2014). **Poster** on: Development of Transient Current Technique Measurement Setup At Delhi University.

3. Schools

3.1: SIMDET 2016, 2nd School on Silicon sensors Simulation, LPNHE, Paris, France (2016). **Invited Talk** on: Uses of SILVACO in high-energy physics experiments.

3.2: X SERC School on Experimental High Energy Physics, University of Delhi, Delhi, India (2016). Volunteered in organising the school and participated as a student.

3.3: Winter School on Accelerator, Nuclear & Particle Physics, Banaras Hindu University, Banaras, India (2014). **Poster** on: Transient Current Technique (TCT) Measurements & Simulations at Delhi University.

Acknowledgments - A token of Thanks!

Let us be grateful to the people who make us happy; they are the charming gardeners who make our souls blossom.

(Marcel Proust)

Good, better, best. Never let it rest. 'Til your good is better and your better is best.

(St. Jerome)

I take this opportunity with great pleasure to acknowledge and thank all the people for their efforts, guidance and never-ending support which made this work possible.

Firstly, I would like to express my sincere gratitude to my supervisor *Dr. Ashutosh Bhardwaj* for his continuous support towards my Ph.D study and related research through his patience, motivation, and immense knowledge. His guidance helped me in all the time during the research period and then writing of this thesis. I could not have imagined having a better advisor and mentor for my Ph.D study.

I would also like to thank *Prof. Kirti Ranjan*, member of my advisory committee, for not only his insightful comments and encouragement, but also for the intellectual discussions which incented me to widen my research perspective.

I thank *Dr. Ashok Kumar*, also member of my advisory committee, for sharing innovative research ideas which provided me with inquisitive vision.

My sincere thanks also goes to *Michael Moll, Frank Hartmann, Alberto Messineo, Alexander Dierlamm, and Marko Dragicevic* who provided me an opportunity to work in research groups like the CMS Outer Tracker Sensor Upgrade, the CMS Device Simulation Meeting, the Phase 2 Pixel Sensors, and the RD50 Collaboration of CERN, Switzerland. Special thanks to *Michael Moll, Frank Hartmann, and Alexander Dierlamm* for providing access to the CERN and Karlsruhe Institute of Technology (KIT), Germany laboratory and research facilities. It would not have been possible to conduct this research without they precious support.

To my other colleagues scattered around the world - *Robert Eber, Daniel Schell, Marius Metzler, Felix Ehrler, Marcos Fernandez, Laura Franconi, Sofia Ugobono, Esteban Rivera, Hannes Neugebaure, Christian Gallrapp, and Timo Peltola*; thank you for all the knowledge exchange.

I thank my fellow labmates at CDRST, University of Delhi - *Ranjeet Dalal, Ankit Gaur, Sumit Keshri, Ramkrishana Sharma, Preeti Kumari, Lakshay Jain, Chakresh Jain, Surabhi Sharma, Abhijeet Sisodia, Ruchika Nayyar, Yachika Manglik, Ajay Kumar, Aashiq Shah, Arun Mittal, Vijendra Sharma, Shivali Malhotra, Varun Sharma, Daljeet Kaur, Arjun Chettri, and Rocky Bala*; for the healthy research environment and stimulating discussions. Also I thank my friends in other institutions - *Aditya Mishra, Anisa Khatun, Chetan Verma, Jyotiprasad Deka, Sheetal Deewan, Bharati Naik, Shaan Ameer, Neelam, Naveen Saini, and Ankita Verma*; for all the knowledge exchange and fun we had during our research meetings. In particular, I am grateful to *Ankit Gaur* for his friendship and support during these Ph.D. years. I would also like to thank the lab staff *Md. Yunus, Aamir, and Puran* for providing basic facilities in the laboratory. I personally thank and acknowledge all the people (who I may have missed here) who have supported me to complete the thesis work.

To my friends - *Saloni Bhatiani, Geetanjali Kohli, and Paromita Dutta*, thank you for listening, offering me advice, and supporting me through this entire process. The discussions, debates, and advices were all greatly appreciated.

Last but not the least, I would like to thank my parents - *Nem Nath Jain and Sucheta Jain*, from the bottom of my heart for their selfless love, care, pain and sacrifice during the course of my Ph.D. Thank you mumma papa for the spiritual support and motivation on my tough days. This Ph.D. thesis would not have been a reality without your seamless support in everything I did. I would also extend the token of thanks to my dear sister and brother - *Vandana Jain and Nitin Jain*, for making me understand the lighter side of life. You have been utmost source of motivation to me and guided me through the stressful phases of my Ph.D. Thanks a million for keeping my secrets and adoring me as I am. I feel so lucky and blessed to have you in my life. Thank you for always being there for me. I love you all to the moon and back, forever and ever.

Finally, I thank *God* for keeping me strong and going.

Geetika Jain

Abstract

Silicon sensors play a key role in High Energy Physics (HEP) experiments due to their superior performance in terms of robust and reliable charged particle tracks and vertex reconstruction. Owing to the placement of these sensors in a harsh radiation environment imposed by current and future HEP experiments like Compact Muon Solenoid (CMS) in the Large Hadron Collider (LHC) phase and the high luminosity LHC (HL-LHC) phase, the radiation hardness study is inevitable. It is imperative to optimize the sensor design or develop new sensor configurations which can withstand such radiation scenario. This has generated an interest in the development and improvement of the radiation tolerance of the sensors which require better designs and better engineering technologies.

This thesis is devoted to the characterization studies of the silicon sensors for their performance and study of novel sensor designs through Technological Computer Aided Design (TCAD) simulations for their survival in harsh radiation sectors.

The characterization studies involved development and characterization of AC-coupled, poly-silicon biased, p-on-n silicon strip sensors. While the fabrication of the sensors were carried out in Bharat Electronics Limited (BEL), the characterization study was performed in Karlsruhe Institute of Technology (KIT). The non-irradiated sensors were subject to several tests defined in the characterization scheme for the quality assurance of the fabricated sensors. The details of the process steps involved in the fabrication cycle and the performance characteristics of the fabricated sensors are discussed. The measured data shows a good control of the process parameters governing the poly-silicon deposition and the quality and uniformity of the coupling oxide layer. The radiation tolerance of the fabricated sensors has also been evaluated and results are presented in the thesis. It is to be noted that this is the first radiation hardness study performed on AC-coupled sensors developed in India.

As part of the characterization study, various automated and programmable characterization systems were developed to carry out a ‘Quality Assurance’ inspection of the pad and strip sensors. The system consists of a current-voltage, capacitance-voltage (CVIV) setup, and a Transient Current Technique (TCT) setup; capable of measuring global sensor, strip, inter-strip parameters and charge collection. The thesis lists the most noticeable features of the setups, their operation, and measurement results. The system, is proposed to be used

as a ‘Sensor Qualification Centre’ and will be utilized for the qualification of the 2S multi-strip sensors of the CMS outer tracker in the HL-LHC phase.

The n-on-p silicon sensors employed in strip configurations in the CMS experiment experience a rapid fall in the collected charge (CC) with progressing radiation damage. This results in an inefficient signal read-out and hence silicon sensors become unfit for particle tracking in extremely high radiation environment. Hence, it is important to develop and evaluate new thin sensor technologies which can provide intrinsic charge multiplication (gain) for a high signal to noise ratio (S/N), and survive at high fluences. In this thesis, the behaviour of Low Gain Avalanche Detector (LGAD) in radiation environment is explored through TCAD device simulations. The simulation predictions provide a reasonable qualitative description of both the non-irradiated and irradiated LGAD device behaviour. It has been emphasized that the gain of the non-irradiated LGAD devices is strongly influenced by the overall doping profiles of the p-well and n^+ implantations.

Design optimization of pixel sensors using TCAD device simulations has been carried out for the Phase-II CMS tracker upgrade. Simulations were carried out on two n-on-p planar pixel sensor geometries, $50 \times 50\ \mu m^2$ and $100 \times 25\ \mu m^2$, for two wafer thicknesses of 150 μm and 200 μm. A stepwise approach for identification of a radiation hard design is described.

The requirement for reduced material budget has made the silicon sensor community to explore thinner sensor options. Simulation studies of low resistivity or high bulk doping concentration silicon substrate sensors with respect to thickness and radiation hardness (for proton damage) are presented. It is found that thin and highly doped substrates are attractive candidates as the radiation hard sensors for the reported values of resistivities and bias voltage.

The research work carried out on the development of the AC-coupled, poly-silicon biased silicon sensors and establishment of characterization laboratory at DU has laid a foundation for future advancements of the silicon sensor instrumentation technology in India. The radiation hardness simulation studies on LGAD, pixel, and low resistivity silicon sensors has provided useful inputs for the development of novel sensor technology for high luminosity HEP experiments.

Contents

Chapter 1

Silicon Sensors at the Large Hadron Collider

The pursuit to unravel the mystery of the evolution of our Universe necessitated mankind to advance the frontiers of our understanding and determine the fundamental building blocks of the matter and the interaction between these particles. In modern times, it began with the discovery of atoms in early 1800s, which were thought to be the smallest constituent of matter [1]. Over the decades, evidences for the existence of even smaller particles like electron[2], proton [3], and neutron [4] were found. In fact, by the end of the 20^{th} century, evidence of many new particles were seen with the invention of particle accelerators. The attempt to group the particles on the basis of their properties led to the theoretical construct and validation of the 'Standard Model' (SM) of particle physics [5]. The SM is based on the interaction through three fundamental interactions, i.e. the electromagnetism, the strong and the weak among the following elementary particles and anti-particles: leptons, anti-leptons, quarks, anti-quarks, and boson mediators (see Table 1.1). However, there are still many unresolved mysteries like the asymmetry between matter and antimatter, composition of dark matter and dark energy, unification of all three forces at higher energies, higher dimensions, supersymmetry (SUSY), physics beyond the SM, etc. [6].

A powerful particle collider capable of achieving high energies may help to answer these fundamental open questions and provide an insight to the subatomic world. The particles produced as a result of the collision can be collected by a detector system. Utilizing the unique signatures of the particles, several sub-systems have to be designed to measure their

Table 1.1: Classification of elementary particles.

Fermions (spin = half-integer)	**Quarks** (spin = $\frac{1}{2}$)	up ($u^{+\frac{2}{3}}$), down ($d^{-\frac{1}{3}}$), charm ($c^{+\frac{2}{3}}$), strange ($s^{-\frac{1}{3}}$), top ($t^{+\frac{2}{3}}$), bottom ($b^{-\frac{1}{3}}$).
	Anti-quarks (spin = $\frac{1}{2}$)	anti-up ($\bar{u}^{-\frac{2}{3}}$), anti-down ($\bar{d}^{+\frac{1}{3}}$), anti-charm ($\bar{c}^{-\frac{2}{3}}$), anti-strange ($\bar{s}^{+\frac{1}{3}}$), anti-top ($\bar{t}^{-\frac{2}{3}}$), anti-bottom ($\bar{b}^{+\frac{1}{3}}$).
	Leptons (spin = $\frac{1}{2}$)	electron (e^-), muon (μ^-), tau (τ^-), electron neutrino (ν_{e^-}), muon neutrino (ν_{μ^-}), tau neutrino (ν_{τ^-}).
	Anti-Leptons (spin = $\frac{1}{2}$)	positron (e^+), anti-muon (μ^+), anti-tau (τ^+), electron anti-neutrino ($\bar{\nu}_e$), muon anti-neutrino ($\bar{\nu}_\mu$), tau anti-neutrino ($\bar{\nu}_\tau$).
Bosons (spin = integer)	**Gauge** (spin = 1) **Scalar** (spin = 0)	gluons (g), photon (γ), Z boson (Z), W boson (W). Higgs boson (H).

energy, momentum, etc. to reconstruct the collision products.

The Large Hadron Collider (LHC) is at present the accelerator with highest achievable energy. It accelerates both proton (p) and lead (Pb) ion beam and provides pp, PbPb, and pPb collisions. The LHC physics programme comprises of looking for rare and statistically limited SM processes with greater precision. Further, LHC aims to perform BSM studies by the observation of decay channels with low production cross-section, SUSY, extra dimensions, etc. The Compact Muon Solenoid (CMS) detector is one of the many particle detectors installed at the LHC, capable of achieving the physics goals as mentioned earlier. Of all the CMS sub-detectors, the all-silicon CMS tracker system is crucial in vertexing and tracking of the particle, thereby useful in determining the momentum of the particle. Since the tracker is placed close to the particle collision point, an appropriate technology of silicon sensors must be used that can survive in the radiation environment. More details on the LHC, CMS, all-silicon tracker can be found in section 1.2.

This thesis presents the results of the characterization studies performed on silicon strip sensors fabricated at BEL, Bangalore, development of silicon sensor hardware facility for sensor quality check and radiation hard study of novel sensor designs through Technological Computer Aided Design (TCAD) simulations. The 2D TCAD device simulations were performed using the Silvaco simulator. The simulations were aimed at understanding and optimizing the designs of Low Gain Avalanche Detector (LGAD), pixel detectors, and low resistivity substrate silicon detectors. The parametrization of bulk and surface proton radiation damage model developed was used to simulate radiation damage.

The thesis primarily deals with the usage of silicon sensors in intense radiation environment, for example the environment faced by the Silicon Tracking System of the Compact Muon Solenoid (CMS) experiment at the Large Hadron Collider (LHC) (discussed in detail in next few sections of this chapter). Hence, this chapter starts with the historical development of silicon sensors in particle physics experiments. Next, an overview to the LHC and the different sub-systems of the CMS detector is provided. The present tracker system and the expected upgrade requirement of the silicon sensor technology for survival in harsher radiation environment are further described in this chapter. Lastly, the motivation for the work performed in this thesis and the thesis organization are presented.

1.1 History of usage of silicon sensors

The silicon sensors were first used in 1981 in the NA11 fixed target experiment [7]. The requirement of silicon sensors came from the fact that the theoretical prediction of the lifetime of the charm particle was found to be of the order of 10^{-13} s. Thus, to record the presence of charm events, a spatial resolution of $10\,\mu\mathrm{m}$ and a high rate handling capability of 1 MHz (low dead time) was required, which was achievable by the silicon sensors. The experiment resulted in a successful measurement of the lifetime of the charm meson. However, the small active area of the silicon sensor compared to the bulky readout electronics in the NA11 experiment was a major drawback in using them in large quantities.

The miniature VLSI readout electronics was developed [8] and used in Mark II experiment [9] at the SLAC Linear Collider (SLAC) [10]. The goal of the experiment was to make measurements with high precision and a position resolution of $5\,\mu\mathrm{m}$. The advancement of the silicon sensor technology used in the Mark II experiment led to the reconstruction of the B mesons through the measurements of its decay particles - D^- mesons and charged leptons.

By 1990s, the silicon sensor technology evolved into vertex detectors. This led to the possibility of study of heavy quarks and their decays physics. The four detectors of the

Large Electron and Positron (LEP) collider - DEtector with Lepton, Photon and Hadron Identification (DELPHI) [11], ALEPH [12], OPAL [13] and L3 [14]; employed this sensor technology. The major achievement of the DELPHI detector was the lifetime measurements of heavy quarks and the τ lepton with unprecedented precision.

Soon the silicon sensors were deployed in hadron colliders, which required radiation hard electronics. The two multi-purpose Collider Detector at Fermilab (CDF) [15] and D0 [16] at the proton-antiproton TEVATRON collider, installed with such silicon sensor technology, announced the top quark discovery in 1995.

The constant increase in particle flux (as foreseen by future colliders) and requirement of a low occupancy for good track reconstruction, requires the development of better spatial resolution, fast and radiation hard silicon sensor technology. Silicon sensors with large detector area are presently being used in the four detectors of the LHC (discussed in the next section). A detailed review of the historical evolution of the silicon sensors from strip sensors to pixel detectors is given in Ref. [17].

1.2 The Large Hadron Collider

The Conseil Europeen pour la Recherche Nucleaire, also known as CERN [18], is the world's largest experimental particle physics facility located at Geneva in Switzerland. Among the many experiments at CERN, 'The Large Hadron Collider' (LHC) [19, 20] is the world's largest and most powerful circular particle collider, designed to achieve a centre of mass energy ($\sqrt{s}$) of 14 TeV. LHC was built in collaboration with scientists from universities all over the world. A chain of small accelerators boost particles to their maximum energies and finally the boosted beam is fed to the LHC for collisions. The complex accelerator map can be viewed in Fig. 1.1. The LHC tunnel, with a circumference of approximately 27 km, is installed 100 m below the ground. Protons, ionized from the hydrogen atoms, are injected into the following accelerators: (i) Linac 2 - 50 MeV, (ii) Proton Synchrotron Booster (PSB) - 1.4 GeV, (iii) Proton Synchrotron (PS) - 25 GeV, and (iv) Super Proton Synchrotron (SPS) - 450 GeV, before injecting the proton bunches into the LHC tunnel where they are accelerated to 6.5-7 TeV. These bunches are separated from one another with a bunch spacing (B_s) of 25 ns (or, bunch crossing frequency of 40 MHz) and there are a total of 2835 bunches, with 1.15×10^{11} protons per bunch (N_p), injected in the

LHC ring at one time. The proton beam is kept focussed and on track by superconducting dipole magnets of 8.3 T, cooled to a temperature of 1.9 K by liquid helium. Proton beams are collided at a centre of mass energy of $\sqrt{s}$ = 13 TeV with a cross section of 60 mb, which translates to approximately 25 inelastic collisions on an average taking place per bunch crossing, also known as pile-up. It may also be talked in terms of instantaneous luminosity (L) (presently of the order of 10^{34} cm^{-2}.s^{-1}), which is the measure of the number of collisions in an accelerator per unit area per unit time.

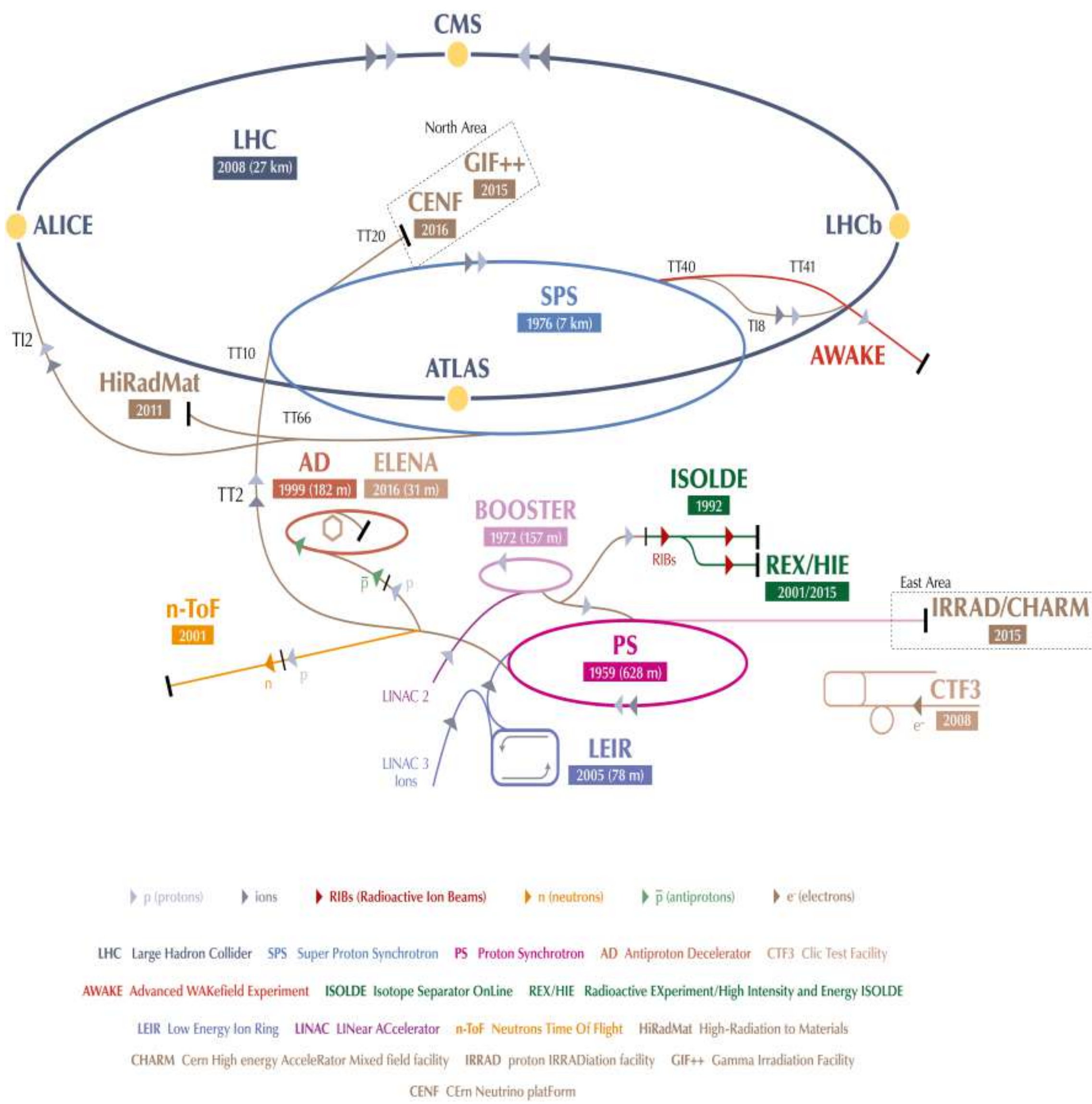

Figure 1.1: The LHC ring along with its several small accelerator rings. [21]

1.2.1 Detectors at the LHC

The collision takes place at four points where the detector systems are installed. The physics goals of the detector systems are given below.

A Large Ion Collider Experiment (ALICE) [22]

Since the Big Bang Theory predicts the existence of quark-gluon plasma before they were bound to form protons and neutrons, its main goal is to recreate the state and study the physics of strongly interacting matter at extreme energy densities created in PbPb collisions.

Large Hadron Collider beauty (LHCb) [23]

It is believed that equal quantities of matter and antimatter were formed at the time of the Big Bang. However, as the universe cooled and expanded, only matter existed. The experiment is aimed to investigate the difference in the quantities of matter and antimatter.

A Toroidal LHC Apparatus (ATLAS) and Compact Muon Solenoid (CMS) [24, 25]

Although ATLAS and CMS use different designs, both the detector systems share similar physics goals and therefore corroborate each other's findings. In June 2011, both ATLAS and CMS confirmed the evidence of Higgs boson like particle [26–28]. Further, the aim is to - (i) study the properties of the discovered Higgs boson, (ii) look for evidence beyond SM (BSM) like supersymmetry, extra-dimensions, etc. (iii) explore physics at TeV scale, (iv) investigate charge parity (CP) violation, (v) perform precision measurements, etc.

1.2.2 The CMS detector

The CMS detector is 22 m long, 15 m wide and weighs about 12.5 t. It is composed of several components, which are discussed below. The components are placed such that the collision event can be reconstructed from the data collected by each component. The CMS detector along with its components is shown in Fig. 1.2.

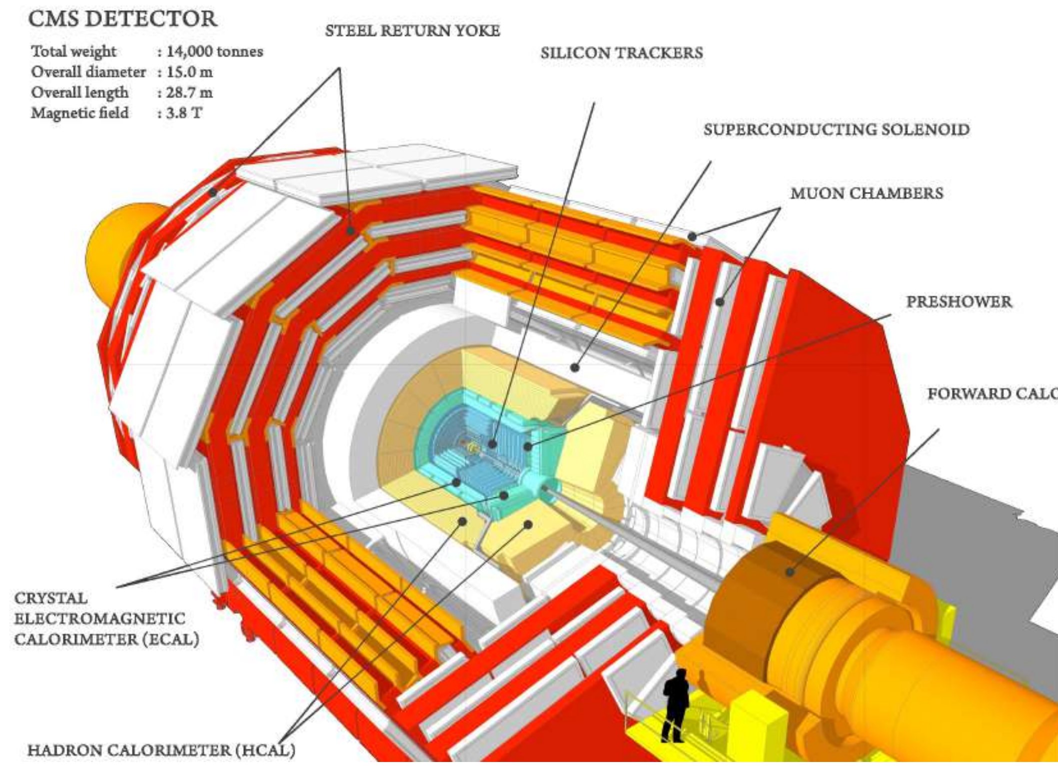

Figure 1.2: The CMS detector and its components.

Silicon tracker

The tracker (discussed in detail in section 1.2.3) is assembled with silicon pixel and micro-strip detectors. It can reconstruct TRACKS OF high transverse momentum (p_T) muons, isolated electrons and CHARGED hadrons with a high momentum resolution and an efficiency better than 98%.

Electromagnetic calorimeter (ECAL)

The choice of lead tungstate ($PbWO_4$) crystals for the ECAL is because of their high density and small radiation length. The electrons, positrons, and photons are completely absorbed in the ECAL, thereby generating a cascade of secondary particles due to Bremsstrahlung or pair production, the signal is then amplified by photodiodes.

Hadron calorimeter (HCAL)

HCAL uses alternate layers of active material - plastic scintillator, and passive absorber material - copper and steel. It enables the identification of quarks and gluons as jets and neutrinos through missing transverse energy.

Solenoid magnet

The solenoid magnet is a 13 m long superconducting magnetic coil and a 6 m inner diameter, with a uniform magnetic field of 3.8 T inside its coil. Such a high value of the magnetic field was chosen for large bending of the charge particles to measure their momentum with precision in the tracker and to identify them in the calorimeters.

Muon system

Three types of gaseous detectors - (i) Drift Tubes (DT), (ii) Cathode Strip Chambers (CSC), and (iii) Resistive Parallel Plate Chambers (RPC) are used for the muon detection.

Co-ordinate system

By convention, the co-ordinate origin for CMS is set to the collision origin. From the collision origin, the vertically upward axis is the Y-axis, the X-axis points vertically inwards to the centre of the LHC ring, and the Z-axis is in the direction of the anticlockwise beam. In the polar coordinates, the azimuthal angle, ϕ and radial coordinate, r are defined in the XY-plane. The polar angle, θ is defined in the rZ-plane. But, since θ is not a Lorentz invariant quantity, a new co-ordinate known as pseudorapidity (η) is defined as: η = - ln tan(θ/2), where η_2 - η_1 is lorentz invariant.

1.2.3 The silicon tracker system

The CMS tracker system consists of several layers of pixel and micro-strip silicon sensors. When a particle passes through the tracker system, a hit is recorded at the sensor and the layer level. This data is then used to reconstruct the path of the particle. For an accurate track reconstruction, the tracker must have a good position resolution and should minimally disturb the incident particle. A low occupancy [1] along with high spatial resolution and fast read-out is desirable for good pattern recognition.

[1] An occupancy is defined as the percentage of the signal read-out channels with respect to all read-out channels.

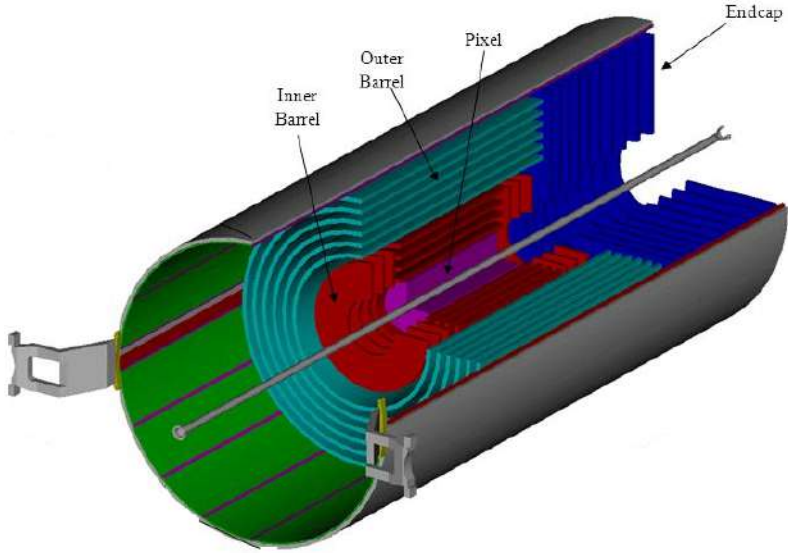

Figure 1.3: The layout of the CMS silicon tracker [29].

Layout

The layout of the silicon tracker system comes from the motivation that it should be robust, and reliable in track reconstruction and momentum measurement in a dense particle environment (see Fig. 1.3). Therefore, based on this, a geometry of concentric cylindrical barrel layers and annular end-caps to ensure maximum η coverage. While the silicon strip sensors in the barrel, also known as the r-ϕ sensors, are oriented along the beam direction (i.e. Z-axis), thereby providing an accurate measurement in the bending plane; in the forward (end-cap) region, the strips are placed perpendicular to the beam direction, to obtain an optimum measurement of ϕ coordinate. Stereo angle sensors (or, L1 trigger based sensors) are further helpful in improving the vertex measurement and track reconstruction. More details on the choice of the design and layout of the tracker can be found in Ref. [30].

Spatial resolution

The spatial or position resolution (σ_{position}) of a sensor depends on two parameters - strip pitch (s_p) and readout method (digital and analog). For the digital readout, σ_{position} can be calculated [61] to be -

$$\sigma_{position,digital} = \frac{s_p}{\sqrt{12}} \tag{1.1}$$

However, an additional improvement in the σ_{position} is seen for the analog readout. The σ_{position} depends on the choice of reconstruction algorithm and the amount of charge sharing between two read-out channels.

$$\sigma_{position,analog} = \frac{s_p}{SNR} \tag{1.2}$$

where, SNR is signal to noise ratio.

Momentum of particle

With the application of a magnetic field ($\vec{B}$), the charged particle of mass m, moving at a tangential speed of $v_\perp$, along a path with radius of curvature, R experiences Lorentz force ($\vec{F}_{Lorentz}$), which when balanced with the centripetal force ($F_{centripetal}$) yields [31] -

$$p_\perp c[GeV] = 0.3 \quad B[T] \quad R[m] \tag{1.3}$$

where $p_\perp$ is transverse momentum.

Charge of particle

The left handed or right handed curvature of the incoming particle gives hint of the positive or negative charge of the particle.

1.3 Radiation environment experienced by silicon sensors

Since tracking sensors are situated close to the interaction point, they suffer a high particle flux environment of charged (protons, pions, etc.) and neutral (neutron and photons) radiation. This can lead to the formation of crystal defects, causing damage to the bulk and surface properties of the silicon. A change in the sensor full depletion voltage, increase in the total leakage current and a drastic decrease in the charge collection efficiency (CCE) is observed. The properties further degrade with a long term operation of the detector in the radiation environment, ultimately making it unfit for particle detection [32–35]. The bulk and the surface damage in silicon are briefly described in the following section.

Table 1.2: Threshold energy for the creation of point and cluster defects [36, 37].

Particle	$E_{th,point}$	$E_{th,cluster}$
Electron	255 keV	8000 keV
Proton	0.19 keV	5 keV
Neutron	0.19 keV	35 keV
Cobalt-60 gamma	1000 keV	No cluster

1.3.1 Bulk damage

Incident particles, apart from ionizing the silicon lattice, also interact with the silicon atoms via the non-ionizing energy loss (NIEL) [38]. If the particle transfers an energy greater than the threshold energy (E_{th}), the silicon atom (primary knock-on atom, PKA) gets displaced from its lattice site, creating a vacancy (V) and an interstitial (I) elsewhere. The PKA can further cause ionization and displacements (Frenkel defects - V, I) along its track in the lattice. These V's and I's migrate into the silicon bulk and form stable defect complexes with other V's and I's or impurities (like carbon, oxygen, etc.). The point and cluster defects thus formed induce electrically active acceptor and donor type of traps. Depending on the trap's energy level in the silicon band gap, electron and hole capture cross-section, introduction rate, etc., the trap acts as either a recombination-generation centre (increasing the leakage current with irradiation), a deep trap centre (affects the bulk space charge), or a trap centre for electron or hole charge carriers (reducing the CCE). Table 1.2 lists the values of E_{th} for an electron, proton and neutron.

The comparison of radiation damage for different incident particles, with energies is done through the NIEL hypothesis, which states that damage due to the silicon atom displacement can be scaled linearly with the amount of energy imparted in the displacement collisions irrespective of the interaction mechanisms of the particles, with the bulk damage caused by the mono-energetic 1 MeV neutrons considered as calibration reference. Thus, particle fluence (ϕ) is defined as 1 MeV neutron equivalent fluence (ϕ_{eq}) multiplied with an appropriate hardness factor (κ), where κ depends on the particle type and its energy.

$$\phi = \kappa \times \phi_{eq} \tag{1.4}$$

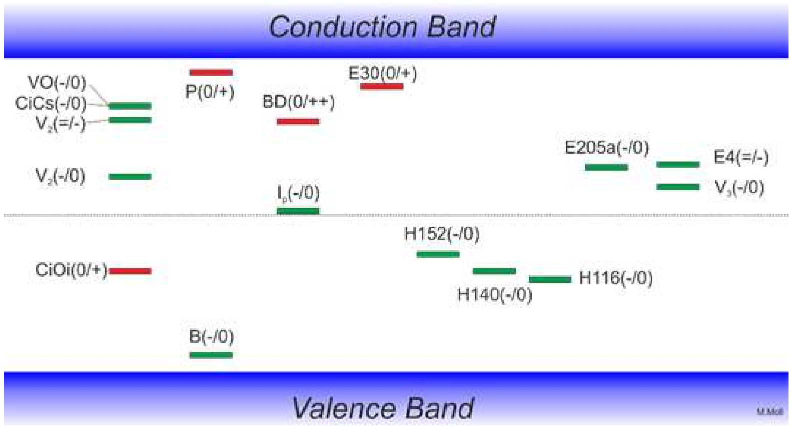

Figure 1.4: A few experimentally observed defects [39].

1.3.2 Surface damage

Unlike the bulk damage, the surface damage is caused by ionization (electron-hole pair generation) of SiO_2 rather than atomic displacement. A complete recombination does not take place in the SiO_2 because the electrons with higher mobility, drift quickly to the metal electrode, but the holes drift via the hopping mechanism. The defect concentration is high at the Si-SiO_2 interface due to the lattice distortion and the dangling bonds. Therefore, holes get trapped in these defects and form a positive fixed charge traps (N_{ox}). Further, the deep traps along the interface act as recombination-generation centre, contributing to surface leakage current or as trap centres known as interface traps (N_{it}). The presence of N_{ox} attracts electrons towards the surface, leading to formation of an electron accumulation layer. Such an accumulation of electrons at the p^+ strip implants creates a region of high electric field which may lead to decrease in the breakdown voltage. It may also lead to non-depleted regions which may result in loss of signal. Additionally, it leads to an increase in interstrip capacitance (noise increase) and decrease in interstrip resistance (cross-talk increase). A spread in the signal leads to a loss of the position resolution of the sensor.

1.3.3 Defects identification techniques

There exist several defects identification techniques like deep level transient spectroscopy (DLTS), thermally stimulated current (TSC), etc. The DLTS technique requires to reverse bias the PN junction and fill the defect levels by laser pulsing. The emission spectra gives information of the defect levels. However, this technique is relevant only if the defect concentration is lower than the effective doping concentration. Therefore, DLTS is not useful for highly irradiated PN junction. On the other hand, TSC involves reverse biasing the PN junction and cooling it to low temperatures. The defects are then filled up by illumination. As the PN junction is heated, maintaining the reverse bias condition, the TSC spectrum is recorded. A peak at a particular temperature corresponds to the emission of the carrier from the corresponding defect level. This techniques is useful in measuring highly irradiated devices. Fig. 1.4 shows the different levels created in the band gap due to experimentally found defect.

Table 1.3: The LHC operation schedule (taken from [40]).

Time period	**Phase**	$\sqrt{s}$ **TeV**	**L** $\mathbf{cm^{-2}.s^{-1}}$	$\mathbf{N_p}$ $\mathbf{10^{11}}$	$\mathbf{B_s}$ **ns**	**Int. L** $\mathbf{fb^{-1}}$	**Pile-up**
2010 to 2012	Run-1	7-8	0.8×10^{34}	1.7	50	20-25	21
2013 to 2014	Longshutdown-1						
2015 to 2018	Run-2	13-14	2×10^{34}	1.2	25	75-100	21-50
2019 to 2020	Longshutdown-2						
2021 to 2023	Run-3	14	2×10^{34}	1.2	25	350	21-50
2024 to 2025	Longshutdown-3						
2025 to 2035	Run-4 (HL-LHC)	14	5×10^{34}	2.2	25	3000	140

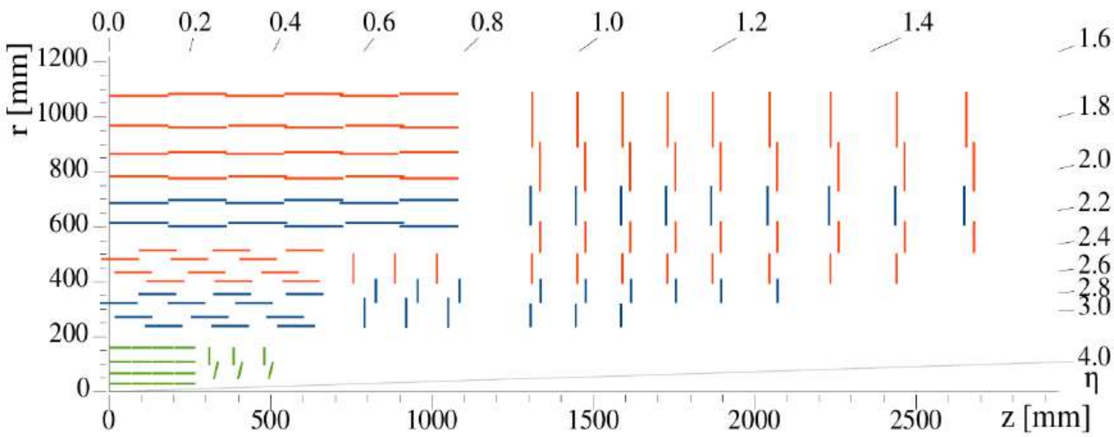

(a)

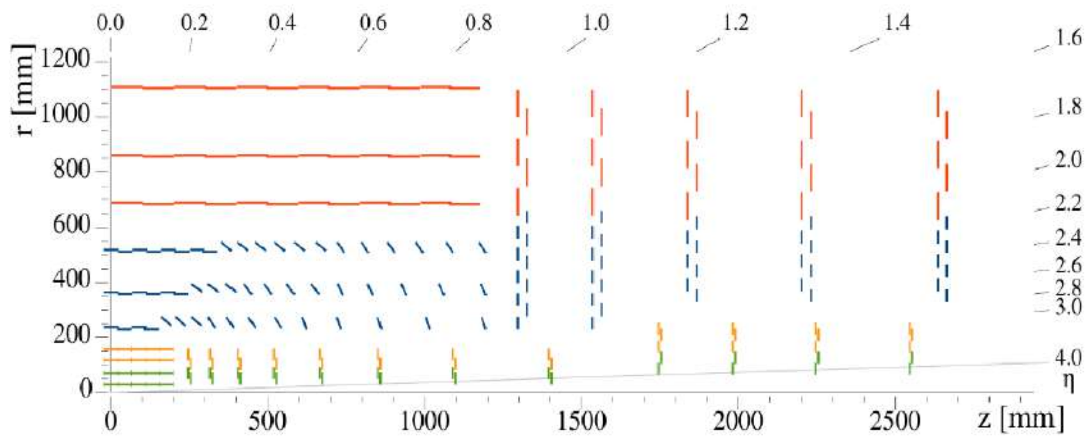

(b)

Figure 1.5: One quarter of tracker system layout during - (a) Phase I (Pixel detector, Single sided strip modules, Double sided strip modules) and (b) Phase II (Pixel detector, 2S modules, PS modules).

1.4 The High-Luminosity (HL) - LHC phase

The LHC plans to enter the High Luminosity LHC (HL-LHC) phase [41–43] and the expected change in the LHC parameters from LHC to HL-LHC phase are listed in Table 1.3. The tracker layout in the LHC and the HL-LHC phase are shown in Fig. 1.5. The conditions in the HL-LHC phase will create an even harsher radiation environment (enormous increase in particle flux) for the detector operation, especially for the tracker system. It can be viewed from Fig. 1.6 that the FLUKA simulated 1 MeV neutron equivalent hadron fluence inside the CMS tracker foresee almost a ten times increase in the fluence for the HL-LHC phase than the LHC phase.

Keeping in mind the challenging radiation environment and the effect of radiation damage on the silicon sensors; the requirements and the features of the proposed CMS tracker system are listed in this section. A detailed information can be found in Ref. [44].

Requirements of an upgraded tracker

1. To be radiation tolerant and operational up to an integrated luminosity of 3000 fb^{-1} as the particle flux will be 10 times higher than the current flux.
2. To have an increased granularity, i.e. high channel density, in order to keep low channel occupancy of less than 1%.
3. To reduce material budget for enhanced performance of tracker and calorimeter so as to improve tracking and thereby event reconstruction.
4. To introduce Level-1 trigger for selection of only interesting physics events due to high pile up in the HL-LHC phase.
5. To possess an efficient layout to enable robust pattern recognition for efficient tracking.
6. To extend the tracking acceptance to ameliorate the CMS physics capabilities.
7. To be operated at a temperature so as to minimise power consumption.

Features of the proposed upgrade tracker

1. Silicon sensors of n-in-p type are being considered - planar and 3D sensors for inner tracker and 2S and PS modules (discussed in next section) for outer tracker.
2. The dimensions for the smallest unit of, (i) pixel - $50\,\mu\text{m} \times 50\,\mu\text{m}$ or $25\,\mu\text{m} \times 100\,\mu\text{m}$, (ii) 2S - 5 cm $\times$ $90\,\mu\text{m}$, and (iii) PS - 2.4 cm $\times$ $100\,\mu\text{m}$ and 1.5 mm $\times$ $100\,\mu\text{m}$, are being examined.

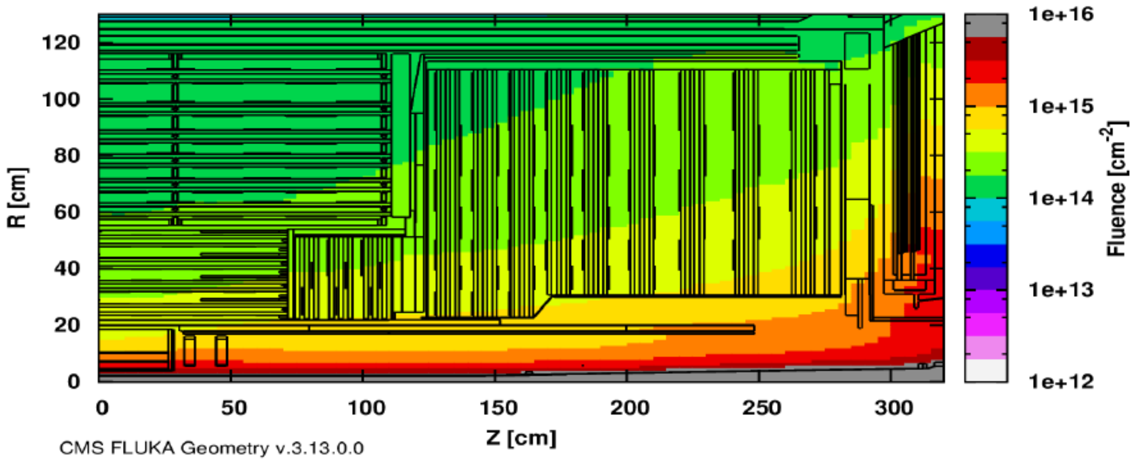

(a)

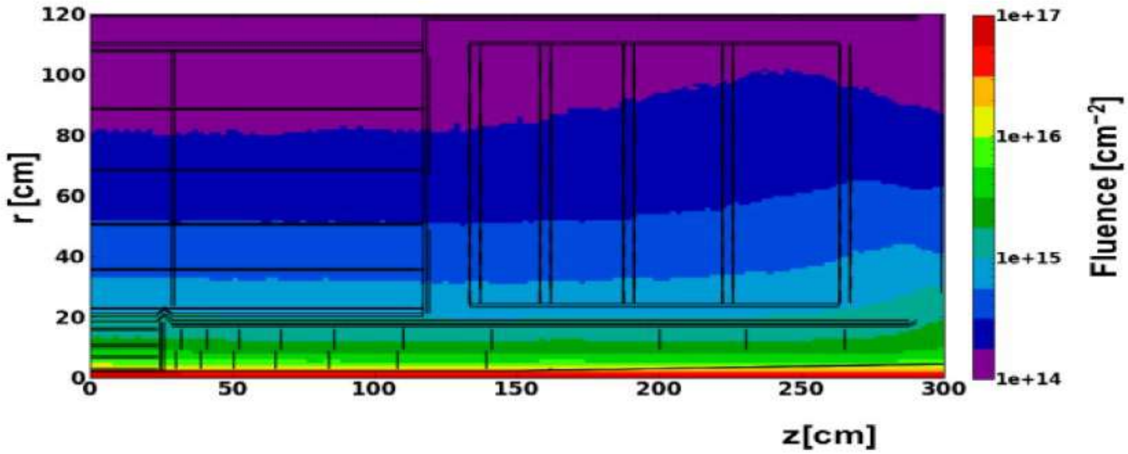

(b)

Figure 1.6: The simulated expected hadron fluence in FLUKA (in units of 1 MeV n_{eq}.cm^{-2}) on the CMS tracker during (a) LHC run for 300 fb^{-1}, and (b) HL-LHC run for 3000 fb^{-1} (from Refs. [45, 46]).

3. While the choice of the thickness for the inner tracker will be between 100 and $150\,\mu\mathrm{m}$, for the outer tracker it will be 200, 240, or $300\,\mu\mathrm{m}$. For the outer tracker, the number of layers have been reduced from 10 to 6 and 12 to 5 in the barrel and end cap regions respectively.

4. The correlation of the signals in the two sensors of a module, connected by the same front end ASIC readout. If it lies outside the defined 'selection window', the event is rejected as low p_T particle (< 2 GeV). If it lies inside the selection window, then it is accepted and is defined as a 'stub' (see Fig. 1.7a). This will allow a data reduction of about 10-100 times at the detector level.

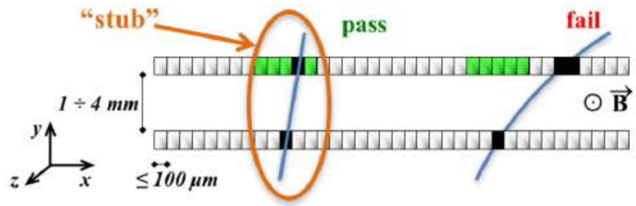

(a)

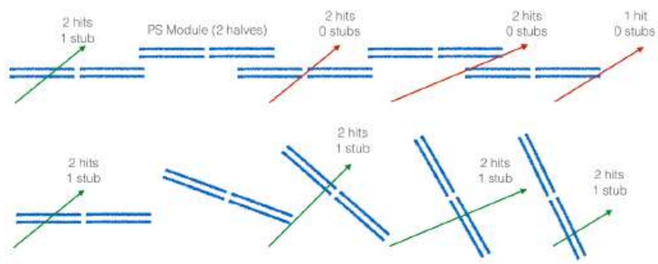

(b)

Figure 1.7: (a) The concept of ‘stub’ formation. (b) Tilted barrel to maximise the stub efficiency.

5. In order to optimize the stub efficiency, a tilted barrel will be used for some regions containing PS modules (see Fig. 1.7b).
6. An extended eta coverage from $\eta \leq 2.4$ to 4 is planned to increase the forward acceptance and mitigate pile up effects in the forward region.
7. The tracker will be operated at a temperature of $\leq$ -20 °C.

Few change in properties of the CMS tracker in the HL-LHC phase from the LHC phase are listed in Table 1.4.

Table 1.4: CMS Tracker in LHC and HL-LHC phase (from [47]).

	Property	**LHC phase**	**HL-LHC phase**
Inner tracker	Barrel layer	3+1 pixel	4 pixel
	End-cap layers	2 pixel	10 pixel
	Sensor thickness	285 μm	100-300 μm
	η	< 2.5	< 4
	Temperature	263 K	253 K
Outer tracker	Barrel layer	10 strip	3 p_T PS module, 3 p_T 2S module
	End-cap layers	12 strip	5 p_T PS and 2S modules
	Sensor thickness	320, 500 μm	200, 240, 300 μm
	η	< 2.5	< 4
	Temperature	263 K	253 K

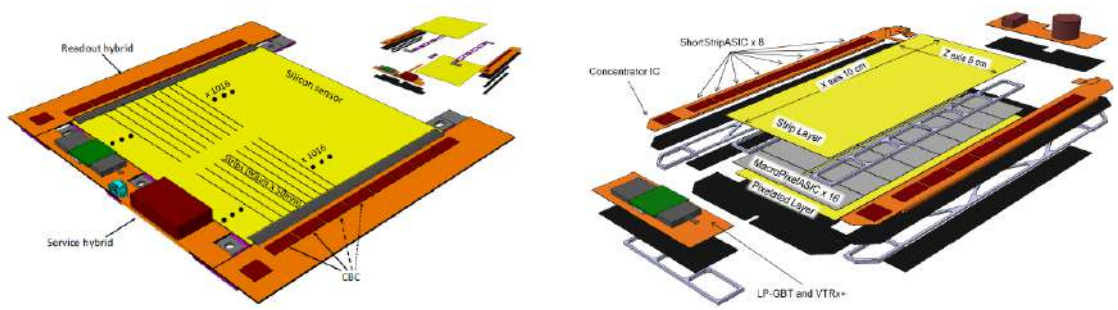

(a) (b)

Figure 1.8: Perspective view of (a) 2S and (b) PS modules (from Refs. [48, 49]).

2S and PS modules

As discussed above, the upgrade tracker will be composed of 2 types of p_T modules - 2S and PS (see Fig. 1.8). Both the modules are composed of 2 sensors stacked in parallel and separated by some distance. The 2S module is composed of 2 AC-coupled strip sensors of 10 cm $\times$ 10 cm size, with 2 rows of strips of 5 cm length and $90\,\mu\mathrm{m}$ pitch. The PS module is composed of - (a) 1 AC-coupled strip sensor of 5 cm $\times$ 10 cm size, with 2 rows of strips of 2.5 cm length and $100\,\mu\mathrm{m}$ pitch and (b) 1 macro-pixel DC-coupled sensor of 5 cm $\times$ 10 cm size, with 32 rows of macro-pixels of 1.5 mm length and $100\,\mu\mathrm{m}$ pitch. A spacing of 1.8, 4 mm and 1.6, 2.6 and 4 mm is foreseen for the 2S and PS modules.

1.5 Motivation of the work

The silicon strip sensors play a key role in HEP experiments due to their superior performance in terms of radiation hardness resulting in robust and reliable charged particle tracks and vertex reconstruction. However, owing to the placement of these sensors in the (harsh) radiation environment imposed by current and future HEP experiments, the radiation hardness study is invaluable both for optimizing the sensor design or developing new sensor configurations. Further, the usage of a large quantity of sensors meeting stringent tolerances in various experiments demands for a quality assurance scheme.

This thesis is devoted to the characterization studies of the silicon sensors for their performance and study of novel sensor designs through Technological Computer Aided Design (TCAD) simulations for their survival in harsh radiation sectors. The research work consists of non-irradiated and irradiated characterization study of the AC-coupled, polysilicon biased silicon strip sensors developed in India. The establishment of the silicon sensor characterization laboratory at University of Delhi is also discussed. On the simulation front, radiation hardness studies were performed on Low Gain Avalanche Detector (LGAD), pixel, and low resistivity silicon sensors.

1.6 Thesis Outline

This thesis is devoted to the studies of the performance of the silicon sensors and their survival in harsh radiation sectors. The thesis is described in seven chapters, an overview of each of the chapters is given below.

Chapter one aims to give an overview of the LHC and the different sub-systems of the CMS detector. It provides a brief introduction of the current all - silicon tracker system of the CMS detector highlighting the major features of the silicon sensors. Further, it describes the expected upgrade requirement of the silicon sensor technology for survival in harsher radiation environment of the planned LHC upgrade. Lastly, the motivation for the work performed and the thesis organization are described.

Chapter two provides an introduction to silicon and its properties that make it suitable for tracker and calorimeter of the HEP experiments. The various methods for the production of a silicon wafer and the process for fabricating it into a polysilicon biased, AC-coupled silicon sensor are discussed. The deterioration of silicon sensor properties due to harsh radiation environment is explained. This is followed by discussion on the different design parameters that must be taken into account for a good quality silicon detector. It also underlines the importance of high signal to noise ratio and the components affecting it. The various configurations of silicon sensors prevalent in the HEP community and proposed novel silicon sensors are discussed. A brief account of radiation damage on its properties is explained to understand the performance degradation in terms of particle detection of the silicon sensor. This chapter also contains details of the Technology Computer Aided Design (TCAD) tool, Silvaco and the radiation damage model employed for simulation results reported in this thesis.

Chapter three reports the development of p-on-n silicon strip sensors having multiple guard-ring structures for High Energy Physics applications. The study constitutes the optimization of the sensor design; indigenous fabrication of AC-coupled, poly-silicon biased sensors of strip width of $30\,\mu\mathrm{m}$ and strip pitch of $55\,\mu\mathrm{m}$ on 4 inch n-type wafers of thickness of $300\,\mu\mathrm{m}$, with an average resistivity of 2-5 $\mathrm{k}\Omega\cdot\mathrm{cm}$; and their electrical characterization to qualify them as particle sensors. The electrical characterization comprises of - global measurements of total leakage current, and backplane capacitance; strip and voltage scans of strip leakage current, poly-silicon resistance, interstrip capacitance, interstrip resistance, coupling capacitance, and dielectric current, and Alibava based charge collection. The results of the same are reported. Since the silicon sensors to be deployed in the next generation high energy physics experiments for operation in high luminosity scenarios require a high level of radiation tolerance, few of the fabricated strip sensors were irradiated with protons at different fluences at the Karlsruhe Cyclotron facility under the Advanced European Infrastructures for sensors at Accelerators (AIDA). The chapter also reports on the radiation hardness study performed on the fabricated sensors, where the characterization comprises of electrical tests, including total current, voltage and strip scans and charge collection studies.

Chapter four contains details of installation and commissioning of the characterization systems at the University of Delhi (DU), along with a few measurement results. The CMS tracking system will demand a large quantity of multi-strip silicon sensors, which must fulfil stringent tolerance criteria to maintain the physics performance in the High Luminosity (HL) phase of the LHC. Thus, a subset of the fabricated sensors (from a given batch of fabricated sensors) must be extensively tested prior to the installation in the main detector system. This will be achieved through measurement of various global and strip parameters of silicon strip sensors as envisaged in a detailed quality assurance program for phase II upgrade of CMS tracker. In order, to handle the large quantity of the strip sensors, the characterization setup should have multi-functionality features, including automation. A fully automated and programmable characterization system for testing silicon multi-strip sensors has been installed at the University of Delhi, and is described in this chapter.

Chapter five is dedicated to understand the radiation damage using simulations on the Low Gain Avalanche sensors (LGADs) that have a unique characteristic to provide amplification to the particle signal by using a controlled local avalanche mechanism. These devices are being explored by the HEP community since it is known that in standard silicon sensors the signal-to-noise ratio falls drastically with fluence, in LGAD devices this can be made sufficiently high to potentially overcome this problem. However, the existing irradiation studies show that the LGAD internal gain disappears at high fluences and is no more significant. In this chapter, detailed simulation using TCAD Silvaco has been carried out on non-irradiated and irradiated LGADs. The effects of different design parameters and proton irradiation on LGAD operation are discussed in detail. The TCAD simulation for irradiated LGAD devices produce decreasing gain with increasing fluence, similar to the measurement results.The space charge density and electric field distribution are used to illustrate the possible reasons for the degradation of gain of the irradiated LGAD devices. Additionally, the effect of various design parameters of the LGAD device on its gain characteristic, at different irradiation levels has been studied.

Chapter six is a compilation of (a) TCAD simulation results of radiation hardness studies on pixel sensors and (b) low bulk resistivity sensors.
To develop radiation hard pixel sensors for the CMS phase 2 upgrade and the HL-LHC radiation environment, simulations have been performed using Silvaco, to obtain design parameters. The effect of various design parameters like pixel size, pixel depth etc. on the leakage current and critical electric field are studied for both non-irradiated as well as irradiated pixel sensors. These simulation results of planar pixels are useful for providing insight into the behaviour of silicon pixel sensors.
Moreover, as a novel sensor design and owing to their better ability for higher charge collection efficiency and internal charge multiplication, there has been an increased interest for the relatively higher bulk doping density (10^{13} - 10^{14} cm^{-3}) Si sensors. However, detailed investigations are required for studying the radiation damage effects on these low resistivity devices. In the present work, a systematic TCAD simulation study for the effect of proton fluence (up to 3×10^{15} n_{eq}.cm^{-2}) on charge collection efficiency, leakage current and electric field distribution etc. of p-type Si diodes of varied thicknesses is reported. The results show promising future for these devices.

Chapter seven summarizes the complete work performed in this thesis.

Chapter 2

The physics of silicon sensors and the simulation framework

The chapter aims to give an introduction to semiconductor (SC) physics, the trending SC - silicon and its characteristic properties that make it fit for particle detection. The various methods for the production of a silicon wafer and the process for fabricating it into a silicon sensor are discussed. The chapter not only highlights the different design parameters that must be taken into account for a good quality particle sensor, but also underlines the importance of requirement of a high signal to noise ratio (SNR) and the parameters affecting it. Based on the proposition, various configurations of silicon sensors prevalent in the HEP community and proposed novel designs are described. Since the physics of silicon sensor would be incomplete without pointing out its operational behaviour in a radiation environment, a brief account of radiation damage on its properties is explained to understand the performance degradation in terms of particle detection. The change in the silicon lattice due to incident radiation is also explained.

Furthermore, the TCAD simulation tool - Silvaco has been used for investigating different aspects of silicon sensors in Chapters 5 and 6 of this thesis. The experimental challenges, cost, environmental conditions, availability of human and material resources, etc. associated with the fabrication and measurement of sensors are limiting for an elaborate R&D study. Here, the device simulation comes into picture. After an initial calibration of the models, etc., the simulations can be used to optimize the various design parameters as per requirement. Thus, simulations not only save lot of efforts, but can also be used to explore novel detector designs. For this reason, the operation of the tool and its calibration is described in detail in this chapter.

2.1 Silicon - The trending semiconductor

2.1.1 The band theory of solid-state physics

When atoms come close together to form a lattice, a redistribution of electron energies takes place. Instead of discrete energy levels, a continuum of closely spaced energy levels, effectively known as energy bands - conduction band (CB) and valence band (VB), separated by an energy band gap (BG) are formed. Depending on the BG, a material is classified as a metal (VB and CB overlap), an insulator (BG $\geq$ 5 eV), or a semiconductor (SC) (BG $\sim$ 0.1-5 eV). The mathematical expressions provided in the subsequent sections are taken from Refs. [50, 51].

2.1.2 Semiconductor Physics

Intrinsic SC

In a SC, when an electron excites from the VB to the CB by thermal excitation or absorption of a photon, it does so by leaving behind a hole [1]. The equation of motion is governed by electrons and holes in CB and VB respectively. Thus, the number of electrons in CB (number of holes in VB) - $n(p)$ can be written in terms of:
(i) $E_{CB(VB)}$ - the lowest energy level of CB (highest energy level of VB),
(ii) $D_{CB(E)}$ and $D_{VB(E)}$ - the available density of states in CB (VB),
(iii) $m^*_{n(p)}$ - the effective mass of electron in CB (hole in VB) [2], and
(iv) $f(E,T)$ - the probability for the occupancy of a state is given by fermi function (where E_F is the energy level at which the probability of states being occupied is 50%).

$$n = \int_{E_{CB}}^{\infty} D_{CB}(E) \,.\, f(E,T)\, dE \quad \text{and} \quad p = \int_{-\infty}^{E_{VB}} D_{VB}(E) \,.\, \Big[1 - f(E,T)\Big] dE \tag{2.1}$$

[1] The motion of the valence electron into an empty state can be thought to be equivalent to the motion of the positively charged empty state itself. This positively charged empty state is known as the hole.

[2] The motion of the electron in a crystal can be considered equivalent to a free electron if its effective mass takes into account the mass of the electron and the effect of the internal forces.

where,

$$D_{CB}\left(E\right)=\frac{2m_{n}^{*3/2}}{2\pi^{2}\hbar^{3}}\sqrt{E-E_{CB}}\quad\text{and}\quad D_{VB}\left(E\right)=\frac{2m_{p}^{*3/2}}{2\pi^{2}\hbar^{3}}\sqrt{E_{VB}-E}\tag{2.2}$$

$$f\left(E,T\right)=\frac{1}{exp\left(\frac{E-E_{F}}{k_{B}T}\right)+1},E>E_{F}\tag{2.3}$$

For an intrinsic SC, the number of intrinsic charge carriers (n_i) is equal to both the number of electrons in CB and to the number of holes in VB. This is also known as the *mass action law*.

$$n_{i}^{2}=n=p\tag{2.4}$$

The value of the resistivity (ρ) or, conductance (σ) of a SC material gives information about its electrical conduction behaviour. It is defined as following (e is the electronic charge and $\mu_{e,h}$ is the mobility of electrons in CB and holes in VB):

$$\frac{1}{\rho}=\sigma=e\left(n\mu_{e}+p\mu_{h}\right)\tag{2.5}$$

Extrinsic SC

Extrinsic SC (p-type and n-type) are formed by doping (addition of impurities to an intrinsic SC) the SC with trivalent (acceptor) and pentavalent (donor) elements respectively. This addition of acceptor (N_a) and donor (N_d) concentrations leads to the creation of new energy levels within the BG. A p-type SC has holes and electrons as the majority and minority carriers respectively, where as it is the opposite for a n-type SC. It may be noted that the law of mass action is valid for both p-type and n-type SCs, i.e.

$$n_{i}^{2}=n_{n}p_{n}=n_{p}p_{p}\tag{2.6}$$

where $n_{n,p}$ and $p_{n,p}$ are the electron and hole concentrations in n- and p-type SCs.

Additionally, it may be noted that an extrinsic SC is in the 'complete ionization' state at 300 K [3] and the number of thermal electrons (holes) are negligible compared to that from N_d (N_a). This implies that for a n-type SC, $en_n \sim |+e|N_d$ and for a p-type SC, $ep_{\mathrm{p}} \sim |-e|N_a$.

[3] Complete ionization implies that electrons of almost all donor impurity atoms have ionized to the CB.

This means that for n-type and p-type SC, the expression for ρ effectively becomes equal to:

$$\frac{1}{\rho_n} = |+e|N_d\mu_e \quad \text{and} \quad \frac{1}{\rho_p} = |-e|N_a\mu_h \tag{2.7}$$

2.1.3 PN Junction

A pn junction (see Fig. 2.1) is obtained when p-type and n-type SCs are diffused together. The difference in the concentration of carriers on either side causes diffusion to take place (i.e. electrons move from n- to p-type and holes move from p- to n-type). However, with diffusion a space charge region (SCR), also called the depletion region, is formed. This acts as a barrier potential to further diffusion, known as the built-in potential, V_{bi}. By considering a uniformly doped pn junction and taking the abrupt junction approximation [4], the electric field (E) and the potential (V^{pot}) can be calculated by solving the Poisson equation, where ρ_{pn} and ϵ_{SC} are charge density of pn junction and permittivity of SC (= ϵ_0 * ϵ_{Si}^{rel}) respectively:

$$\frac{\partial E}{\partial x} = -\frac{d^2V^{pot}}{dx^2} = \frac{\rho_{pn}(x)}{\epsilon_{SC}} = \frac{e(-N_a + N_d)}{\epsilon_{SC}} \tag{2.8}$$

Expression for electric field

Using the boundary condition, $E_p(-x_p) = 0$ and $E_n(x_n) = 0$, where $x_{p(n)}$ is space charge depth inside $p(n)$-type SC; the expression for E becomes:

$$E_p = \frac{-eN_a(x + x_p)}{\epsilon_{SC}} \quad \text{and} \quad E_n = \frac{eN_d(x - x_n)}{\epsilon_{SC}} \tag{2.9}$$

The expressions for the maximum E (E_{max}) at the junction (i.e. x = 0) is calculated by using another boundary condition, which is $E_{\text{p-type}}(0) = E_{\text{n-type}}(0) = E_{max}$.

$$E_{max} = \frac{-eN_ax_p}{\epsilon_{SC}} = \frac{-eN_dx_n}{\epsilon_{SC}} \tag{2.10}$$

This expression also shows the charge neutrality in the pn junction, $|+eN_dx_n = |-e|N_ax_p$.

[4] The abrupt junction approximation assumes that the space charge region abruptly ends at +x_n and -x_p.

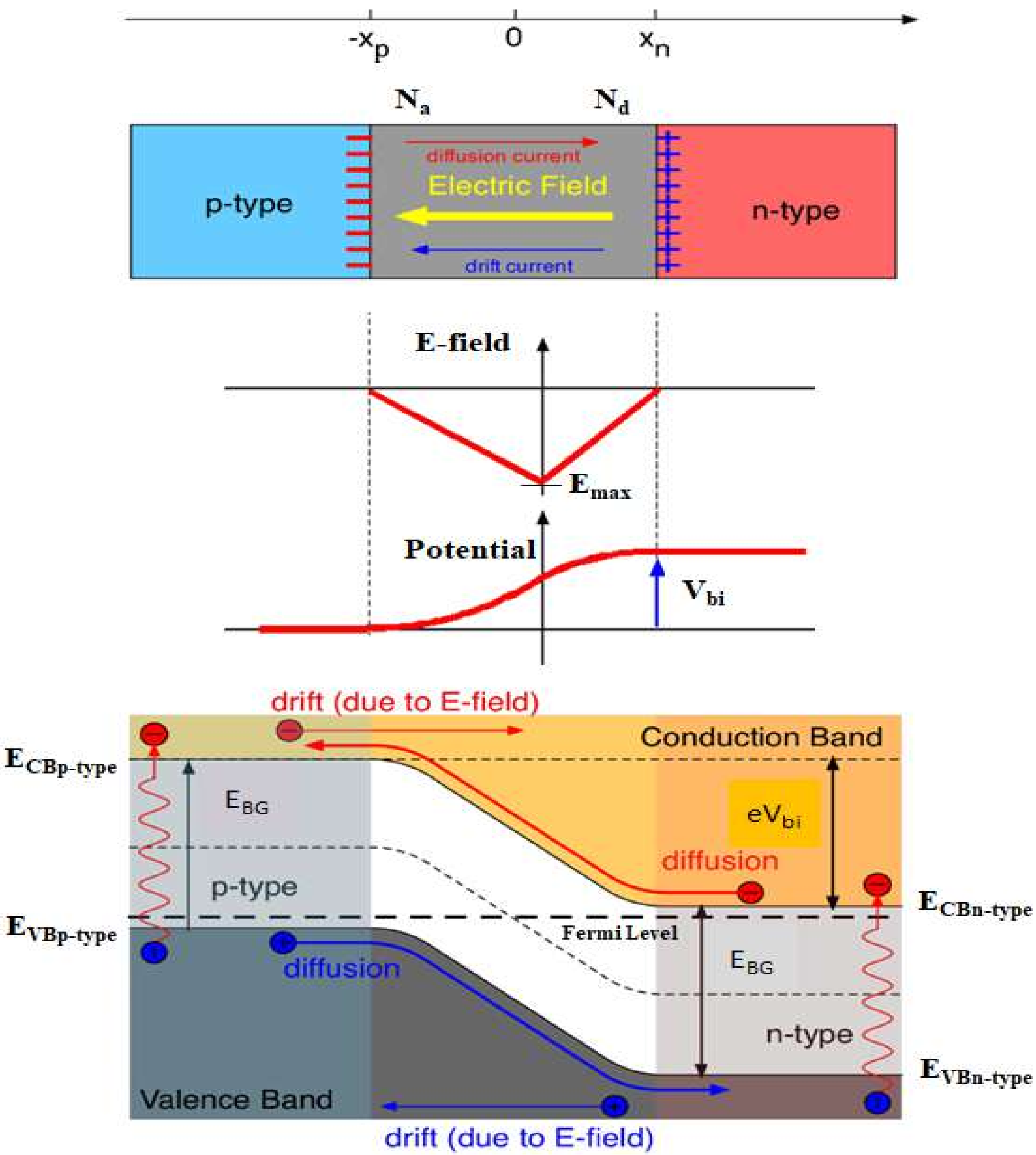

Figure 2.1: The figure shows the pn junction, the electric field profile and electric potential developed inside it. Additionally, the flow of diffusion and drift currents are shown pictorially. (Figure taken from Ref. [52].)

Expression for potential

Since, it is the potential difference that has significance rather than absolute potential, for convenience $V_{pot,p}(-x_p) = 0$ is assumed. By also using the boundary condition of $V_{pot,p}(0)$

= $V_{pot,n}(0)$, the above given expressions simplify to:

$$V_{pot,p} = \frac{eN_a}{2\epsilon_{SC}} (x + x_p)^2 \quad \text{and} \quad V_{pot,n} = \frac{eN_d}{\epsilon_{SC}} \left(\frac{-x^2}{2} + x_n x \right) + \frac{eN_a}{\epsilon_{SC}} \left(\frac{x_p^2}{2} \right) \tag{2.11}$$

The expression for V_{bi} is then given as the difference of $V_{pot,n}(x_n)$ and $V_{pot,p}(-x_p)$, as below:

$$V_{bi} = \frac{e}{2\epsilon_{SC}} \left(N_a x_p^2 + N_d x_n^2 \right) \tag{2.12}$$

Expression for space charge width

The depletion width or the SCR width (w) is the sum of x_p and x_n.

$$w = x_p + x_n = \left[\frac{2\epsilon_{SC} V_{bi}}{e} \frac{1}{N_a + N_d} \right]^{\frac{1}{2}} \left[\left(\frac{N_d}{N_a} \right)^{\frac{1}{2}} + \left(\frac{N_a}{N_d} \right)^{\frac{1}{2}} \right] = \left(\frac{2\epsilon_{SC} V_{bi}}{e} \frac{N_a + N_d}{N_a N_d} \right)^{\frac{1}{2}} \tag{2.13}$$

Equations for one-sided junction

A one-sided junction has a thin lightly doped side and a thick heavily doped side. So, for a p^+n junction ($^+$ represents heavy doping), $N_a \gg N_d$ and the above expressions reduce as following:

$$w = \left(\frac{2\epsilon_{SC} V_{bi}}{eN_d} \right)^{\frac{1}{2}} \sim x_n \tag{2.14}$$

$$E_{max} = \frac{-2V_{bi}}{w} \tag{2.15}$$

In presence of an external bias

A pn junction can be operated in 2 modes - forward bias and reverse bias. In all the above expressions, V_{bi} is replaced by V_{bi} - V_{fb} in the forward bias and by V_{bi} + V_{rb} in the reverse bias, where $V_{fb,rb}$ is the external applied forward and reverse bias voltages.

Expression for Current

- *Thermal generation current*
  The thermal generation current (I_{th}) is inversely proportional to the effective lifetime

of minority carriers (τ_{min}), and is given by:

$$I_{th} = e \times \frac{1}{2}\frac{n_i A}{2\tau_{min}} \times w = e \times \frac{1}{2} n_i A \sigma_{min} v_{th} N_t \times w \tag{2.16}$$

where σ_{min} = cross-section, v_{th} = thermal velocity, and A = area of junction.

- *Surface leakage current*
  The surface leakage current is an indication of bad processing, dicing, scratches, surface impurities etc. Since it is independent of temperature, it can be easily separated out from the bulk leakage current.

- *Bulk leakage current*
  There are two types of current that flow across the junction - diffusion current (I_{diff}) and drift current (I_{dr}). While I_{diff} is due to the charge carrier concentration gradient; I_{dr} is due to the electric field generated in the SCR. The currents are in opposite direction to each other. Thus, the total current (I) is a contribution from 4 components - (i) electrons diffusing from n- to p-type, (ii) holes diffusing from p- to n-type, (iii) electrons drifting from p- to n-type and (iv) holes drifting from n- to p-type.

$$I_{diff} = C_5 exp\left(\frac{-eV_{bi}}{kT}\right) \quad \text{and} \quad I_{dr} = C_6 exp\left(\frac{-E_{BG}}{kT}\right) \tag{2.17}$$

  Since, no current flows in an open circuit, I_{diff} should be equal to I_{dr}, i.e. I_{diff} = I_{dr} = I_0 where I_0 is a constant and is given by:

$$I_0 = Aen_i^2\left(\frac{D_p}{L_p N_D} + \frac{D_n}{L_n N_A}\right) \tag{2.18}$$

  where $D_{p,n}$ and $L_{p,n}$ are the diffusion coefficient and diffusion length of holes and electrons respectively. The typical order of I_0 is 10^{-18} A.
  However, in the presence of an external bias, the expressions for the total forward current (I_{fb}) and the total reverse current (I_{rb}) are as given below.

$$I_{fb} = C_5 exp\left(\frac{-e(V_{bi} - V_{fb})}{kT}\right) - C_6 exp\left(\frac{-E_{BG}}{kT}\right) = I_0\left[exp\left(\frac{eV_{fb}}{kT}\right) - 1\right] \tag{2.19}$$

$$I_{rb} = C_6 exp\left(\frac{-E_{BG}}{kT}\right) - C_5 exp\left(\frac{-e(V_{bi} + V_{rb})}{kT}\right) = I_0\left[1 - exp\left(\frac{-eV_{rb}}{kT}\right)\right] \tag{2.20}$$

Expression for Breakdown voltage

The breakdown voltage is that reverse bias voltage at which a rapid increase in the reverse saturation current occurs. There are three mechanisms which give rise to breakdown - Thermal runaway, Zener effect and Avalanche effect.

- *Thermal runaway*
  A high leakage current implies large heating power and thereby leads to an increase in temperature. The increase in the temperature causes the current to further increase, thereby putting the system into a positive feedback. This dependence of the leakage current on temperature leads to thermal runaway. Thus, to avoid overheating of the system, it must be cooled down.

- *Zener effect*
  Zener breakdown occurs in highly doped pn junctions via tunnelling of electrons from VB to CB. With increase in the electric field, numerous covalent bonds break causing the creation of large number of electron-hole pairs. This large number of electron-hole pairs lead to a drastic increase in the current, causing breakdown to occur.

- *Avalanche effect*
  Avalanche breakdown occurs when electron-hole pairs acquire sufficient energy from the electric field to ionize other atoms and creating more electron-hole pairs, leading to an avalanche.
  The increment in electron current at a distance x is given as -

$$dI_n(x) = I_n(x)\alpha_n dx + I_p(x)\alpha_p dx \tag{2.21}$$

where α_n and α_p are electron and hole ionization rates, respectively. The ionization rates are defined as the number of electron-hole pairs generated per unit length by an electron or a hole. Since the total current, I = I_n(x) + I_p(x) and assuming α_n = α_p = α; the integration of Eq. 2.21 yields -

$$I_n(x_n) - I_n(x_p) = I\int_{-x_p}^{x_n} \alpha dx \quad \text{or,} \quad I_n(w) - I_n(0) = I\int_0^w \alpha dx \tag{2.22}$$

Since I $\sim$ I_n(w) and I_n(w) = M_n I_n(0), where M_n is the multiplication factor, the equation reduces to the following expression -

$$1 - \frac{1}{M_n} = \int_0^w \alpha dx \tag{2.23}$$

The avalanche breakdown occurs when M_n approaches infinity, i.e. -

$$\int_0^w \alpha dx = 1 \tag{2.24}$$

Thus, for a one-sided pn junction, using Eqs. 2.10 and 2.14 the expression for the breakdown voltage (V_{bd}) in terms of critical electric field (E_{cr}) is given as following -

$$V_{bd} = \frac{\epsilon_{SC} E_{cr}^2}{2eN_d} \tag{2.25}$$

However, this expression is valid only for uniformly doped planar junctions. The breakdown voltage further degrades for cylindrical and spherical junctions.

Expression for Capacitance

A special quantity called the junction capacitance (C) is defined as:

$$C = \frac{dQ}{dV_{rb}} = \frac{eN_d dx_n}{dV_{rb}} = \left[\frac{e\epsilon_{SC} N_a N_d}{2(V_{bi} + V_{rb})(N_a + N_d)}\right]^{\frac{1}{2}} \tag{2.26}$$

However, for a one-side p^+n junction, this reduces to -

$$C = \left[\frac{e\epsilon_{SC} N_d}{2(V_{bi} + V_{rb})}\right]^{\frac{1}{2}} \tag{2.27}$$

Expression for Full depletion voltage

The full depletion voltage (V_{fd}) is that voltage for which C reaches its minimum saturated value. Thus, C is C_{min} for V_{bi}+V_{rb} $\sim$ V_{fd} in Eq. 2.27 and w = d in Eq. 2.14.

$$C_{min} = \left[\frac{e\epsilon_{SC} N_d}{2V_{fd}}\right]^{\frac{1}{2}} \tag{2.28}$$

$$d = \left(\frac{2\epsilon_{SC} V_{fd}}{eN_d}\right)^{\frac{1}{2}} = (2\epsilon_{SC} V_{fd} \rho_n \mu_e)^{\frac{1}{2}} \tag{2.29}$$

Table 2.1: Properties of silicon [53].

Property	Value
Atomic number (Z)	14
Atomic weight (A)	28.09 amu
Density (ρ)	2.329 g·cm^{-3}
Lattice constant (a)	5.4321 $\mathring{A}$
Energy band gap (BG) at 300 K	1.12 eV
Energy band gap (BG) at 0 K	1.17 eV
Relative permittivity (ϵ_{Si}^{rel})	11.9
Intrinsic carrier concentration (n_i)	1.45 * 10^{10} cm^{-3}
Density of states in CB (N_{CB})	cm^{-3}
Density of states in VB (N_{VB})	cm^{-3}
Built in potential (V_{bi})	0.7 eV
Effective e^- mass ($\frac{m^*}{m_e}$)	0.33
Effective h mass ($\frac{m^*}{m_h}$)	0.5
Mobility of electrons (μ_e) at 300 K	1350 cm^2·V^{-1}·s^{-1}
Mobility of holes (μ_e) at 300 K	450 cm^2·V^{-1}·s^{-1}
Average ionization energy	3.6 eV
Energy loss ($-\frac{dE}{\rho dx}$)	1.7 MeV·g^{-1}·cm^2

2.1.4 The semiconductor - Silicon

Silicon is the second most abundant element on Earth's crust after oxygen. Due to its large abundance and useful characteristics, it is extensively used in the industry. It forms a cubic diamond structure with a lattice constant of 5.2 Å and shares four bonds with other atoms. It has a specific conductance of 10^2 - 10^{-9} $(\Omega cm)^{-1}$, which lies between that of metal and an insulator. It has a favorable BG of 1.12 eV at a temperature of 300 K, the energy required for the creation of 1 electron-hole pair is 3.6 eV. This is because of the fact that silicon is an indirect BG SC, i.e the minimum of the CB does not lie at the same momentum vector as that of the maximum of VB. This means that any transition between VB and CB must include an interaction with the crystal, i.e. phonons in order to have energy-momentum conservation. While the density of atoms in a silicon crystal is 5×10^{22} cm^{-3}, it has an intrinsic carrier density (n_i) of 1.45×10^{10} cm^{-3} at 300 K. A high $\mu_{e,h}$ of 1350 (450) cm^{2}V^{-1}s^{-1} allows for fast detector operation. Some of the properties of silicon are listed in Table 2.1 and more details can be found in Refs. [54, 55].

2.1.5 Silicon as a particle sensor

Configuration of operation

There can be three possibilities in which silicon can be used as a sensor: (i) intrinsic silicon, (ii) silicon abrupt pn junction in forward bias, and (iii) silicon abrupt pn junction in reverse bias. Out of these options, the best configuration is the one with the least amount of free charge carriers to make it easier to distinguish the particle signal and the free carrier signal. While for an intrinsic silicon, $n_i \sim 10^{10}$ cm^{-3}; for n-type extrinsic silicon, if n = 10^{18} cm^{-3}, then by Eq. 2.6 p = 10^2 cm^{-3}. It is known that the current in a pn junction in forward bias is due to the majority charge carriers and in the reverse bias is due to the minority charge carriers. Hence, number of free charge carriers in all the three cases mentioned above are calculated to be - (i) 10^8, (ii) 10^{16} and (iii) 10^0, for a $100\,\mu\mathrm{m} \times 1$ cm $\times$ 1 cm.
Since, the number of free charge carriers is least for the third configuration, silicon is operated as an abrupt pn junction in reverse bias for the detection of particles. Additionally, one-sided junction is preferred to obtain a linear behaviour of the electric field in the active region.

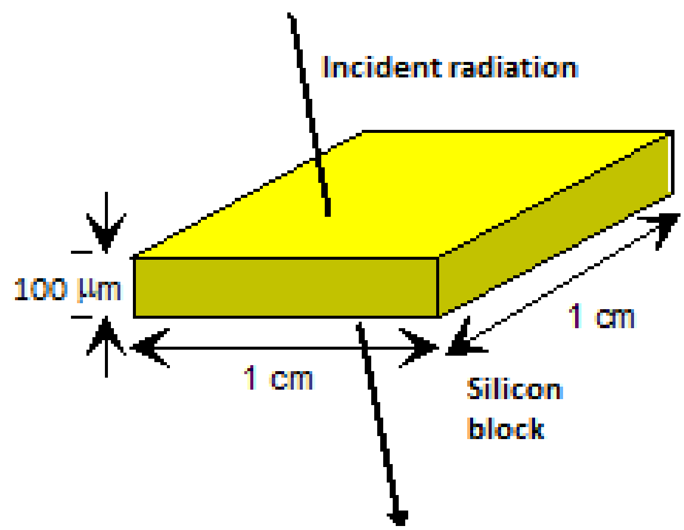

Figure 2.2: The sketch for understanding the principle of operation of silicon detectors.

Principle of operation

The generated charge carriers drift in the electric field developed as a result of biasing the silicon sensor towards their respective electrodes (see Fig. 2.2). A transient current as a function of time is induced on the electrodes by the principle of Ramo's Theorem [56, 57] and is known as the particle signal. The theorem states that the charge induced (δQ_{coll}) on the electrodes by the charge carriers generated (Q_{gen}) is proportional to the displacement (δx) of those charge carriers, where the proportionality constant is the sensor thickness (d), which is approximately the thickness of the lightly doped side in the pn junction.

$$\delta Q_{coll} = Q_{gen}\frac{\delta x}{d} \tag{2.30}$$

$$\delta I_{coll} = Q_{gen}\frac{v_{dr}}{d} \tag{2.31}$$

The area under the particle signal gives the number of charge carriers collected (CC). For a non-irradiated sensor, the number of charge carriers collected is equal to the number of charge carriers created. Thus, for the sensor geometry of $100\,\mu\text{m}$ $\times$ 1 cm $\times$ 1 cm, the average number of charge carriers collected is equal to 1.08×10^4.

2.2 Manufacturing of a silicon sensor

A silicon sensor is manufactured based on various parameters and therefore involves a number of manufacturing steps. These steps are discussed below.

2.2.1 Purification of silicon

The first step in the purification of silicon involves the reduction of distilled quartz sand (SiO_2) with carbon to obtain a low purity form of silicon known as the metallurgical grade silicon (MG-silicon). MG-silicon is then treated with hydrochloric acid (HCl) to form trichlorosilane ($SiHCl_3$), thereby removing most of the impurities. By the method of Chemical Vapour Deposition (CVD) - vaporization with hydrogen, a 99.999999999$\%$ pure silicon known as the Electronic Grade Silicon (EGS) is obtained. EGS is used as starting seed material for growth into large single crystals.

2.2.2 Production of silicon wafers

The different techniques for wafer manufacturing [58, 59] and the addition of impurities during growth for radiation hard engineering are discussed below.

Czochralski (Cz)

In this process, melted EGS and the desired concentration of dopants are kept in a crucible along with fused silica (SiO_2). The temperature is set to a few degrees higher than the melting point. A seed-holder containing a single-crystal seed of the desired plane orientation is introduced into the melt. As the holder is pulled out under rotation, the freezing at the solid-liquid interface yields the formation of a large single-crystal with the same characteristics as that of the seed. Many impurities like oxygen, carbon, etc. are introduced into the melt from the crucible wall. Since the concentration of oxygen introduced in the crystal is of the order of 10^{18} cm^{-3}, high ρ ($\geq$ 10 Ωcm) silicon substrate can not be obtained.

Magnetic Czochralski (MCz)

A MCz wafer growth is similar to that of a Cz crystal, but in the presence of a magnetic field. This is helpful in achieving a homogeneous oxygen distribution throughout the wafer.

Standard Float zone (Fz)

A polycrystalline silicon rod is held in vertical position with a single-crystal seed exactly at its bottom tip. A movable radio-frequency (RF) heater melts a small zone of the rod called the floating-zone. As the RF heater moves up, the melt solidifies with the same characteristics as of the seed. The desired dopant concentration is mixed into the inert atmosphere in which the growth is carried out. This process allows for the production of high ρ ($\geq$ 1 kΩcm) material since the oxygen concentration is low. But, since it is seen that high oxygen concentration improves radiation tolerance, oxygen is added to Fz wafer through diffusion. Such a Fz wafer is known as Diffusion Oxygenated Fz (DOFz).

Deep diffused float zone (ddFz)

The ddFz wafer is usually of a physical thickness of $320\,\mu\mathrm{m}$. In order to obtain, say an active thickness of $200\,\mu\mathrm{m}$, it is achieved by $120\,\mu\mathrm{m}$ backside implantation using the deep diffusion process.

Epitaxial (Ep)

In this technique, a layer of silicon atoms is deposited on a single-crystal silicon substrate either through sputtering or vapour deposition. The resultant grown layer is an exact crystalline extension of the substrate. The substrate is usually a Cz 600 μm thick. This method is used to produce very thin (100-200 μm) silicon wafers. These have high impurity concentration than standard Fz wafers.

The large single crystals are sliced into wafers and polished on both sides to make them fit for sensor fabrication.

2.2.3 Fabrication of sensor

Silicon sensors can be fabricated using any of the above mentioned wafers by the planar processing or photolithography technique [60]. In this technique, successive patterned masks for doping, polysilicon resistors, coupling oxide, metallisation, passivation, etc. are placed on the bare wafer for the manufacture of the final sensor. The mask is generally a glass or quartz plate covered by a thin film of chrome, with photoresist deposited on the chrome. The photoresist is sensitive to UV light and hardens on its exposure. This can be then etched out, leaving behind an imprint of the pattern of the mask on the wafer, where ion implantation (Radiation damage caused by ion implantation is removed by annealing.) is followed by oxide (integrated coupling capacitor), metal (ohmic contact), etc. fabrication steps.

2.3 Baseline for sensor design

2.3.1 Geometry of sensor

Thickness of substrate

Both material budget of a detector system and fabrication technology limitation are the deciding factors in choosing the appropriate thickness d of the sensors. Since silicon sensors are mostly employed in the tracker system, it is preferred that the sensor be of a small d so that the performance of the calorimeters and thereby the overall track reconstruction is not influenced. The usual d of the silicon sensors in present tracker systems ranges from 50 - $320\,\mu\mathrm{m}$.

Plane orientation of substrate

Although <111> has high atom density than <100>, the preferred plane orientation is <100> because <111> has large quantity of dangling bonds. Also, this allows for suppression of surface damage i.e., only small increase of C_{int} after irradiation.

Polarity of substrate

The configuration of p-on-n type sensors is generally chosen as they are relatively much cheaper than the fabrication of n-on-p and n-on-n sensors. Both n-on-p and n-on-n require one additional lithography mask for the introduction of isolation structures. Thus, the present technology of silicon sensors in use is p-on-n type. However, it has been observed that p-on-n configuration starts showing non-gaussian noise behaviour at large bias voltages. Besides, this configuration is not radiation hard and does not provide sufficient charge collection at high fluences. Therefore, the current technology is now shifting towards n-on-p configuration.

Resistivity of substrate

If the sensor is applied with a reverse bias voltage such that it is only partially depleted, any charge carrier created in the undepleted zone has the tendency to recombine with the free majority carriers or the corresponding generation carrier and becomes unavailable for collection at the electrodes. But if the bias voltage is increased too high, it may lead to sensor breakdown. Thus, the operational voltage of the sensor must be chosen wisely. It is usually operated at a voltage slightly higher (50$\%$ more) than the V_{fd}. However, V_{fd} is related to ρ of the sensor substrate by Eq. 2.29. Thus, ρ is an important sensor parameter. For d = $320\,\mu\mathrm{m}$ and a range of V_{fd} from 50 - 300 V, ρ is found to be equal to 7-1 kΩ·cm.

Segmentation of anode

To increase the position resolution, out of the 2 electrodes - anode and cathode, the anode is segmented into either long strips or square pixels. While the strips provide 1-D information, the pixels provide 2-D information of a particle hit on the sensor.

Strip width and pitch

The strip width (s_w), strip pitch (s_p), and pixel side (p_s) are usually chosen of the order of 10's of μm, 50 - 100 μm, and 25 - 150 μm respectively. Both s_w and s_p affect the breakdown voltage of the system. The position resolution of a strip sensor is also given as $\sigma_{pos} = \frac{s_p}{\sqrt{12}}$. Since the strip capacitance is a function of $\frac{s_w}{s_p}$, the 2 quantities must be chosen carefully as they contribute to noise.

Isolation structure

The n-on-p sensor suffers from a low position resolution. In the reverse bias mode, the electrons are collected by the n-type electrode. However, if the bias voltage is not sufficiently high, the electrons accumulate at the surface between the n-type strips. This leads to the formation of a conductive channel between the strips, thereby short-circuiting them and destroying position resolution. Thus, p^+ implantations, also known as pstop and pspray, between the strips are employed to act as isolation structures to the electron accumulation layer.

Poly-silicon biasing scheme

In order to reverse bias the sensor, a potential difference has to be applied between the cathode and the segmented anode. However, to avoid shorting of the strips electrically, each strip is connected to a bias ring (BR) through poly-silicon resistors. The reverse bias is then applied between the cathode and the bias ring. Further, poly-silicon resistor material is chosen since it is radiation hard.

Guard ring

After the full depletion of the sensor bulk, the depletion region starts growing laterally. Several current components may be introduced from the diced (cut) edge of the sensor due to lattice deformation and dangling bonds. Thus, a guard ring (GR) of the same implantation as that of the bias ring (BR) is implemented, surrounding the BR. It is kept at floating potential to ensure additional currents components to be constrained from entering the main segmented P^+-N junction. A multi-GR structure implements several concentric GRs, where the potential drops from one ring to the next and so on. The optimum GR spacing for the multi-GR structure is the one at which the potential is equally shared by the GRs and the junction.

Implant active edge structure

The n^+ implant active edge structure is implemented surrounding the GR to minimize the dead space at the edge of the sensor. Usually under the effect of bias, the depletion region grows from the anode to the cathode, but having an implant of the same type as that of the cathode leads to the extension of the depletion region sideways also. This enhances the efficiency of the detector as the dead space is only the area under the GR in this case.

AC coupling readout

Usually, the leakage current for the non-irradiated sensor is small. However, with irradiation, it increases by several orders. In order to remove this unwanted high DC component at the electrodes, high pass filters, i.e. a coupling oxide as an integrated capacitor is introduced in the sensor design. By minimizing the thickness of the oxide, the coupling capacitance can be increased.

Metal overhang

The increase in the reverse bias voltage, results in an increase in the the electric field within the substrate; the electric field lines crowd at the readout due to high drift velocity and less trapping probability of the charge carriers. This may lead to an early breakdown of the detector. Therefore, aluminium strips over the coupling oxide are made wider than the implant strips and this is known as the metal overhang (MO). The MO re-distributes the electric field lines such that the crowding shifts from the region around the implant corners into the coupling oxide. The breakdown is suppressed in the coupling oxide due to its large energy BG. Thus, it is necessary to optimize the thickness of the oxide.

Backside contact

The backside implant is heavily doped with the same material as that of the substrate, followed by an unsegmented aluminium implant. The high potential is applied to this backside ohmic contact during the reverse biasing of the sensor.

2.3.2 Noise contribution in a sensor

The electron-hole pairs from the incident particle contribute to the signal, however, sources of statistical and electronic fluctuating electron-holes also exist which contribute to Equivalent Noise Charge (ENC). ENC has a strong dependence on integration time window (t_w) and temperature (T) [61]. Since signal can not be increased, it is important to minimize the ENC to improve signal to noise (S/N) ratio. The different components contributing to ENC are discussed in this section. Each component is summed up in quadrature to give the total ENC.

Shot noise

It is the parallel noise contribution due to the statistical fluctuation in the number of charge carriers of a single strip, also called the leakage current (I_{leak}). It is required that a sensor have a small I_{leak}.

$$ENC_{shot} = 107\sqrt{\frac{I_{leak}}{nA} \cdot \frac{t_w}{\mu s}} \tag{2.32}$$

Thermal noise

It is due to the thermal fluctuation of the electron distribution in poly-silicon bias resistors (R_{bias}). Since it is a parallel resistance contributing to noise, it should be kept high to reduce noise.

$$ENC_{bias} = 44.5\sqrt{\frac{\frac{T}{K} \cdot \frac{t_w}{\mu s}}{\frac{R_{bias}}{M\Omega}}} \tag{2.33}$$

Metal noise

The aluminium metal strip acts as a resistor (R_{metal}) in series with the readout and hence contributes to serial noise. A small value of series R_{metal} must be chosen to minimize the noise component.

$$ENC_{metal} = 0.025\frac{C_{strip}}{pF}\sqrt{\frac{\frac{T}{K} \cdot \frac{R_{metal}}{\Omega}}{\frac{t_w}{\mu s}}} \tag{2.34}$$

Table 2.2: Noise contribution for CMS for t_w = 50 ns and T = 263 K [61].

Property	Value	$\mathbf{ENC}_{component}$	No. of electrons
$\mathbf{I_{leak}}$	1 nA (non-irradiated) - 1 µA (irradiated)	ENC_{shot}	24 - 756
$\mathbf{R_{bias}}$	1.5 MΩ	ENC_{bias}	131
$\mathbf{R_{metal}}$	50 Ω	ENC_{metal}	230
$\mathbf{C_{tot}}$	18 pF	$ENC_{capacitance}$	954
		ENC_{total}	1339 - 2071

Capacitance noise

A small load capacitance is preferred for a small contribution to ENC. The capacitance noise component is given as:

$$ENC_{capacitance} = a + b \cdot C_{strip} \tag{2.35}$$

where, a and b are parameters of the pre-amplifier used.

2.3.3 Total noise

Thus, the total ENC contribution is given as -

$$ENC_{total} = \sqrt{ENC^2_{shot} + ENC^2_{bias} + ENC^2_{metal} + ENC^2_{capacitance}} \tag{2.36}$$

The values of the various noise contributions in CMS are provided in Table 2.2. It can be seen from the table that an approximate of 2000 electrons are from noise. Thus, the signal threshold is set to be 2000 electrons.

2.3.4 Charge collection in a sensor

Besides the determination of noise in a sensor, it is equally important to ascertain the response of the sensor to an incoming MIP. It is well established that the sensor must be operated in the over-depleted mode to allow faster charge collection (CC) and maximum charge collection efficiency (CCE), i.e. minimum loss of charge due to recombination or trapping.

Signal by electromagnetic radiation

The absorption coefficient α is related to photon energy ($h * \nu$) by the Tauc equation [62] as:

$$\alpha h\nu = \beta\left(h\nu - BG\right)^{n} \tag{2.37}$$

where β = constant (10^5 - 10^6 cm^{-1}), $n = \frac{1}{2}$ for a direct BG SC and 2 for an indirect BG SC.

The Lambert-Beer Law states the exponential decay of initial intensity (I_0) of the absorbed electromagnetic radiation as a function of distance travelled within the material (x), is given by:

$$I(x) = I_0 exp(-\alpha x) \tag{2.38}$$

Signal by charged particle

When a particle passes through a material, it looses energy as given by the Bethe-Bloch equation [50, 51],

$$-\frac{1}{\rho}\frac{dE}{dx} = 4\pi N_A r_e^2 m_e c^2 z^2 \frac{Z}{A}\frac{1}{\beta^2}\left[\frac{1}{2}ln\left(\frac{2m_e c^2\beta^2\gamma^2 T_{max}}{I^2}\right) - \beta^2 - \frac{\delta(\gamma)}{2} - \frac{C}{Z}\right] \tag{2.39}$$

This equation represents the differential energy loss per mass surface density in units of $MeV.g^{-1}.cm^2$, where ze, N_A, Z, A, m_e, r_e, T_{max}, and I are charge of the incoming particle, Avagadro's number, atomic number of material, atomic mass of material, mass of electron, classical radius of electron, maximum kinetic energy, and mean excitation energy. There are two correction terms as well - (i) $\delta(\gamma)$ represents the correction for the shielding of the particle's electric field by the atomic electrons, and (ii) C denotes the shell correction which corrects for the violation of the assumption of static atomic electrons at low incoming particle energies.

For a minimum ionizing particle (MIP) incident on the silicon sensor, the average energy loss per unit length ($-\frac{dE}{\rho . dx}$) is 1.7 $MeVcm^2g^{-1}$. This is equivalent to a loss of $\sim$ 390 eV of energy per µm, or in other words a creation of $\sim$ 108 electron-hole pairs/µm. So, for a sensor geometry of 1 cm $\times$ 1 cm $\times$ 300 µm, the number of charge carriers created by an incident MIP is equal to 3.24×10^4.

Thus, a sensor characterized by either low noise or high signal does not ensure its good performance as a particle sensor. A good quality particle sensor is one with high SNR.

2.4 Different types of silicon sensors

Based on the silicon sensor baseline as described in the previous section, HEP experiment uses silicon sensors in various configurations depending on their usage in an experiment (see Fig. 2.3). Few commonly used configurations are described below.

Pad diode detector

The simplest geometry of the silicon sensor is a pad diode detector. A p-type pad implantation is doped onto an n-type substrate. Such a configuration may have a single or multi GR structures surrounding it.

Multi-Strip detector

A single-sided micro-strip detector is a silicon sensor segmented in long, narrow elements where each strip is an independent p-n reverse-biased junction and provides the measurement of one co-ordinate per layer of the particles crossing point with high precision. When a charge particle passes through it, it creates electron-hole pairs which, under the influence of electric field move to the respective electrodes. When the holes reach the p-type strips in a p-on-n strip detector, they are collected and induce a measurable charge on the associated aluminium strips which are further connected to sensitive electronic read out channels. By recording which electronic channel is fired, it is possible to determine where the charged particle passed through the detector.

Pixel detector

It is a two dimensional array of sensors monolithically integrated on a single silicon wafer and has the same working principle as the silicon strip sensors. The development of these detectors has been primarily because of the possibility of studying short-lived particles and high rate particle handling capability. It is able to track the path of the penetrating particles with desired accuracy and provides two dimensional information per layer about the position of the particle.

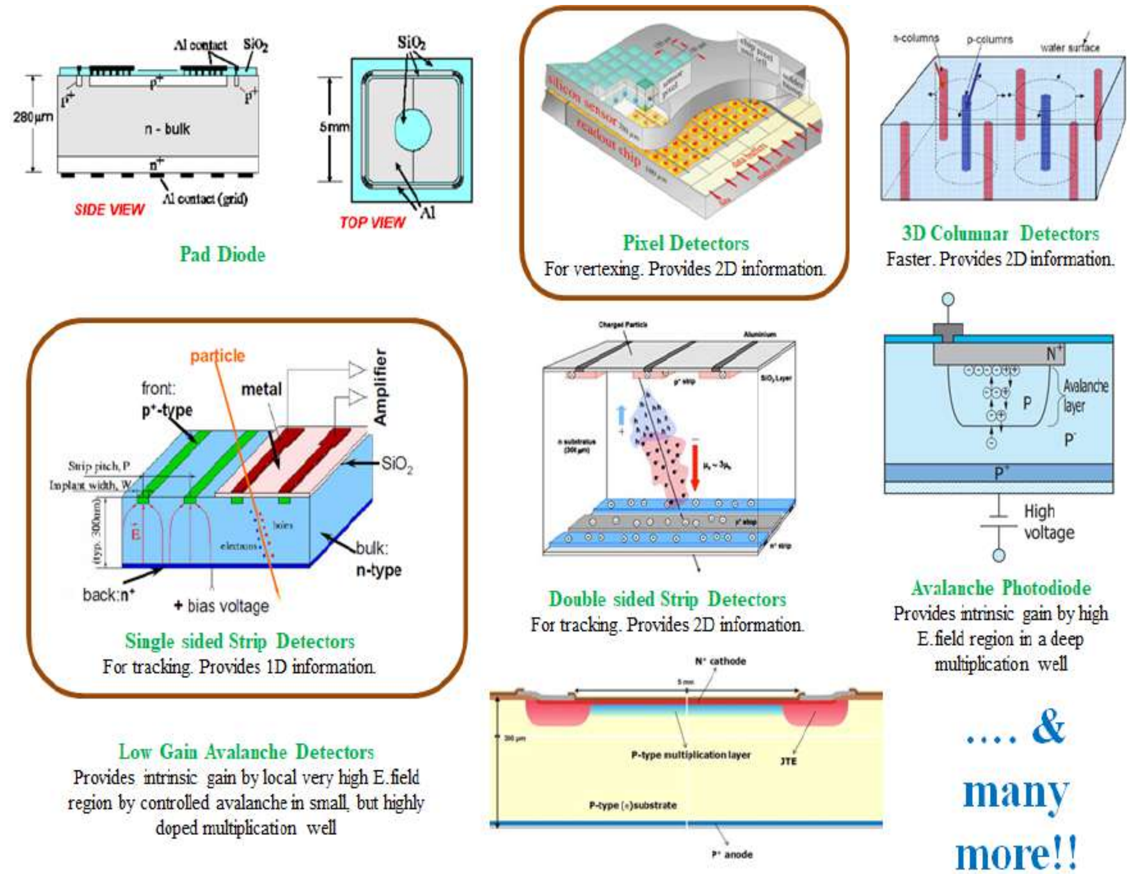

Figure 2.3: The different configurations of silicon sensors.

Low gain avalanche detector (LGAD)

The strip and pixel detectors suffer from the loss of signal with irradiation. A novel design, LGAD, based on the principle of controlled avalanche multiplication was introduced in the recent years, as it provides the possibility of an internal gain. In this detector, a deep p-type multiplication layer is doped onto the n-implant of the n-on-p detector. Under the effect of bias, the increase in the electric field at the junction of the implant and the multiplication layer causes an avalanche to occur, thereby, increasing the particle signal.

Avalanche photodiode detector (APD)

The APDs are based on a similar internal gain mechanism as that of LGADs. Instead of the generation of avalanche locally like in LGADs, in APDs, the avalanche occurs in a larger detector volume. A p^+-type implant is deep diffused into a low resistivity p-type substrate, in addition to the n^+ implant. The resultant gain by the APD is 3 orders greater than that by the LGAD. However, the APDs have to be operated at a much higher voltage.

3-D detector

In these detectors instead of having n- and p-type electrodes on the front and back surfaces, there are grids of n- and p-type electrode columns passing through the thickness of a silicon substrate. As the spacing between the electrodes is reduced significantly in these 3-D silicon detectors, the depletion voltage and collection time of these detectors are relatively very small without affecting the charge generated in the device by an ionizing particle.

2.5 Static characterization of sensors

The electrical defects may be identified during an optical inspection of the sensor, which comprises of looking for visible scratches, burns, corrosion marks, shorts, breaks, etc. on the sensor. Static properties involve identifying the noise sources. As stated in Sec. 2.3.2, noise limits the ability of detection of the particle signal. The static global parameters are as following - (i) total leakage current (I_{tot}) and (ii) backplane capacitance (C_{tot}). For the more complicated sensor design like strip sensors, strip and voltage scans of following static strip parameters are also required in addition to the ones mentioned above (i) strip leakage current (I_{strip}), (ii) poly-silicon resistance (R_{poly}), (iii) interstrip capacitance (C_{int}), (iv) interstrip resistance (R_{int}), (v) coupling capacitance (C_{coup}), and (vi) dielectric current (I_{diel}). The parameters are listed in Table 2.3 and their effect is discussed in detail in [61].

2.5.1 Optical Inspection

The optical inspection provides a quick and immediate inspection of any damage to the structure of the detector, like dust particles, scratches, etc. during the fabrication, packaging, or shipping of the sensors.

2.5.2 Global parameters

Total leakage current

The I_{tot} determines the overall quality of the detector. It is the measurement of the current generated by the detector while it is maintained in the reverse bias mode. This current is

Table 2.3: Parameters to be monitored for silicon strip sensor qualification.

Type of quantity	List of parameters
Environmental conditions	Temperature, Humidity
Global parameters	Total Leakage Current, Backplane Capacitance
Strip parameters	Strip Leakage Current, Poly-silicon Resistance, Dielectric Current, Coupling Capacitance
Inter-strip parameters	Inter-strip Resistance, Inter-strip Capacitance

a source of shot noise in a readout system, thereby affecting the total power consumption. Therefore, this current must be as small as possible, with a strict current limit of $1\,\mu A$, which should not be exceeded.

Backplane capacitance

This measurement characterizes the development of the depletion region with voltage. Since the full charge collection of a detector is ensured by operating it beyond the full depletion voltage (V_{fd}), which can be determined from the $1/C^2_{tot}$ vs. applied reverse bias (V) plot, when the capacitance becomes constant, the detector is said to be fully depleted.

2.5.3 Strip parameters

Strip leakage current

The I_{strip} measurement is the leakage current of a single strip. Since it describes the fraction of one strip current to the total leakage current, the sum of all the single strip leakage currents should be approximately equal to the I_{tot}. Any discrepancy in the calculation are an indication of leaky strip(s) in the detector.

Poly-silicon resistance

In order to avoid shorting the strips and to ensure the application of same potential to the strips, the value of R_{poly} must be homogeneous. To reduce the parallel thermal noise in a detector, a high value of R_{poly}, of the order of $M\Omega$, together with its uniformity among the strips, is desired.

Coupling capacitance

The signal of the read-out electronics is directly proportional to the C_{coup}, which depends on the thickness of the dielectric layer between the implant and the readout aluminium strip. A high value of the order of 1 pF$\cdot$cm$^{-1}\cdot\mu$m guarantees high electric strength and therefore good signal coupling.

Dielectric current

This parameter indicates the current flow through the dielectric oxide. Shorts or ohmic contacts between the aluminium readout and the strip implant (pinholes) can be determined by the measurement of I_{diel}. For a good oxide quality, the current should be less than 10 pA. The identified pinhole strips are not connected to the readout chips in the final assembly of the detectors.

2.5.4 Inter-strip parameters

Interstrip capacitance

The most significant contribution to the total noise comes from the load capacitance, which comprises of C_{tot} and C_{int}. Besides contributing to the noise, C_{int} also plays a significant role in charge sharing between two adjacent strips.

Interstrip resistance

A high value of R_{int} is important to accomplish the isolation of individual strips, and should be of the order of GΩ for a non-irradiated detector. Its value falls to a few hundreds of MΩ after irradiation.

2.6 The Transient Current Technique

The TCT was first developed by the Ioffe Institute in St. Petersburg, Russia and the Brookhaven National Laboratory, USA [63]. When the device under test (DUT) is illuminated, free charge carriers, electrons and holes, are generated along the path of the laser, depending on the penetration depth of the laser light. The TCT technique is based on the motion of these charge carriers in the electric field existing within the reverse biased DUT.

The drifting of the carriers, induces a current pulse signal at the electrodes by the principle of the Ramo-Shockley Theorem. The induced current signal is then fed to the electronics for amplification and pulse shaping. A sample TCT signal may be seen in Fig. 2.4.

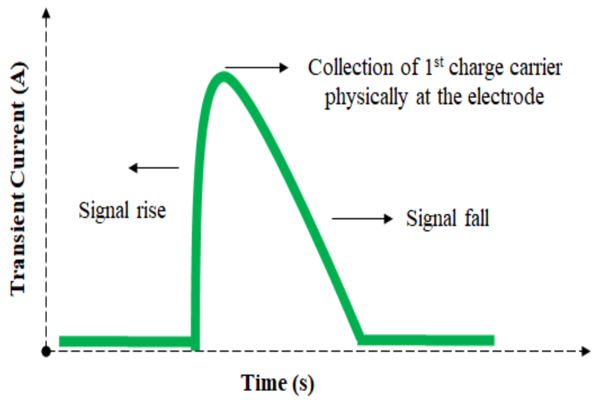

Figure 2.4: Explanation of TCT pulse formation.

2.6.1 Types of TCT

There are three types of TCT: (i) Red Laser TCT, (ii) Infrared (IR) Laser TCT, (iii) Edge TCT (e-TCT). These are described below in detail.

Red Laser TCT

The red laser has a wavelength of 660 nm (energy = 1.882 eV), which means that the charge carriers are created only within a small distance from the incident silicon surface (3-4 μm at 293 K). Then, the output signal is only a pure electron or a hole signal because one of the charge carriers has to travel the entire volume of the DUT, whereas the other charge carrier being very close to its collecting electrode reaches the electrode almost instantaneously (faster than the read-out electronics can respond) and therefore does not significantly contribute to the output signal. In this technique, the individual characteristics of the charge carriers in the DUT can be studied. The pictorial representation of the technique is shown in Fig. 2.5a. So, for a detector with n-type substrate, with front-side laser illumination, the output signal is the electron signal and with rear-side laser illumination, the output signal is the hole signal.

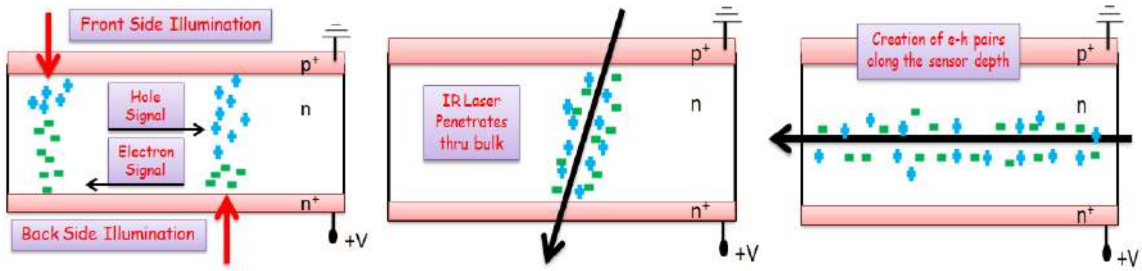

(a) (b) (c)

Figure 2.5: A pictorial representation of the (a) red, (b) infrared, and (c) edge laser TCT.

IR Laser TCT

The IR laser, with a wavelength of 1064 nm (energy = 1.167 eV), is able to penetrate throughout the bulk of the DUT (shown in Fig. 2.5b). A homogeneous amount of charge carriers are created along the IR laser path. It is to be noted that the output signal in this case is a resultant from both the electron-hole charge carriers. Also, the signal generated mimics the behaviour similar to a MIP. The IR TCT is more reliable than red TCT in terms of determining CC, V_{fd}, etc.

e-TCT

In this case, the IR laser is shone through the edge of the DUT, instead from the surface as shown in Fig. 2.5c. This type of TCT is used to investigate the electric field profile across the length of the DUT and also the spatial resolution.

2.6.2 Analysis using TCT

The output TCT signal can be used to extract various sensor properties as discussed below.

Charge collected

The amount of CC is obtained by integrating the TCT signal over time in a given time window.

Charge collection efficiency

The CCE is given by the ratio of the CC by an irradiated sensor at a fluence over the CC by a non-irradiated sensor. The non-irradiated CC is chosen as reference because it is expected that all the laser created charges are collected in absence of traps.

Rise time

The rise time (t_r) is defined as the time taken by the signal to rise from 10 % to 90 % of its peak height.

Charge collection time

The FWHM of the TCT signal gives the time taken for the CC.

Electric field profile

The electric field profile can be determined from the shape of the peak of the TCT signal (see Fig. 2.6).

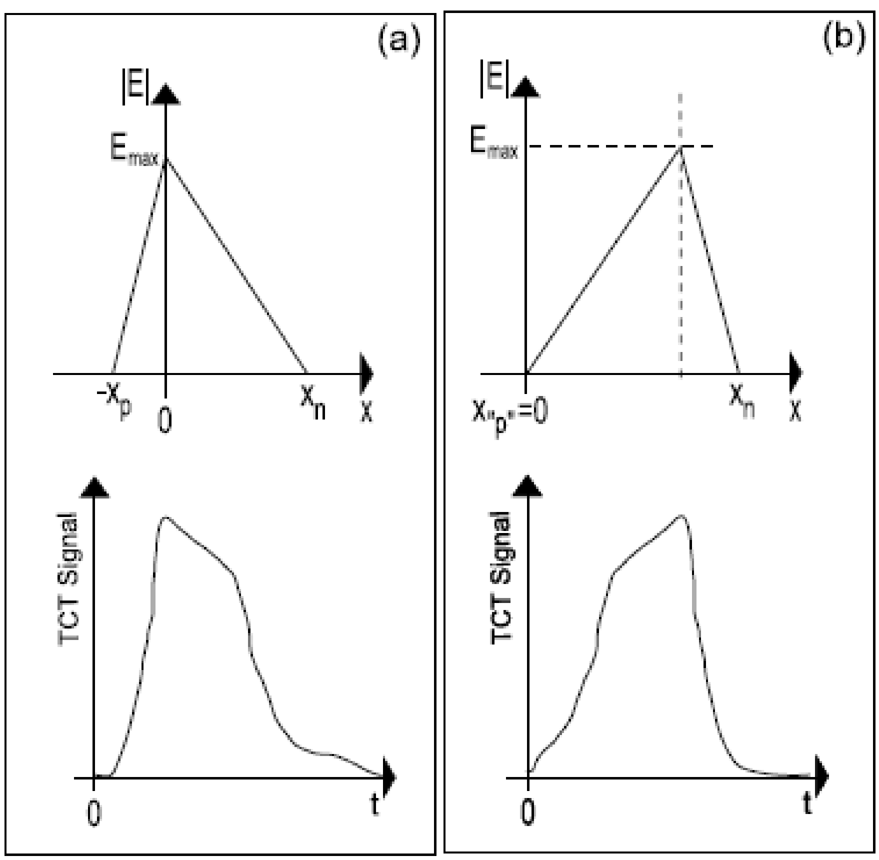

Figure 2.6: The electric field profile and the generated transient signal for - (a) p-on-n sensors, and (b) inverted p-on-n sensor.

Space charge sign

The maximum electric field in the detector is at the pn junction. So, for a frontside illumination, it is expected that the signal will be of descending type with increasing time. However, if the signal is an ascending one, it means that the junction has shifted towards the backside (see Fig. 2.6). And then the reason for the space charge inversion can be investigated.

Drift velocity

The drift velocity (v_d) is the product of the mobility of the charge carrier and the electric field within the DUT and can be calculated from the formula - $v_d = \mu_{e,h} \cdot |\vec{E}|$, where $\mu_{e,h}$ is the saturated electron and hole mobility.

Full depletion voltage

The CC rises steeply with an increasing voltage, until a certain voltage called the full depletion voltage (V_{fd}), beyond which the collected charge for a non-irradiated sensor saturates.

Effective trapping time

The effective trapping time ($\tau_{\text{eff-e,h}}$) can be calculated by correcting the TCT signal using an exponential term taking into account the trapping effect. More details are discussed in Chapter 6.

2.7 A Liverpool Barcelona and Valencia System

The A Liverpool Barcelona and Valencia System (ALiBaVa) [64] utilizes a radioactive source for generating the particle signal. A beta source - ^{90}Sr is commonly used since it has its maximum end point energy lying in the range of a MIP.

2.8 Effect of radiation damage on sensor properties

Particle irradiation causes a change in the macroscopic properties of the sensor by an introduction of several defect levels and thus, leads to the deterioration of the sensor performance. Therefore, it is necessary to understand the effect of radiation damage on the sensor

Table 2.4: Effect of the bulk defects on macroscopic properties [65].

Name	Irradiation	Effect
E30	Generated more during proton irradiation	Introduces positive space charge
BD_A	Generated more during proton irradiation	Introduces positive space charge
BD_B	Generated more during proton irradiation	Introduces positive space charge
Ip, d	Due to γ irradiation	Introduces negative space charge & increases leakage current
Ip, a	Due to γ irradiation	Introduces negative space charge & increases leakage current
E_4	Forms in hadron irradiation	Strongly increases leakage current
E_5	Forms in hadron irradiation	Strongly increases leakage current
H116	Do not form by γ irradiation	Introduces negative space charge (leads to reverse annealing)
H140	Do not form by γ irradiation	Introduces negative space charge (leads to reverse annealing)
H152	Do not form by γ irradiation	Introduces negative space charge (leads to reverse annealing) & trapping centre

properties. Table 2.4 contains information about some of the measured defects and their effect on the detector macroscopic parameters. The material defect engineering is such that either the creation of these defects is avoided or balancing counter-effects be generated.

2.8.1 Total leakage current

It has been observed in experiments that the increase in the I_{tot} (ΔI_{tot}) is proportional to ϕ_{eq} and sensor volume (Vol), where the proportionality constant, $\alpha(T)$ is defined as the reverse current damage constant. However, this linear behaviour breaks at high irradiation levels of about 1 $\times 10^{15} n_{eq}/cm^2$ fluence and above due to the initiation of the charge multiplication process [38].

$$\Delta I_{tot} = I_{tot}(\phi_{eq}) - I_{tot}(non - irradiated) = \alpha(T) \times \phi_{eq} \times Vol \qquad (2.40)$$

It may be noted from the equation that neither does it have dependence on the initial ρ, material, polarity of substrate; nor on the incident radiation type or energy (see Fig. 2.7a). Additionally, $\alpha(T)$ depends on temperature and the dependence is given by the following equation.

$$\alpha(T2) = \alpha(T1)\frac{T2}{T1}exp\left(-\frac{E_{BG}}{2k_B}\frac{T2 - T1}{T2 \cdot T1}\right) \qquad (2.41)$$

Apart from this, a constant decrease in $\alpha(T)$ is achievable by annealing, characterized by annealing time (t_{anneal}) and annealing temperature (T_{anneal}). The value pf α(293K) is equal to 4 $\times 10^{-17}$ A/cm as calculated from Fig. 2.7b and α(253K) is calculated to be 8.9 $\times 10^{-19}$ A/cm from Eq. 2.41.

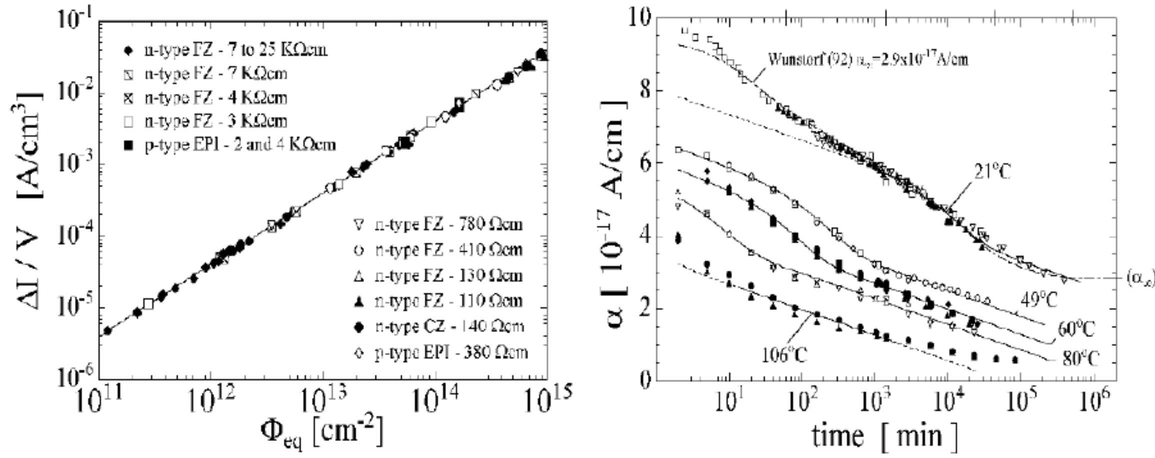

(a) (b)

Figure 2.7: (a) Increase of leakage current per unit volume with fluence after an annealing for 80 minutes at 60 °C. The measurements are carried out at 20 °C and hence $\alpha(293K)$ turns out to be equal to (3.99 $\pm$ 0.03) $\times$ 10^{17} A$\cdot$cm^{-1}. (b) The reverse current damage constant as a function of annealing. (Figures taken from Ref. [38].)

2.8.2 Effective bulk doping and full depletion voltage

Unlike I_{tot}, C_{tot} does not monotonically increase or decrease with irradiation. Irradiation generates acceptors and donors in the bulk of the sensor, with number of acceptors being larger than the donors. For an n-type substrate, the depletion region consisting of donors is compensated by the introduction of acceptors with increasing irradiation. Further, increase in the irradiation leads to creation of more acceptors than donors, thereby type inverting the n-type substrate to p-type. Hence, N_{eff} initially decreases with irradiation, but then starts to monotonically increase. This results in change in the full depletion voltage. It decreases until type-inversion and then starts increasing. The variation of N_{eff} and full depletion voltage is shown in Fig. 2.8a.

The N_{eff} is also sensitive to annealing (see Fig. 2.8b) and its behaviour is described by the Hamburg model, which is given by the following set of equations.

$$\Delta N_{eff}(\phi_{eq},T,t) = N_{eff}(non-irradiated) - N_{eff}(\phi_{eq},T,t) = N_C + N_A + N_Y \quad (2.42)$$

$$N_C(\phi_{eq}) = N_{C,0}\left(1 - exp(-c\phi_{eq})\right) + g_C\phi_{eq} \quad (2.43)$$

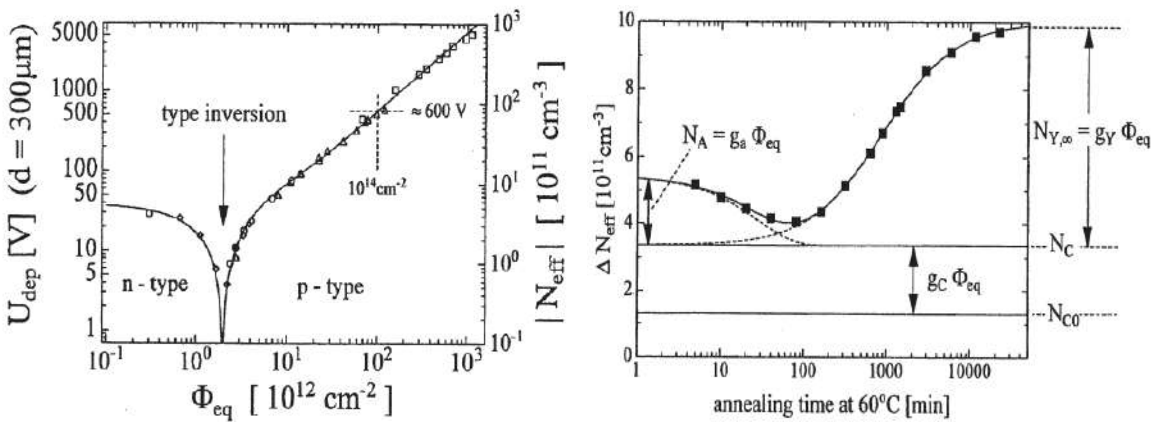

(a) (b)

Figure 2.8: (a) The full depletion voltage and the effective doping concentration as a function of fluence at beneficial annealing. (b) The annealing of the effective doping concentration after irradiation indicating beneficial annealing and reverse annealing. Figures taken from Ref. [38].

$$N_A(\phi_{eq}, T, t) = g_A \phi_{eq} \cdot exp\left(\frac{t}{\tau_A(T)}\right) \tag{2.44}$$

$$N_Y(\phi_{eq}, T, t) = N_{Y,\infty}\left(1 - \frac{1}{1 + \frac{t}{\tau_Y(T)}}\right) \tag{2.45}$$

Here, N_C, N_A, N_Y is the constant damage, beneficial annealing, and reverse annealing terms. The value of other parameters can be found in Ref. [38].

2.8.3 Charge collection

The defects are generated with irradiation, which trap the signal charge carriers. These charge carriers are not released before the readout times, they are lost for collection, resulting in decrease in CCE with irradiation. The CC may increase a bit with increase in voltage, however, 100 % CC for irradiated sensors is not achievable (see Fig. 2.9). The trapping is diminished in thin sensors since the charge carriers have a small distance to travel for readout. It has been observed that both neutrons and charged particles have the same defect spectra. Both lead to a creation of a negative space charge and has been reported by [66]. However, for charged particle an extra defect is present, the E(30K) defect [67] that is responsible for the positive space charge. Initially, it is low in number and hence the negative space charge governs the N_{eff} inside the silicon bulk. But with increase in irradia-

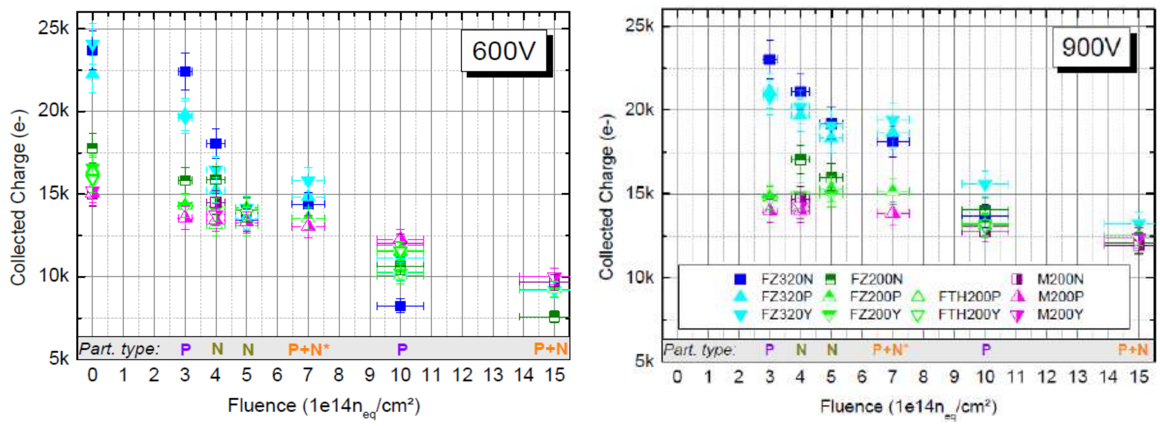

(a) (b)

Figure 2.9: The charge collection as a function of fluence at - (a) 600 V, and (b) 900 V. Figures taken from Ref. [68].

Table 2.5: Effect on sensor electrical parameters.

Property	Effect on sensor operation	Before Irradiation	After Irradiation
I_{tot}	Power dissipation	μA	Increases (mA)
C_{tot}	For determination of V_{fd}	50-150 V	Increases
I_{strip}	Shot noise	nA	Increases (μA)
R_{poly}	For uniform biasing condition	MΩ	No change (MΩ)
C_{int}	Readout noise	pF	Increases (pF)
R_{int}	Isolation of strips	GΩ	Decreases (MΩ)
C_{coup}	Signal readout	nF	Decreases (nF)
I_{diel}	Pinhole	pA	No change (pA)

tion, the space charge goes to zero, i.e. completely balances the negative space charge and then starts to increase. Also, it is important to note here that the E(30K) defect is generated more efficiently in oxygen rich devices rather than the standard devices.

2.8.4 Strip and Inter-strip parameters

The I_{strip} scales similar to the I_{tot} with irradiation. While C_{int} increases, R_{int} decreases significantly due to formation of surface defects. A small dip is also seen in the C_{coup}. No change in the behaviour of R_{poly} and I_{diel} is observed. (see Figs. 2.10 and 2.11)

The effect of all the parameters mentioned above are summarized in Table 2.5.

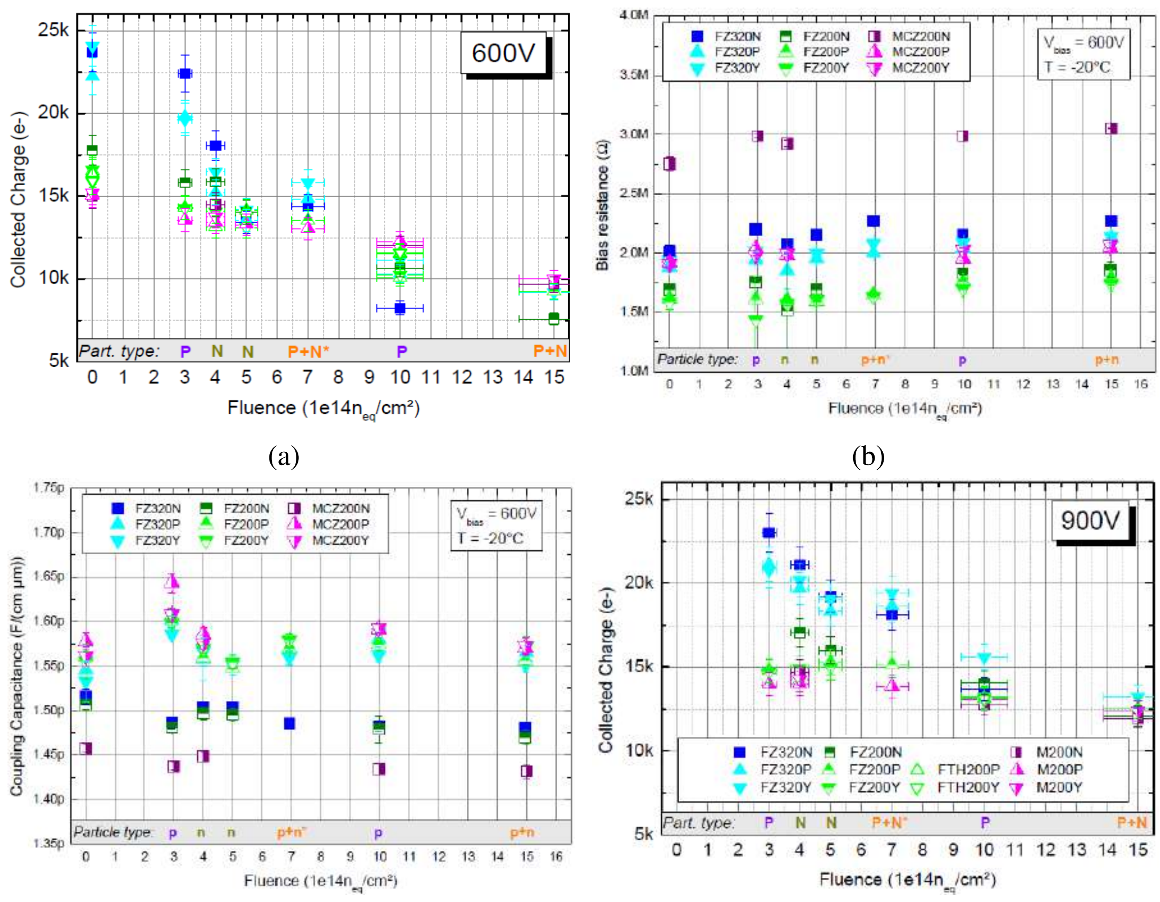

(a) (b)

(c) (d)

Figure 2.10: The behaviour of - (a) strip leakage current, (b) poly-silicon resistance, (c) coupling capacitance, and (d) dielectric current; as a function of fluence. Figures taken from Ref. [68].

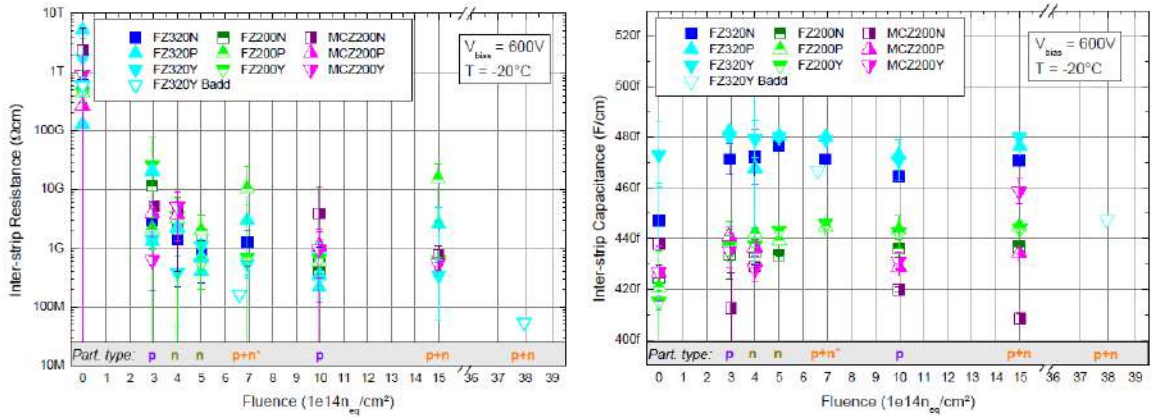

(a) (b)

Figure 2.11: The behaviour of - (a) interstrip resistance, and (b) interstrip capacitance; as a function of fluence. Figures taken from Ref. [68].

2.9 TCAD device simulations

Advantages of simulations

The exceptional performance of the silicon sensors in the radiation environment has led to their extensive usability in HEP experiments. Even so, the future experiments foresee these sensors to be exposed to higher radiation levels. Radiation induces a change in the macroscopic properties of the sensor, thus, severely affecting the sensor performance and ultimately becoming the limiting factor for its operation. With an aim to extend the radiation hardness capabilities of the silicon sensors for the future experiments there has been a growing interest in sensors with novel designs and unique characteristic of intrinsic charge multiplication. Fabrication and experimenting novel designs can be extremely costly and time consuming. It may also be limited by availability of human and material resources and unwanted influence of environmental or experimental conditions on the measurement data. It is here that carrying out simulations can be extremely helpful since these are unaffected by environmental conditions, activity time, and resource availability. Not only this, simulations can provide a better learning handle of the physics inside the sensor as the events can be tracked from the initial to the final step. This leads to an insightful evaluation of the phenomenon taking place at the microscopic level, thereby building a better understanding of the radiation damage mechanism and avoiding design mistakes. Further, simulations allow prediction of the sensor operation for change in parameters like bulk material, thickness, polarity, device geometry etc.

Simulation modelling

As stated in the previous section, measurements are limited by experimental problems, environmental conditions, financial constraints, manpower and resources, etc. for a comprehensive research study in the investigation of new sensor technology. For this reason, the device simulations are useful, which by the finite element method, solve the Poisson equation coupled with the current continuity equations in the main device, typically with the drift-diffusion current modelling. Additionally, the tools provide an insight into the sensor operation both in the non-irradiated and the irradiated scenario in order to predict the voltage dependence of the leakage current, charge collection and electrical field distribution as a function of fluence. This has required the development of a radiation damage model within the simulation tools. They can be tuned and modelled to mimic the known measurement data and then further be used for optimizing the various design parameters. Thus, simulations are not only economic, they also save a lot of efforts in the investigation of a new detector technology.

The most popular simulation packages in the HEP community are Silvaco [69], Sentaurus [70], and Cogenda [71]. In all of these simulators, a physical structure of interest is first designed, which requires to specify the following parameters - the dimensions of the structure; the front, back, and bulk doping profiles and type of doping (whether uniform, gaussian, plane parallel, etc.); the DC and the AC aluminium contacts; the thickness; and choice of the coupling and the passivation layers (SiO_2 or/& Si_3N_4), etc.). Next, an intelligent selection of the grid points known as the mesh is created on the structure, on which the physical equations are computed. The physical equations include the Poisson equation, the current density equation and the continuity equation. The choice and application of the physical models for the mobility, impact ionization, generation & recombination, oxide physics, statistics, tunnelling, etc. is different in different simulators. Also, the various default parameters are different in these simulators. Further to simulate radiation, the bulk and the surface traps (interface and positive fixed oxide) with other parameters like acceptor or donor, energy levels, their cross-section, introduction rate, etc. should be specified. Finally, the bias conditions are defined and the numerical method(s) like Newton, Gummel, Block, etc. for calculation are selected.

In a simulation modeling, the simulated results are tuned with the measurement results by different choice of physical models & their parameters. This requires sensitivity studies and tweaking of process and design parameters. Next, an optimization (in a multi-dimensional parameter phase space) is carried out as per desired sensor specifications. The design is then fabricated with the optimized design parameters and the prototype sensors are tested for macroscopic properties. Finally a mass production is ordered, provided the measurement results of the pre-production run meet the various criteria as specified.

Since, in this thesis, Silvaco, has been used to perform the research; it has been discussed in detail.

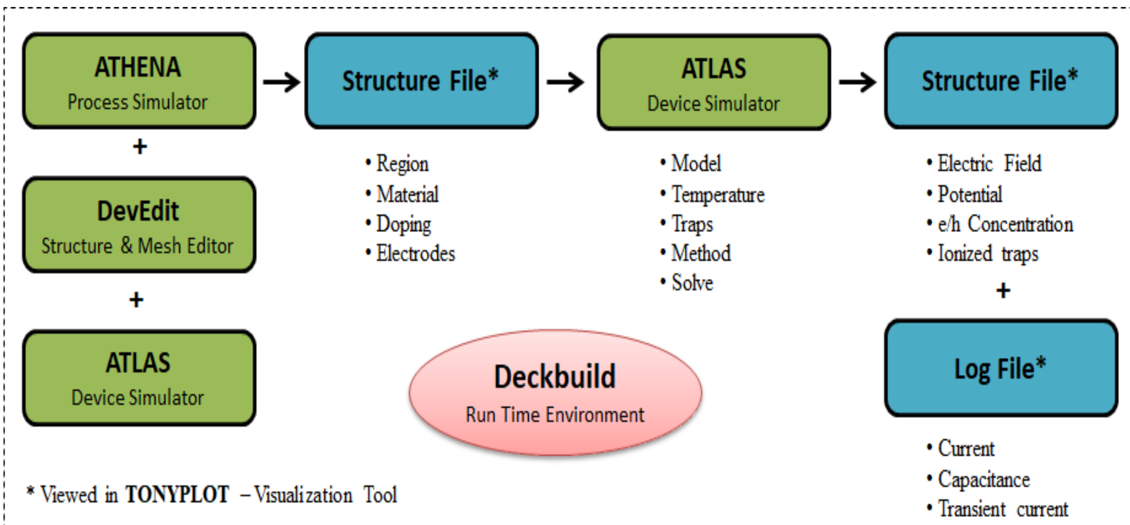

Figure 2.12: A flowchart describing the Silvaco simulation framework.

2.10 Silvaco

Silvaco is a device simulation software that provides Technology Computer Aided Design (TCAD) and Electronic Design Automation (EDA) tools. It utilizes $DevEdit$ as its text editor (in $.in$ format) for writing the details of the design and geometry of a semiconductor device. These details are then fed into $Deckbuild$, which is the run time engine and generates a structure file (in $.str$ format). $Atlas$ is also the TCAD device simulator that enables simulation of electrical and optical behaviour of a semiconductor device. The semiconductor physical models, mobility models, biasing conditions, etc. are implemented through $Atlas$ and once again fed to $Deckbuild$. The MixedMode - an EDA circuit simulator, using electrical circuit models can also be implemented for full circuit simulation along with the device. At this level, two files are generated - (i) a structure file (in $.str$ format) containing 2D profiling of electric field, potential, electron (hole) concentrations, etc., and (ii) a log file (in $.log$ format) consisting information of corresponding current, capacitance, voltage, etc. Silvaco additionally offers Tonyplot - an interactive TCAD tool that provides necessary GUI-based interface for viewing $.str$ and $.log$ files. The complete flowchart can be seen in Fig. 2.12. A brief description of all the tools used is given below.

```
### Structure
go devedit
DevEdit version="2.0" library="1.14"
work.area left=0 top=-10 right=80 bottom=310
### Bulk
region reg=1 name=Silicon mat=Silicon color=0xffc000 pattern=0x3  \
       points="0,0 10,0 10,300 0,300 0,0"

### Bulk_impurity
impurity id=1 region.id=1 imp=phosphorus color=0x906000  \
       x1=0 x2=10 y1=0 y2=300 \
       peak.value=1e12 ref.value=0 comb.func=Multiply \
       rolloff.y=both conc.func.y=Constant \
       rolloff.x=both conc.func.x=Constant
constr.mesh region=1 default

### Anode
region reg=3 name=anode mat=Aluminum elec.id=1 work.func=4.1 color=0xffc8c8 pattern=0x6  \
       points="0,0 10,0 10,-1 0,-1 0,0"
constr.mesh region=3 default

### Cathode
region reg=5 name=cathode mat=Aluminum elec.id=6 work.func=4.1 color=0xffc8c8 pattern=0x6 \
       points="0,300 10,300 10,301 0,301 0,300"
constr.mesh region=5 default

### Anode_impurity1
impurity id=2 region.id=1 imp=boron color=0x906000 \
       x1=0 x2=10 y1=0 y2=0 \
       peak.value=1e18 ref.value=1e12 comb.func=Multiply \
       rolloff.y=both conc.func.y="Gaussian (Dist)" conc.param.y=1 \
       rolloff.x=both conc.func.x="Gaussian (Dist)" conc.param.x=0.7 \

### Cathode_impurity
impurity id=7 region.id=1 imp=phosphorus color=0x906000 \
       x1=0 x2=10 y1=300 y2=300 \
       peak.value=1e18 ref.value=1e11 comb.func=Multiply \
       rolloff.y=both conc.func.y="Gaussian (Dist)" conc.param.y=1 \
       rolloff.x=both conc.func.x="Gaussian (Dist)" conc.param.x=0.7 \

### Base_mesh
base.mesh height=20 width=20
bound.cond !apply max.slope=28 max.ratio=300 rnd.unit=0.001 line.straightening=1 align.points when=automatic
imp.refine imp="NetDoping" sensitivity=1.25
constr.mesh max.angle=180 max.ratio=300 max.height=2 max.width=2 min.height=0.01 min.width=0.01

### Construct_mesh
Mesh Mode=MeshBuild
constr.mesh type=Semiconductor default
constr.mesh type=Insulator default
constr.mesh type=Metal default
constr.mesh type=Other default

### Refine_mesh
refine mode=x x1=0 y1=-1 x2=80 y2=20
refine mode=y x1=0 y1=-1 x2=80 y2=20
refine mode=y x1=0 y1=-1 x2=80 y2=20
refine mode=y x1=0 y1=-1 x2=80 y2=20

### Structure_output
structure outf=d300.str
```

Figure 2.13: An example of a script written in $DevEdit$.

2.10.1 DevEdit

It is a device structure editor and tool for mesh specification and refinement. The order of structure specification is - (i) outlining the geometry of the device, (ii) defining the different regions (example - silicon, oxide, DC electrode, AC electrode, etc.), (iii) specifying the doping profiles, (iv) construction of mesh, and finally, (v) saving the structure as a $.str$ file. A screenshot of a script written in $DevEdit$ is shown in Fig. 2.13.

Doping profiles

In this work, two types of doping profiles have been used - uniform and gaussian functions. The analytical forms of these functions is defined such that $p \cdot P$ gives the value of the doping concentration at a distance, d; where P is peak doping concentration and p is given as -

$$\text{Uniform:} \quad p = 1 \quad \text{and} \quad \text{Gaussian:} \quad p = exp\left(\frac{d^2}{D^2} \cdot ln\frac{R}{P}\right) \tag{2.46}$$

Here, R is reference peak concentration and D is the distance upto which the doping profile is defined. The 1D doping profile may be viewed in Fig. 2.14.

Meshing

A mesh is 2D or 3D array of points constructed on the device using the finite element analysis method. Constructing of a good mesh is highly critical in device simulation since the physical equations are calculated on its grid points. Although accuracy requires a fine mesh; numerical efficiency is greater for a coarse mesh. Hence, a smart mesh must be constructed such that only the critical areas (high electric field regions, areas of large impact ionization, etc.) have a refined mesh. The number of mesh points can also be significantly reduced by exploiting the device symmetry, thereby largely decreasing the simulation time. A typical mesh around the junction area can be seen in Fig. 2.15a.

An example of a generated structure file is shown in Fig. 2.15b. This structure is fed to $Atlas$ for the prediction of its electrical behaviour.

2.10.2 Deckbuild

$Deckbuild$ is an interactive, graphical run-time environment for operating Silvaco. The commands are loaded from the script written in the text editor. The $deckbuild$ environment

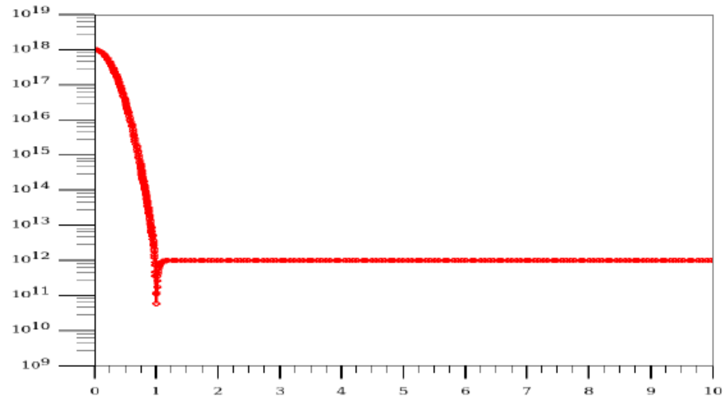

Figure 2.14: Illustration of 1D doping profile.

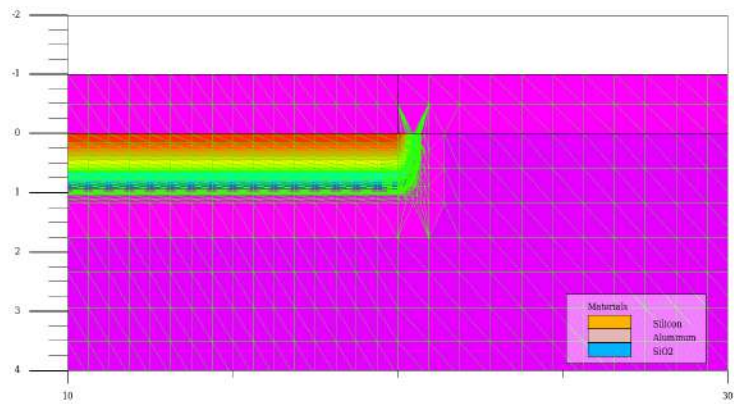

(a)

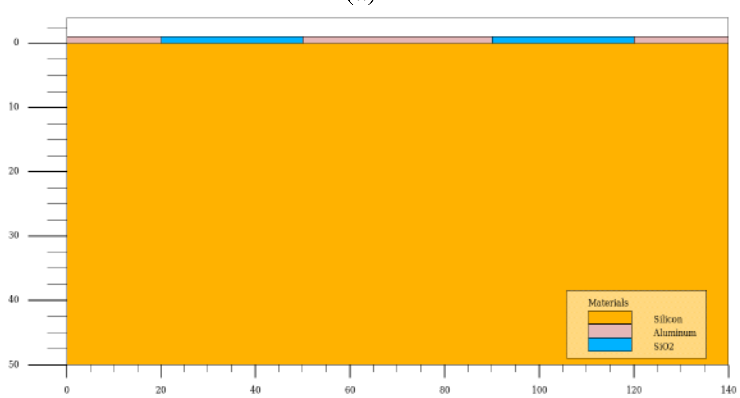

(b)

Figure 2.15: Illustrations of - (a) generated mesh using Devedit, and (b) the structure generated.

displays the execution of each command in the script and issues instant status, warnings and error messages for each simulation run. This run-time output can be saved to an output file for examination in future. A batch mode *deckbuild* window is shown in Fig. 2.16.

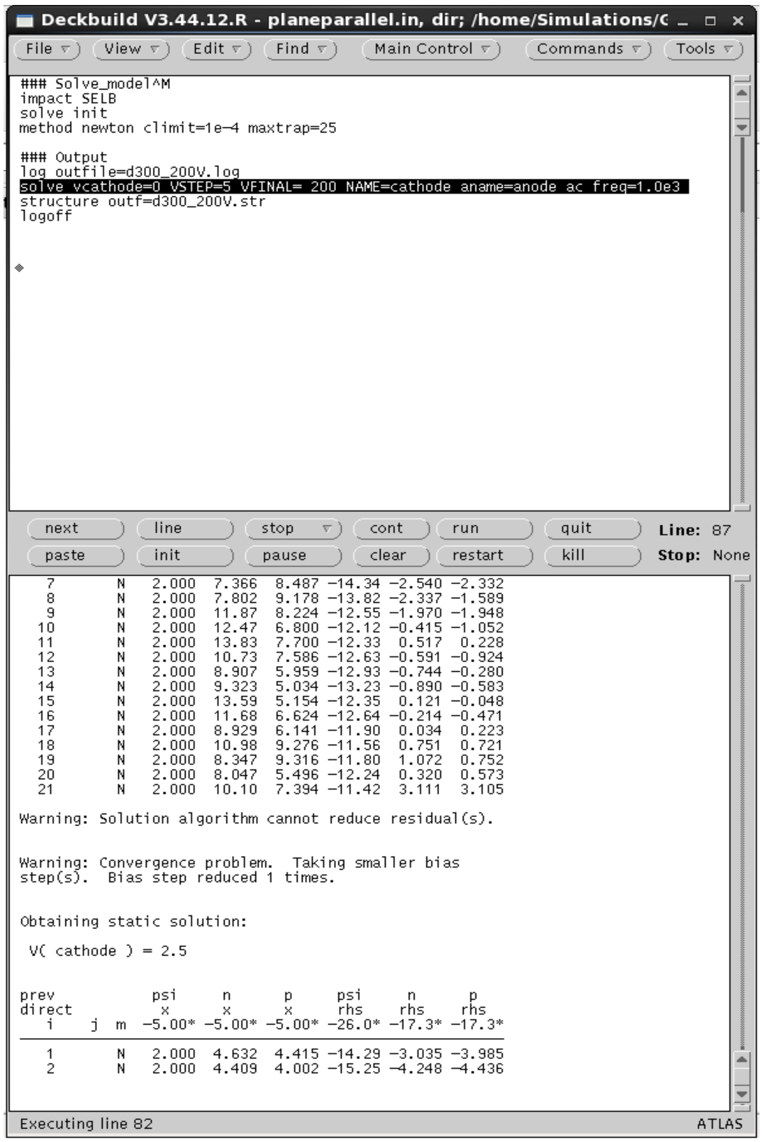

Figure 2.16: The upper half of the window shows the commands and the lower half displays run-time status. The buttons on the panel allow for specific control (pause, continue, etc.) of the simulation.

```
go atlas simflags="-P 11"
mesh infile=d300.str

material material=silicon region=1 Eg300=1.12

### Temperature
model bipolar temp=297.0 print

### Solve_model
impact SELB
solve init
method newton climit=1e-4 maxtrap=25

### Output
log outfile=d300_200V.log
solve vcathode=0 VSTEP=5 VFINAL= 200 NAME=cathode aname=anode ac freq=1.0e3
structure outf=d300_200V.str
logoff
```

Figure 2.17: A script written in $Atlas$.

2.10.3 Atlas

$Atlas$ is a physically-based device simulator that predicts the electrical behaviour of semiconductor devices at specified bias conditions. The list of models and methods specification consists of - (i) specifying the structure to be simulated, (ii) selection of physical models, (iii) specifying boundary conditions, (iv) choice of numerical methods, (v) application of bias conditions, and finally, (vi) saving the structure as a $.str$ file. A screenshot of a script written in $Atlas$ is shown in Fig. 2.17.

Physical models

The mathematical model that describes semiconductor device physics consists of a set of fundamental equations derived from Maxwell's laws. While the Poisson equation relates electrostatic potential (V^{pot}) to local carrier densities (ρ) (sum of all mobile and fixed charges, including electrons, holes, and ionized impurities); the continuity and constitutive equations describe the evolution of the electron and hole concentrations (n, p) as a function of transport (time t), current densities ($\overrightarrow{J}_{n,p}$), generation ($g_{n,p}$), recombination ($r_{n,p}$), mobility ($\mu_{n,p}$), and diffusion ($D_{n,p}$) processes. The mathematical expressions for these equations are given as:

$$\nabla^2 V^{pot} = -\frac{\rho}{\epsilon_{SC}} \quad \text{and} \quad \rho = p - n + N_d^+ - N_a^- \tag{2.47}$$

$$\frac{\partial n}{\partial t} = \frac{1}{e}\nabla \cdot \overrightarrow{J_n} - r_n + g_n \quad \text{and} \quad \frac{\partial p}{\partial t} = -\frac{1}{e}\nabla \cdot \overrightarrow{J_p} - r_p + g_p \tag{2.48}$$

$$J_n = en\mu_n E + eD_n \nabla n \quad \text{and} \quad J_p = en\mu_p E - eD_p \nabla p \tag{2.49}$$

Thus, the physical models are grouped into 5 classes (The mathematical model(s) used to carry out the simulations reported in this work are listed against each physical model.) -

- *Mobility*: This model states that though the charge carriers are accelerated in the external electric field, they lose energy by scattering with the impurity ions and lattice imperfections. Further lattice vibrations lead to reduction in their momentum. Concentration dependent mobility and parallel electric field dependent mobility models have been used in this work.
- *Recombination*: This model describes those processes through which the semiconductor material returns back to its equilibrium state. Shockley-Read-Hall (SRH) recombination with concentration dependent lifetimes and auger recombination models are used.
- *Carrier statistics*: Bandgap narrowing
- *Impact ionization*: This model describes the generation of secondary charge carriers. The Selberherr model is used to carry out simulations.
- *Tunneling*: Band-to-band

Boundary conditions

If ‘u’ is an unknown quantity defined by a partial differential equation, then - (i) if the value of ‘u’ is defined at the boundary, it is a Dirichlet boundary condition (bc), and (ii) if the value of the first derivative of ’u’ is defined at the boundary, it is a Neumann bc. In semiconductor physics, these are defined as follows -

- *Dirichlet condition*: The majority and the minority carrier quasi-Fermi potentials are equal to the applied reverse bias voltage at the electrodes, i.e. $\phi_n = \phi_p = V_{br}$, thereby making it an ohmic contact.
- *Neumann condition*: The difference between the normal components of the dielectric displacement along the SC - insulator interface is equal to any surface charge, i.e. $\hat{n}.\epsilon_{SC}\nabla\psi_{SC} - \hat{n}.\epsilon_{insulator}\nabla\psi_{insulator} = \rho_{surface}$. Thus, the Neumann condition ensures that current flows only through the contacts and not through the detector edges.

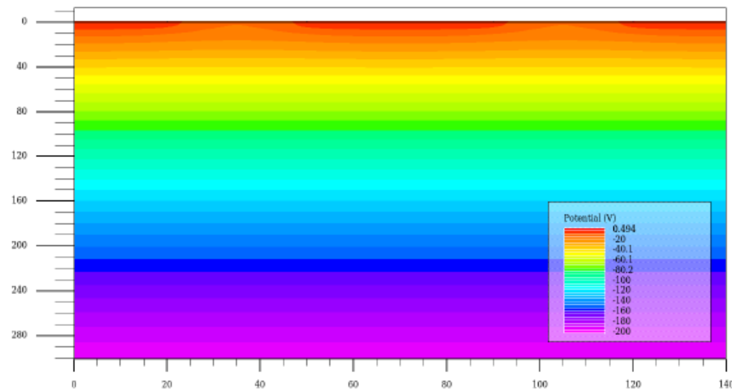

(a)

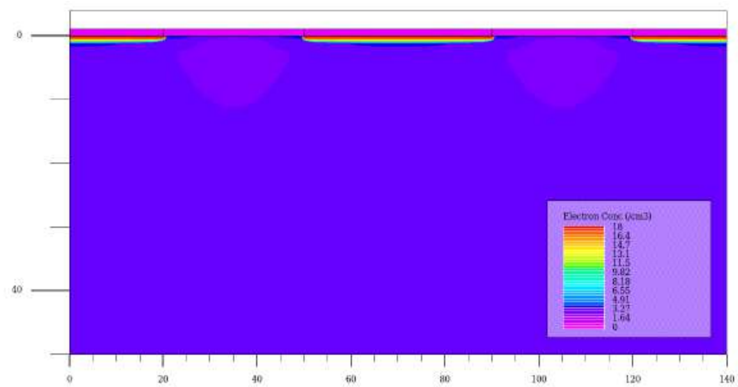

(b)

Figure 2.18: Screenshots of - (a) the potential contour, and (b) the electron concentration.

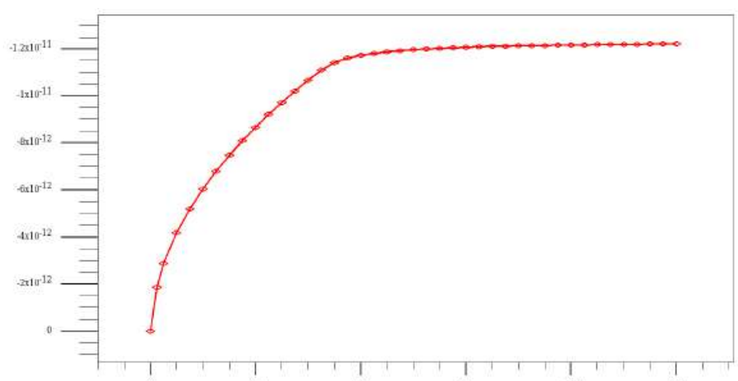

Figure 2.19: The current vs voltage plot using the $.log$ file.

Numerical methods

$Atlas$ offers several numerical methods for calculating the unknowns on the grid points defined by the mesh. The methods are based on the iteration procedure where an iterative procedure is used to refine the initial guess solution provided. The iteration continues until the convergence criteria is met. However, many times a solution may fail to converge. This requires use of a different mesh, initial guess, or numerical method. The $Newton$ iteration method is employed to solve the strongly coupled, non-linear, partial differential equations.

Structure file

The generated $.str$ structure file allows display and evaluation of various parameters like electric field, potential, electron concentration, etc. Screenshots of the electric field profile and the electron concentration are shown in Figs. 2.18a and 2.18b.

Log file

The $.log$ log file stores - (i) current and voltages at electrodes in DC simulation, (ii) time is stored in transient simulation, and (iii) capacitances, conductances, and small signal frequency in AC simulation. An example of the total current from the structure is shown in Fig. 2.19.

2.10.4 Tonyplot

$Tonyplot$ not only allows viewing of $.log$ and $.str$ files, but also offers the option to export the data. Additionally, multiple files can be overlapped to compare data. It can be also used to define new quantities as a function of simulated quantities. Cutline slices (1D) can be viewed for 2D profiles (see Fig. 2.20).

2.10.5 MixedMode

While a circuit simulator like $SPICE$ [72] solves systems of equations that describe the behaviour of the electrical circuits; a physically-based device simulator like $MixedMode$ solves systems of equations that describe the physics of device operation. In $Atlas$, the script is written in two parts - (i) $SPICE$-like that describes the circuit elements netlist and analysis, and (ii) $Atlas$-like that describes the device simulation model parameters. In

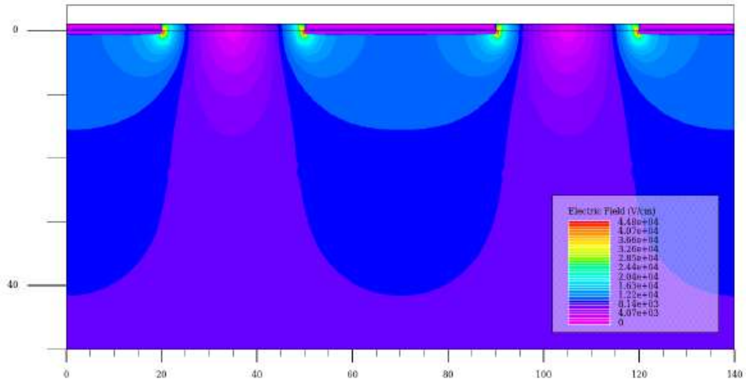

(a)

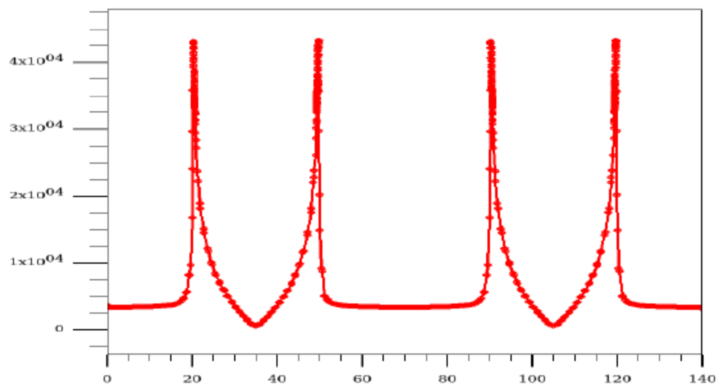

(b)

Figure 2.20: An example of - (a) the 2D electric field profile and (b) the 1D electric field generated using a horizontal cutline at $0.5\,\mu m$ below the oxide.

the script, nodes are defined where two or more elements are connected. By default, the ground node is set by specifying node number as '0'. An example of the script is shown in Fig. 2.21. This is the script for TCT simulations and the value of the circuit elements chosen are similar to the ones in the experimental TCT setup. The illustration of the TCT node circuit elements used in the simulations can be seen in Fig. 2.22.

2.11 Radiation damage modelling

For a comparison of the measurements with the TCAD simulations, a proton radiation damage model was developed. Due to computational and software constraints, the model is usually based on three to five effective traps only, even when there are plenty of traps seen in measurements. However, these traps are tuned such that the simulated results

```
go atlas simflags="-P 1l"
.begin

V1 2 0 0

## D1 1 0.0 pulse 0.0 $laserpower 2.E-9 1E-10 1E-10 1E-10 $t_plot
O1 1 0 pulse 0.0 1 2.E-9 1E-10 1E-10 1E-10 25e-9

Cstray 1 0 2e-12
Lstray 1 3 2e-9

RbiasT 2 3 3.127e3

## Bias-T decoupling
R2 3 4 2e9
CbiasT 3 4 3.3e-9

#scope termination
RL 4 0 50

ADIODE 1=cathode 0=anode WIDTH=312500 INFILE=Np3e16.str
.options relpot dc.write=0

set start= 0
set stop = -500.0
set step = -2.5
.DC V1 $start $stop $step

.log outfile=Np3e16_fluence0_500V
.save master=Np3e16_fluence0_500V TSAVE="2.0E-9,2.5E-9,3E-9,3.5E-9,4E-9,4.5E-9,7E-9,7.5E-9,10E-9,12E-9,14E-9"
.tran 1e-14 25e-9

.end

beam DEVICE=ADIODE num=1 x.origin=40 y.origin=-10 angle=90 wavelength=1.060 \
xmin=-0.5 xmax=0.5 GAUSSIAN MEAN=0 SIGMA=1 RAYS=200

material material=silicon region=1 Eg300=1.12 TAUN0=1e-4 TAUP0=1e-4
model bipolar temp=253.0 print

impact SELB

solve init
method  newton climit=1e-4 maxtrap=25

go atlas simflags="-P 1l"
```

Figure 2.21: An example of a script written with MixedMode included.

satisfactorily describe the measurement results (characteristics like I_{tot}, C_{tot} / V_{fd}, C_{int}, R_{int}, CC, etc.). The five trap model is a combination of - 2 bulk traps, 1 N_{ox}, and 2 N_{it}; forming a combined bulk and surface radiation damage model. Tables 2.6 and 2.7 list all the trap parameters. Each trap is defined as a function of energy level, defect concentration which is a function of fluence and capture cross-sections of electrons & holes (σ_e & σ_h). The detailed modelling and refine tuning of the model and its parameters is described in Ref. [73–75]. The model is based on the original work by Ref. [76].

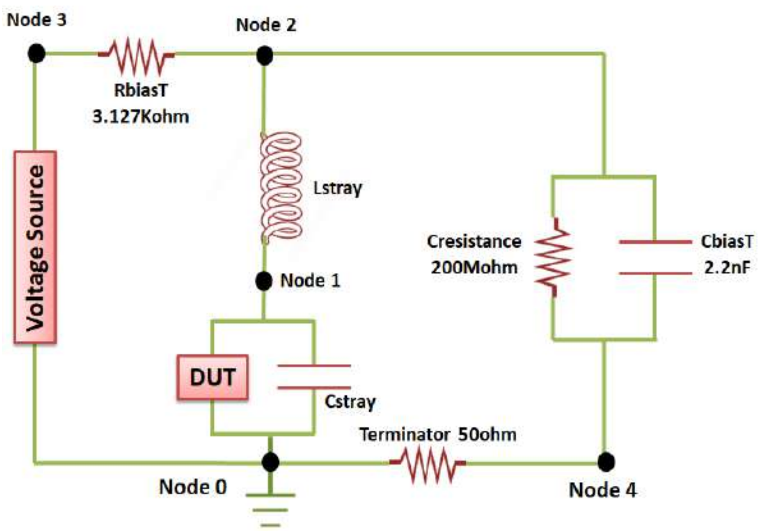

Figure 2.22: The schematics of the TCT circuit elements built on the node concept in the simulator.

Table 2.6: Bulk and surface radiation damage trap model - I.

Fluence ($n_{eq}.cm^{-2}$)	**Density of N_{ox} (cm^{-3})**
Non-Irradiated	5×10^{10} to 5×10^{11}
1×10^{14}	1×10^{11} to 8×10^{11}
5×10^{14}	5×10^{11} to 12×10^{11}
1×10^{15}	8×10^{11} to 20×10^{11}

Table 2.7: Bulk and surface radiation damage trap model - II.

Damage	**Trap type**	**Energy level (eV)**	**Density (cm^{-3})**	σ_e **(cm^2)**	σ_h **(cm^2)**
Bulk	Acceptor	E_C - 0.51	$4 \times \phi$	2.0×10^{-14}	2.6×10^{-14}
Bulk	Donor	E_V + 0.48	$3 \times \phi$	2.0×10^{-14}	2.0×10^{-14}
Interface	Acceptor	E_C - 0.60	$0.6 \times N_{ox}$	0.1×10^{-14}	0.1×10^{-14}
Interface	Acceptor	E_C - 0.39	$0.4 \times N_{ox}$	0.1×10^{-14}	0.1×10^{-14}

2.12 Calibration of simulations with measurements

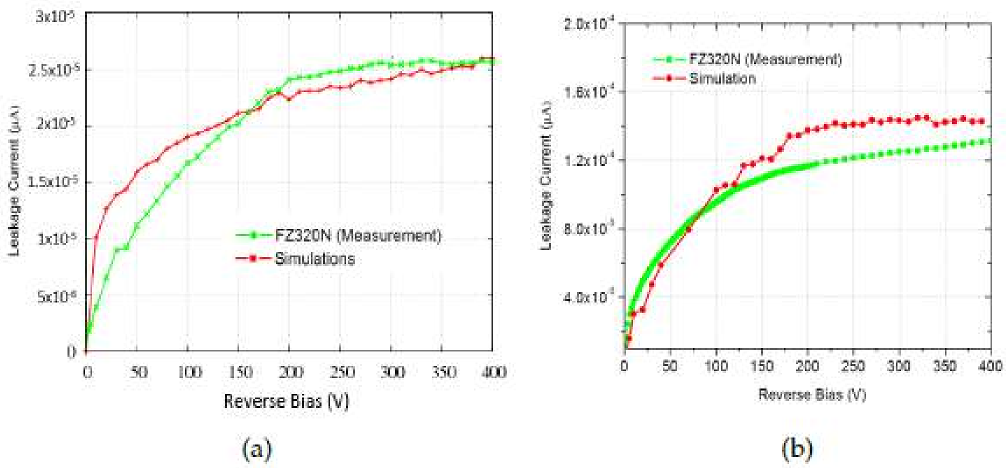

Figure 2.23: Comparison of measured and simulated IV characteristics for small and large diodes.

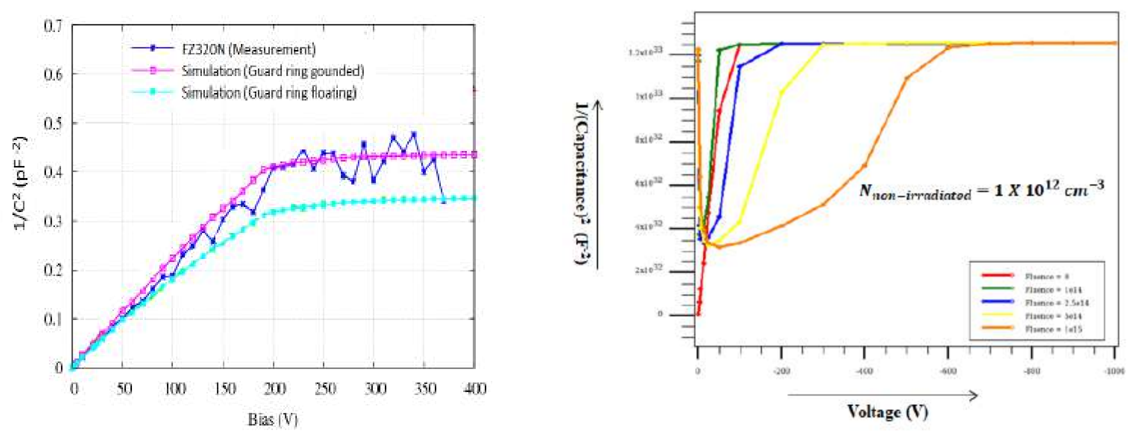

(a) (b)

Figure 2.24: (a) Comparison of measured and simulated $C^{-2}V$ characteristics for a non-irradiated pad diode. (b) Simulated $C^{-2}V$ characteristics at different fluence values.

Total leakage current

An excellent comparison of simulated result of the leakage current with the measured data - for (a) small, and (b) large diode structures and at T = 293 K can be seen in Fig. 2.23.

Backplane capacitance

The comparison of simulation with measurements for capacitance at different fluence values as a funtion of bias is shown in Fig. 2.24.

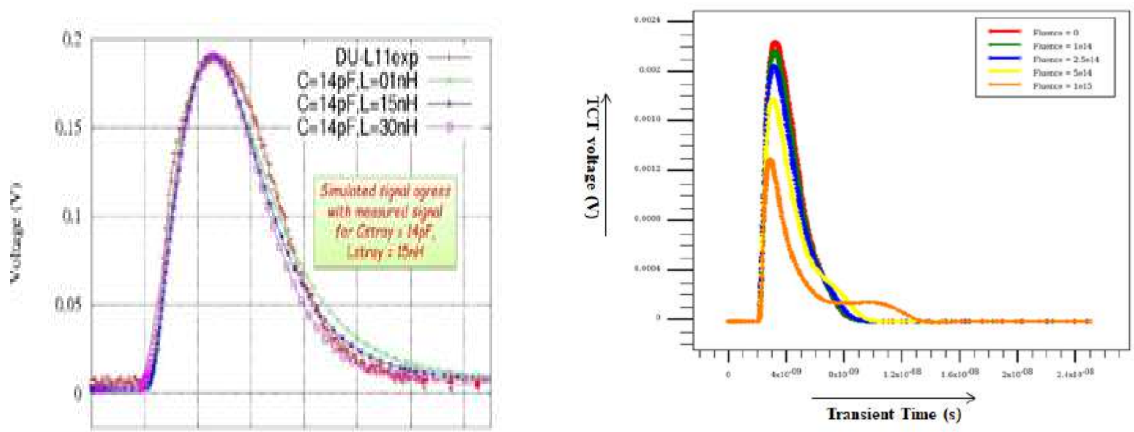

(a) (b)

Figure 2.25: (a) Variation of C_{stray} and L_{stray} values. (b) The electron simulated TCT signal at various bias voltages for a pad diode.

Signal formation and charge collection

The values of the circuit elements in MixedMode used in the simulations are taken equal to the measurement setup. C_{stray} and L_{stray} (in Fig. 2.22) represent the capacitance and inductance of the cables and connectors in the circuit. Both C_{stray} and L_{stray} have been tuned to 14 pF and 15 nH (see Fig. 2.25a), respectively such that there is a good agreement of the simulated TCT signal with the measured TCT signal. Fig. 2.25b shows the simulated electron signal for increasing fluence at a bias voltage of 200 V, when the p+-n-n+ diode is illuminated from the front side. It can be seen from the plot that as irradiation is increased, less and less charge is collected. This means that at higher fluence values, trapping effects increase significantly.

Inter-strip resistance

The close agreement of the simulated inter-strip resistance with the measured inter-strip resistance may be viewed in Fig. 2.26.

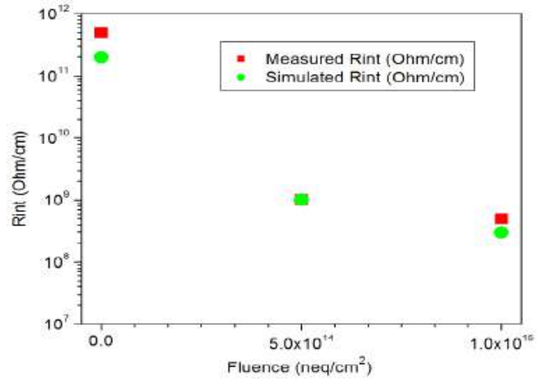

Figure 2.26: Measured and simulated inter-strip resistance as a function of fluence.

Inter-strip capacitance

Fig. 2.27 shows the comparison of the inter-strip capacitance simulation results with measurements for some of the multi-strip silicon sensor configurations for FZ320N detectors.

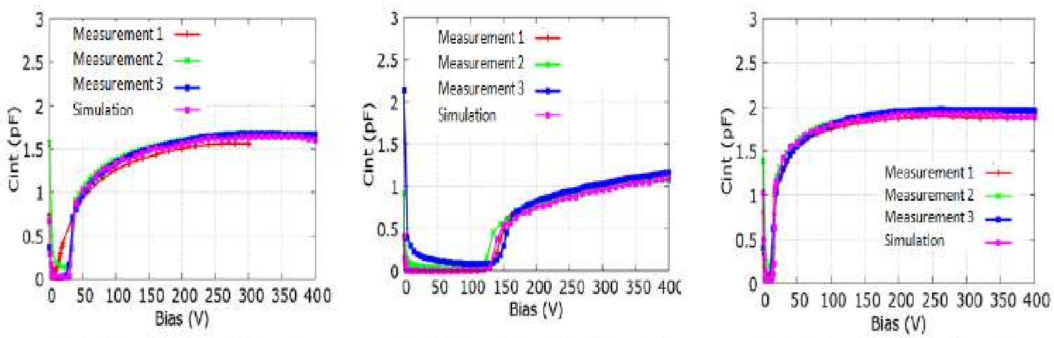

(a) Region 1 (pitch 120 μm) (b) Region 2 (pitch 240 μm) (c) Region 3 (pitch 80 μm)

Figure 2.27: Measured and simulated inter-strip capacitance for different strip pitches.

2.13 CMS simulation group

The CMS device simulation group has DESY, Helsinki Institute of Physics, Karlsruhe Institute of Technology, University of Delhi and University of Pisa working together. The groups aims are as following - (a) to provide input to the CMS sensor designs for the upgrade, (b) to simulate capacitances & verify isolation techniques, (c) to perform charge collection and read-out simulations for research optimal layout, (d) to derive a trap model to simulate radiation damage, and (e) to compare different simulation tools.

2.14 Conclusion

TCAD simulation is a powerful tool for investigation of silicon sensors. However, a comparison of the measurements with TCAD simulations is important to tune the models and the various simulation parameters. It is important to develop radiation damage model to describe and understand the whole set of available measurements. Due to computational issues all the models are based on 2 or 3 most effective levels. Also there is a need to develop a model suitable for different set of detectors and irradiations which will be helpful in understanding the behaviour of the novel detectors and design optimization.

Chapter 3

Design, Fabrication and Measurement of BEL fabricated silicon sensors

The tracker system of the HEP experiments imposes stringent specifications on the sensor specifications like low total leakage current I_{tot}, low full depletion voltage V_{fd}, high breakdown voltage V_{bd}, choice of appropriate strip width (s_w) and strip pitch (s_p) for low interstrip capacitance C_{int} and high interstrip resistance R_{int}, and appropriate oxide thickness and quality for adequate coupling oxide, etc.

In view of same, AC-coupled and poly-silicon biased silicon strip sensors; fabricated on 4-inch, $300\,\mu\text{m}$ thick n-type wafers with an initial resistivity of 2-5 k$\Omega\cdot$ cm; having a strip width (s_w) and a strip pitch (s_p) of $30\,\mu\text{m}$ and $55\,\mu\text{m}$ respectively; and having multiple guard-ring structures, have been developed by the Delhi University (DU). The development is performed in collaboration with Fermi National Accelerator Laboratory (Fermilab), Argonne National Laboratory (ANL), US and Karlsruhe Institute of Technology (KIT), Germany. The research work constituted -

- Optimization of the sensor design through simulations
- Fabrication of sensors using the optimized sensor design
- Quality assurance of the fabricated yield for different characterization parameters
- Radiation tolerance studies at four different values of fluences.

The chapter provides an overview of the optimization and fabrication of the developed micro-strip sensors at DU. Further, the results of the non-irradiated and the irradiated characterization studies are reported in this chapter.

It may be noted that this successful development will pave the path to development of challenging sensor technologies and radiation hard sensors in India for future nuclear and HEP experiments.

3.1 Motivation for the development

The HEP group at the DU had participated in the design, fabrication and characterization of silicon sensors for the CMS Preshower [77, 78]. These sensors were DC-coupled and with a s_w and s_p of the order of 2 mm [79]. The work was carried out in collaboration with the Bhabha Atomic Research Centre (BARC), Mumbai and Bharat Electronics Limited (BEL), Bengaluru. The sensors were fabricated at the BEL foundry. The characterization setup developed at DU was used for testing the fabricated sensors at BEL.

However, instead of DC-coupled sensors, the tracker system of the HEP experiments employs AC-coupled silicon strip sensors having a s_w and a s_p of about 15-80 μm and 80-180 μm, respectively. Thus, an R&D effort was initiated by the DU HEP group to develop AC-coupled, poly-silicon biased silicon micro-strip sensors with the desired s_w and s_p, for the tracker system (and other relevant detector systems) indigenously. Additionally, the purpose of the project was to test the quality assurance of the foundry and the radiation tolerance capabilities of the developed sensors against the desired tolerances of the HEP experiments.

3.2 Design, layout and fabrication of the sensors

3.2.1 Sensor design optimization

The design of the single sided AC-coupled silicon sensors was optimized [80] using TCAD Silvaco software [69]. The initial design was chosen after reviewing the sensor designs used at earlier experiments, mainly D0 at Fermilab. Further, the guard ring (GR) and metal overhang (MO) designs like spacing between two consecutive GRs, GR width, number of GRs, MO inward extension, MO outward extension, etc. were optimized to meet the requirements in terms of obtaining an improved V_{bd} and other parameters like I_{tot}, V_{fd}, C_{int}, R_{int}, etc. to ensure reliable sensor operation characteristics.

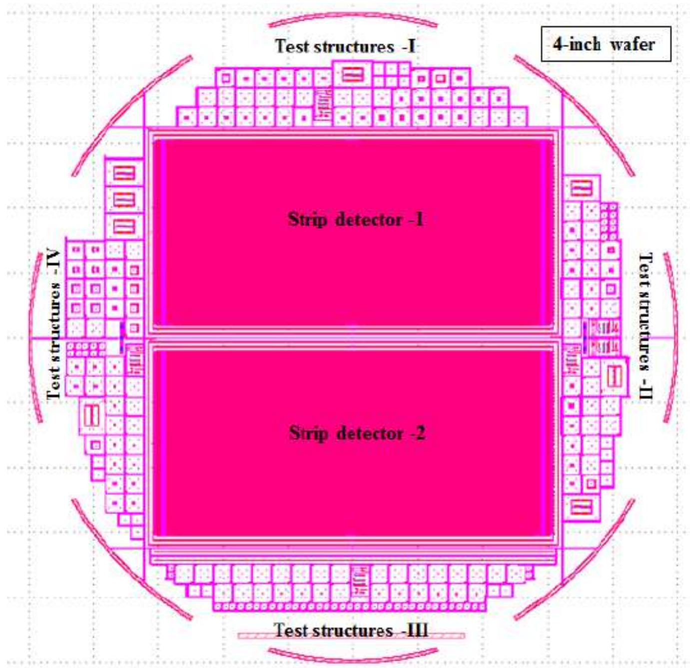

Figure 3.1: The layout of the wafer consists of two silicon strip sensors and several test structures on the periphery of the wafer. This layout is built in the kLayout [81] software.

Table 3.1: Design specifications chosen for the AC-coupled, poly-silicon biased, p-on-n silicon strip sensors.

Parameters	Value
Sensor geometry	6.43 cm × 3.25 cm
Resistivity	2-5 kΩ · cm
Number of strips	512
Strip width	30 µm
Strip pitch	55 µm
Strip length	6 cm
sensor thickness	300 ± 20 µm
Metal overhang	5 µm on both sides of the strip
Number of guard rings	4
Width of guard rings	50 µm for innermost, 25 µm for others
Spacing between strip and guard ring	25 µm
Spacing between guard rings	25, 30, 40 µm
Aluminium contacts	DC and AC pads

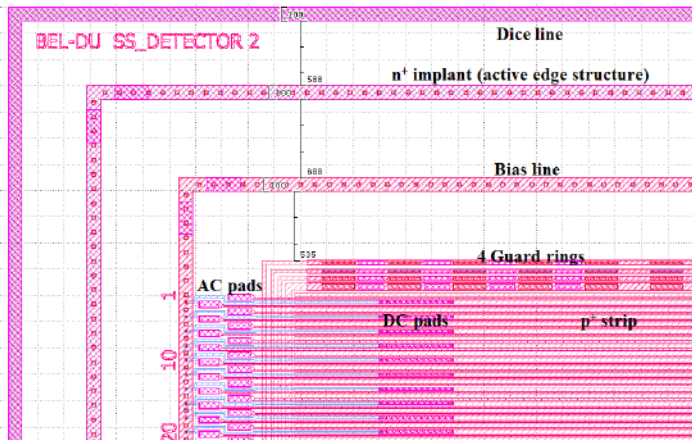

Figure 3.2: The enlarged view of the strips, the guard ring structures, the bias line and the dice line.

3.2.2 Layout of the micro-strip sensors

The wafer layout, which is shown in Fig. 3.1, includes two strip sensors along with several test structures (Designs built on ideas described in Ref. [82]), like MOS capacitors, pad diodes in different configurations, mini-strip sensors, etc. placed at the periphery of the wafer (referred to as "Test Structures I-IV").

Each of the strip sensors has a surface area of 6.43 cm (length) $\times$ 3.25 cm (width), processed on a 4-inch, $300\,\mu m$ thick silicon wafer. Each sensor has 512 strips of s_w of $30\,\mu m$ and s_p of $55\,\mu m$ surrounded by four GRs having different spacing. The first GR is $50\,\mu m$ wide followed by three GRs, each of equal width of $25\,\mu m$. A distance of $535\,\mu m$ from the last GR separates the $100\,\mu m$ wide p^+ doped bias line. Further, a $100\,\mu m$ n^+ implant active edge structure separated by a distance of $600\,\mu m$ from the bias line edge is provided. This has been implemented to minimize the dead space at the edge of the sensor. Usually under the effect of bias, the depletion region grows from the anode to the cathode, but having an implant of the same type as that of the cathode leads to the extension of the depletion region sideways also. This enhances the efficiency of the sensor as the dead space is only the area under the GR in this case [83]. Another $100\,\mu m$ n^+ implant is provided at a distance of $500\,\mu m$ for dicing the sensors. The DC readout pads, placed alternately on left and right end of the strips and inside the bias line structure perimeter, have been included to provide electrical contacts to the p-implants for the characterization. The staggered AC pads are provided at both ends of the strips and serve as wire-bonding points for the connection to the readout. The design specifications are listed in Table 3.1 and the enlarged view of the layout is shown in Fig. 3.2, depicting the design aspects.

3.2.3 Fabrication

N-type, 4-inch diameter silicon wafers with crystal orientation of $<111>$ having a nominal thickness of $300 \pm 20\,\mu\text{m}$ and average resistivity of 2-5 $k\Omega \cdot$ cm, procured from Silicon Quest International (SQI) Incorporated, USA and Topsil, Copenhagen Cleantech Park were used to fabricate the sensors. The mask set used for the fabrication includes eight different levels, each one associated to a different photolithography step. These are listed below in detail:

- **Bare wafer substrate**: A sacrificial oxidation layer of 0.42-$0.45\,\mu\text{m}$ is grown on the bare high resistivity n-type wafer. The back side of the wafer is stripped off the oxide for the purpose of gettering [1], followed by the stripping of the front side oxide.

- ***Mask 1* - The p^+ implants**: An initial oxide of 1.0-1.01 μm thickness is grown, being subsequently etched at appropriate places, making windows for the p^+ strip implantations (512 strips, 4 different GRs, and 1 bias line) by the photolithographic process using *mask 1*. A thin oxide is regrown in the windows to prevent implantation damage. After a boron implantation of dose 9×10^{13} cm^{-2} at an energy of 80 keV (peak concentration of $7 \times 10^{17}\ cm^{-3}$ and a depth of $4\,\mu\text{m}$, in a gaussian profile), the dopant activation and drive-in diffusion was performed by employing the drive-in cycles at a temperature of 1373 K, to reach a depth of 3.5-$4.0\,\mu\text{m}$. The simulated doping profile of the p^+ region and the drive-in cycle are illustrated in Fig. 3.3. The measured value of the sheet resistance is found to be 462 $k\Omega$ per ■ (kilo-ohm per square).

- ***Mask 2* - The n^+ implants**: Subsequently, the n^+ implant (dice line and active edge structure) on the front side was lithographically defined by *mask 2* and phosphorus implantation dose of $1 \times 10^{16}\ cm^{-2}$, at an energy of 50 keV (peak concentration of $2 \times 10^{20}\ cm^{-3}$ and a depth of $1.1\,\mu\text{m}$, in a gaussian profile) was performed first on the front side and then on the back side, followed by the drive-in cycle to form the n^+ implants on the front p-side and ohmic contact on the back side. The simulated

[1] Gettering is the process of introduction of a getter (Argon, in our case) that absorbs impurities, if any.

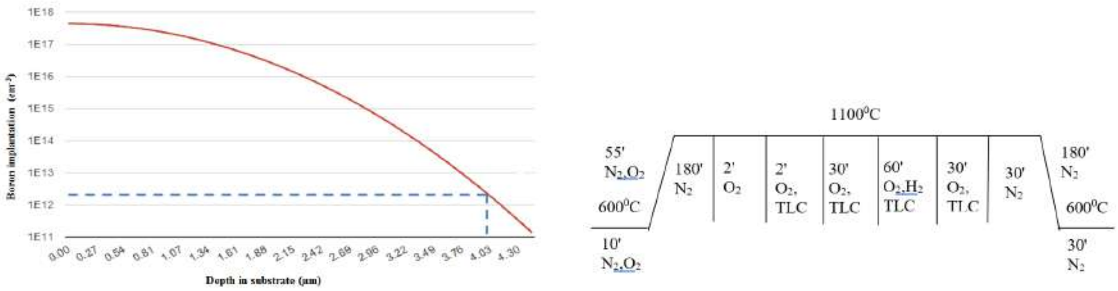

(a) (b)

Figure 3.3: (a) The frontside simulated p^+ implantation doping profile, and (b) the boron drive-in cycle during ion implantation.

doping profile of the n^+ region and the drive-in cycle are shown in Fig. 3.4. The measured value of the sheet resistance is found to be 214 kΩ per ■.

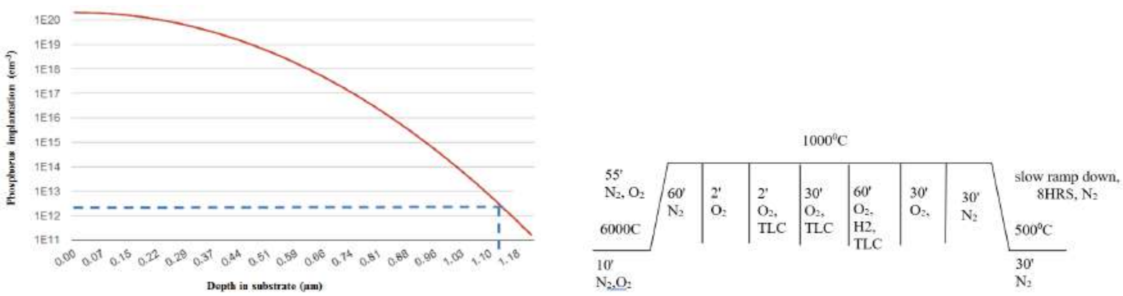

(a) (b)

Figure 3.4: (a) The backside simulated n^+ implantation doping profile, and (b) the phosphorus drive-in cycle.

- ***Mask 3* - The silicon dioxide (SiO_2) capacitors**: The coupling capacitors (*mask 3*) were then lithographically defined on the front side followed by a step employing the dry-wet-dry ambient regime, resulting in a thickness of 400 nm. The oxide layer formed on top of the p^+ strips creates an AC coupling path for the signal readout.

- ***Mask 4 and 5* - Poly-silicon resistors**: Further, using *mask 4*, oxide openings over strip implants and bias line region were defined to provide contact of the poly-silicon with the under-lying strip implant regions. Next, lithographic patterning of the poly-silicon was done using *mask 5*, followed by deposition of the poly-silicon of thickness 0.250-$0.253\,\mu m$ and boron implantation of dose of 4.5 $\times\ 10^{14}\ cm^{-2}$ at an energy of 80 keV was performed to form the poly-silicon resistors. The drive-in schedule

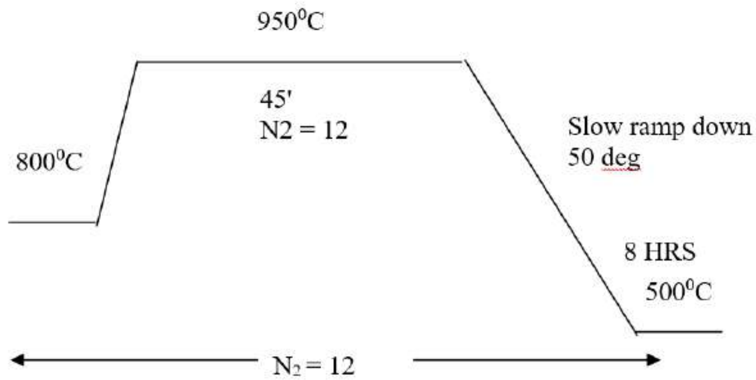

Figure 3.5: The drive-in schedule for the formation of poly-silicon resistors.

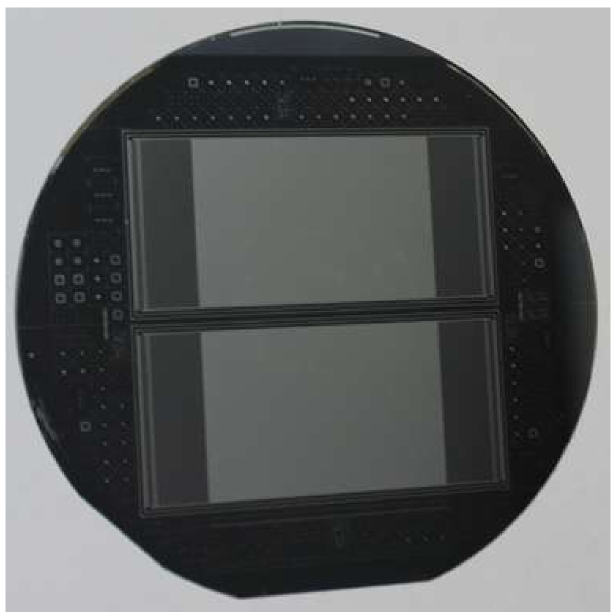

Figure 3.6: The fabricated wafer consisting of two silicon micro-strip sensors along with several test structures.

performed is shown in Fig. 3.5. This is followed by a short annealing step of 45 minutes at a temperature of 1223 K, was carried out for dopant activation of the species in the poly-silicon layer. The sheet resistance of the resistors is 10 kΩ per ■.

- ***Mask 6 and 7*** **- Aluminium contacts**: *Mask 6* was used for the contact lithography to open windows through the oxide for making contact with aluminium, i.e. contact between active n^+ edge, bias ring, and guard rings to their respective upper aluminium coverage. The various electrical contacts were defined using *mask 7* by patterning the metal layer. The contacts are of $1.5\,\mu m$ thickness, with MO of $5\,\mu m$

on both sides of the strip. This is followed by passivation of the entire sensor by a protective phospho-silicate glass (PSG) and silicon dioxide layer.

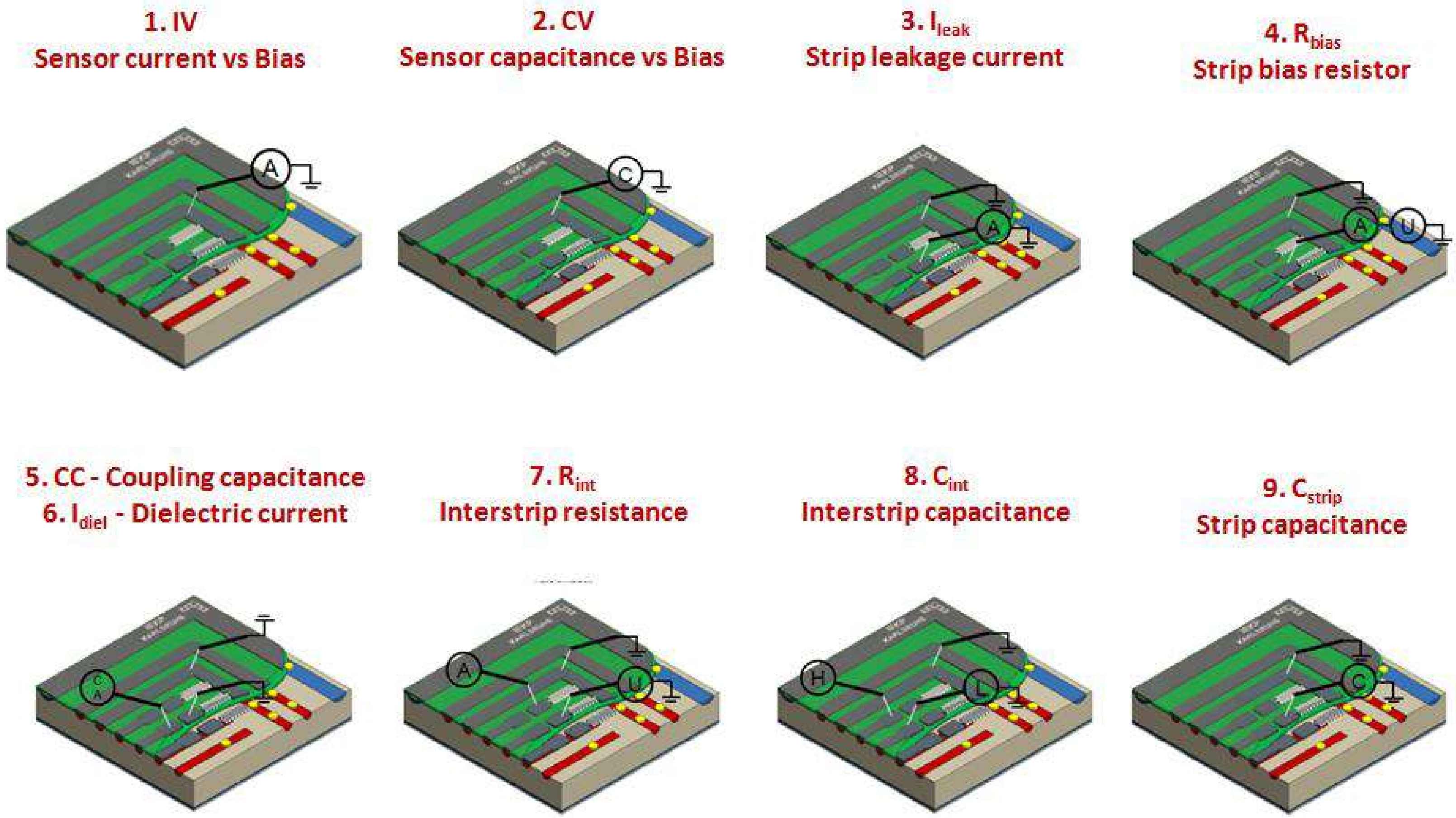

Figure 3.7: A total of 9 static electrical measurements can be performed using the probe station characterization system. Schematics to measure various sensor parameters [61]. Of all the measurements, C_{strip} is not frequently performed and so have not been reported here.

- ***Mask 8*** **- Metal openings**: The last lithography step (*mask 8*) on the front surface resulted in opening to the metal bond pads for connection to the read-out electronics and biasing. An aluminium metallization was finally carried out over the back surface.

The fabricated strip sensors and the test structures on the periphery of the wafer are shown in Fig. 3.6.

3.3 Measurement Setups

The measurement facilities at KIT and DU were used to carry out the static and dynamic characterization tests. The different probe needle connections for the electrical tests is illustrated in Fig. 3.7 and the values of the associated parameters for the sensor to qualify the acceptance criterion are listed in Table 3.2 (taken from Ref. [84]). A brief description of the setups are given below.

Table 3.2: Specifications for a typical sensor to qualify for use in HEP experiments.

Specifications	Tolerance limit
Total leakage current (I_{tot})	< 2 nA/mm^3 at 500 V
Junction breakdown (V_{bd})	> 700 V
Full depletion voltage (V_{fd})	< 100 V
Strip leakage current (I_{leak})	< 2 nA/cm at 500 V
Poly-silicon resistance (R_{poly})	1.5 ± 0.3 MΩ
Interstrip capacitance (C_{int})	< 1 pF/cm
Interstrip resistance (R_{int})	> 10 GΩ·cm
Coupling capacitance (C_{coup})	> 1 pF/cm·µm
Dielectric current (I_{diel})	< 1 nA at 10 V
No. of bad strips	$< 1\%$ per detector

3.3.1 The probe station setups at KIT

The lab at KIT has two probe stations (shown in Fig. 3.8), each equipped with a microscope-monitor system, a chuck plate with an extended platform, micro-positioners, microprobe needles, and a relay network. The system is placed on a heavy metal table to minimize mechanical vibrations. Since the initial sensor orientation has to be done manually before automated measurements, these probe stations are termed as semi-automatic. The silicon sensor is placed on an automated and programmable stepping stage, with translation in all

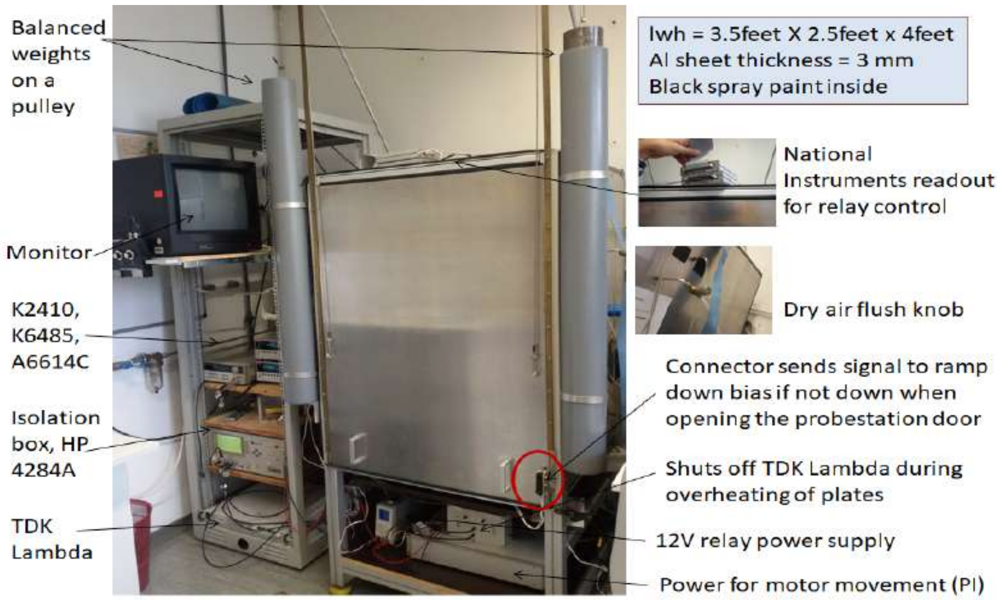

(a)

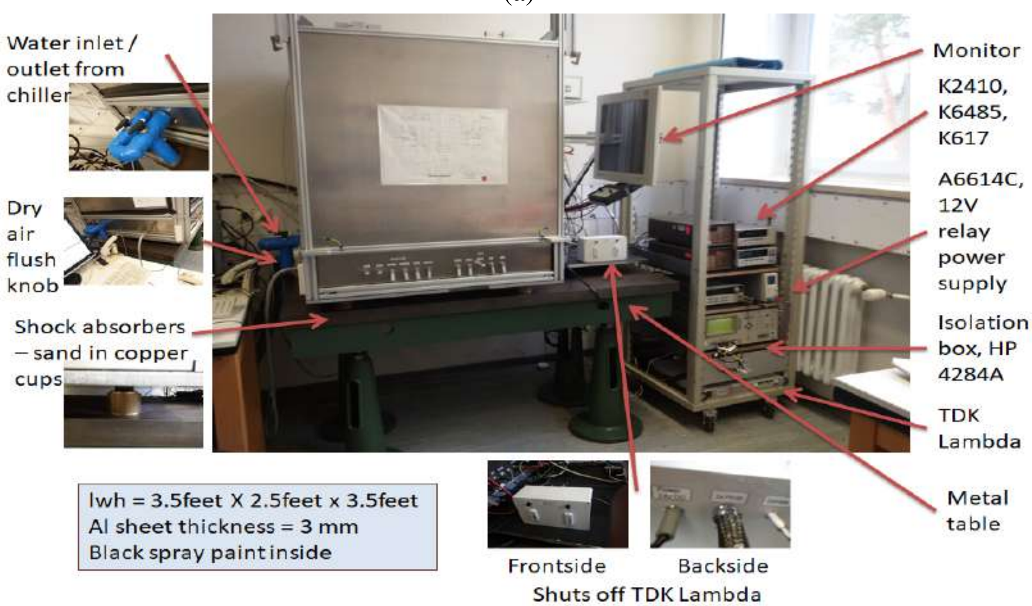

(b)

Figure 3.8: The two probe stations installed at KIT, Germany [85–87].

three coordinates (XYZ stage). The sensor is then aligned for automated measurements. The electrical equipment's (shown in Fig. 3.9a) involve two source measuring units (SMU) - Keithley 2410 and Agilent 6614C, a pico-ampere meter - Keithley 6485, and a capacitance voltage unit (CVU) - Hewlett Packard 4284A. These instruments are connected to

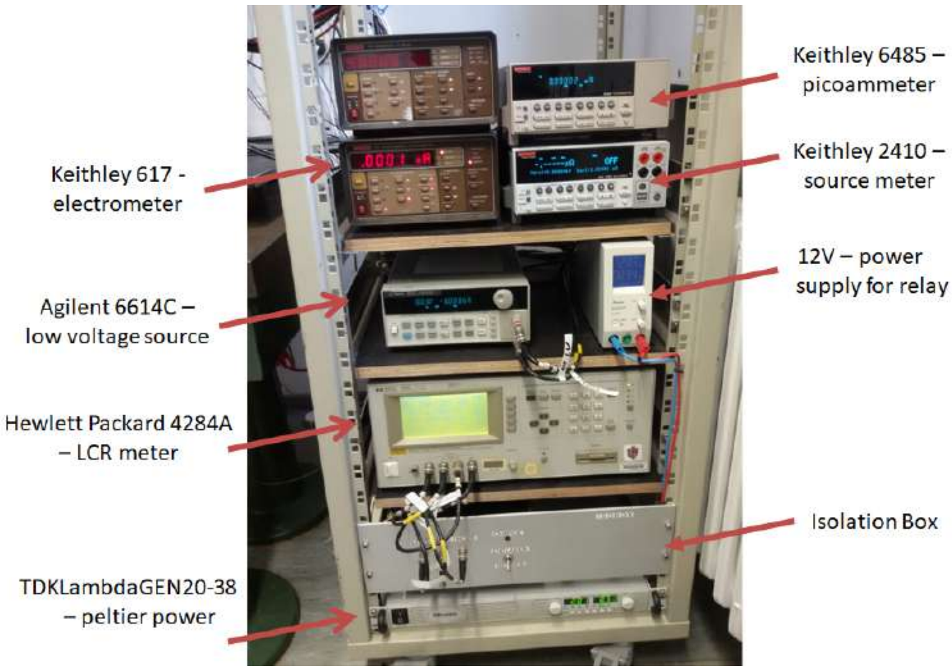

(a)

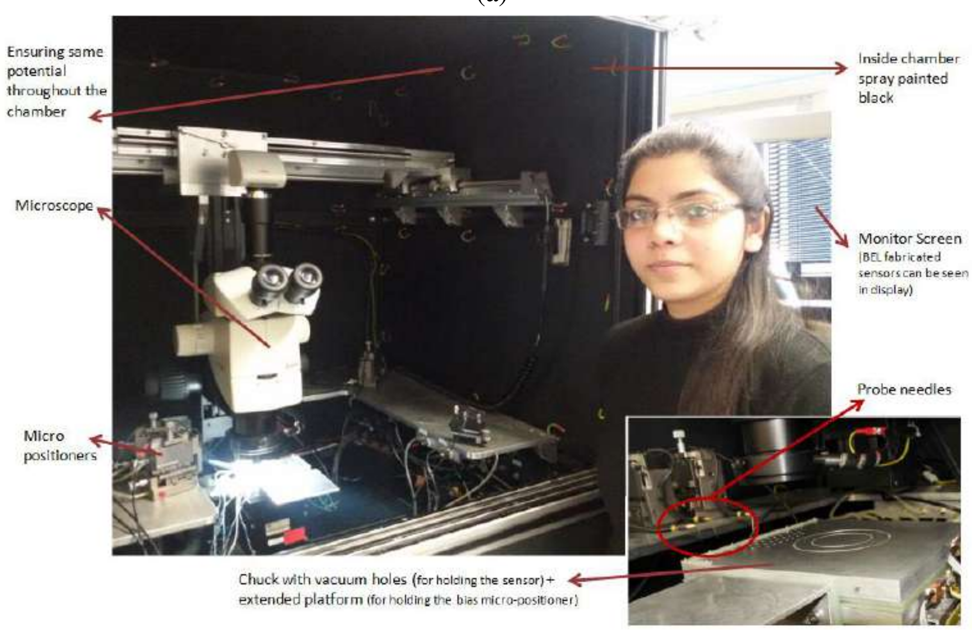

(b)

Figure 3.9: (a) The electrical equipments used with the probe station to carry out sensor characterization at KIT. (b) An inside view of one of the KIT setups.

the micro-positioners of the probe station through a relay switching matrix, the connections of which are activated through LabView program, to perform the 8 measurements sequentially. The schematics and details of the measurement tests can be found in Ref. [85]. An inside view of the probe station can also be view in Fig. 3.9b. The exhaustive description of the setups can be found in Ref. [85–87].

3.3.2 The probe station setup at DU

A photograph of the semi-automated probe station installed at DU is shown in Fig. 3.10. Because of lack of a relay network, the only instruments that were used alongwith this probe station were: Keithley 237 - as source and current meter, and a capacitance voltage unit - 590 CV Analyser. Therefore, only the I_{tot} and C_{tot} measurements could be carried out with the setup. The results are reported in [88].

Figure 3.10: The semi-automated probe station setup at DU. This probe station does not have a relay network and therefore only the global parameters measurements were performed.

3.3.3 The ALiBaVa setup at KIT

For the charge collection (CC) measurements, the ALiBaVa setup [89] at KIT consists of a table, a board to mount the sensor, a daughter-board, a source, a scintillation detector placed inside, and a mother-board placed outside of an electromagnetic shielded box. The mother-board and the daughter-board are the components of the ALiBaVa readout system,

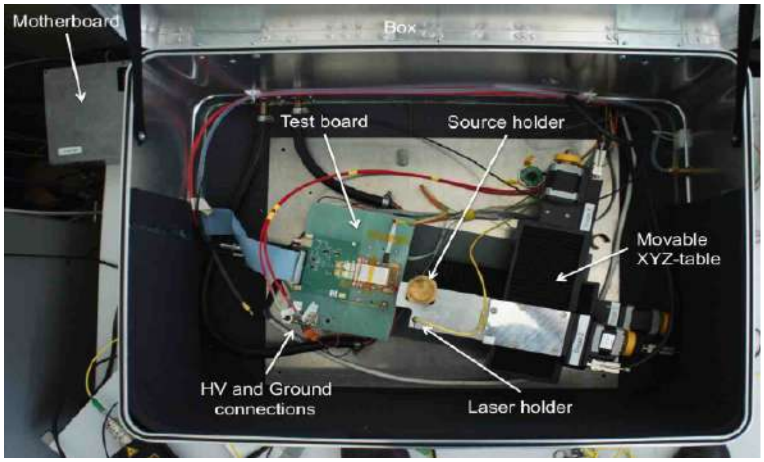

Figure 3.11: This photograph of the KIT ALiBaVa is taken from Ref. [86].

which use two Beetle chips [90, 91]. The Beetle chip has a system clock with a time period of 25 ns, as the other LHC strip read-out chips. A photo of the setup is given in Fig. 3.11Ref. [86]. For the measurements, a ^{90}Sr source, emitting β^- particles, and having a mean energy of 939 keV, is placed on top, at a certain distance from the sensor. A small section of the sensor strips (about 45 strips) is wire bonded to Beetle chip channels (1 Beetle chip consists of 128 readout channels, hereafter 'strip' will be referred as 'channel' through the pitch adaptors, which is in turn connected to the other readout electronics. There are three kinds of runs - pedestal run, radioactive source (RS) run, and calibration run. During the 'pedestal run', the readout is taken from all the channels in the absence of the source. A sample plot for the ADC counts recorded by 256 channels for 1 event is shown in Fig. 3.12a. The unbonded channels and the channels with ADC counts greater than 7 ADCs are masked (shown in solid red line), i.e. not used in further analysis. The correction for the electronic readout fluctuations over different events (called the 'common mode') is applied. The 'threshold signal' for each channel is then defined as the standard deviation of the pedestal after correcting for each event for the common mode. For the 'RS run', the hit map, i.e number of events a channel for which the strip is hit in the presence of ^{90}Sr source, can be viewed in Fig. 3.12b. The channel having a signal three times larger than the threshold signal is considered as the 'seed signal' and the neighbouring channels with signal higher than two times the threshold signal are added to the seed signal to form a 'cluster signal'. Finally, a 'calibration run' is performed where the system injects a known quantity of charge into the Beetle readout channels. The corresponding ADC counts recorded are said to be equivalent to the number of electrons injected, in each channel. The sample plot

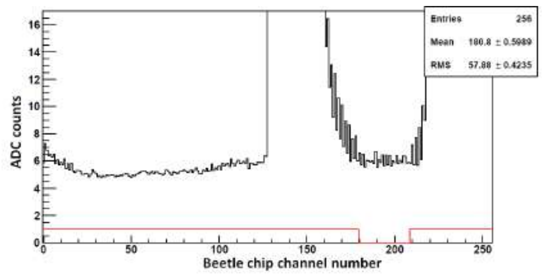

(a)

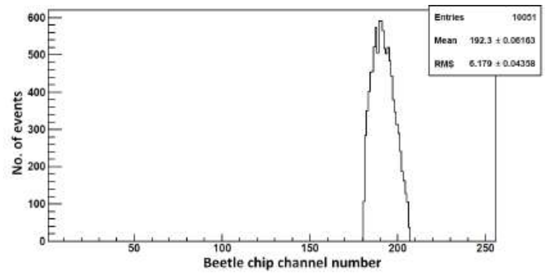

(b)

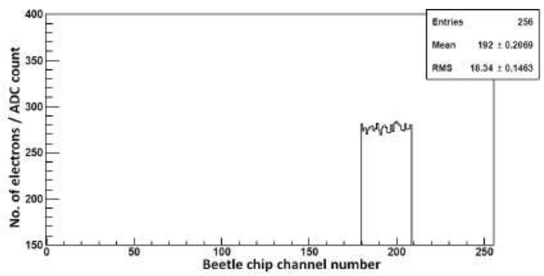

(c)

Figure 3.12: A sample recorded distribution of the (a) pedestal scan, (b) hit map, and (c) calibration run; is shown.

for this is shown in Fig. 3.12c.

3.4 Proton Irradiation at Karlsruhe

Besides the qualification of the sensor parameters for the sensor on irradiated directly from the foundary, the radiation tolerance of the BEL sensors has also been evaluated. The sensors were irradiated with a proton beam of 23 MeV energy at the compact cyclotron [92] operated by ZAG Zyklotron AG, Karlsruhe, under the Advanced European Infrastructures for Detectors at Accelerators (AIDA) [93] programme. More details on the centre can be found in [86]. A total of four sensors were irradiated at the ZAG facility to different values of fluence. The values of fluence are chosen to be 1×10^{14}, 5×10^{14}, 1×10^{15}, and 5×10^{15} $n_{eq}\cdot cm^{-2}$, which were selected to reflect the particle flux environment at which the silicon sensors are expected to be exposed in future HEP experiments. These fluence values have been selected to reflect the present particle flux environment hitting the silicon sensors in HEP experiments. Also proton beam was chosen as the irradiation beam over neutron beam, because of its easy availability and the fact that the flux of the charged particles is greater than the flux of the neutral particles on the inner layers of the tracker. All the above mentioned performance parameters are analyzed and discussed in the coming sections.

3.5 Measurement results

For the strip parameters, both voltage and strip scans are performed. The scan of the strip parameter as a function of voltage, at any one strip, is defined as the voltage scan; whereas strip scan is the measurement of the strip parameter at a constant V, on all the strips of the sensor. While the voltage scans depict the behaviour of the strip parameters as a function of increasing voltage, the strip scans show the uniformity of the strip parameters after irradiation. For the measurements reported in this thesis, a random strip from the centre of one of the three (randomly chosen) sensors was used to carry out the voltage scan. A strip scan was performed at a constant voltage of 200 V. For the non-irradiated case, a histogram distribution of the strip scans for 3 sensors is also presented.

3.5.1 Non-irradiated

All the non-irradiated measurements were carried out in a controlled low humidity (RH $<$ 40-50 %) and clean environment and at a room temperature of 20 °C.

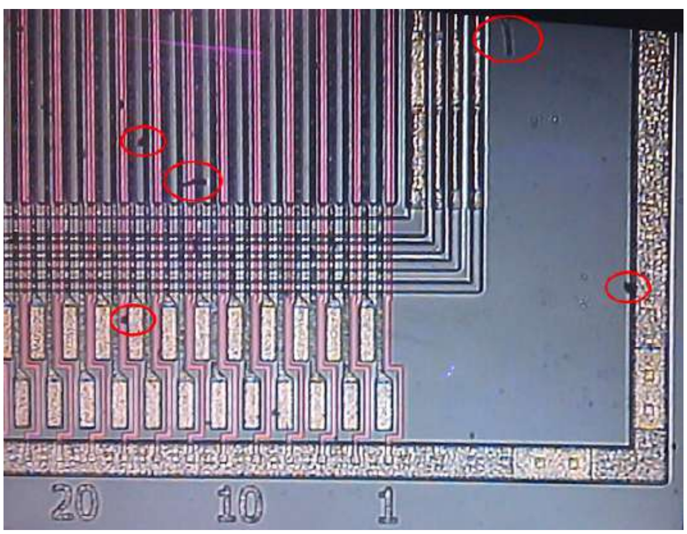

Figure 3.13: A small region of the sensor seen through a microscope for optical inspection. The red circles in the figure possibly show the dust particles on the sensor. The sensor has to be cleaned before placing it in the probe station for measurement.

- **Optical inspection**: At a first glance, the sensor is seen through the microscope for any dust particles, scratches, short-circuited implants, uneven edges, non-uniform strips, etc. Fig. 3.13 shows a photograph of one of the strip sensors inspected under

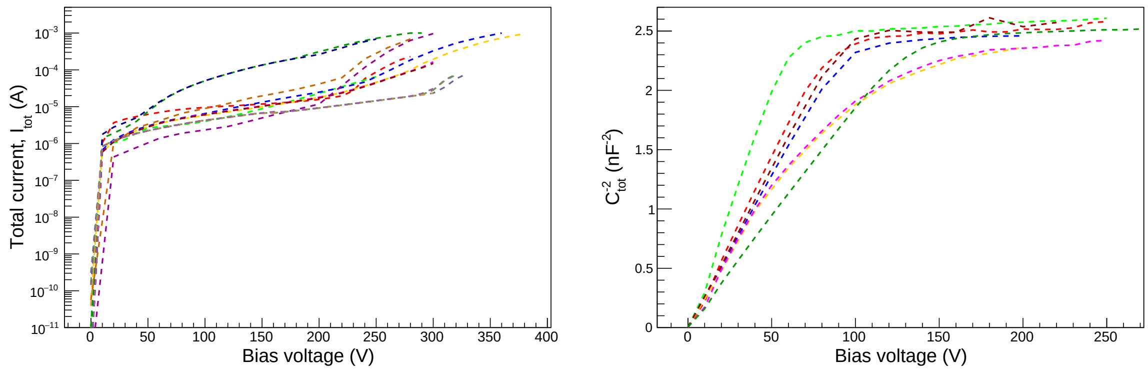

(a) (b)

Figure 3.14: The measurement results of (a) the total leakage current, and (b) the inverse square of the backplane capacitance, measured as a function of reverse bias voltage.

a microscope. Most of the sensors were qualified under the inspection; a very few showing the possibility of having dust particles on them.

- **Total leakage current**: Fig. 3.14a shows a plot of the I_{tot} as a function of V, keeping all the four guard rings floating. Except for two detectors, the I_{tot} for all the detectors lie in the range of $9\,\mu A$ to $40\,\mu A$ at 200 V. The onset of the gradual increase in the leakage current in the detectors lies between 230 V to 300 V.

- **Backplane capacitance**: Fig. 3.14b shows a plot of C_{tot}^{-2} vs V. The C_{tot} is measured from 0 V to 200 V in a step size of 10 V under reverse bias mode, keeping the guard rings floating, at a frequency of 1 kHz. Using the linear intersection method, V_{fd} was extracted and is found to lie between 60 V - 120 V range, for different detectors. Using the value of the V_{fd} and C_{tot}, the detector thickness and bulk resistivity values are calculated to be around $320\,\mu m$ and 2-5 $k\Omega \cdot$ cm respectively, which are consistent with their design values.

- **Strip leakage current**: Fig. 3.15a shows the voltage scan of I_{leak} for one of the representative detector. The plot shows the expected increase in I_{leak} with V, with the current remaining below 10 nA at 200 V. The strip scan plot, shown in Fig. 3.16a, depicts the uniformity of I_{leak} and lies in the range of 1 nA to 10 nA at 200 V, for most of the strips. Very few low current outliers are observed in the plot, which can be attributed to loss of connection between the probe needle and the detector pad during the measurement. Fig. 3.17a, showing the histogram representation of the strip scan of three detectors, illustrates that on an average, less than 3% of the strips in a sensor have $I_{strip} > 30$ nA.

- **Poly-silicon resistance**: For the R_{poly} measurement, a fixed DC voltage of 2 V is applied on the DC contact of a particular strip and the difference in the current of that strip(i.e. with DC voltage of 2 V) with respect to the original current in that strip (i.e. without DC voltage of 2 V) is calculated. The ratio of the voltage (2 V) and this difference in the current gives the R_{poly} value. The voltage and the strip scans of R_{poly} are shown in Figs. 3.15b and 3.16b. It can be concluded from the plots that the value of the R_{poly} remains uniform throughout at around 1.1-1.2 MΩ for majority of the strips, which is consistent with the acceptance criterion. In addition to this, the R_{poly} is fairly uniform for the other detectors as well, and its value lies between 0.9-2.0 MΩ. This can be seen from Fig. 3.17b, which is the histogram plot of the strip scans, for the three detectors.

- **Interstrip resistance**: Similar to the R_{poly} measurement, for the R_{int} measurement, a voltage ramp is applied on the DC pad of a strip and the current is measured from one of its immediate neighbouring strip. The inverse of the slope of voltage vs current plot is used to derive the R_{int} value. The variation of R_{int} with voltage is shown in Fig. 3.15c. The Fig. 3.16c illustrates that for most of the strips on a detector, the R_{int} is consistent with the acceptance criterion. Also, a histogram representation of the strip scan for three detectors, in Fig. 3.17c, emphasizes the consistency in the R_{int}.

- **Coupling capacitance**: The voltage and the strip scans for the C_{coup} are shown in Figs. 3.15d and 3.16d. The measurement was performed at an AC frequency of 100 Hz, with an open calibration, followed by C_{coup} measurements. From the plots, it can be deduced that the mean value of the coupling capacitance is approximately 0.16 nF (0.88 pF/cm-μm). This is consistent with the specifications given in the acceptance criterion. The histogram of the strip scan distribution, illustrated in Fig. 3.17d, shows a small spread from the average coupling capacitance value, which highlights the uniformity of the oxide layer, indicating a good quality control in the fabrication process.

- **Interstrip capacitance**: The C_{int} is measured, between a DC strip and one of its immediate neighbouring DC strip. First an open calibration is performed by the internal calibration procedure of the LCR meter. This calibration is then applied for each sub-

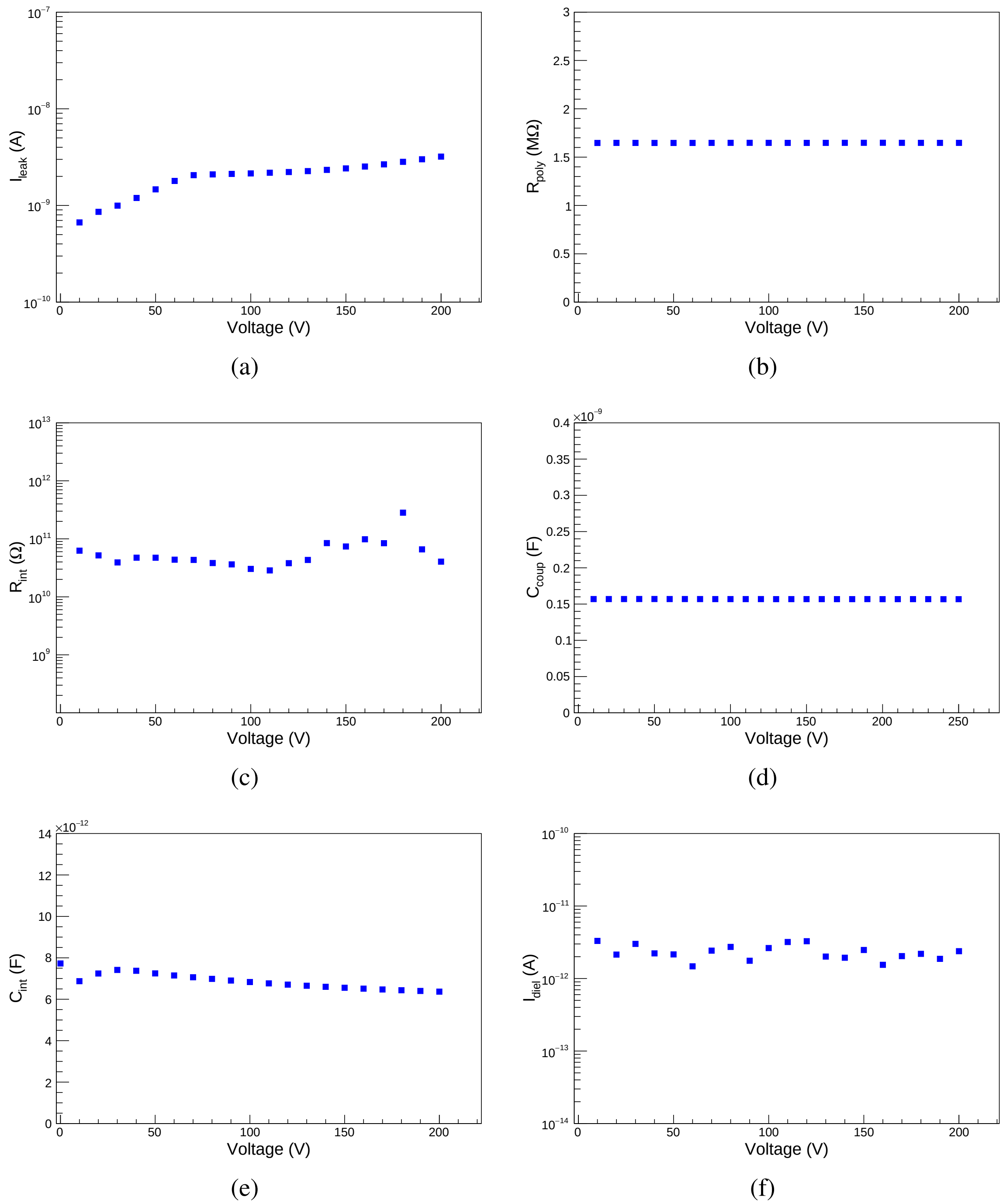

Figure 3.15: The voltage scans of the non-irradiated BEL sensors at a fixed strip for (a) strip leakage current, (b) poly-silicon resistance, (c) interstrip resistance, (d) coupling capacitance, (e) interstrip capacitance, and (f) dielectric current.

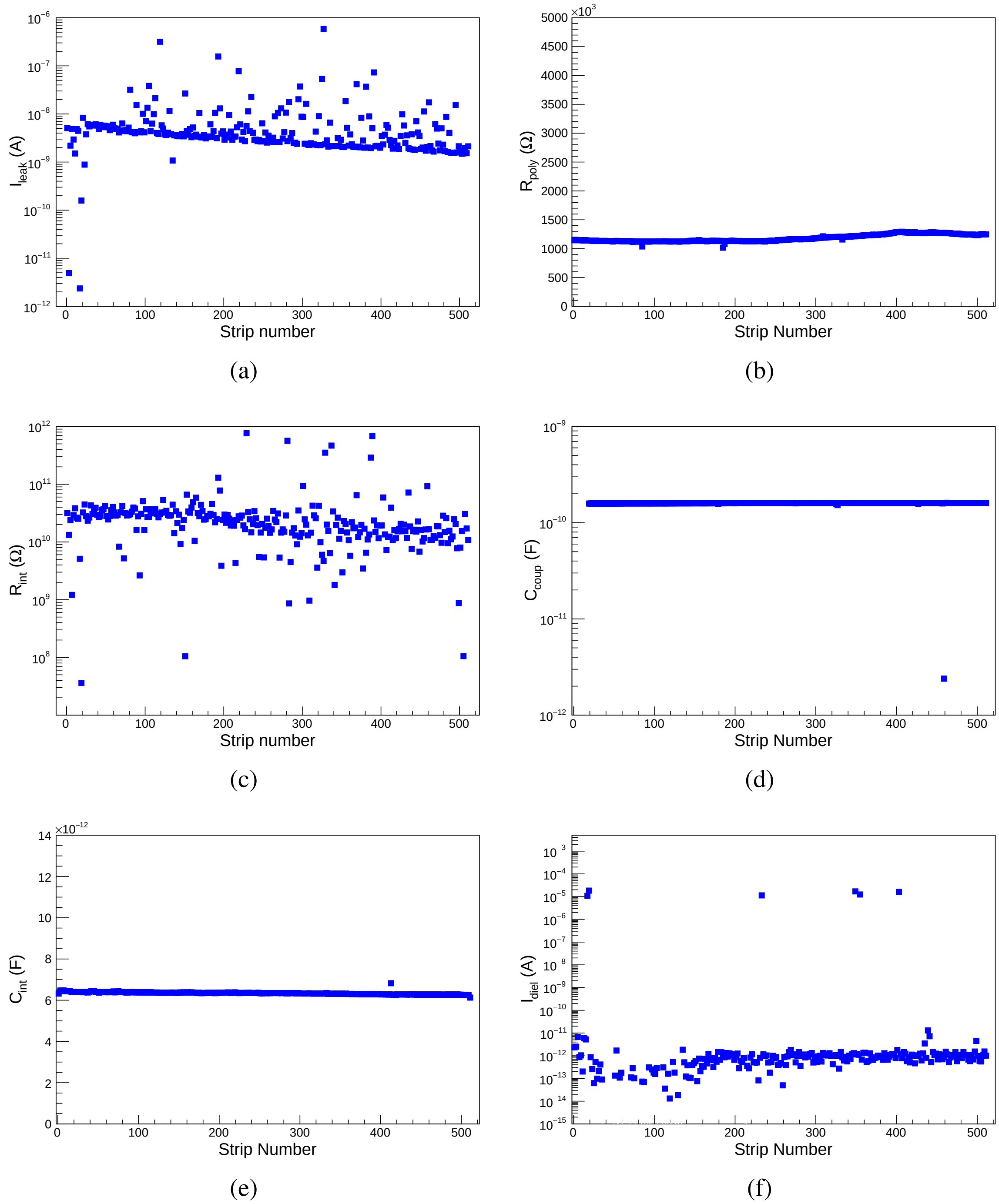

Figure 3.16: The strip scans of the non-irradiated BEL sensors at a constant bias voltage of 200 V for (a) strip leakage current, (b) poly-silicon resistance, (c) interstrip resistance, (d) coupling capacitance, (e) interstrip capacitance, and (f) dielectric current.

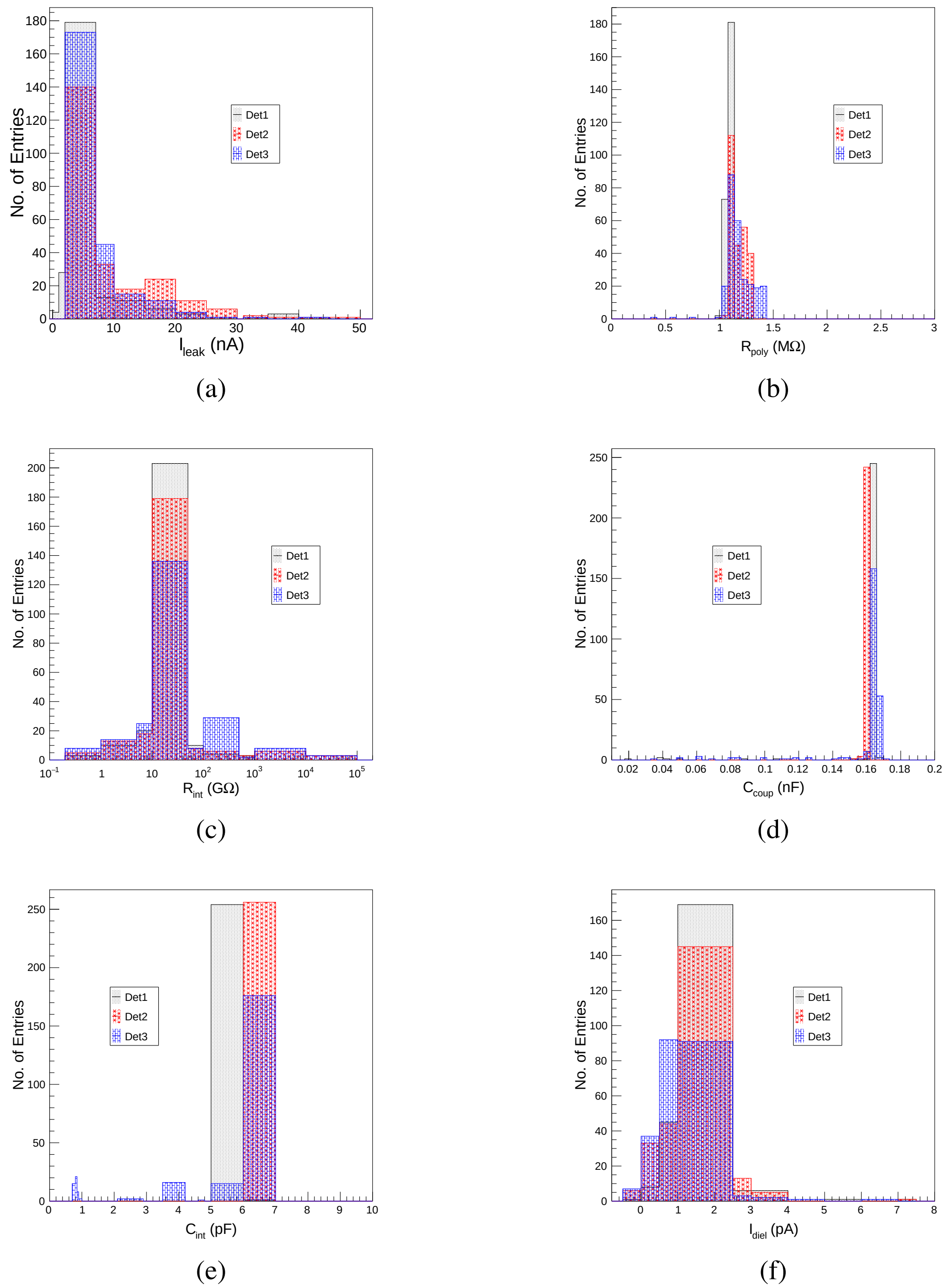

Figure 3.17: The histogram distribution of the non-irradiated BEL sensors for (a) strip leakage current, (b) poly-silicon resistance, (c) interstrip resistance, (d) coupling capacitance, (e) interstrip capacitance, and (f) dielectric current.

sequent C_{int} measurement. The measurement is performed at an AC frequency of 1 MHz. The C_{int} increases with V and then saturates at approximately 6-7 pF, which is close to the value of 7 pF for strip length of 6 cm, lies well within in the acceptance criterion. This can be seen in Fig. 3.15e. Further, Figs. 3.16e and 3.17e show that the measured value of C_{int} is quite uniform throughout the detector, indicating the good quality of the fabrication process.

- **Dielectric current**: A DC voltage of 10 V is applied on the DC pad of one of the strips of the sensor, and the current through its corresponding AC pad is recorded. If there is a presence of a pinhole in the oxide layer (short connection between the DC and the AC contacts), an excessive current is recorded at the read-out electronics. If this I_{diel} exceeds 1 nA, at 10 V, the strip is defined as defective and is rejected for connection to the readout. The voltage and the strip scans for the I_{diel} are illustrated in Figs. 3.15f and 3.16f. The presence of spikes at a few strips can be attributed to the presence of pinholes on those strips of the detector. A distribution plot of the strip scan of the I_{diel} on three detectors (Fig. 3.17f), highlights the average number of detected pinholes in the detector batch. One of the sensors show less than 1% of the strips having excessive current, whereas other sensor shows 2% and the third shows 5% of such strips.

- **Charge collection**: The sensor was mounted onto the ALiBaVA board and biased to a voltage of 150 V. During the RS run, a total of 10015 events were recorded with a sampling time of 25 ns. The CC distribution of the number of electrons collected for these 10051 events, shown in Fig. 3.18, is fitted with a convolution of a Landau and a Gaussian distribution. It can be seen that the most probable value (MPV) of the cluster signal is approximately 27570 electrons, or 86 electrons per μm for a 320 μm thick sensor. Since the internal gain calibration has an uncertainty of $\sim$10% (spread of capacitance in chip) and in addition there is a $\sim$2-3% higher signal due to low energetic electrons from ^{90}Sr; the observed MPV is close to the expected 79 electrons per μm [94].

3.5.2 Irradiated

The measurements on the irradiated sensors are carried out in a clean environment having a controlled low humidity (RH $<$ 10 %) at a temperature of -20 °C, except wherever tem-

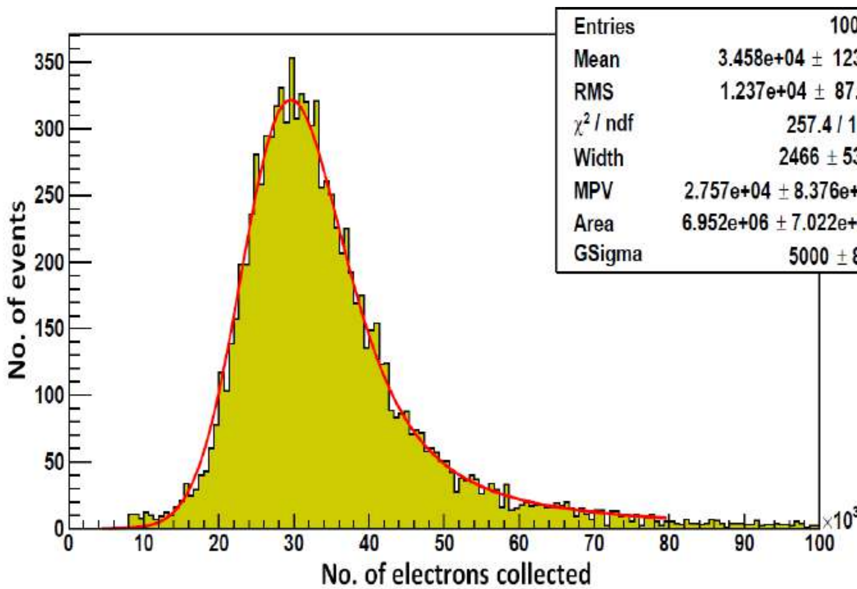

Figure 3.18: The non-irradiated charge collection distribution for one of the fabricated sensors at a reverse bias voltage of 150 V.

perature variation studies are performed. A typical behaviour of the non-irradiated sensor is also included in the results for comparison purposes. It may be noted that the results of certain parameters could not be measured for a few radiation steps due to hardware issues and hence are missing from the results shown. Nevertheless, the measured data is sufficient to draw conclusions on the radiation tolerance capabilities of the sensors.

- **Total leakage current**: The DC characteristics of the sensors as a function of bias voltage is measured before irradiation and after irradiation and is shown in Fig. 3.19. As expected, the irradiated sensors show a significant increase in the current compared to their non-irradiated counterpart. It is expected that the soft breakdown observed for (a) the non-irradiated scenario and (b) the higher currents at a lower fluence of 1×10^{14} $n_{eq}\cdot cm^{-2}$ at large voltages ($>$ 200 V) may be due to local discharges. This behaviour is no longer observed at higher fluence. Thus, we consider three values of fluence, i.e. 5×10^{14}, 1×10^{15}, and 5×10^{15} $n_{eq}\cdot cm^{-2}$ for estimating the leakage current damage constant, $\alpha(T)$, where T is temperature. The $\alpha(T)$, as estimated from this work, is found to be 9.57×10^{-19} $A\cdot cm^{-1}$ at 500 V and an approximate annealing of 1 hour at RT for these strip sensors, which is in reasonable agreement with the theoretically calculated value of 8.80×10^{-19} $A\cdot cm^{-1}$ at a temperature of -20 °C [38].

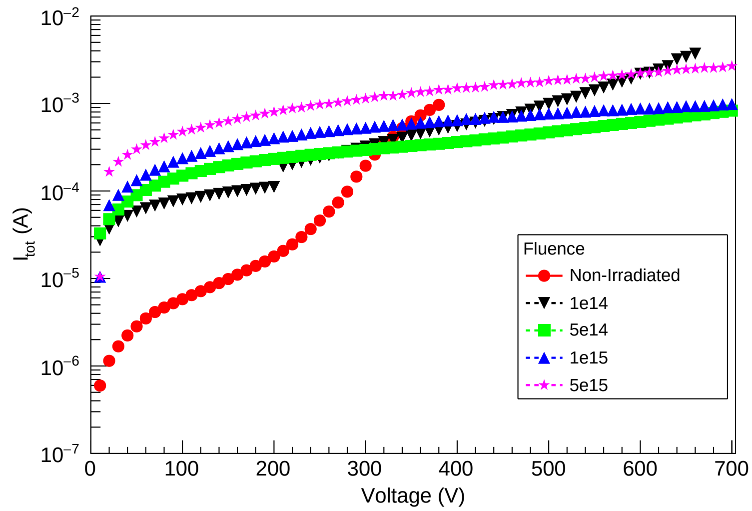

Figure 3.19: The total leakage current of the irradiated sensors as a function of reverse bias voltage measured at -20 °C. The measurement on non-irradiated sensor is shown for comparison purposes.

- **Strip leakage current**: It is observed from Figs. 3.20a and 3.21a that I_{leak} remains below 1 μA after irradiation.

- **Poly-silicon resistance**: R_{poly} is found to lie in the range of 1-2.5 MΩ for fluence = 1×10^{14} and 5×10^{14} $n_{eq}\cdot cm^{-2}$. Figs. 3.20b and 3.21b show a small change with fluence.

- **Interstrip resistance**: Figs. 3.20c and 3.21c show that the value of R_{int} decreases significantly from an order of 100 GΩs to 0.01-1 GΩs. For a suitable sensor operation, R_{poly} should be lower than R_{int} while maintaining uniformity over the strips of the sensor even after irradiation [84]. The measured R_{poly} values is atleast an order of magnitude less than the R_{int} values and also displays a reasonable homogeneity.

- **Coupling capacitance**: No change in C_{coup} (Figs. 3.20d and 3.21d) is observed within the measurement accuracy.

- **Interstrip capacitance**: Fig. 3.21e shows a decrease in the value of C_{int} for fluence = 1×10^{14} $n_{eq}\cdot cm^{-2}$.

- **Dielectric current**: The current through the dielectric, I_{diel} does not change as shown in Fig. 3.21f and only a few pinholes are observed, which demonstrates a good oxide

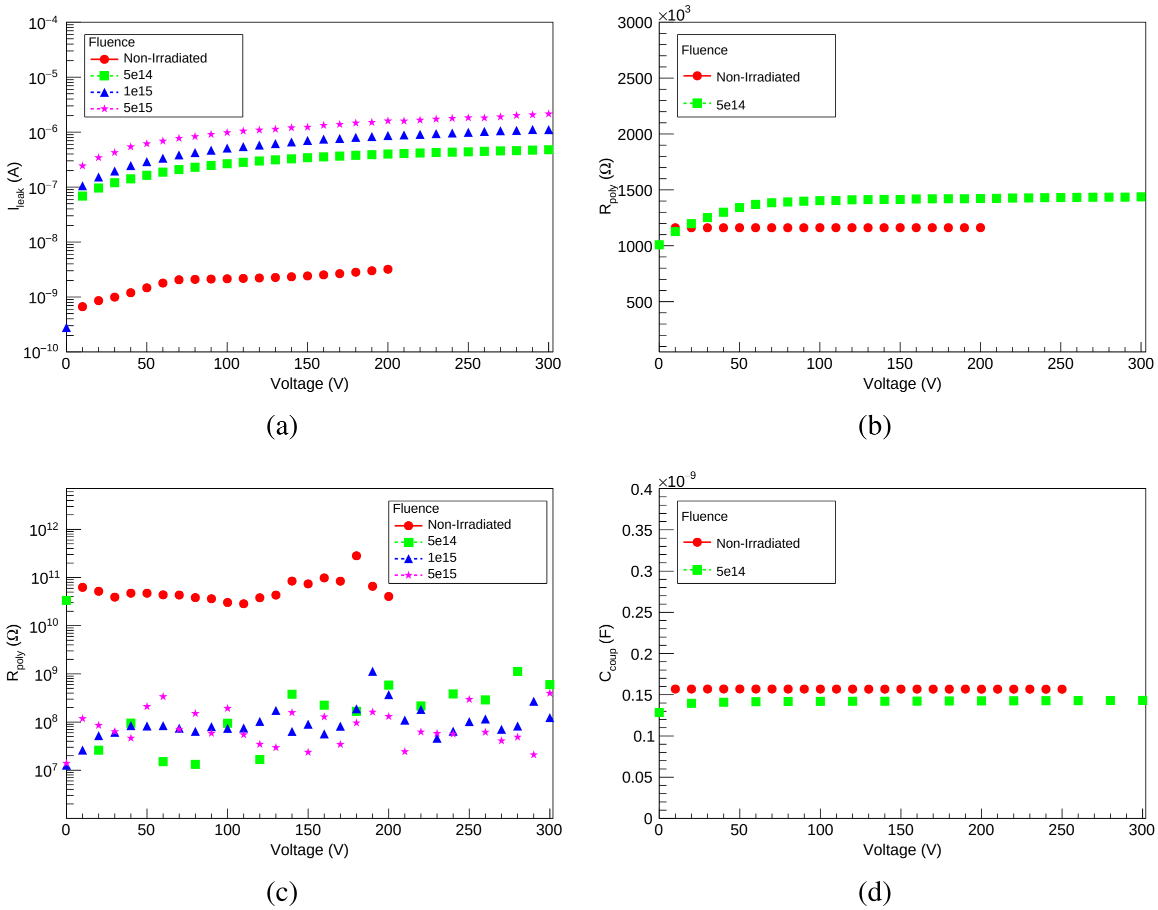

Figure 3.20: The voltage scans of (a) strip leakage current, (b) poly-silicon resistance, (c) interstrip resistance, and (d) coupling capacitance, before and after irradiation.

quality and a control over pinholes after irradiation.

- **Charge collection**: The CC distribution at the maximum measured bias voltage for all the fluence values along with the fit is shown in Fig. 3.22 and the response of CC as a function of bias voltage is represented in Fig. 3.23. It is observed that the non-irradiated sensor of 300 μm thickness collects a MPV charge of 27k e^-s at 150 V. However, as the fluence is increased to 1×10^{14}, 5×10^{14}, and 1×10^{15} n_{eq}·cm^{-2}, the corresponding MPV charge decreases to 21k, 17k, and 14k e^-s at bias voltages of 350, 600, and 900 V respectively. It is observed that for the sensor irradiated with the maximum fluence of 5×10^{15} n_{eq}·cm^{-2}, the signal could not be distinguished from noise even at a maximum applicable bias of 1100 V and hence is not reported here. Besides fluence, other parameters like measurement temperature and annealing may

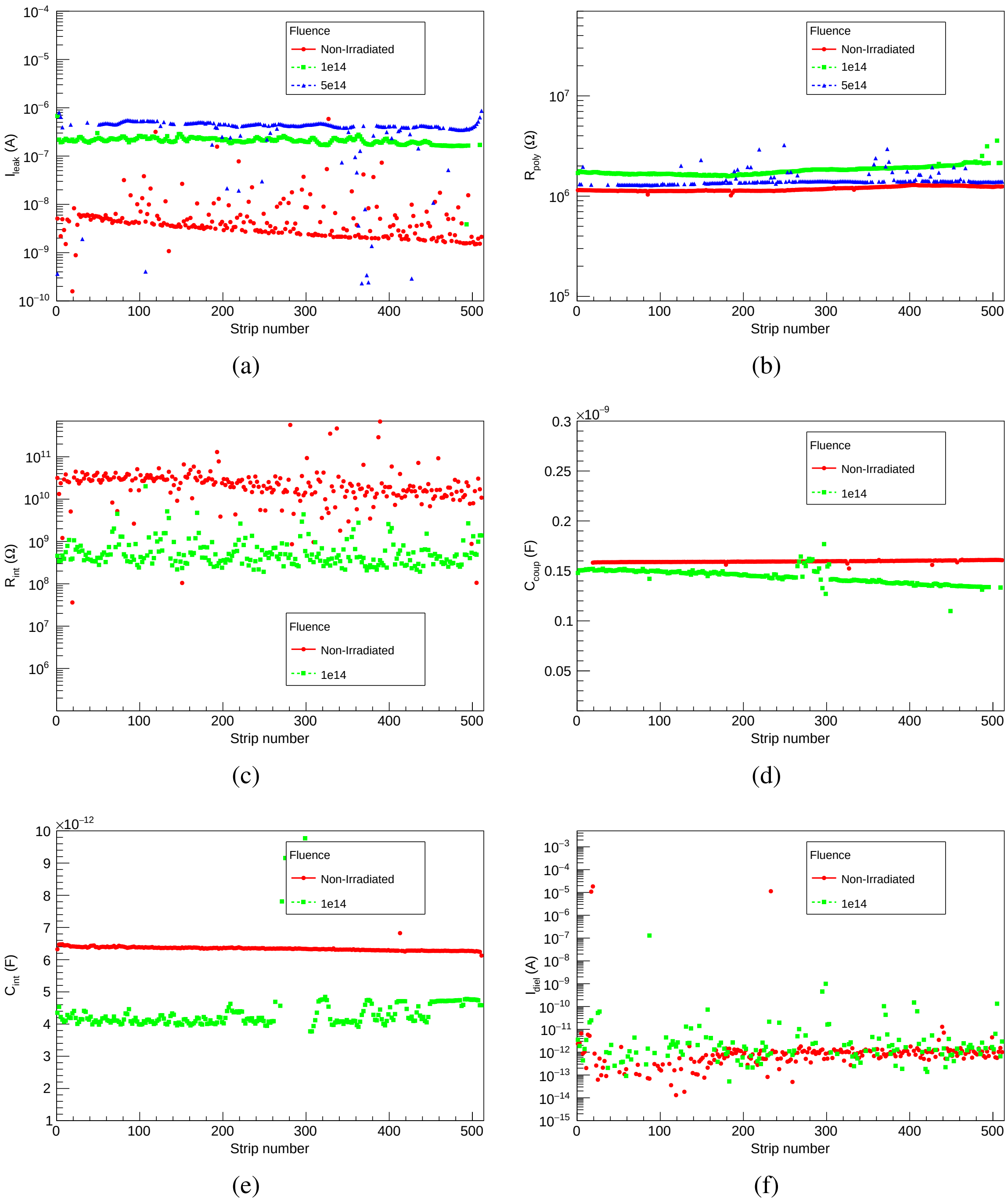

Figure 3.21: The strip scans at a constant voltage of 200 V for (a) strip leakage current, (b) poly-silicon resistance, (c) interstrip resistance, (d) coupling capacitance, (e) interstrip capacitance, and (f) dielectric current, before and after irradiation.

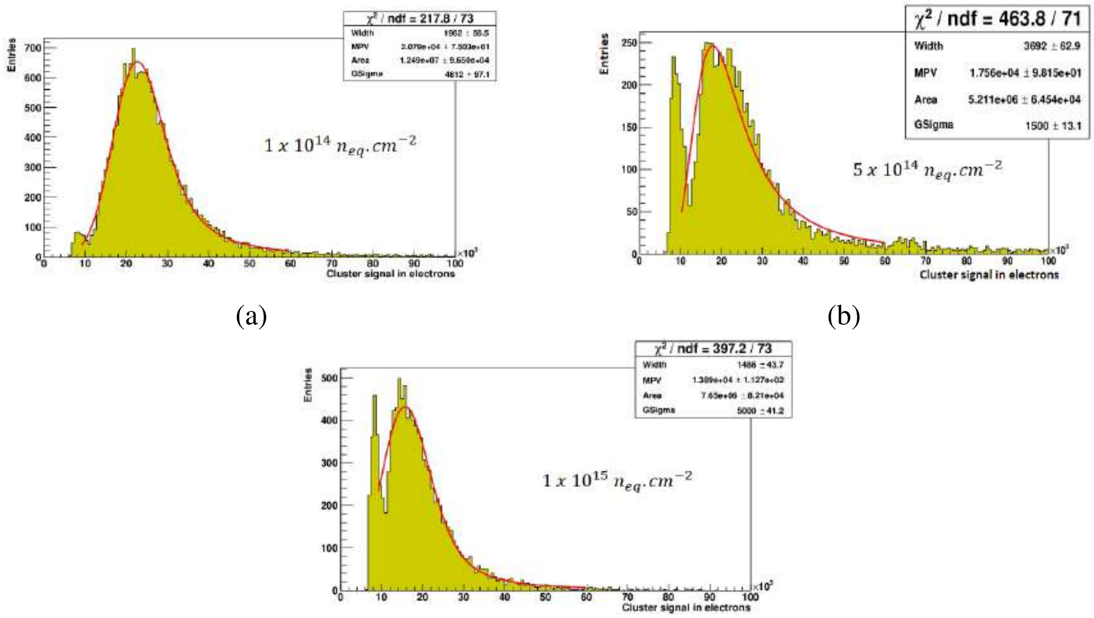

(a) (b) (c)

Figure 3.22: The charge collection distribution of the sensors irradiated to a fluence of (a) 1×10^{14}, (b) 5×10^{14}, and (c) 1×10^{15} $n_{eq} \cdot cm^{-2}$, at a bias voltage of 350, 600, and 900 V respectively.

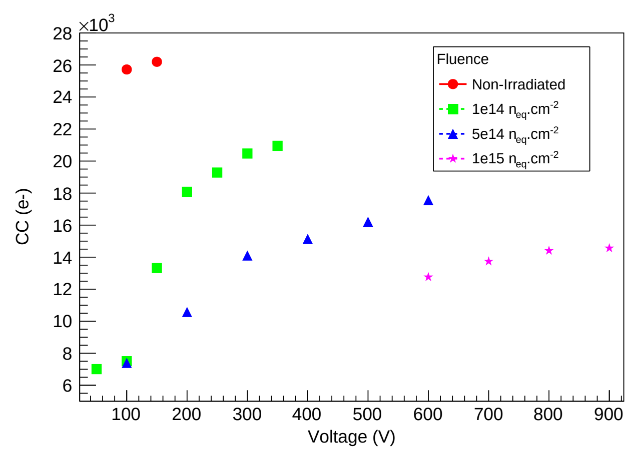

Figure 3.23: The charge collected for the non-irradiated and the irradiated sensors.

also affect the CC of a sensor. Thus the CC is investigated as a function of voltage for two cases - (a) with varying measurement temperature with 1 hour at RT annealing and (b) by performing several annealing steps and measuring at a temperature of -20 °C. The corresponding plots are shown in Figs. 3.24a and 3.24b respectively. It is observed from Fig. 3.24a that beyond full depletion, CC decreases with increase in temperature. Fig. 3.24b shows a notable increase in CC with increasing annealing for low bias voltages. Further, at higher bias voltages, CC tends to attain a constant value irrespective of the annealing.

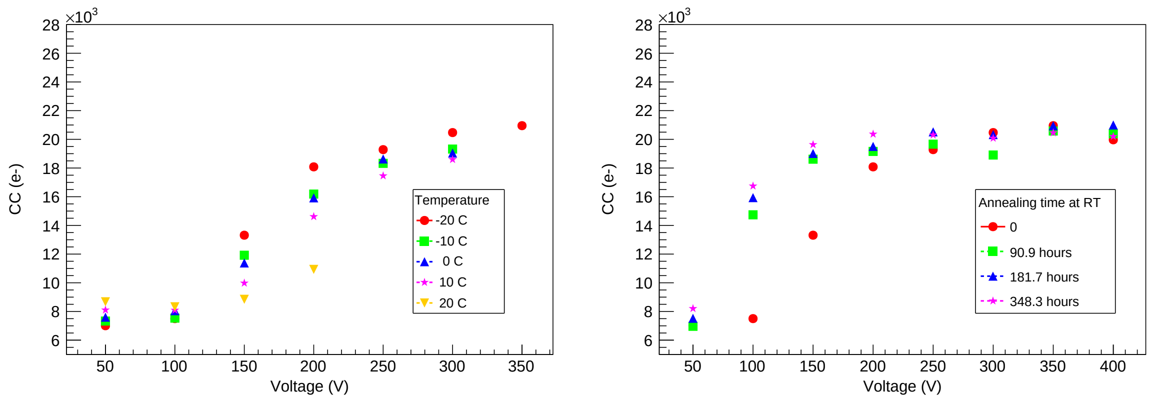

(a) (b)

Figure 3.24: The charge collection as a function of bias voltage for the sensor irradiated to a fluence = 1×10^{14} $n_{eq} \cdot cm^{-2}$ for (a) varying measurement temperature with 1 hour at RT annealing on the sensor; and (b) increasing annealing at constant measurement temperature of -20 °C. The annealing is performed in steps of - (i) 60 °C for 20 minutes, (ii) followed by an additional 60 °C for 20 minutes, and (iii) additional 60 °C for 40 minutes. The legend lists the normalisation to RT based on the parametrization given in Ref. [38].

3.6 Some results of measurements on test structures

Test structures are fabricated in addition to the strip sensors, on the periphery of the wafer. Measurements on the test structures can provide information of various parameters like leakage current, V_{bd}, flat-band voltage (V_{fb}), fixed oxide charge density (N_{ox}), V_{fd}, etc. that can be useful in the understanding of the characteristics of the strip sensor. In this section, the V_{bd} results for diodes with - (i) increasing GR spacing and (ii) number of GRs; and capacitance measurements of Metal Oxide Semiconductor (MOS) devices are discussed. An optically zoomed image of the diode is shown in Fig. 3.25. These results are reported in Ref. [95].

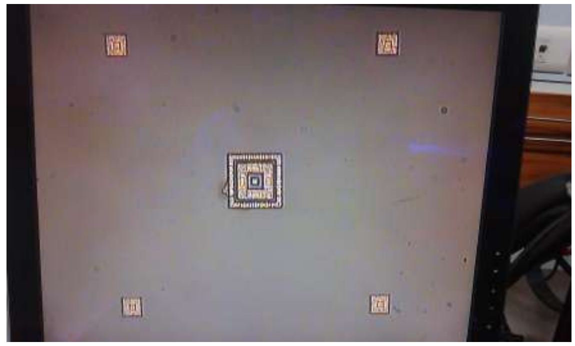

Figure 3.25: A diode test structure with 2 guard rings can be viewed.

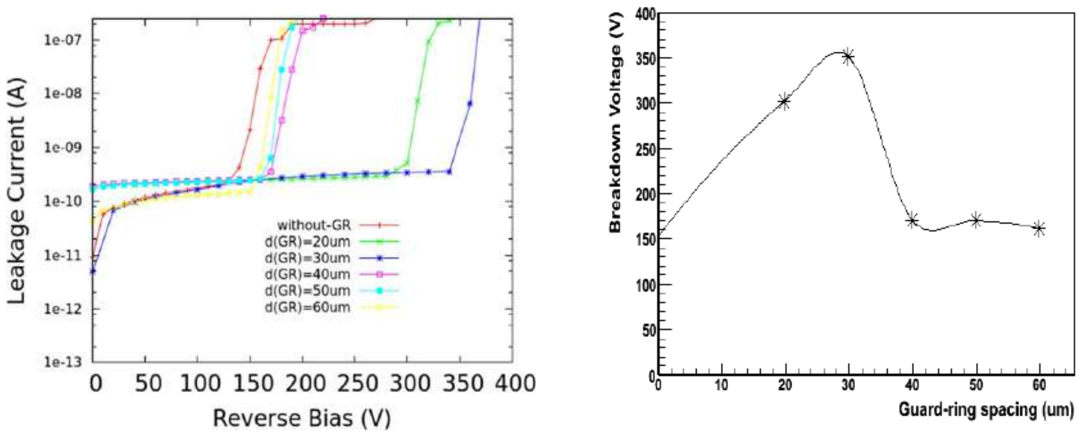

(a) (b)

Figure 3.26: (a) Leakage current as a function of reverse bias and (b) breakdown voltage as a function of reverse bias; for diodes without and with one guard ring structures.

3.6.1 Diode

GRs are useful to reduce the surface leakage current from diced edges and improve the breakdown performance by establishing a uniform potential drop along the silicon surface.

- **Guard ring spacing**: The measurements are performed on diodes having single GR, with varying GR spacing of 20, 30, 40, 50 and $60\,\mu\mathrm{m}$. Fig. 3.26a shows the effect of GR spacing on leakage current as a function of reverse bias voltage. For reference, the IV characteristics of diode without GR is also shown. The plot for V_{bd} vs GR spacing is plotted in Fig. 3.26b. It can be deduced that maximum V_{bd} is equal to 350 V which corresponds to the diode having GR spacing of $30\,\mu\mathrm{m}$.

- **Number of guard rings**: To study the effect of number of GRs on the breakdown

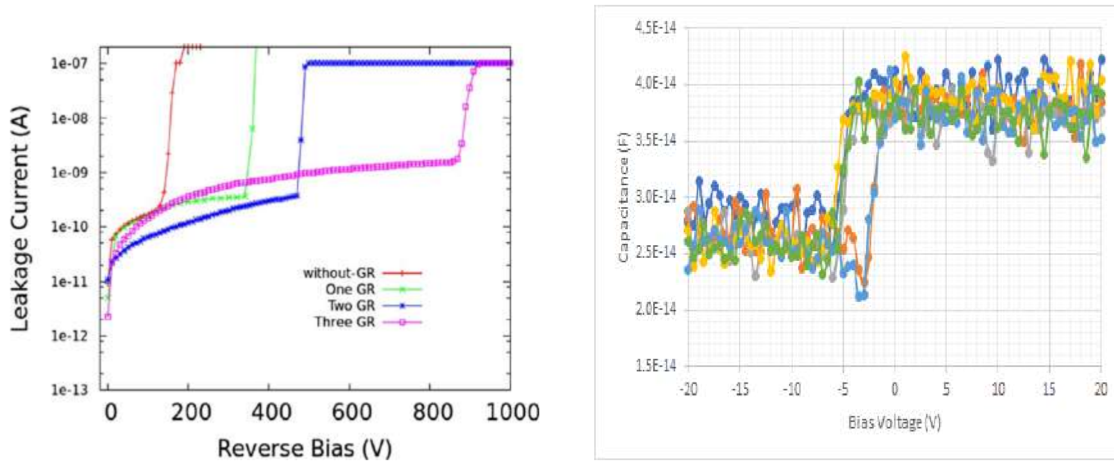

(a) (b)

Figure 3.27: (a) Effect of number of guard ring on breakdown voltage. (b) MOS capacitance as a function of bias voltage.

performance, measurements are also performed on diodes having different number of GRs. It can be seen from Fig. 3.27a that on increasing the number of GRs, V_{bd} improves.

The measurement results clearly indicate that it is important to optimize both the GR spacing as well as the number of GRs. It is recommended to have a GR spacing of $30\,\mu m$ for a single GR structure. Further, additional GRs are beneficial to improve the breakdown performance of the silicon strip sensors.

3.6.2 MOS

Capacitance measurement of a MOS can reveal information about the amount of surface damage caused during the fabrication itself. This is also denoted by N_{ox} and the formula to calculate it is as given below:

$$N_{ox} = \frac{C_{ox}}{e.A_{cv}}.(\phi_{ms} + V_{fb}) \tag{3.1}$$

where C_{ox} is accumulation capacitance of MOS, A_{cv} is area of MOS, and ϕ is metal-semiconductor work function.
From Fig. 3.27b, C_{ox} is taken on average to be equal to 3.7×10^{-14} F and 3 values of V_{fb} are observed - (i) 2 V, (ii) 5 V, and (iii) 6 V. Since the measured MOS has A_{cv} = $30\,\mu m$ $\times$

$30\,\mu m$ and n-type MOS implies phi = -0.5 V, the 3 values of N_{ox} are found to be - (i) 0.38 $\times 10^{11}$ cm^{-2}, (ii) 0.97 $\times 10^{11}$ cm^{-2}, and (iii) 1.41 $\times 10^{11}$ cm^{-2}, respectively.

3.7 Summary

Table 3.3: The mean values of the strip parameters at a reverse bias voltage of 200 V.

Strip parameter **Fluence ($n_{eq}\cdot cm^{-2}$)** **Temperature**	**Non-irradiated** **0** **20 °C**	**Irradiated** **1×10^{14}** **-20 °C**	**Irradiated** **5×10^{14}** **-20 °C**	**Irradiated** **1×10^{15}** **-20 °C**	**Irradiated** **5×10^{15}** **-20 °C**
Strip leakage current	1-10 nA	0.1-0.3 µA	0.4-0.6 µA	$\approx$ 1 µA	$\approx$ 2 µA
Poly-silicon resistance	1-2 MΩ	1-2 MΩ	$>$ 2 MΩ for few strips	–	–
Interstrip resistance	$>$ 10 GΩ	$>$ 0.4 GΩ	$\approx$ 0.4 GΩ	$\approx$ 0.3 GΩ	$\approx$ 0.1 GΩ
Coupling capacitance	0.16 nF	0.13-0.15 nF	$\approx$ 0.14 nF	–	–
Interstrip capacitance	6-7 pF	4-5 pF	–	–	–
Dielectric current	$<$ 1 nA at 10 V	$<$ 1 nA at 10 V	–	–	–

An indigenous AC-coupled, poly-silicon biased, p-on-n, silicon strip sensor development has been carried out at DU. The sensors were fabricated on 4-inch wafers at the BEL, and then characterized at DU and KIT facilities. A set of electrical measurements, consisting of both bulk and strip parameters, have been identified and performed on the fabricated non-irradiated and irradiated sensors. Table 3.3 summarizes the mean strip parameters of the measured voltage and strip scans, before and after irradiation at a bias voltage of 200 V.

Chapter 4

The Silicon Sensor Testing Facility Developed at University of Delhi

A major concern with the use of any sensor in a HEP experiment is its survival in the radiation environment. This becomes highly critical particularly for the silicon sensors as they are located close to the interaction point. The large shower of secondary particles received by them affects their long-term sustainability due to the distortion of the silicon lattice structure. The detrimental effect of radiation on its static and dynamic properties is discussed in Sec. 2.8. In order to maintain the desired physics performance during its operation silicon sensors must satisfy stringent specifications. These sensors, before being installed in the experiment, must be tested for various static and dynamic parameters. The *CMS outer tracker sensor upgrade* group has sketched a comprehensive tolerance criteria for qualification of sensors during production. This is envisaged through different state of the art sensor qualification centres developed at 4 to 5 chosen institutes all over the world.

This chapter contains the details of the development of the sensor qualification centre and other accompanying qualification facilities developed at DU.

- The multi- and micro- strip characterization system
- The current-voltage & capacitance-voltage system
- The red laser transient current technique system

The work further reports measurements performed on a few strip and pad sensors using the developed facility. The consistency of the measurements has also been checked through already installed measurement setups at KIT and CERN and the comparison of results is also presented in subsequent sections.

4.1 Sensor quality assurance

The CMS tracking system for the HL-LHC phase of the LHC will demand a large quantity of multi-strip silicon sensors, which must fulfil stringent tolerance criteria to maintain the physics performance. Furthermore, it is not possible to easily replace faulty sensors once installed in the main detector. Therefore, it is crucial to ensure the compliance of the various sensor parameters to the electrical specification as demanded by the experiment. This requires for a quality assurance program based on which the sensor is either accepted or rejected.

4.1.1 Quality assurance program

A subset of the fabricated sensors must be extensively tested prior to the installation in the main detector system. This will be achieved through measurement of various global and strip parameters of silicon strip sensors as envisaged in a detailed quality assurance program for phase II upgrade of CMS tracker. Also, to handle the large quantity of the pixel and strip sensors and other constraints, the characterization setup should have multi-functionality features, including automation etc.

4.2 The Multi- and Micro- Strip Characterization System

The multi- and micro- strip characterization system is an automated programmable system for characterizing silicon multi-strip sensors as per the requirements specified by the CMS silicon sensor working group for the Quality Assurance program for phase 2 upgrade sensors. The system has the capability to perform measurements of global and strip parameters of silicon strip sensors as earlier discussed in Sec. 2.5. In order to handle various parameter measurements to be carried out on hundreds of strip sensors having thousands of strips; the characterization system has multi-functionality features like programmability and automation. The details of the features of the characterization system along with measurement results are discussed below.

4.2.1 Delhi - A sensor qualification centre

The CMS upgrade tracking system in the HL phase of the LHC will demand a production of large quantity of silicon sensors. A subset of the fabricated sensors (2 or 3 sensors per fabrication batch) must be extensively tested prior to the installation in the main detector system. An elaborate description of the sensor quality assurance program is given in Sec. 4.1. The DU characterization system, after the certification, will be utilized for the sensor qualification of the 2S multi-strip sensors (see Sec. 1.4), candidates for the CMS outer tracker in the HL-LHC phase. The necessary probe station and electrical equipments are already procured and fully installed along with integration of the CDA. The complete test routine, written in ACS, will be employed for carrying out all the desired test measurements automatically. The measurement run plan for the 2S full sized sensors is shown in Fig. 4.1. In the following sections the detailed description of the characterization is shown.

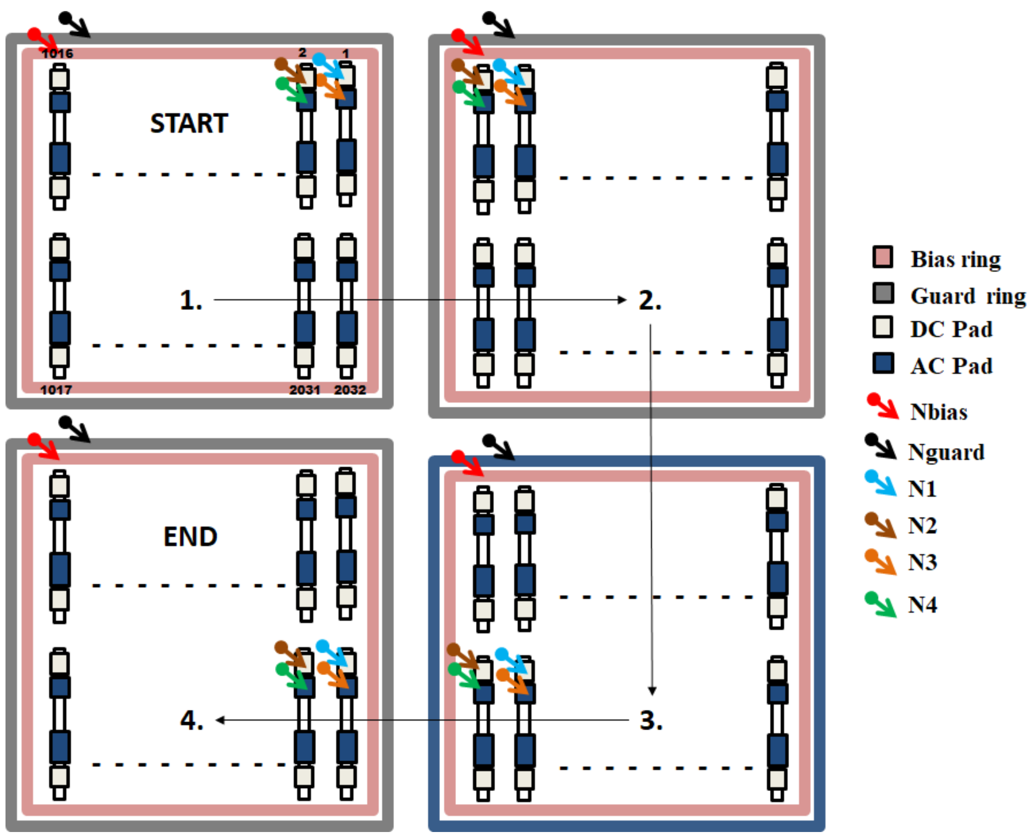

Figure 4.1: Measurement run plan on a 2S full sized sensor.

(a)

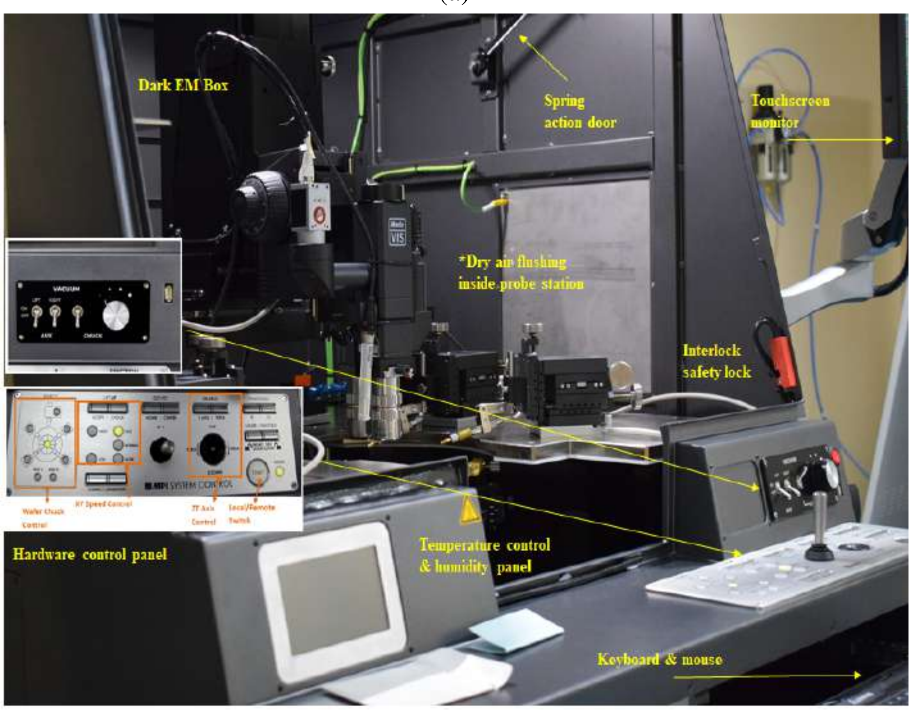

(b)

Figure 4.2: (a) The full view of the probe station and (b) its zoomed view.

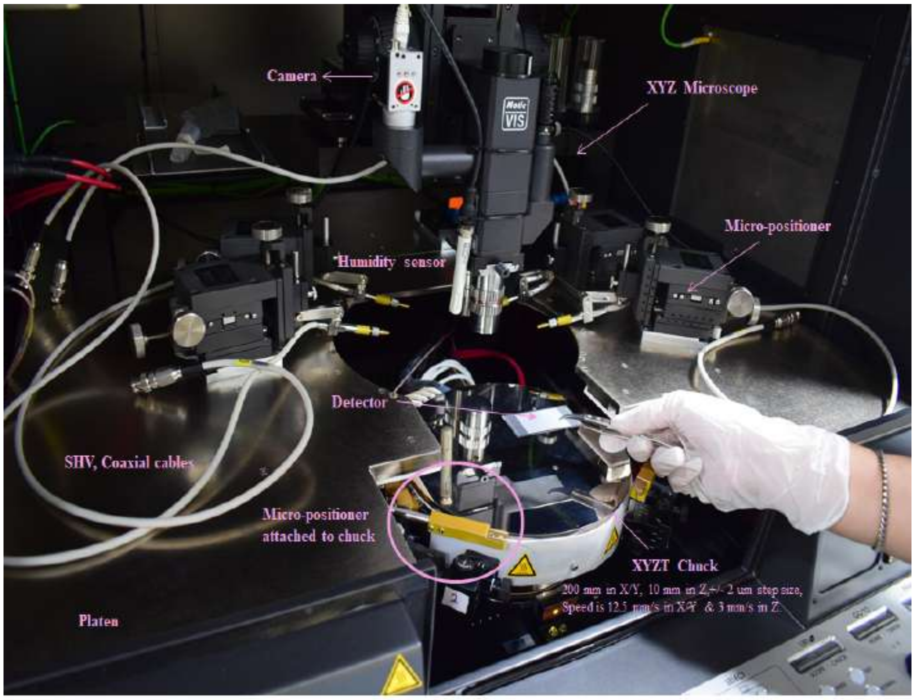

(a)

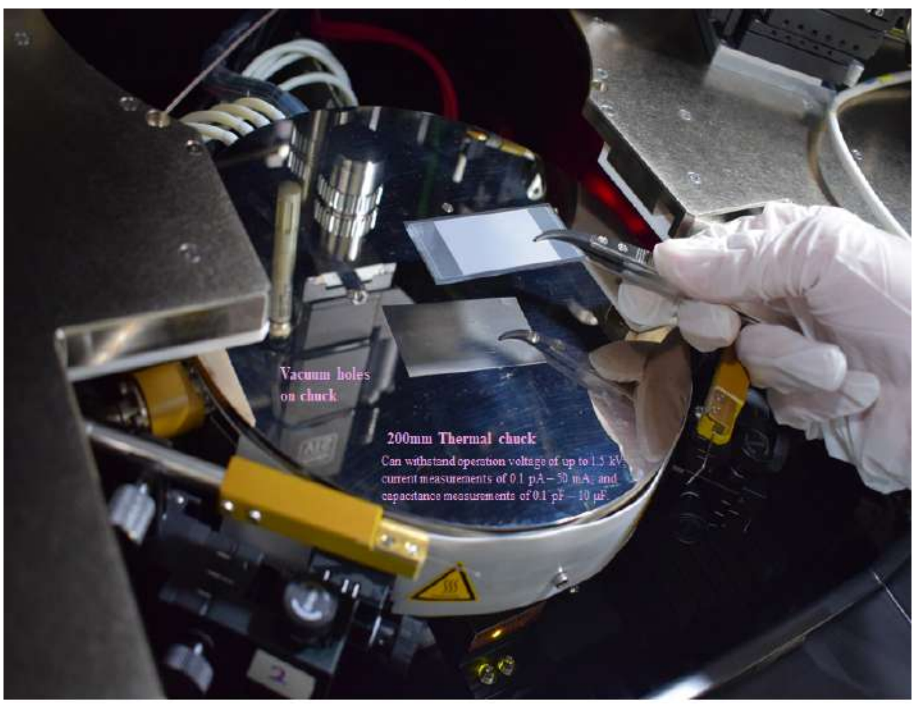

(b)

Figure 4.3: (a) The inside view of the probe station and (b) its zoomed view; while loading a sensor.

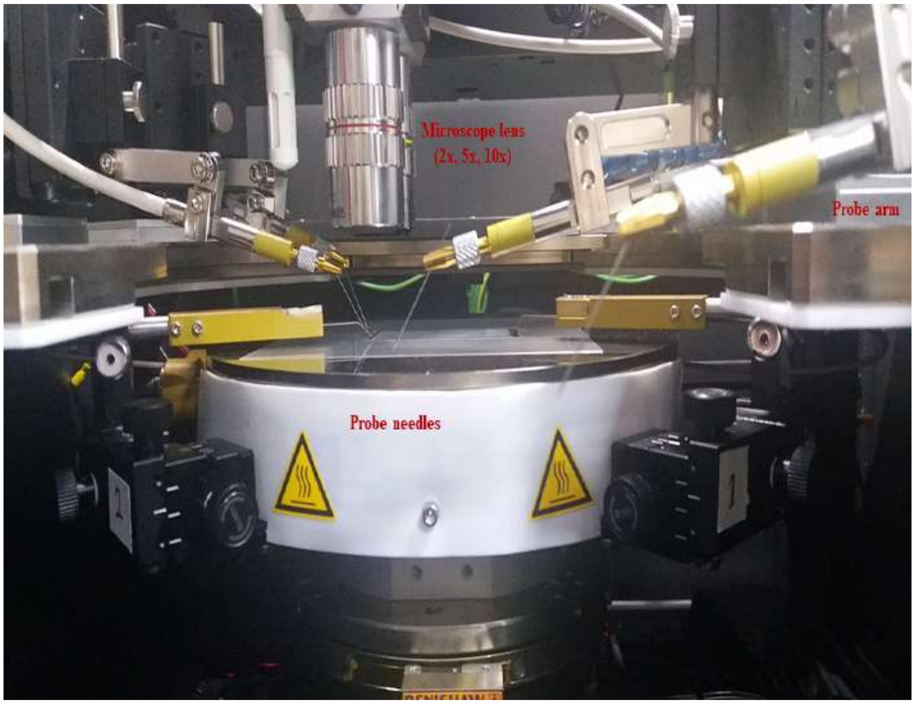

(a)

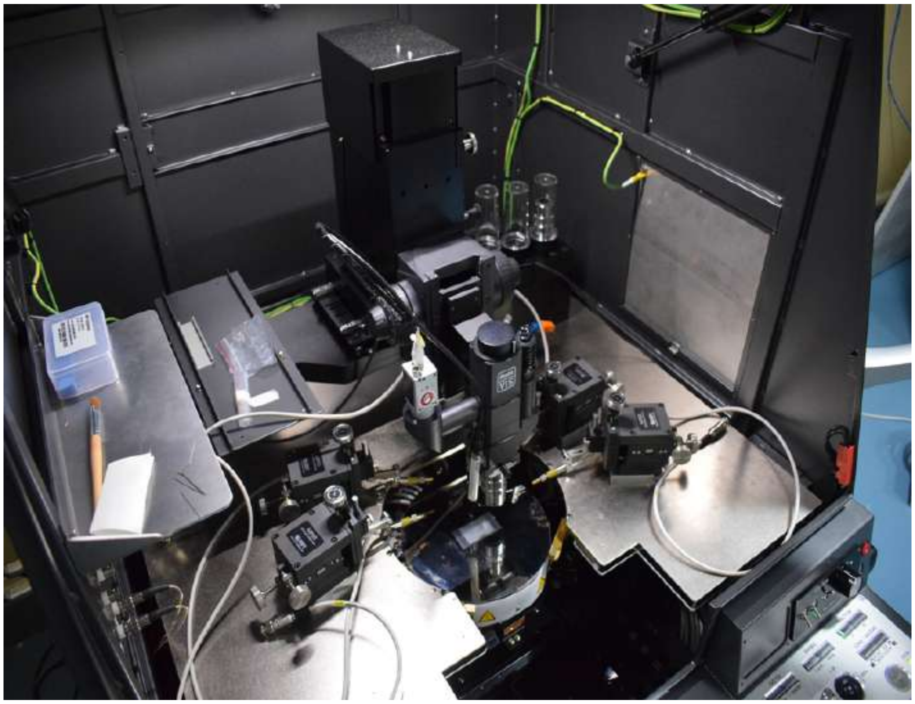

(b)

Figure 4.4: (a) The top view of the chamber and (b) the zoomed view of the sensor placed on the chuck and the probe needles in contact.

4.2.2 Measurement setup

The multi- and micro- strip characterization system is equipped with a probe station and various electrical instruments. The equipments belonging to the measurement setup along with their features are described below.

A MPI TS2000-DP probe station

Figs. 4.2, 4.3 and 4.4 show various photos of the probe station from different angles and views. The features of the probe station are mentioned below and can be found in detail in Ref. [96, 97].

1. An electromagnetically shielded and dark measurement chamber having a provision for earthing to ensure low noise and low leakage current is used for sensor testing. Further, it consists of an advanced DBP-AD interface panel with two Kelvin-triaxial connectors for chuck, four Kelvin-triaxial connectors for probe arms, four co-axial BNC connections.

2. The station has a TC-200T 200 mm diameter nickel plated planar chuck with guard design to provide ultra-low leakage noise measurement, low residual capacitance, and short settling time. It contains multiple vacuum holes and switches for holding DUT of different sizes and has additional capability to handle DUT warpage. It also has a motorized translation stages in each XYZ direction of 210 mm $\times$ 340 mm $\times$ 10 mm with 2 μm precision and $\pm$ 5° fine θ (rotation). This feature allows for easy and quick DUT alignment. Additionally, the chuck can be operated at high bias voltage of upto 1500 V with temperature ranging from +20 to +200 °C.

3. A probe platen arc shield is installed for surviving upto 10 kV of voltage or 400 A of current.

4. A total of two MP60 high-end RF and two MP25 DC micro-positioners is used for back lash-free probe positioning. They are equipped with large knobs for accurate and sensitive XYZ navigation in a travel range of $\sim$ 10 mm, a high screw resolution of $500\,\mu\mathrm{m}$ in XY and $300\,\mu\mathrm{m}$ in Z direction. They have a magnetic base for strong holding to the platen.

5. Two PA-CF-2M probe arms are customized to be attached to the chuck in order to have measurement flexibility and keeping the sensor biased during strip scans.

6. A set of PT-W-S- 2MIC and PT-W-S-12MIC tungsten probe needles (tips) with $2\,\mu m$ and $12\,\mu m$ tip radius are used.

7. There exists a provision for dry air purge by a Compressed Dry Air (CDA) system for humidity control in the chamber and to avoid condensation at low temperature. During the measurement, the system has the capability to maintain a relative humidity of $< 10\%$ at the set temperature of measurement.

8. A stable OP-8080ZUM microscope is mounted on a bridge for XY movement of 80 mm $\times$ 80 mm. It has a pneumatic lift function in the Z direction of 80 mm. It also requires CDA for operation. Moreover, a VIS200-S laser ready video microscope is provided with second C-mount port for CCD-2MP-SENTIO color camera. It consists of a slider mount which can carry 2 objective lens making it easy and convenient for magnification conversion.

9. A choice among three objective lenses of model PSM-OL-2X, PSM-OL-5X, and PSM-OL-10X with a numerical aperture of 0.055, 0.140, and 0.280 respectively can be made according to the desired magnification view.

10. A 4000RHT Hanwell temperature and humidity monitor for recording temperature and humidity inside the chamber is provided.

11. The station has an integrated hardware control panel and keyboard for easy operation.

12. The entire measurement chamber is integrated to a table with VI-TS2000 vibration absorber bases at 4 corners. The bases are high quality air-spring isolators and become operational with a suitable supply of compressed dry air (CDA).

13. A 61100511 YP0660-V1003-P5-1411, 230 V, 50 Hz, 60 W vacuum pump is used for holding the sensor onto the chuck platform.

14. A SENTIO software suite consisting of probe station firmware and all hardware configurations is utilized for translation control of chuck, automated chuck (sensor) alignment, contact with prober, description of sensor sub-structure, and interface $\&$ command control for user remote control. The SENTIO software can be integrated with Keithley's Automated Characterization Suite (ACS) software such that both the chuck translation and measurements from Keithley instruments can be controlled through a singles ACS software.

Figure 4.5: All electrical instruments stacked in a rack.

15. Additionally, the probe station has a safety provision - an interlock, to auto cut off any high bias voltage to the system in case the chamber door is opened during the measurement run and proper grounding in order to ensure that the user does not experience any shock from the instrument.

A set of electrical instruments

The setup consists of a total of four electrical equipments as shown in Fig. 4.5. The specifications of the instruments as given below are taken from reference manuals of the respective instruments [98–103].

1. A Keithley 2657A (K2657A) single channel, high voltage, high power and low current source measuring unit (SMU) for reverse biasing the DUT. It can source upto $\pm$ 3000 V with a resolution of 80 mV and current measurement from 1 nA to 120 mA with a resolution of 1 fA to 100 nA respectively. The typical voltage source settling time is $<$ 1 ms upto 200 V and $<$ 7 ms upto 3000 V.

2. A Keithley 2636B (K2636B) dual channel SMU for low voltage sourcing. It has a voltage source with 200 mV to 200 V range with 100 nV to $100\,\mu V$ resolution respectively and current measurement accuracy of 100 pA to 10 A range with a resolution of 0.1 fA to $10\,\mu A$ respectively. Typically, the unit has a settling time of $< 100\,\mu s$.

3. A Keysight E4980A precision LCR meter capable for performing AC measurements in frequency range from 20 Hz to 2 MHz with a resolution range from 0.01 Hz to 1 kHz is installed. The capacitance measurement display range is from 1×10^{-18} F to 999×10^{18} F. It has an internal DC bias voltage of $\pm$ 40 V with a resolution of $100\,\mu V$. It has a measurement time range of $\sim$ 500 ms to 5 ms, depending on the choice of the frequency. It provides three types of compensation functions: open compensation - compensates errors caused by stray admittance of the DUT, short compensation - compensates errors caused by the residual impedance of the DUT, and load compensation - compensates errors between the actual measured value and a known standard value.

4. A Keithley 707B (K707B) 6-slot semiconductor switch frame installed with 8×12 Keithley 7072 (K7072) and 8×12 Keithley 7072-HV (K7072HV) semiconductor matrix card for handling of low level, high voltage, and high impedance signals. While K7072 has two 200 V sub-pA current paths, two DC to 1 MHz CV paths and four high isolation signal paths capable of switching upto 200 V; K7072HV has two 1300 V, sub-pA current paths current paths and six 200 V paths. The cards have a relay settling time of $<$ 15 ms.

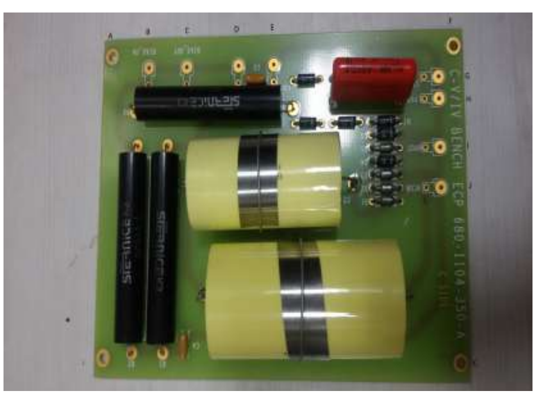

(a)

(b)

Figure 4.6: Photos of the (a) isolation box, and (b) 2657A-LIM-3 LO interconnect module.

Figure 4.7: The compressed dry air system - model Anest Iwata SLP-371E, installed at Delhi.

An isolation box

The isolation box is basically an in-house circuit board designed and developed at CERN for isolating the high voltage bias from the LCR meter (see Fig. 4.6a) consist of capacitors and resistors to isolate E4980A from high voltage DC bias from K2657A. The box has been purchased from Alan, CERN.

A Keithley 2657A-LIM-3 LO interconnect Module

The Keithley 2657A-LIM-3 LO interconnect module establishes measurement commons (LO and sense LO) for a system using multiple SMUs (see Fig. 4.6b). It also creates a single-point interlock connection for all the SMUs connected to the interlock input terminals. Therefore, when the interlock circuit is interrupted by an open interlock switch, the outputs of all the SMUs are disabled. More details on the module can be found in Ref. [104].

An Anest Iwata SLP-371E oil free scroll compressor

The compressor dry air (CDA) system consists of a compressor along with 150 litres storage cylinder and dryers for high quality, oil-free, 100 % dry air output (see Fig. 4.7). The

Figure 4.8: Storage cabinets PLT-261 and PLT-153(B) as installed in the clean room for storing of the sensors.

compressor technology is an ultra-quiet enclosed unit of 535 mm × 686 mm × 743 mm with a weight of 101 kg, low noise equal to 61 dB, low maintenance cost, low starting torque and integrated cooling fan [105]. It has a motor rated output of 3.7 kW with the maximum working pressure of 10 bar and free air delivery or, flow rate of 337 L/min. A dew point of -40 °C is achievable by this CDA unit to avoid condensation inside the probe station chamber.

Tanco storage cabinets

The photos of the storage cabinets for storing the sensors in humidity controlled environment as installed in the clean room are shown in Fig. 4.8. Both the cabinets use microprocessor based proportionalintegralderivative (PID) digital temperature indicator cum controller [106, 107].

1. A PLT-261 humidity and temperature control cabinet has a usable space of 600 mm × 600 mm × 600 mm and an approximate volume of 227 L with a temperature range of 10 °C to 60 °C with an accuracy of ± 1 °C.

2. A PLT-153(B) ultra low temperature cabinet has a chamber size of 500 mm × 400 mm × 845 mm and an approximate volume of 172 L. It has a temperature range of

-10 °C to 80 °C with an accuracy of ± 1 °C.

Automated Characterization Suite

The probe station (via SENTIO, communicates with K2636B through GPIB) and the electrical equipments are interfaced through a Keithley software - an Automated Characterization Suite (ACS) in an automated manner. It is flexible and offers an interactive software test environment designed for semiconductor device characterization. The software supports characterization at various levels:

(i) Cassette level - For multiple wafer testing

(ii) Wafer level - Several test structures on the wafer

(iii) Pattern level - Numerous test patterns may be defined

(iv) Subsite level - Substructures in a sensor

(v) Device level - Different measurement tests

ACS is specially designed to facilitate the creation and sequencing of measurements via Test Modules (TM). It has a rich set of test libraries for fast and easy test setup and execution without programming. It uses python and lua based compilers for TM development and script editor. According to the TMs, changes have to be implemented in the XRC (GUI) and Event (links TM and GUI) files also. A total of 3 TMs are available in ACS:

(i) Interactive TM (ITM) - It is a default script already available in ACS.

(ii) Script TM (STM) - Script based modules created by user

(iii) Python TM (PTM) - Python based modules created by user

Additionally, ACS boasts of Interactive andd real-time data plotting and built-in data analysis tools for quick analysis of parametric data. A quick start guide for operating ACS can be found in Refs. [108, 109].

While K2657A and K707B are connected to K2636B via the Test Script Processor (TSP) link technology (The TSP technology supports creating and running custom user test scripts for high speed test automation.), E4980A is connected to K2636B through the General

Purpose Interface Bus (GPIB), also called IEEE 488 bus cable. Since the entire system operates on the master-slave logic, K2636B is considered as the master. Hence, K2636B gets commands from the computer through the Keithley USB (KUSB) cable and it further communicates with the rest of the instruments. All the electrical instruments require a warm up of about 1 - 2 hours for stable operation.

Table 4.1: Parameters to be monitored for silicon strip sensor qualification.

– Type of quantity	List of parameters
Environmental parameters	Temperature, Humidity
Global parameters	Total Leakage Current, Backplane Capacitance
Strip parameters	Strip Leakage Current, Poly-silicon Resistance, Dielectric Current, Coupling Capacitance
Inter-strip parameters	Inter-strip Resistance, Inter-strip Capacitance

Table 4.2: The connections on the switching matrix for measurements listed in Table 4.1.

– List of measurements	Connections on switching matrix
Total Leakage Current	I26, J26
Backplane Capacitance	E21, F22, G23, H24, I25, J27
Strip Leakage Current	I26, J26, A13
Poly-silicon Resistance	I26, J26, A13
Dielectric Current	I26, J26, A13, B15
Coupling Capacitance	I26, J26, E18, G18, E13, F19, H19, F15
Inter-strip Resistance	I26, J26, A13, B14
Inter-strip Capacitance - DC pads	I26, J26, E18, G18, E13, F19, H19, F14
Inter-strip Capacitance - AC pads	I26, J26, E18, G18, E15, F19, H19, F16

4.2.3 Methodology of measurements

The comprehensive measurement test to qualify silicon sensors comprises of measurement of 10 parameters in total. These parameters are sub-divided into environmental, global, strip, and inter-strip parameters (see Table 4.1). A detailed discussion of the effect of these quantities on the sensor operation is given in Sec. 2.8. The installed setup is customized in order to perform measurement of all the parameters. The schematic of the circuit connection is shown in Fig. 4.9 and the list of control connections according to the measurement to be performed are listed in Table 4.2.

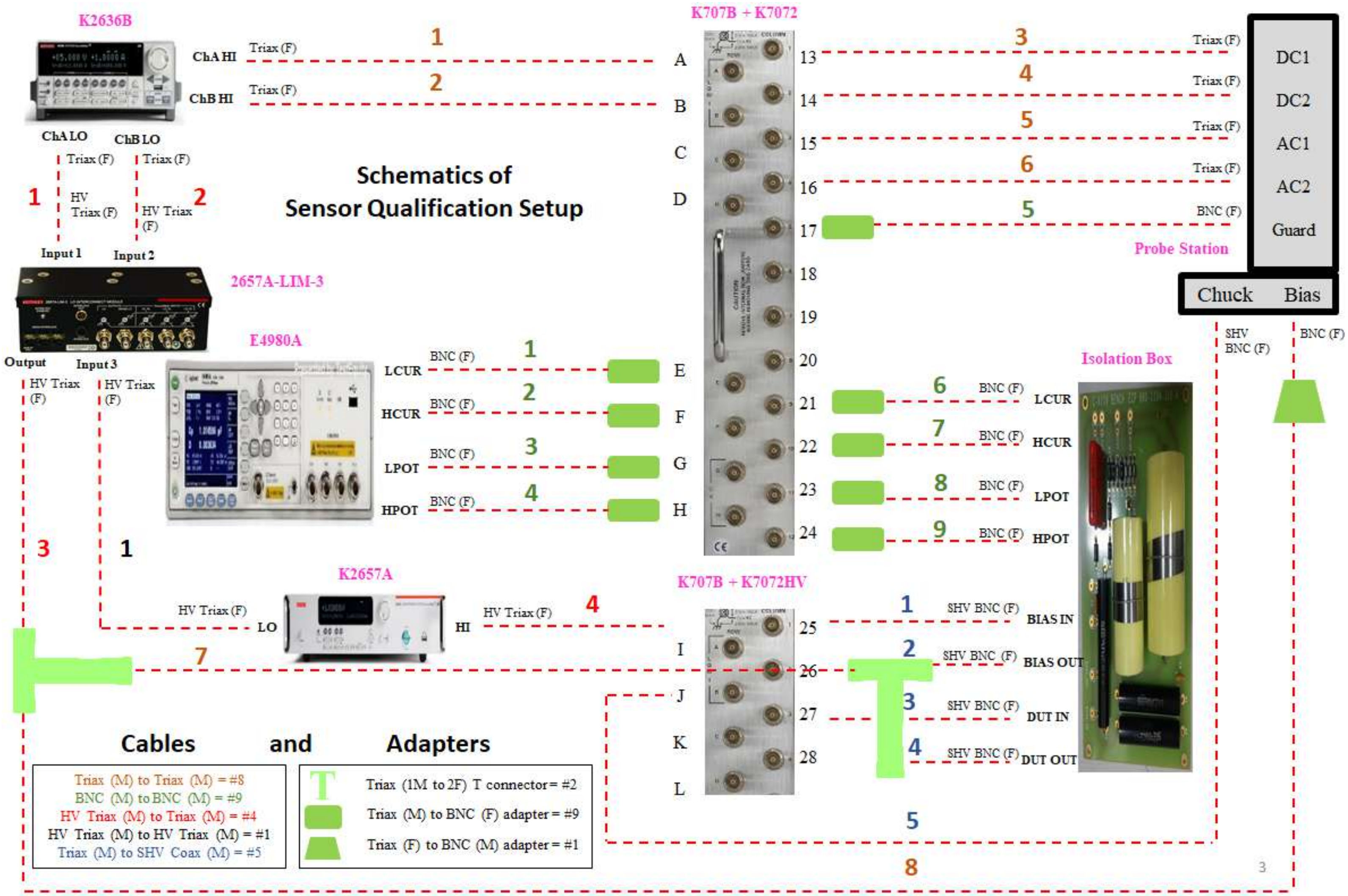

Figure 4.9: The schematic diagram of the probe station with the electrical instruments.

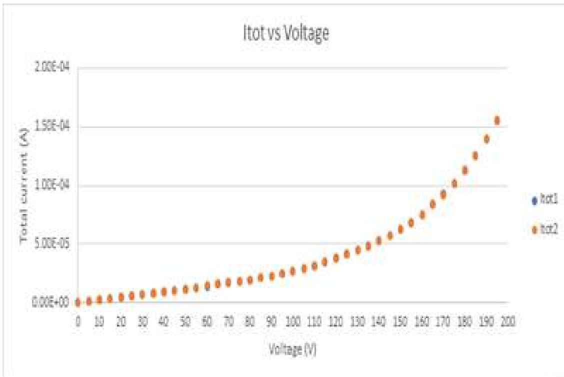

(a)

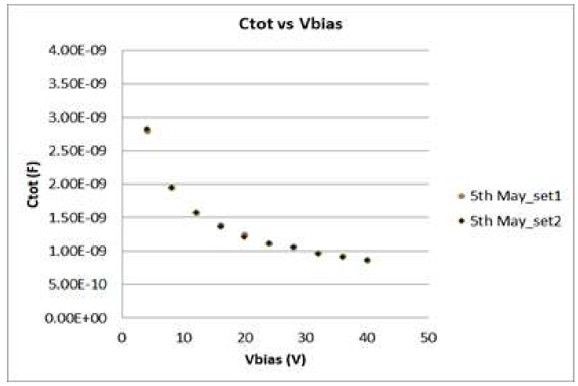

(b)

Figure 4.10: Voltage scan for global parameters - (a) total leakage current and (b) backplane capacitance.

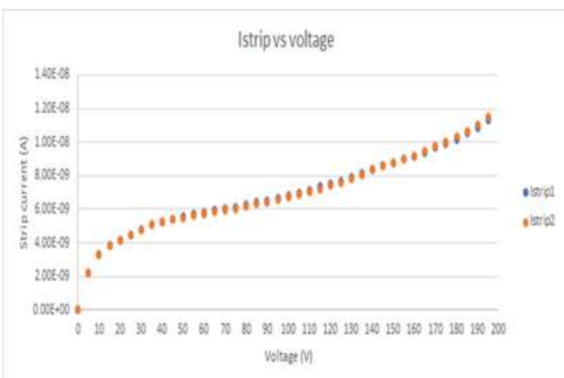

(a)

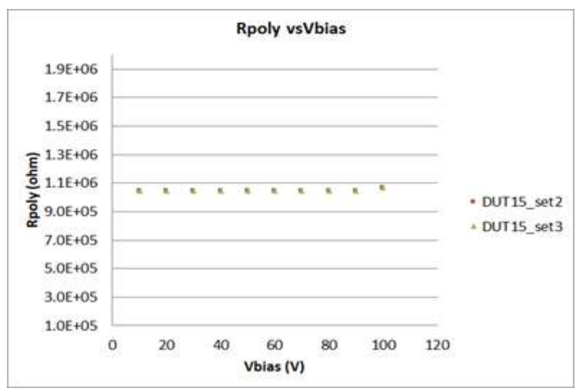

(b)

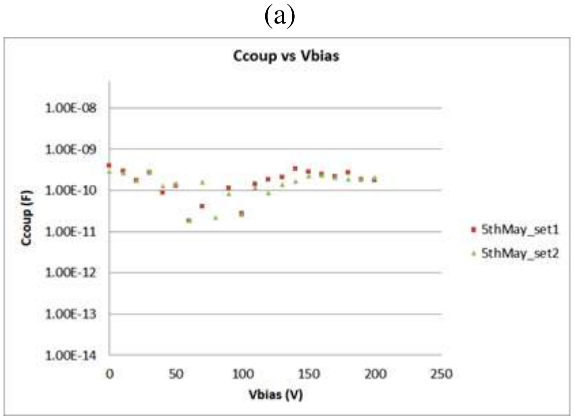

(c)

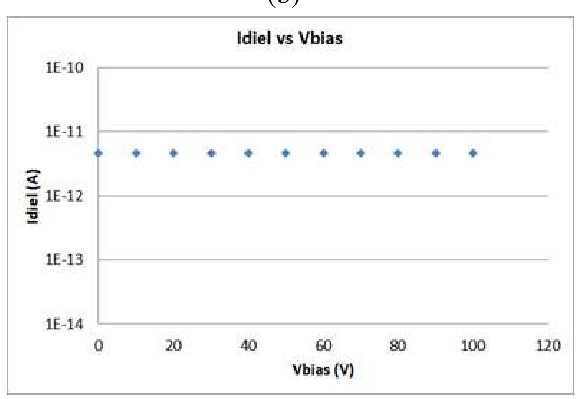

(d)

Figure 4.11: Voltage scans for strip parameters - (a) strip leakage current, (b) poly-silicon resistance, (c) coupling capacitance and (d) dielectric current.

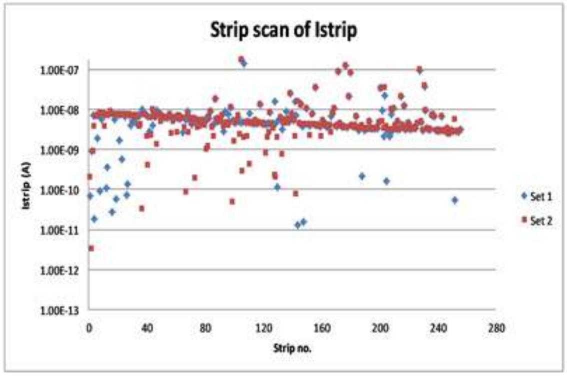

(a)

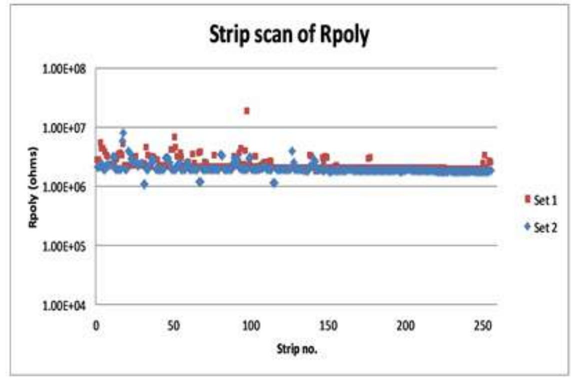

(b)

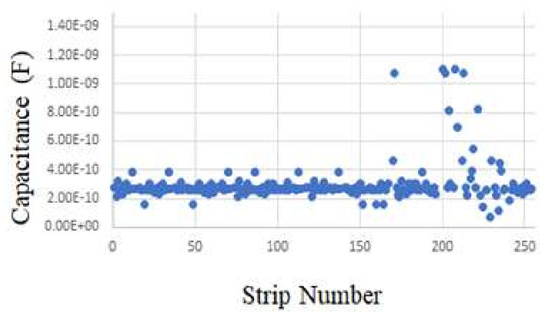

(c)

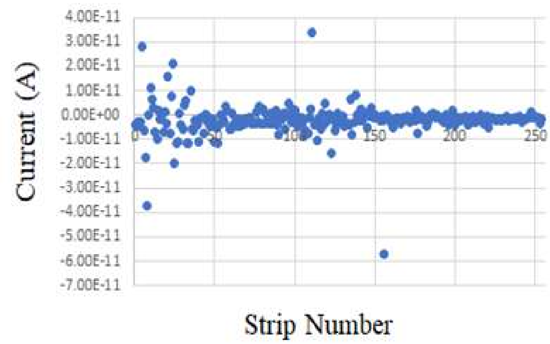

(d)

Figure 4.12: Strip scans for strip parameters - (a) strip leakage current, (b) poly-silicon resistance, (c) coupling capacitance and (d) dielectric current.

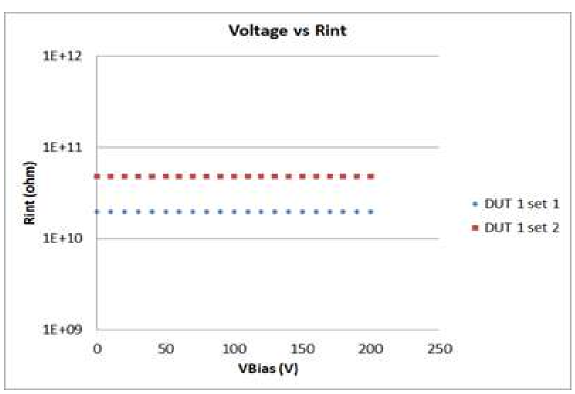

(a)

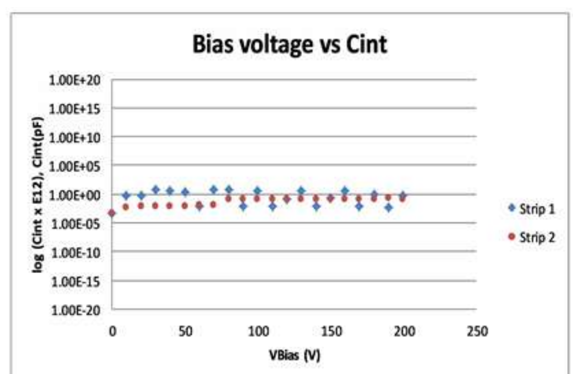

(b)

Figure 4.13: Voltage scans for inter-strip parameters - (a) inter-strip resistance and (b) inter-strip capacitance.

4.2.4 Measurement on BEL micro-strip sensors

The BEL fabricated sensors, described in Chapter 3, measured using the KIT characterization system, were also measured with the DU characterization system. A few representative measurement results of environmental, global, strip and inter-strip parameters are shown in Figs. 4.10, 4.11, 4.12, 4.13, 4.14, and 4.15.

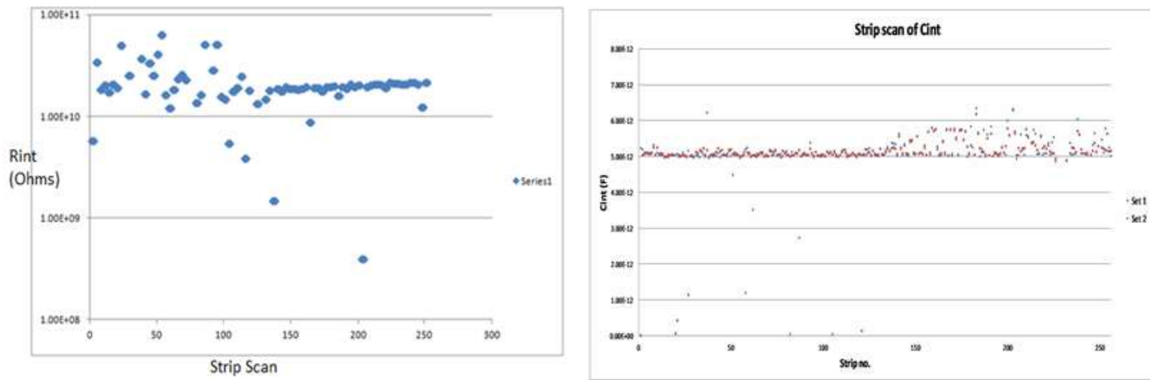

(a) (b)

Figure 4.14: Strip scans for inter-strip parameters - (a) inter-strip resistance and (b) inter-strip capacitance.

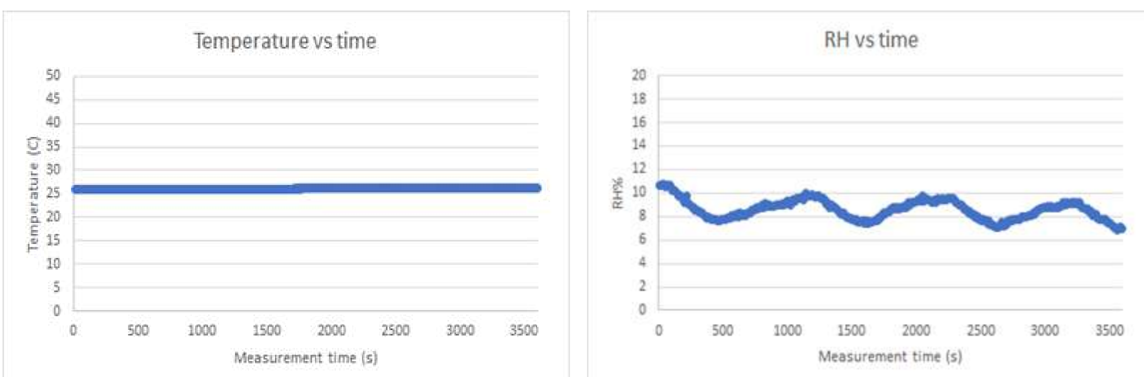

(a) (b)

Figure 4.15: Monitoring of - (a) temperature and (b) humidity throughout the measurement run. It may be noted that the temperature remains quite stable at 25 °C and the humidity is maintained less than 10 %.

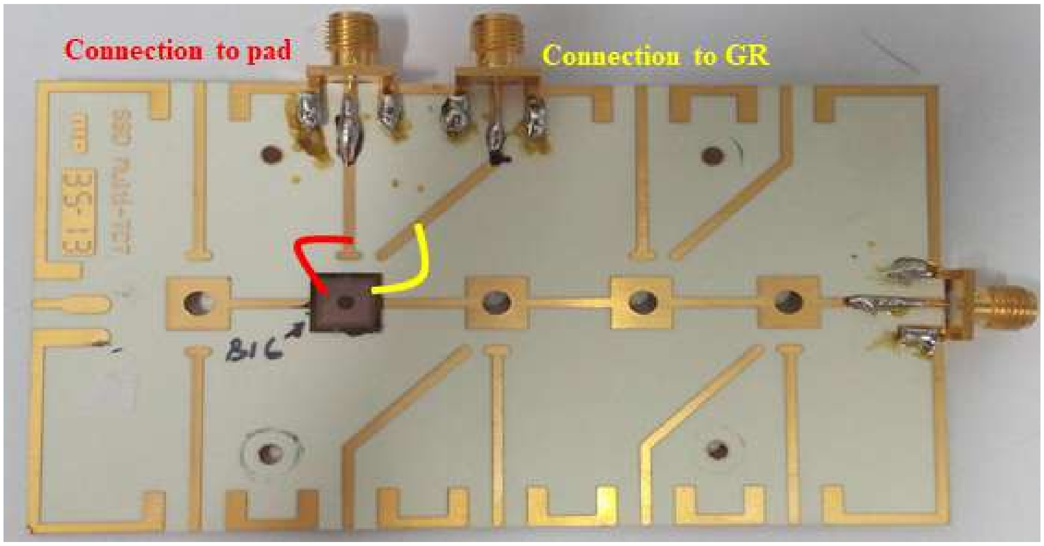

Figure 4.16: Photo of a PCB with a pad diode mounted on it. The wire bonds are shown in red and yellow color for better visibility.

4.3 The current-voltage & capacitance-voltage system

Due to their simple geometrical layout, pad diodes can be used as test structures to perform R&D study in laboratory. The pad sensor is mounted using a conductive silver glue on a bakelite-based Printed Circuit Board (PCB) with copper track designs on it (see Fig. 4.16). The bias line and the GR connection from the DUT to the individual copper tracks is done through zinc wire bonds. The PCB soldered with SMA connectors for wire connection, is placed on the plate inside the chamber and secured with screws.

The static measurements that can be performed on a diode structure are the current (I) and capacitance (C) measurements as a function of the reverse bias voltage (V). The CV-IV setup, installed at University of Delhi, is described in the sections below.

4.3.1 Measurement setup

DU has developed a working CV-IV setup, as shown in Fig. 4.17, in collaboration with CERN PH detector lab under the RD50 organization. The setup consists of the instruments as listed below and their specifications are taken from reference manuals as on Refs. [110–112].

1. A Keithley 237 (K237) source measuring unit (SMU), capable of sourcing and mea-

Figure 4.17: The current-voltage & capacitance-voltage (CV-IV) system installed at University of Delhi.

suring voltage and current individually or simultaneously. It is used to reverse bias the pad diode upto a voltage of ± 1100 V.

2. A Keithley 2410 (K2410) is also a high voltage SMU capable of both sourcing and measuring voltage or/and current. In the CV-IV setup at DU, it is used to measure pad current, since the total current measured by K237 is a total of the pad and the guard currents.

3. A CV Analyser 590 (CV590) is a measurement unit to measure capacitance as a function of voltage. The unit has an internal voltage capability of upto ± 20 V only. However, it has an option for external voltage via a SMU upto ± 200 V. The unit

offers two frequencies - 100 kHz and 1 MHz.

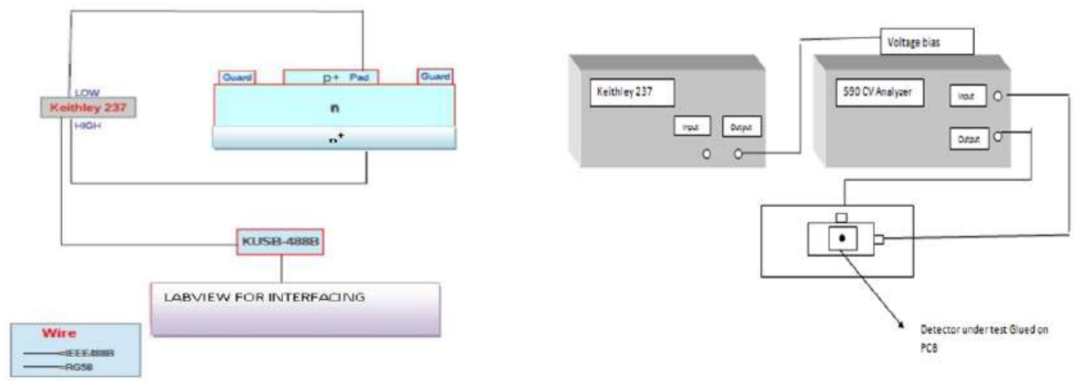

(a) (b)

Figure 4.18: Schematic of - (a) IV, and (b) CV setups.

4.3.2 Methodology of measurements

The following procedure is carried out to perform the measurements -

Current-Voltage

1. Connect the cables as shown in the schematic given in Fig. 4.18a.
2. Place the diode (mounted on PCB) inside the chamber onto the plate and secure it with the help of screws.
3. The details are then filled up in the executable file created by the LabView program (see Fig. 4.19) - (i) Open IVMeasurement.exe. (i) In the window tab *Experimental Details*, enter the name of operator, diode name, set the bulk type, temperature, and remarks if any. Press the save button. (iii) In the *Diode Bias Properties* tab, enter the start, stop and number of voltage step values. (iv) In the window tab, *Type of Operation*, select Single I meter or Two I meters, from the drop down menu.
4. The START button is pressed to start the measurements.

Capacitance-Voltage

1. Connect the cables as shown in the schematic given in Fig. 4.18b.
2. Place the diode (mounted on PCB) inside the chamber onto the plate and secure it with

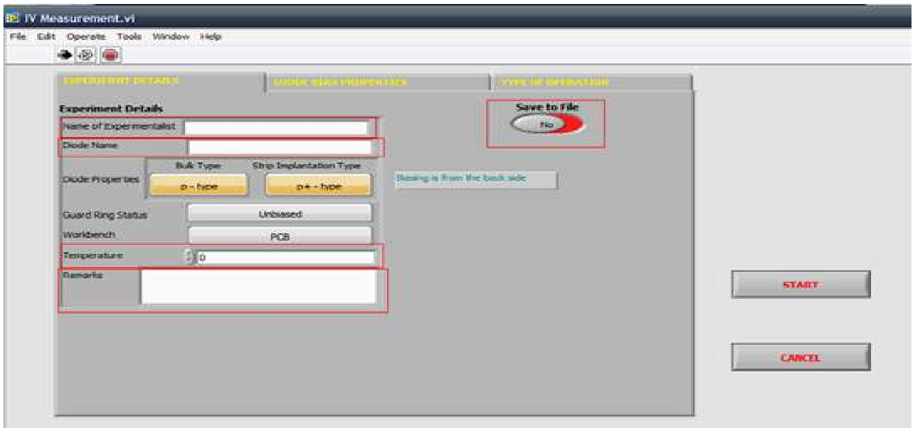

(a)

(b)

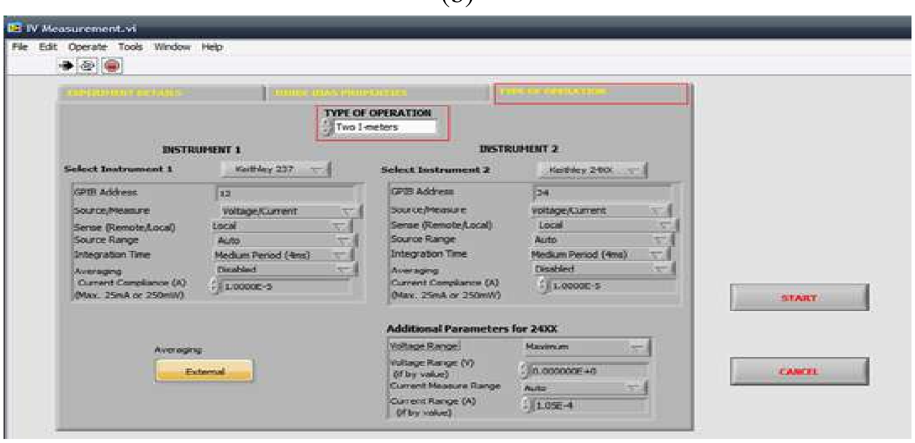

(c)

Figure 4.19: Screenshots of the different settings on the LabView software regarding - (a) experimental details, (b) diode bias properties and (c) type of operation.

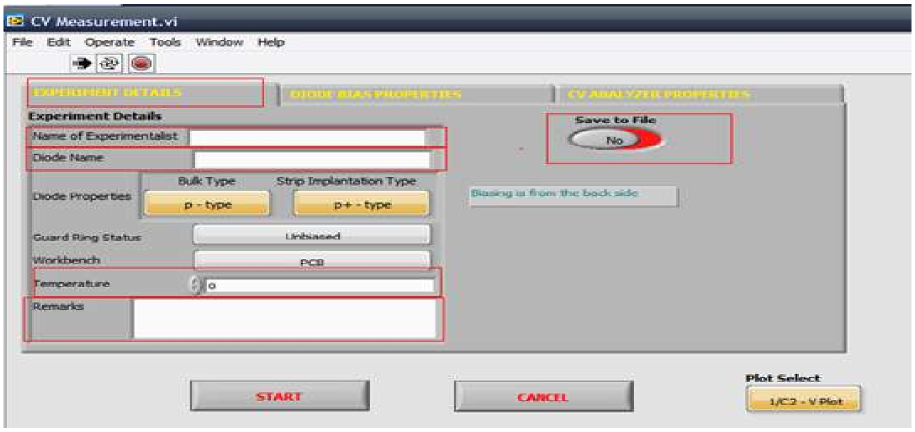

(a)

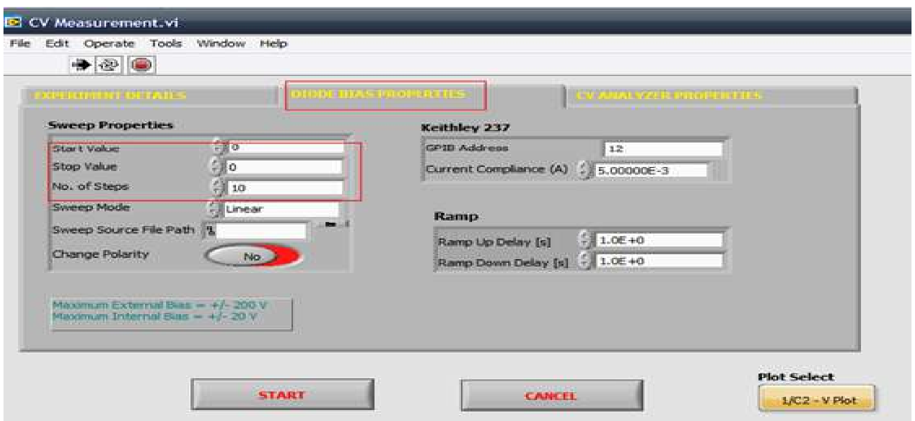

(b)

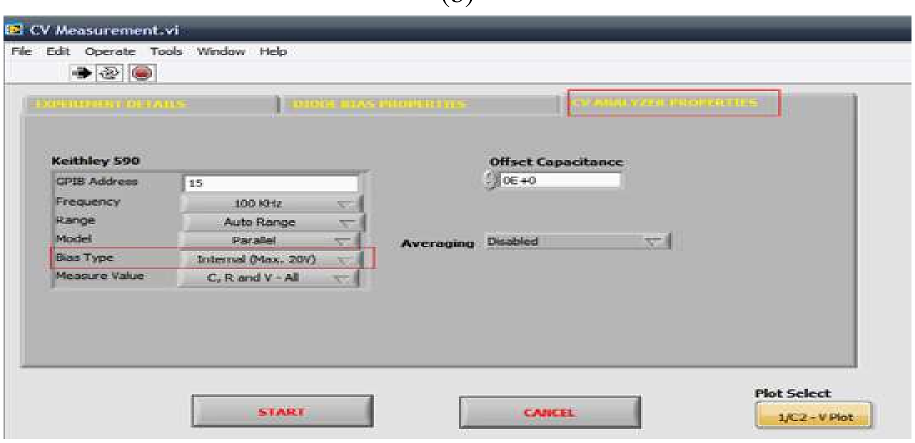

(c)

Figure 4.20: Screenshots of the different settings on the LabView software regarding - (a) experimental details, (b) diode bias properties and (c) CV Analyzer Properties.

the help of screws.
3. The details are then filled up in the executable file created by the LabView program (see Fig. 4.20) - (i) Open CVMeasurement.exe. (i) In the window tab *Experimental Details*, enter the name of operator, diode name, set the bulk type, temperature, and remarks if any. Press the save button. (iii) In the *Diode Bias Properties* tab, enter the start, stop and number of voltage step values. (iv) In the window tab, *CV Analyzer Properties*, select bias type as external voltage (200V), from the drop down menu.
4. The START button is pressed to start the measurements.

Precautions

1. Make sure to check the continuity of the circuits (cables and connectors) using a multimeter. 2. Check for proper grounding of all the devices. 3. Set compliance to $10\,\mu A$ during IV measurements and to 1 m A during CV measurements.

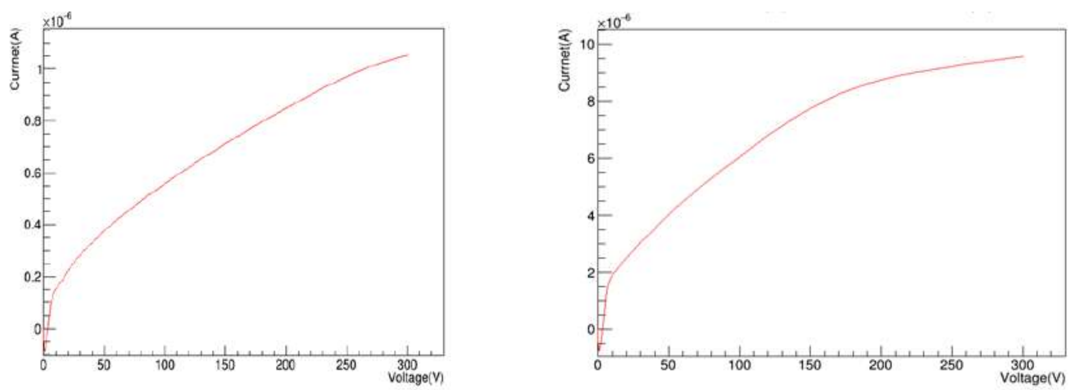

(a) (b)

Figure 4.21: The current vs voltage plot for two FZ n-type diodes namely - (a) G6, and (b) E6.

4.3.3 Measurement on pad silicon sensors

Current-Voltage

The leakage current for a good diode should be of the order of µA or even below, at the operating voltage for a non-irradiated detector as shown in a sample plot in Fig. 4.21. The breakdown voltage is that voltage at which a sharp rise in the leakage current is seen.

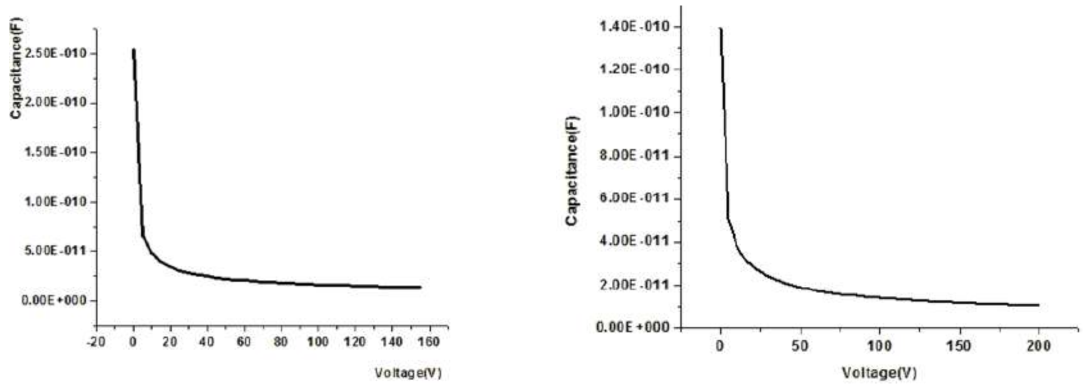

(a) (b)

Figure 4.22: The capacitance vs voltage plot for two FZ n-type diodes namely - (a) G6, and (b) E6.

Capacitance-Voltage

It is visible from the sample plot shown in Fig. 4.22 that capacitance decreases with voltage and then becomes constant. The full depletion voltage is determined by extrapolating the two linear regions in the 1/C2 vs V plot. The intersection point gives the value of the full depletion voltage.

4.4 The red laser transient current technique system

The transient current technique (TCT) is a well established technique that utilizes the drift of electron-hole pairs created inside a reverse biased sensor by laser light. These charge carriers drift under the influence of the electric field and induce a current in the readout circuit. The current pulse contains information about the amount of drifting charge, its drift velocity, electric field within the sensor, full depletion voltage, charge collection, etc.

4.4.1 Measurement setup

DU has developed a working red laser TCT setup, as shown in Fig. 4.23, in collaboration with CERN PH detector lab under the RD50 organization. The setup consists of the following instruments (Refs. [111, 113–117]):

1. An electromagnetic shielded stainless steel chamber of $30 \times 30 \times 40\,\text{cm}^3$ dimensions has been custom-made to prevent stray capacitances. The chamber contains a stand

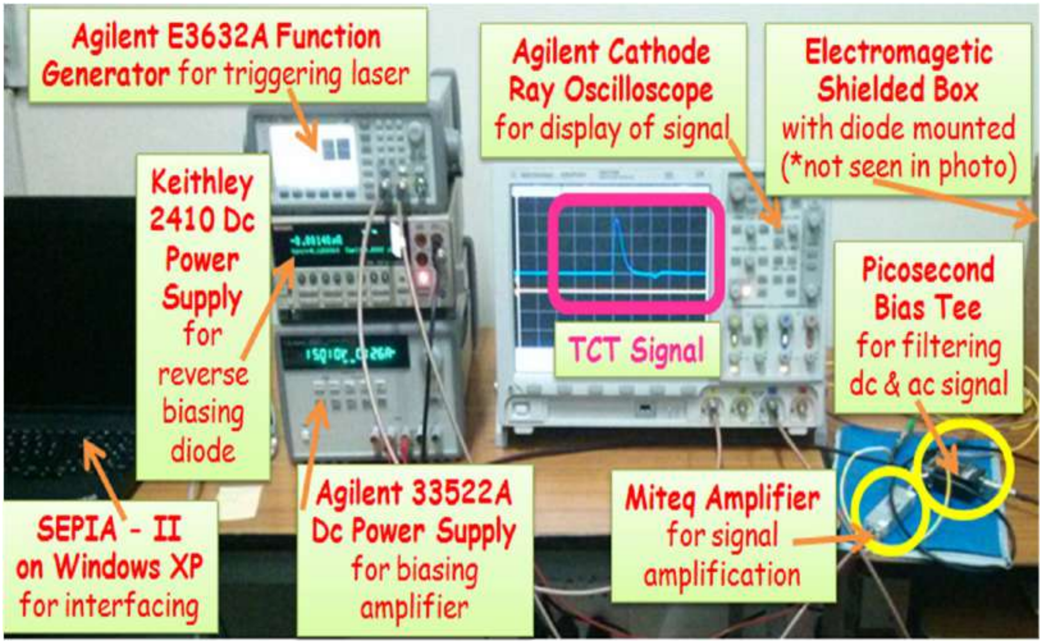

Figure 4.23: The red laser 660 nm TCT setup at DU.

and a DUT-plate for holding the laser lens and DUT respectively. A not-so precise manual translation of the plate in X-axis is provided to ensure illumination of th DUT with the laser spot.

2. A PicoQuant 800-B/808/828 multi-channel pulsed diode laser (PDL) controller (computer controlled via PDL 828 ”Sepia II”) is employed. It offers the possibility of internal trigger at 6 frequencies - 80, 40, 20, 10, 5, and 2.5 MHz and external trigger of NIM-signal.

3. A LDH-P-660 red laser head along with an optical fibre and pigtail (collimator) is used to illuminate the DUT. It provides a laser pulse of 660 nm wavelength, $<$ 90 ps pulse width, and 0.5 (1) mW average power at 40 (80) MHz frequency.

4. An Agilent 33522A function generator is used to provide trigger to the laser controller.

5. A Keithley 2410 Source Measuring Unit (SMU) is utilized to reverse bias the DUT. The maximum operating voltage is $\pm$ 1100 V at $\pm$ 1 A current.

6. A Picosecond 5531 bias tee with a frequency of 12 GHz enables the separation of direct and transient signals.

7. A low noise Miteq AM-1660 amplifier with a frequency of 1.3 GHz and a gain of 58 dB ($\sim$ 1000) is used for amplification of the TCT signal generated.

8. An Agilent E3632A low voltage source (LVS) of $\pm$ 15 V is required to bias the amplifier.

9. An Agilent DSO7104B Digital Storage Oscilloscope (DSO) is operated with a sampling rate of 4 GSa/s if the connection is to channels (one of A or B) and (one of C or D) for viewing the TCT signal.

10. The DUT mounted on the PCB, which is placed on the plate inside the chamber and secured with screws.

The instruments are assembled together to form the TCT setup with the help of cables and adapters. The function generator, SMU, and LVS are interfaced through GPIB; all attached to a KUSB which in turn goes to a computer. The entire system is configured and controlled through a dedicated LabView control software.

(a)

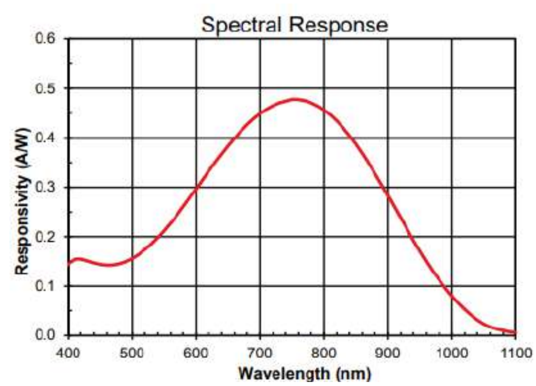

(b)

Figure 4.24: (a) A photo of the reference diode used at DU. (b) Response curve of DET02AFC [118].

4.4.2 Calibration of the setup

A ThorLabs DET02AFC fibre input silicon based detector (see Fig. 4.24a) also known as the reference diode is used for calibrating the setup. The reference diode is actually a silicon photodiode with a reverse bias voltage of 12 V (supplied through a 12 V battery) and operates in the spectral range of 400 - 1100 nm. On being illuminated by light, the photodiode generates a photocurrent, which in turn is linearly proportional to the input optical power and is given as:

$$P = \frac{I}{R(\lambda)} \tag{4.1}$$

where the proportionality constant is inverse of responsivity R(λ). According to the response curve of DET02AFC (shown in in Fig. 4.24b), R(λ) = 0.3989 for 660 nm wavelength.

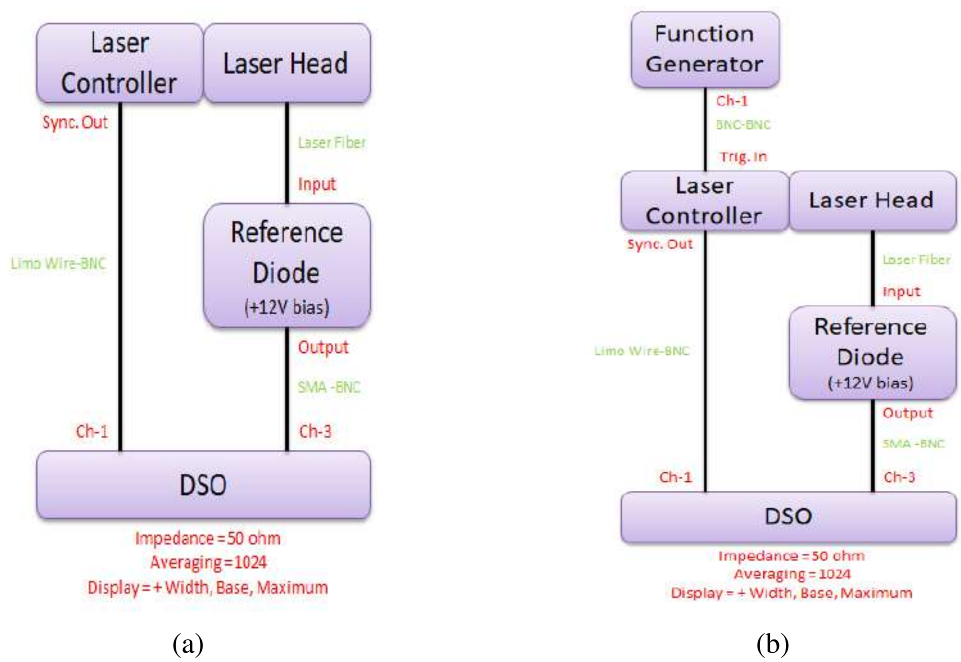

Figure 4.25: Circuit diagram with frequency of - (a) 80 MHz (internal) and (b) 200 Hz (external).

The efficiency of the detector is calculated for 2 trigger frequencies - (i) 80 MHz (internal) and (ii) 200 Hz (external). The circuit diagrams can be seen in Fig. 4.25. The recorded data and the calculations are displayed in Table 4.3. It turns out that the DU TCT system provides an efficiency of approximately 80% at 80 MHz and 83% at 200 Hz, trigger frequencies.

Table 4.3: Calculation of efficiency for the reference diode.

i **Frequency** **(Hz)** set	**ii** **Intensity** **(%)** set	**iii** **Pulse width** **(ps)** recorded	**iv** **Baseline** **(mV)** recorded	**v** **Peak voltage** **(mV)** recorded	**vi** **Peak current** **(mA)** $\frac{v-iv}{50\Omega}$	**vii** **Incident power** **(mW)** $\frac{vi}{0.3989R(\lambda)}$	**viii** **Incident energy** **(eV)** $\frac{vii.10^{-3}\times iii.10^{-12}}{1.6\times10^{-19}}$	**ix** **#photons** $\frac{viii}{1.88eV}$	**x** **#e-h pairs created** $\frac{ix}{1.12eV}$	**xi** **#e-h pairs collected** recorded	**xii** **Efficiency** $\frac{xi}{x}$
80×10^6	74	480	0.88	3.83	0.06	0.15	443720	236021	210733	167246	0.79
80×10^6	76	470	0.75	18.63	0.36	0.90	2633367	1400727	1250649	978855	0.78
80×10^6	78	470	2.44	28.47	0.52	1.31	3833699	2039202	1820716	1173360	0.64
80×10^6	80	470	3.06	33.41	0.61	1.52	4469949	2377632	2122886	1830020	0.86
80×10^6	85	495	2.38	43.96	0.83	2.08	6449643	3430661	3063090	2567960	0.84
80×10^6	90	510	2.25	54.32	1.04	2.61	8321540	4426351	3952099	3329850	0.84
80×10^6	95	520	2	63.64	1.23	3.09	10044121	5342618	4770194	3955120	0.83
80×10^6	100	535	2	69.81	1.36	3.40	11368247	6046940	5399054	4483600	0.83
200	71	460	1	4.06	0.06	0.15	441088	234621	209483	187344	0.89
200	72	480	0.94	12.23	0.23	0.57	1698170	903282	806502	665767	0.83
200	74	460	2.81	28.57	0.52	1.29	3713211	1975112	1763493	1493770	0.85
200	76	480	2.81	35.78	0.66	1.65	4959138	2637839	2355214	1908730	0.81
200	78	480	2.56	40.94	0.77	1.92	5772875	3070678	2741677	2205730	0.80
200	80	480	2.63	45.57	0.86	2.15	6458762	3435511	3067421	2515460	0.82
200	85	520	2.13	60.64	1.17	2.93	9534094	5071326	4527970	3574940	0.79
200	90	520	2.38	72.57	1.40	3.52	11437328	6083685	5431862	4417580	0.81
200	95	520	2	82.55	1.61	4.04	13125470	6981633	6233601	5225140	0.84
200	100	540	2	91.57	1.79	4.49	15156618	8062031	7198242	5980760	0.83

4.4.3 Methodology of measurements

Presently, the DU TCT setup can perform measurements of non-irradiated pad diodes only because of the absence of a cooling apparatus. In this section, the preparation of the pad diode for measurements, steps for measurements, and precautions to be taken care during the experiment are discussed.

Etching

Although a pad diode has a hole (absence of aluminium (Al)) on frontside, the backside of the diode is fully metallized. Hence, a hole has to be created, i.e. aluminium has to be removed or else when the laser is shone from the backside, it will get reflected. This process of exposing the hidden silicon material is known as etching. The following steps are performed to carry out etching (see Fig. 4.26):

1. The diode is kept upside down on a glass peltier plate.

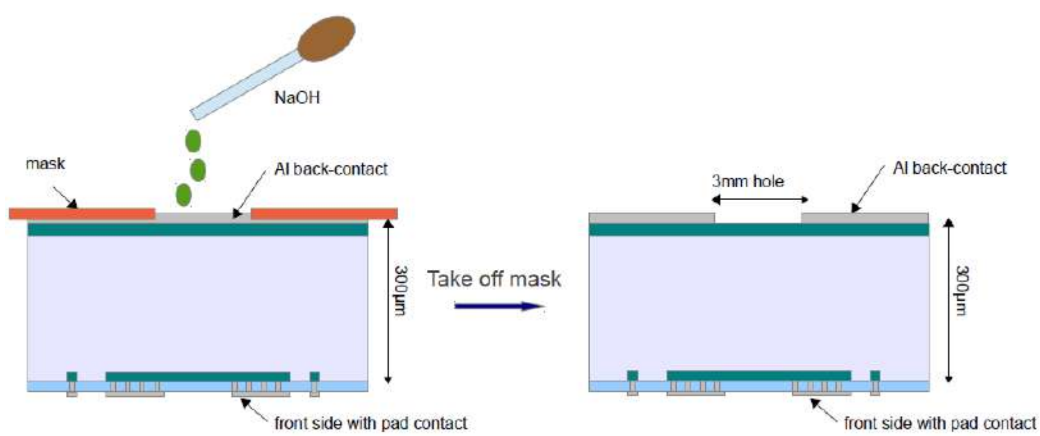

Figure 4.26: The steps followed for etching of the sensor.

2. It is masked with the help of a kapton tape such that only a small square or hole opening is bare at the centre of the DUT.
3. Few sodium hydroxide (NaOH) pellets are dissolved in distilled water, stirred and kept aside for 30-40 seconds.
4. With the help of a dropper, few drops of the prepared NaOH solution are put on the exposed diode backside. Sodium aluminate ($NaAlO_2$) is formed by the action of NaoH on elemental Al which is an amphoteric metal. The reaction is highly exothermic once

established and is accompanied by the rapid evolution of hydrogen gas.

$$2Al + 2NaOH + 2H_2O \rightarrow 2NaAlO_2 + 3H_2 \tag{4.2}$$

5. Since $NaAlO_2$ is soluble in both water and ethanol, the surface of the diode is rinsed well with either of them.
6. Repeat step 4-5 if the silver color (due to aluminium) is not replaced instead by a black color (silicon).
7. Remove the mask and clean the diode with acetone to remove any residues.

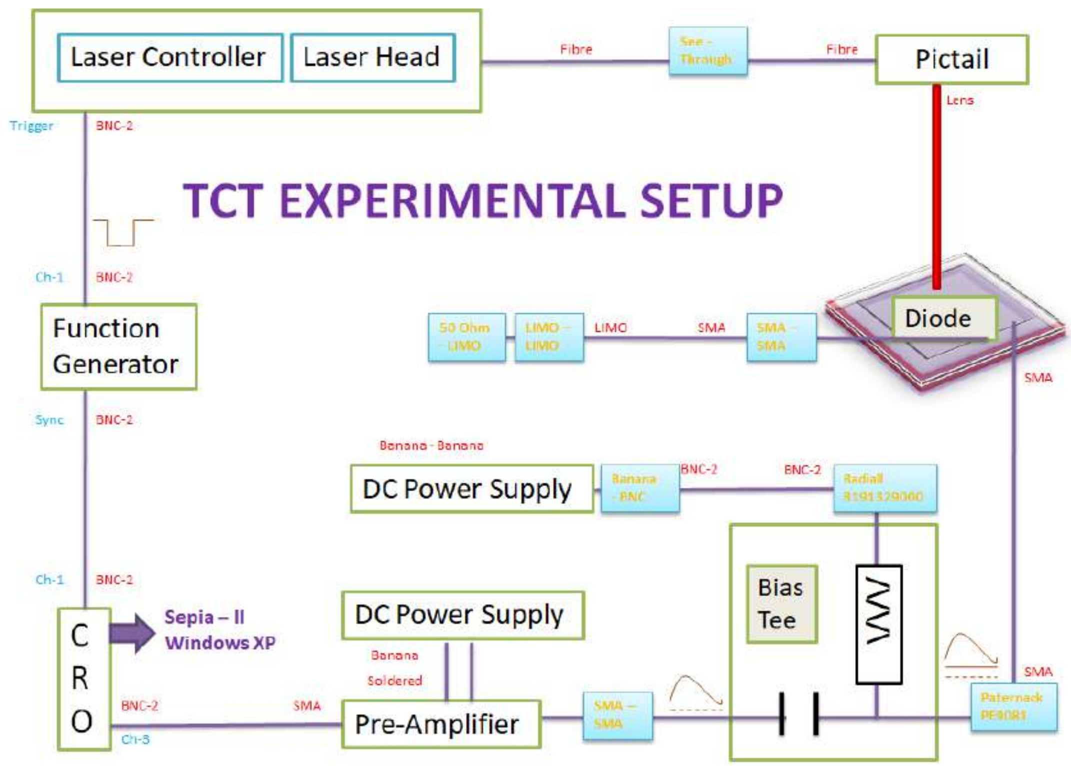

Figure 4.27: The schematics of the experimental TCT setup at DU.

Steps for measurement

The following procedure is carried out to perform the measurements:
1. Ensure that the circuit for the TCT setup is set according to the schematics shown in Fig. 4.27. All the instruments must be switched ON.
2. Place the diode (mounted on PCB) inside the chamber onto the plate and secure it with the help of screws.

3. The next step is to ensure that the laser falls inside the hole on the diode. To ensure this, following steps are to be carried out - (i) Open 'Sepia-II' software in computer. (ii) Turn the key on the laser controller to ON (active) state. (iii) Set an intensity of 80%. (iv) Set frequency to 80 MHz. (At this frequency, the red laser is visible to eye.) (v) Adjust laser beam such that the maximum beam falls onto the diode hole. (vi) Quit.
4. In this step, details are filled up in the executable file created by the LabView program - (i) Open 'TCTMeasurement.exe'. (ii) In the window tab *Experimental Details* enter the name of the operator, diode name, bulk type, temperature, remarks (if any) and press save button. (see Fig. 4.28a) (iii) Then, in the *Diode Bias Properties* tab, enter the start, stop and no. of steps value for the desired reverse bias. (see Fig. 4.28b) (iv) In the *Scope Properties* tab, select DSO7104B for the VISA resource name from the drop down menu, set an averaging of 1024, and integration window to 25E-9. (see Fig. 4.28c). (v) All the other settings are default set, so no need to change them.
5. The START button is pressed to start the measurements.

Precautions

1. Remember to set the compliance before running the experiment.
2. Make a manual check for identification of the polarity of the diode substrate.
3. Ensure that the distance between the pigtail optical lens and the PCB is 4 cm.
4. The frequency of the trigger signal must be less than 4050 MHz or else overlap of signals will occur because new pairs will be created before collection of pairs created by the previous trigger.
5. Remember to match impedances. All instruments by default have 50 Ω resistance. So, to have maximum power transfer, set the DSO resistance to 50 Ω.
6. The amplifier gets hot if it is run for long hours. So, an aluminium or copper plate with a larger surface area can be used as a heat sink, on which the amplifier can be placed.
7. Remember to cap the fibre lenses when not in use.

4.4.4 Measurement results on pad silicon sensors

The size of the diode samples is 8 mm x 8 mm, although the active detecting volume is sized 5 mm x 5 mm.

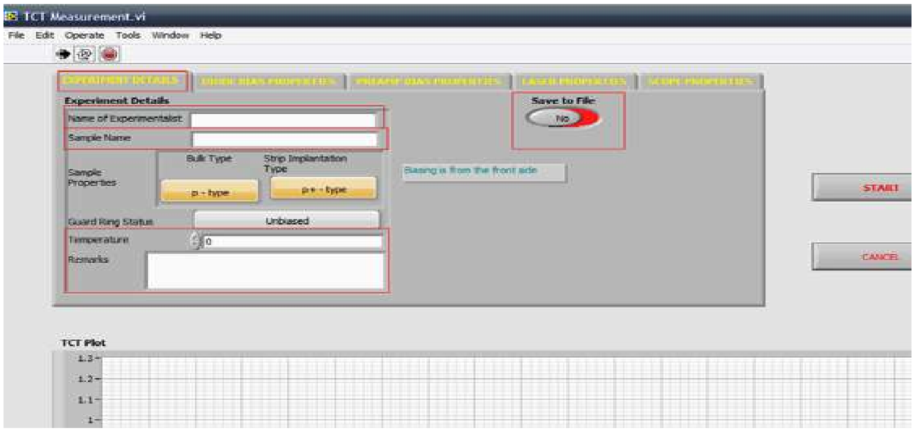

(a)

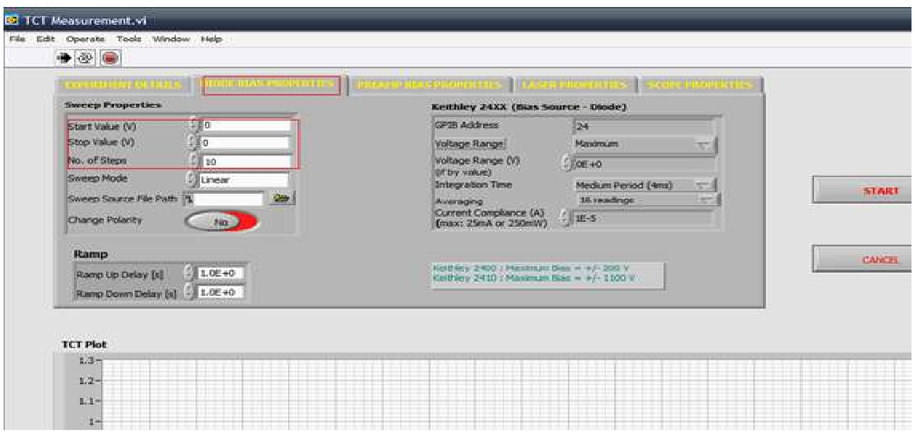

(b)

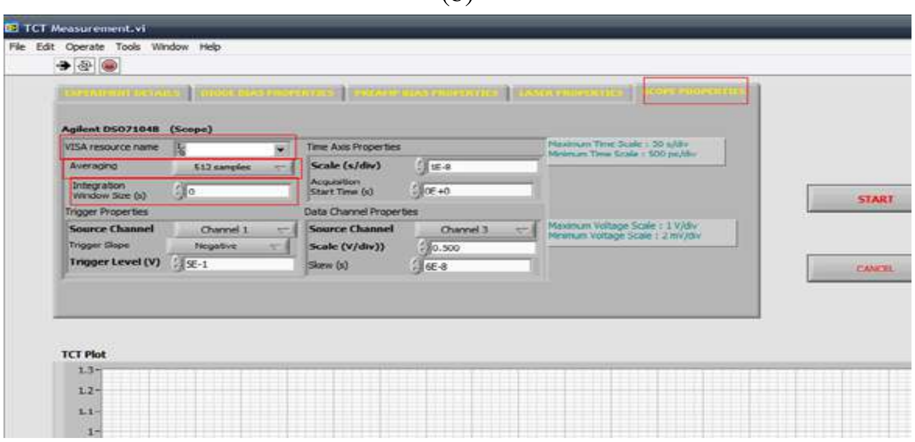

(c)

Figure 4.28: Screenshots of the different settings on the LabView software regarding - (a) experimental details, (b) diode bias properties and (c) scope properties.

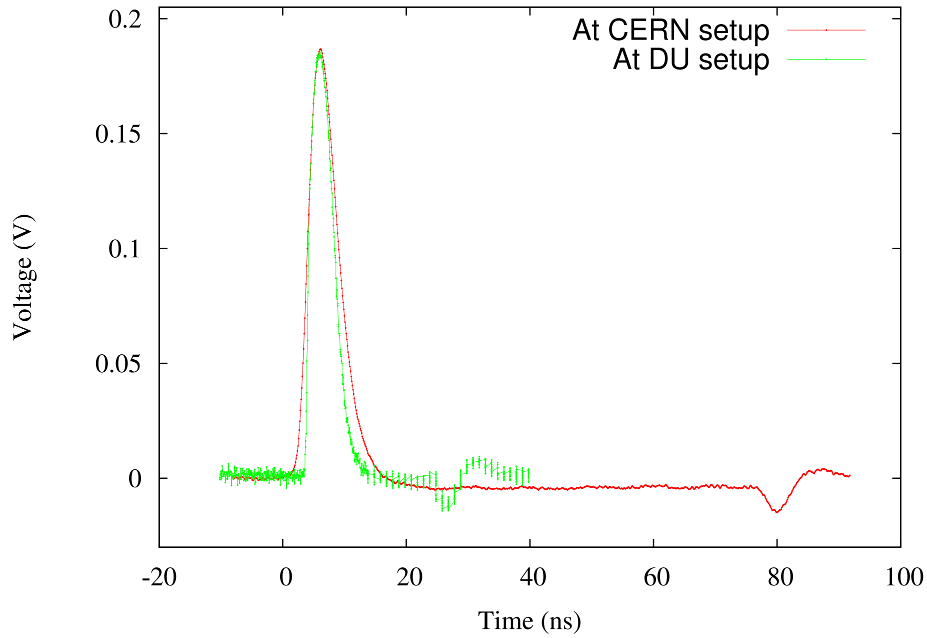

Figure 4.29: Comparison of TCT signals measured with CERN setup and DU setup at 200 V.

Calibration of setup

To check the consistency of the measurements being done on the DU TCT setup, a few measurements have been performed on the CERN TCT setup as well. In Fig. 4.29, an overlap of the signals of a n-type FZ pad diode at 200 V, measured at CERN and at DU, is shown. This validates the working of the TCT setup at University of Delhi.

Frontside TCT signal

The TCT frontside voltage scan of one of the p-type MCz diode is shown in Fig. 4.30a. It is seen from the plot in Fig. 4.31a that as the bias voltage is increased, more and more charge pairs are collected. This means that at higher biases, the recombination effects are reduced significantly as the detector depleted volume increases. However, after a certain voltage, no effect of increase in the charge collection is observed since all the charge that is created is collected. Nonetheless, increase in voltage, reduces the charge collection time, i.e. a faster charge collection is observed with increase in the voltage (below the breakdown voltage).

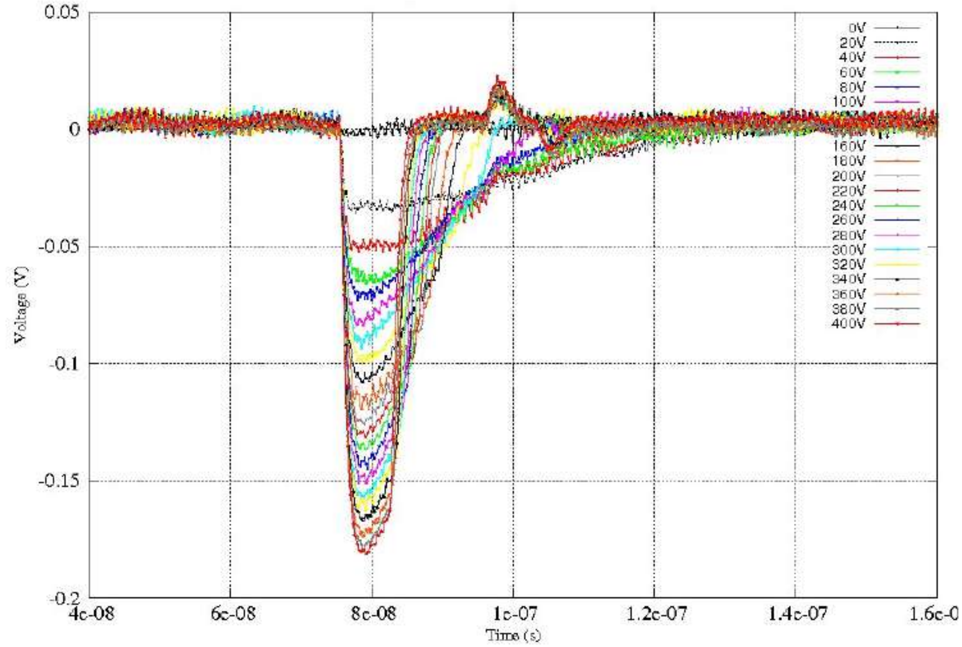

(a)

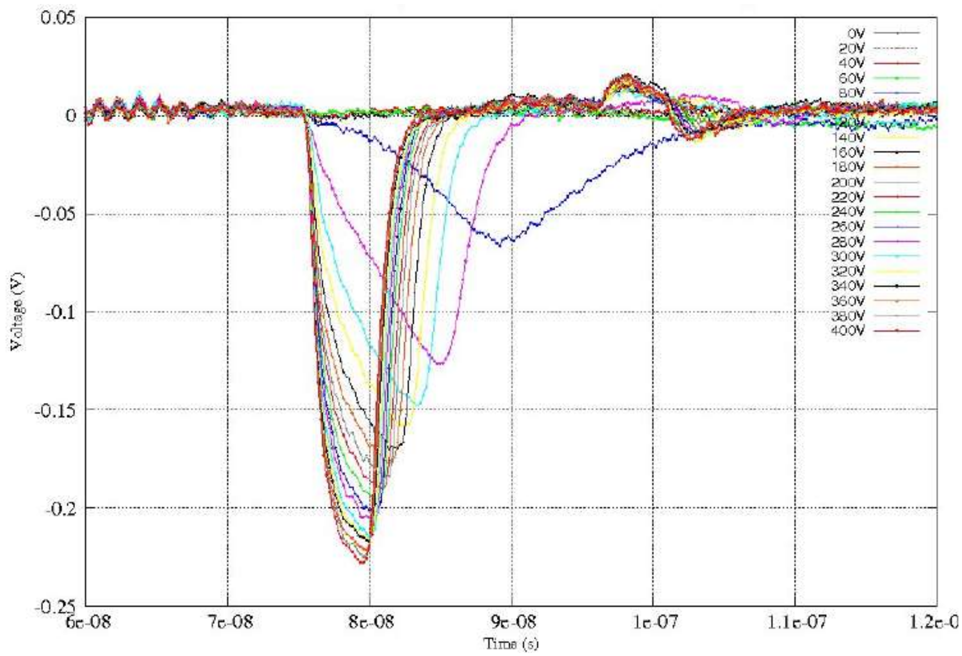

(b)

Figure 4.30: The (a) frontside hole, and (b) backside TCT signals at different bias voltages from 0 to 400 V of a p-type pad diode illuminated with red laser from frontside and backside respectively.

Backside TCT signal

Fig. 4.30b shows the TCT backside voltage scan for the same p-type FZ diode as discussed in the above section. It is observed that very low charge is collected upto 80 V of bias voltage. The charge collection curve saturates beyond 140 V (see Fig. 4.31b). Thus, the backside TCT signal, for a frontside pn junction diode, is an excellent tool to calculate the full depletion voltage for that diode.

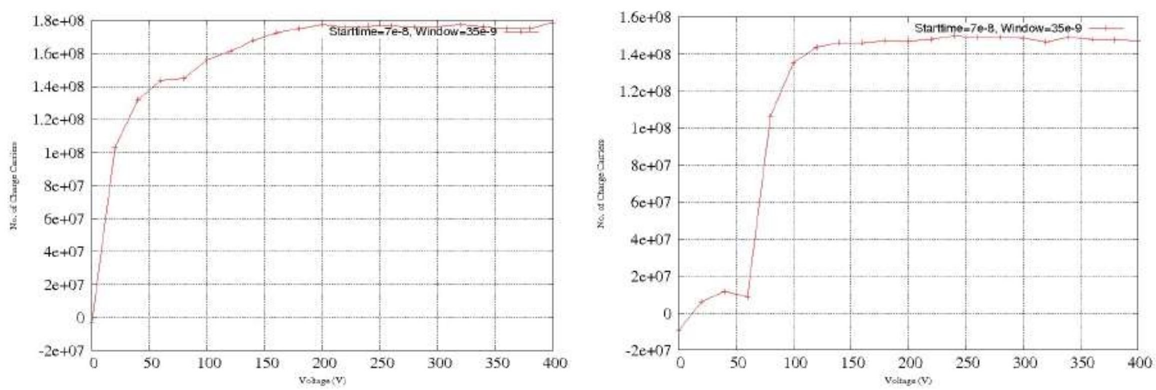

(a) (b)

Figure 4.31: The (a) frontside, and (b) backtside charge collected is plotted for an integration time window of 35 ns.

4.5 Summary

The University of Delhi has established various sensor qualification setups, namely the multi- and micro- strip characterization system, the current-voltage & capacitance-voltage system and the transient current technique setup using red laser. All the setups are successfully installed and commissioned. Measurements have been carried out on pad diodes and micro-strip sensors.

Chapter 5

Radiation hard design of the Low Gain Avalanche Detector

The possibility of attaining higher collision energies and better statistics in future HEP experiments will require the silicon sensors to deal with a large fluence of incoming particles. However, it is well-known that traditional n-on-p sensors experience a rapid fall in the charge collection (CC) with progressing radiation damage [119–122], resulting in an inefficient signal read-out. Therefore, a novel sensor technology is required to replace the existing technology. A Low Gain Avalanche Detector (LGAD) is a suitable candidate considering its ability to cause local avalanche when operated in reverse bias mode. Since the avalanche is controlled, it leads to internal charge multiplication and thereby, a sufficiently high particle signal. Additionally, the LGADs boast a high precision space-time particle tracking [123]. However, experimental results show that the charge multiplication factor tends to decrease with fluence and ultimately vanishes at 7×10^{14} $n_{eq}\cdot cm^{-2}$ [124–127].

In this chapter simulation R&D study on LGADs have been performed with the following aim -

- To understand the effect of design parameters on charge multiplication factor.
- To understand the reason for degradation of charge multiplication factor with irradiation.
- To propose an optimized set of design parameters so as to extend the radiation hardness capability of LGAD detectors.

5.1 The LGAD device

5.1.1 Description and principle of operation

A LGAD device is a n-on-p silicon sensor, with an additional p-type implantation layer, called p-well, just below the n^+ implant and diffused into the p-type substrate [128]. At a suitable operating voltage, an electric field greater than 3×10^5 V/cm develops near the junction formed by the p-well and the n^+ implant, also referred to as 'peak electric field′, which leads to a controlled avalanche mechanism. The charge carriers drift in this generated electric field and get multiplied. A sketch of the LGAD device and the generated electric field is shown in Fig. 5.1.

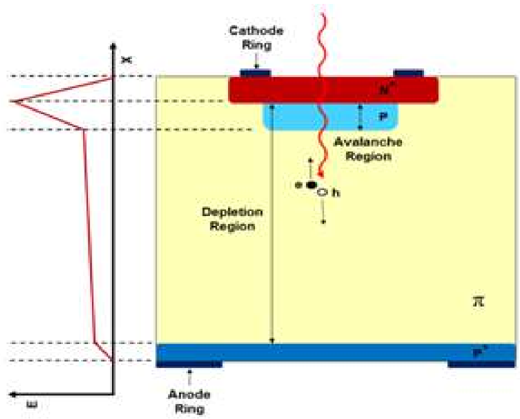

Figure 5.1: A traditional n-on-p detector, but with a deeper p-type multiplication layer called p-well, just below the n+ implant, also called LGAD. This sketch is taken from Ref. [129].

5.1.2 Simulation of LGAD device

Design geometry

In the Silvaco [69] simulation package, the TCAD device structure was chosen to be a plane parallel p-type silicon substrate with a uniform N_b bulk doping concentration and d detector thickness. The structure is further doped on the top side with gaussian n^+ and p-well implants with N_{im} peak implant concentration & d_{im} implant diffusion depth and N_p peak p-well concentration & d_p p-well diffusion depth, respectively. Fig. 5.2 shows the LGAD structure built in the simulation framework with metal contacts etched at the centre of the structure. The 1D doping profile and the electric field developed at the junction,

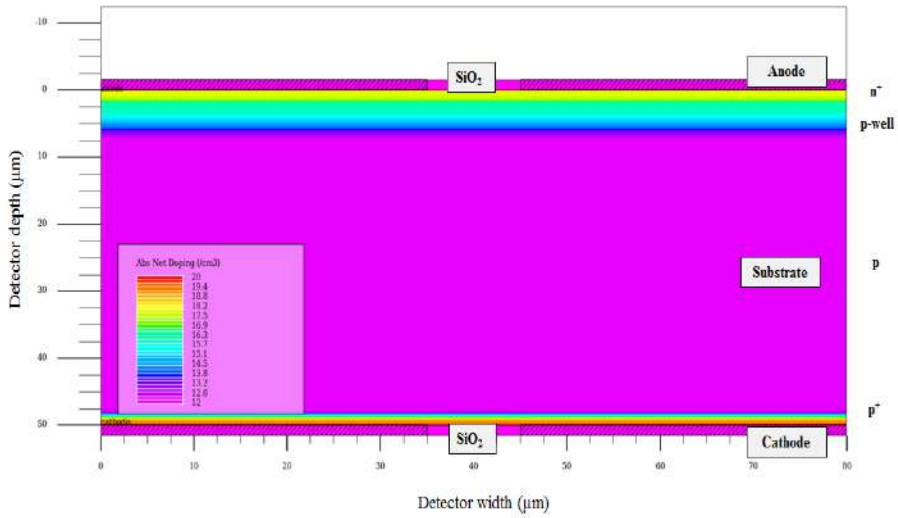

Figure 5.2: LGAD structure of d = 50 µm showing the absolute net doping profile in 2D Tonyplot, a visualization tool in Silvaco framework.

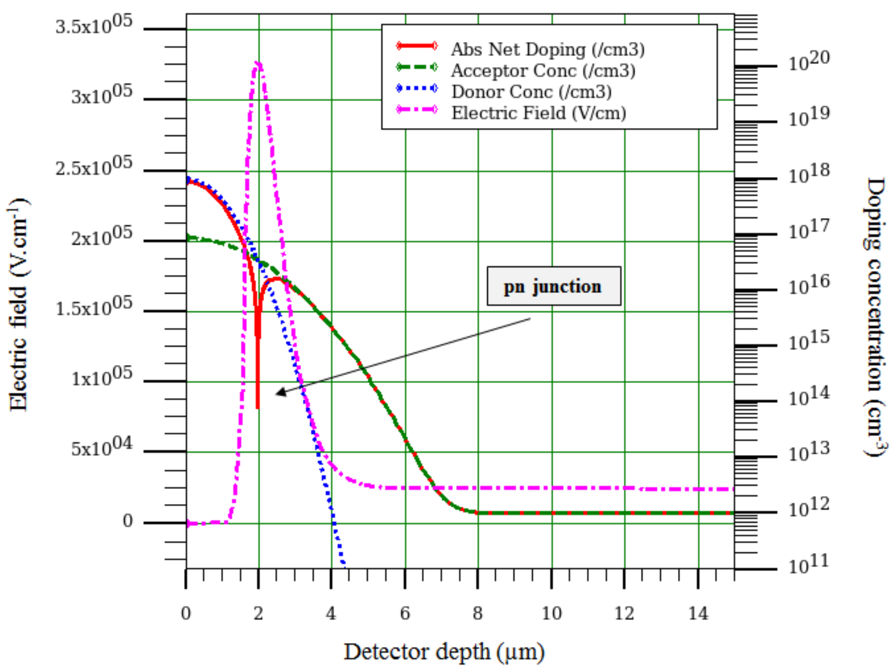

Figure 5.3: The 1D doping profiles of both acceptor (p-well and p) and donor (n^+) concentrations is shown. The electric field peaks in the junction region formed by the p-well and the n^+ implant.

across a vertical cutline into the detector bulk, is shown in Fig. 5.3. The LGAD gain is defined as the ratio of the CC for a LGAD device and that of the reference detector (without p-well). All the design parameters of the reference detector were kept similar to the LGAD device for comparison purposes. The breakdown voltage is simulated by keeping the width of the p-well (58 mm) less than the width of the n^+ implant (80 mm) and by including an additional junction termination extension (JTE) structure.

Table 5.1: The different parameters and their values used in the TCAD 2D device simulation.

Structure parameters	**Value**
Device	n-on-p type with p-well layer
Structure type	Plane parallel
Width	80 μm
Bulk doping concentration ($\mathbf{N_b}$)	1×10^{12}, 5×10^{13}, 2×10^{14}, 3×10^{14} cm^{-3}
Detector thickness (**d**)	300, 200, 100, 50 μm
Frontside implant doping concentration ($\mathbf{N_{im}}$)	1×10^{18} cm^{-3}
Frontside implant doping profile ($\mathbf{d_{im}}$)	gaussian, 4 μm
Backside implant doping concentration	1×10^{18} cm^{-3}
Backside implant doping profile	gaussian, 1.5 μm
p-well doping concentration ($\mathbf{N_p}$)	3.00×10^{16} cm^{-3}, 6.50×10^{16} cm^{-3}, 9.75×10^{16} cm^{-3}
p-well doping profile ($\mathbf{d_p}$)	gaussian, 7 μm
CC parameters	**Value**
Laser wavelength	660 (red back), 1060 (infrared) nm
Laser intensity	1 W $\cdot$ cm^{-2}
CC time window	25 ns
Simulation environment parameters	**Value**
Type	2D simulation
Operating temperature (**T**)	253 K (varied in temperature sensitivity studies)
Radiation damage model	2 bulk traps
Maximum radiation fluence used	5×10^{15} n_{eq} $\cdot$ cm^{-2}

Charge collection

For the CC simulations, a laser of wavelength 1060 nm (infrared laser), or 660 nm (backside red laser) of an intensity of 1 W $\cdot$ cm^{-2} is shone on the device. Since in simulations, only a small cross-section of the actual device is simulated, the results are scaled by an area factor to have a direct comparison with the results of the real devices. The charge carriers generated by the incident laser drift towards the electrodes, thereby inducing a TCT (Transient Current Technique) signal (Current vs Time plot). The TCT signal is integrated in a time window of 25 ns to obtain the CC in the detector. This is divided by a normalisation constant, which is chosen such that the CC in a non-LGAD detector is equivalent to the CC generated by a minimum ionizing particle, i.e. around 80 electrons per μm. The signal

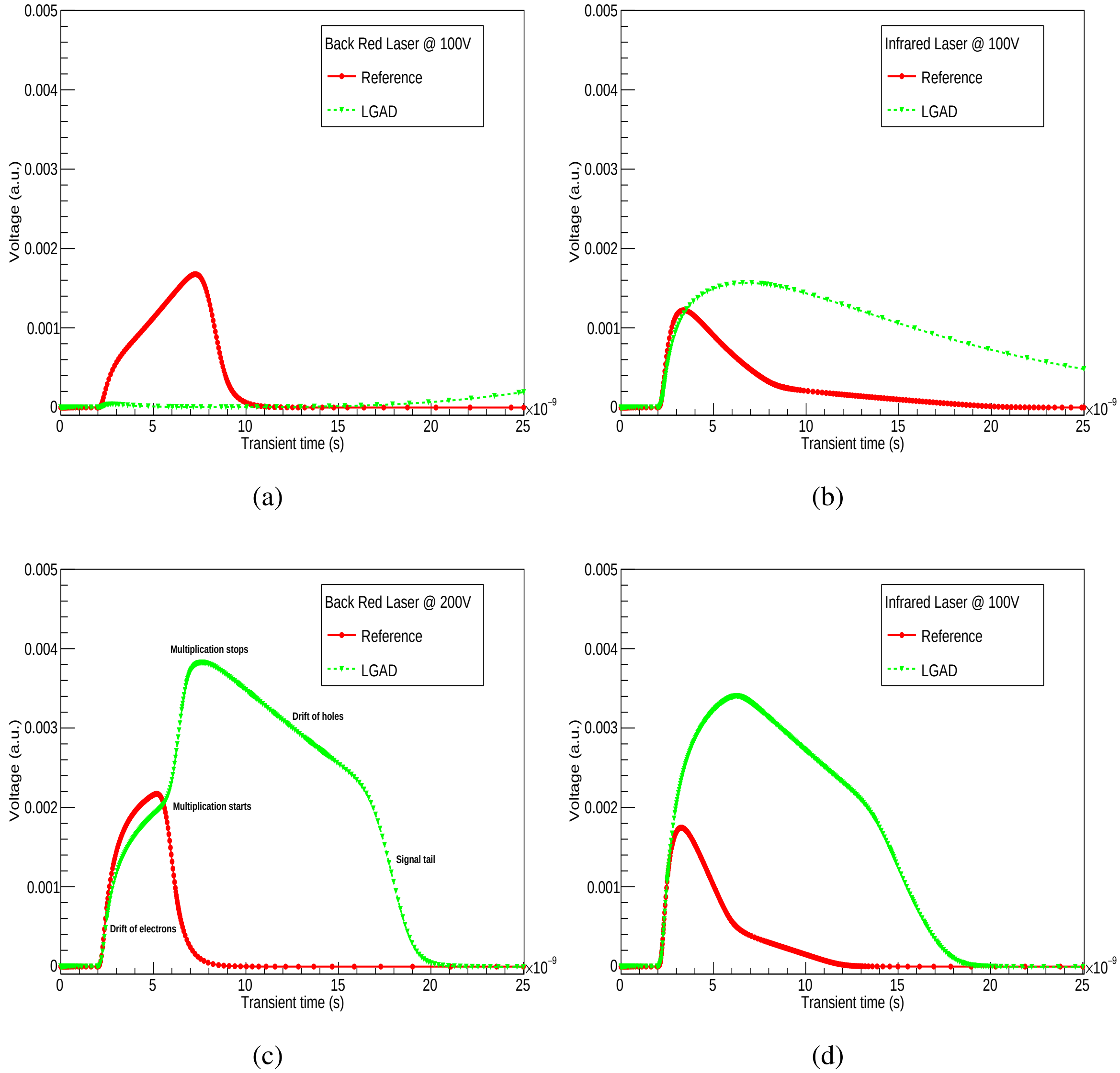

Figure 5.4: TCT signal formation in a reference and a LGAD detector, when illuminated by - (a) backside red laser at 100 V, (b) infrared laser at 100 V, (c) backside red laser at 200 V, and (d) infrared laser at 200 V.
Simulation parameters: $\mathbf{N_b} = 1\times10^{12}$ cm^{-3}; $\mathbf{d} = 300\,\mu$m; $\mathbf{N_{im}} = 1\times10^{18}$ cm^{-3}; $\mathbf{d_{im}} = 4\,\mu$m; $\mathbf{N_p} = 0$ (reference), 9.75×10^{16} cm^{-3} (LGAD); $\mathbf{d_p} = 7\,\mu$m; $\mathbf{T} = 253$ K.

(number of charge carriers) is then obtained by dividing it further by 1 electron charge. The bulk proton radiation damage model developed in Ref. [74] within the same simulator framework, Silvaco, is used to simulate the irradiated LGAD detectors.

A detailed list of the parameters used in the simulations are given in Table 5.1.

5.2 Performance of non-irradiated LGAD

The TCT signals formed in the detectors when illuminated by red laser from backside and infrared laser are shown in Fig. 5.4. The signals are generated at two bias voltages of 100 and 200 V. The signal from the red laser illuminated from backside emphasizes the charge multiplication step-by-step, while the signal formed due to infrared laser mimics the signal formed by a minimum ionizing particle. The signal formed in the reference detector when illuminated with red laser from backside is a contribution of drift of electrons only. However, the electric field distribution is different in the LGAD detector. At 100 V, the electric field is insufficient in the bulk to drift the charge carriers to the p^+ electrode and have any significant TCT signal. However, at 200 V, soon after the generation of the charge carriers due to illumination, the charge carriers are generated in 3-4 μm from the backside surface. Due to the reverse biasing polarity of the detectors, the holes are immediately collected at the backside p^+ electrode. The electrons, on the other hand, drift from the backside towards the n^+ electrode. When these electrons reach the p-well-n^+ junction, an avalanche of electron-hole is generated. The multiplied holes, then drift towards the backside electrode. The signal formation due to *drift of electrons - hole multiplication - drift of holes* is illustrated in Fig. 5.4c. Also this explanation of the shape of the simulated TCT signal is similar to the measured TCT signal as described in Ref. [130].

It is undoubtedly observed that the LGAD detector collects more charge (area under the curve) than a reference detector. The electron-hole pairs that are generated due to controlled avalanche are additionally collected, besides the collection of the primarily generated charge. This additional collection of charge is responsible for providing gain in the LGAD detector over the reference detector.

Fig. 5.5 shows the typical IV characteristics of the representative LGAD device. For comparison purposes, a plot of the reference detector is also shown. The breakdown voltage (V_{BD}) is defined by the sharp increase in the leakage current.

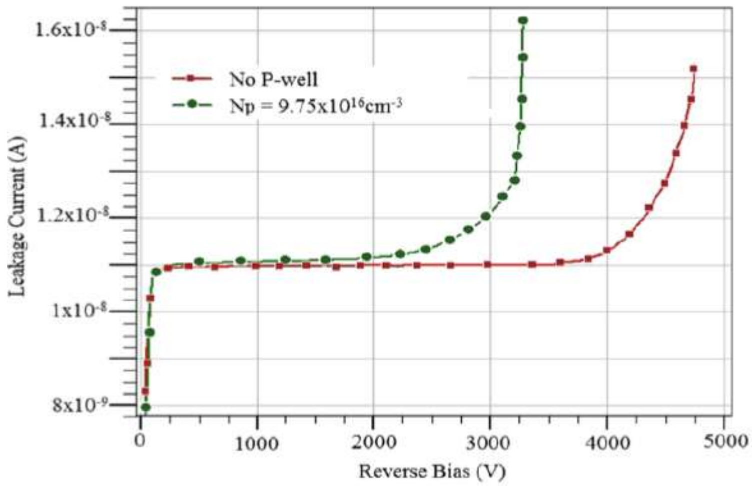

Figure 5.5: The IV characteristics of reference and LGAD detector for the parameters mentioned in Fig. 5.4.

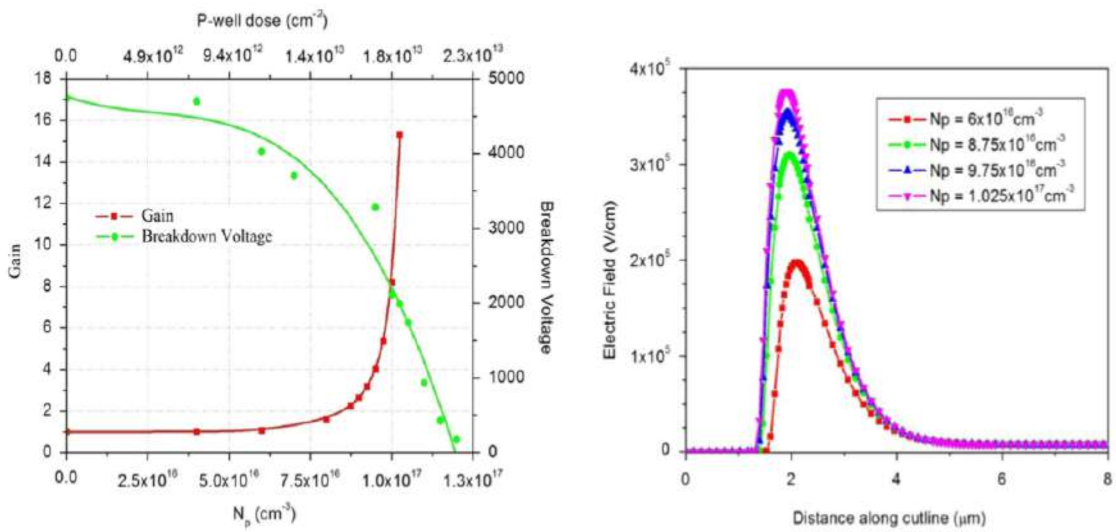

(a) (b)

Figure 5.6: (a) Gain at a reverse bias voltage of 200 V and V_{BD} variation vs. N_p. (b) Simulated electric field near the p-well region for different N_p at 200 V.
Simulation parameters: $\mathbf{N_b}$ = 1×10^{12} cm^{-3}; **d** = $300\,\mu$m; $\mathbf{N_{im}}$ = 1×10^{18} cm^{-3}; $\mathbf{d_{im}}$ = $4\,\mu$m; $\mathbf{N_p}$ = varied; $\mathbf{d_p}$ = $7\,\mu$m; **T** = 263 K.

5.2.1 Gain vs breakdown

On one hand, a high gain is desirable but it can affect the breakdown voltage adversely and on the other hand, a low electric field would result in higher breakdown with little or no gain. Fig. 5.6a shows a plot of the gain and the V_{BD} vs. N_p. It can be seen that the gain remains almost unity up to N_p of 7.6×10^{16} cm^{-3} and then increases sharply with increase in N_p, reaching to a value of 15 for N_p equal to 1.025×10^{17} cm^{-3}. The increase in the gain with the p-well dose is attributed to an increase in the electric field around the n$^+$/p-well junction, as shown in Fig. 5.6b. The overall detector gain depends on the magnitude of the peak electric field as well as the width of the high field region [50] around the n$^+$/p-well junction. Since the width of the high field region is only a few micron for LGAD devices, the peak electric field of around 3×10^5 V/cm or more is significant for producing high gain. It can be seen from Fig. 5.6b that the peak electric field in the multiplication region is about 3×10^5 V/cm for N_p value of 8.75×10^{16} cm^{-3} case and reaches about 3.6×10^5 V/cm for N_p value of 1.025×10^{17} cm^{-3} scenario. The higher gain achieved in LGAD devices, however, is at the expense of the reduced V_{BD}, as shown in Fig. 5.6a. It may be noted that a V_{BD} of ~2000 V is achieved for a N_p value of 1.025×10^{17} cm^{-3} (corresponding to the gain of 15). On the basis of the achieved gain, these LGAD devices are labelled as low gain (~2.5 at 200 V for a N_p dose of 1.61×10^{13} cm^{-2}), moderate gain (~ 5 at 200 V for a dose of 1.78×10^{13} cm^{-2}) and high gain (~15 at 200 V for a dose of 1.87×10^{13} cm^{-2}).

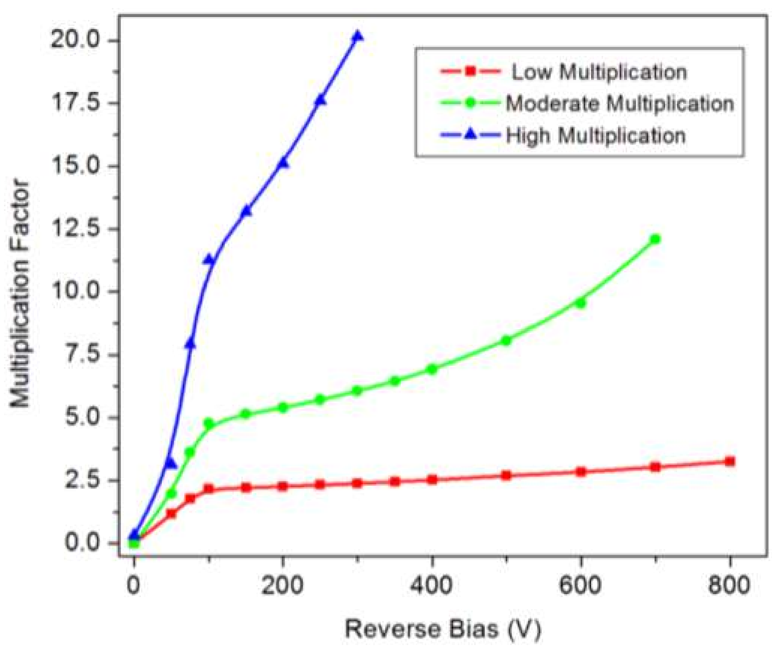

Figure 5.7: Gain vs. reverse bias voltage for three different values of N_p doses. Simulation parameters: $\mathbf{N_b}$ = 1×10^{12} cm^{-3}; **d** = 300 μm; $\mathbf{N_{im}}$ = 1×10^{18} cm^{-3}; $\mathbf{d_{im}}$ = 4 μm; $\mathbf{N_p}$ = 8.75×10^{16} cm^{-3} (low multiplication), 9.75×10^{16} cm^{-3} (medium multiplication), 10.25×10^{16} cm^{-3} (high multiplication); $\mathbf{d_p}$ = 7 μm; **T** = 263 K.

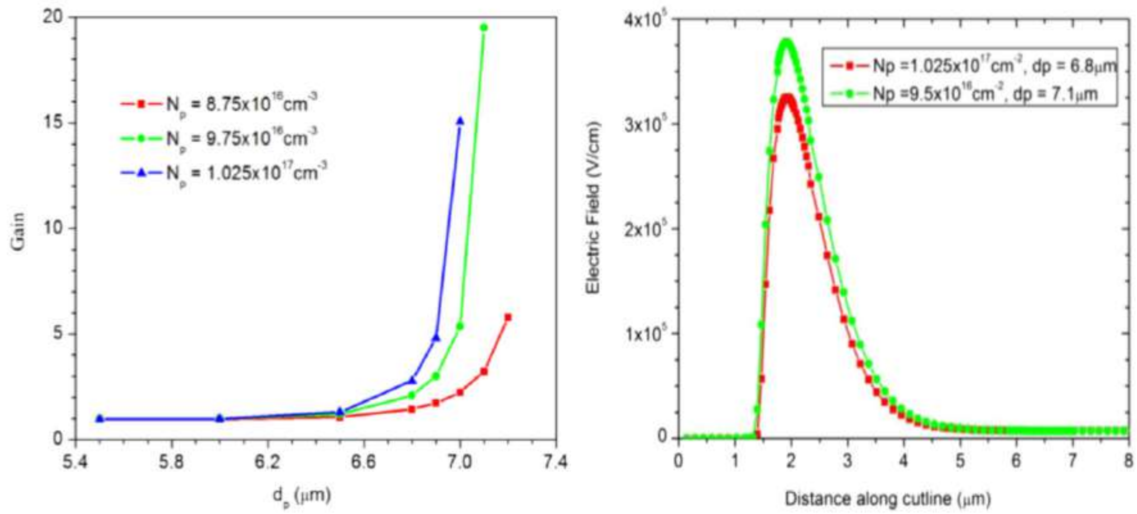

(a) (b)

Figure 5.8: (a) Variation of gain vs. d_p for different values of N_p, and (b) peak electric field variation for two different p-well doping profiles.

Table 5.2: List of N_p dose cm^{-3} and gain (in parentheses) for different values of N_p cm^{-3} and d_p µm.

N_p	d_p				
	5.5	**6**	**6.5**	**6.8**	**7.1**
8.75×10^{16}	1.26×10^{13} (1.0)	1.38×10^{13} (1.0)	1.49×10^{13} (1.1)	1.56×10^{13} (1.4)	1.63×10^{13} (3.2)
9.75×10^{16}	1.40×10^{13} (1.0)	1.53×10^{13} (1.0)	1.66×10^{13} (1.2)	1.73×10^{13} (2.1)	1.81×10^{13} (19.5)
1.025×10^{16}	1.47×10^{13} (1.0)	1.6×10^{13} (1.0)	1.74×10^{13} (1.3)	1.82×10^{13} (2.8)	1.90×10^{13} (-)

5.2.2 Effect of doping profile of p-well

Fig. 5.7 shows the representative plot of the gain as a function of reverse bias voltage considering different p-well doses by varying N_p while keeping other parameters constant. For the low and moderate gain devices, there are two visibly distinct regions: steep increment with voltage before full depletion, and a gradually increasing plateau region for higher biases. However, for the high gain structure, the plateau region no longer remains constant and its slope increases sharply with increase in gain. The simulated moderate gain variation with voltage is similar to the ones reported in earlier measurement studies [125, 126, 130], whereas that of the low gain is similar to the measurements shown in Ref. [130, 131].

A similar variation was studied for different values of d_p. Fig. 5.8a shows the plot of gain vs. d_p for different values of N_p. It can be seen that the gain of the LGAD device is also affected by varying d_p, while keeping the N_p constant. For the simulated N_p values, the gain remains constant for a minimum d_p, beyond which it increases sharply. Increase in the d_p (for a given N_p) results in higher acceptor density and hence leads to a higher peak electric field (Fig. 5.8b), leading to an increase in gain. For a given d_p, the gain increases with increase in N_p beyond a minimum d_p.

To illustrate the relevance of the complete p-well doping profile (as opposed to total p-well dose only) in tailoring the gain of the LGAD devices, Table 5.2 lists the gain (in parentheses) and p-well dose values for different combinations of N_p and d_p. It may be noted from this Table that a dose of about 1.6×10^{13} cm^{-2} can be attained using - (a) N_p = 8.75×10^{16} cm^{-3} with d_p = 7.1 µm; or (b) N_p = 1.025×10^{17} cm^{-3} with d_p = 6 µm. However, these two combinations (for the same p-well dose) give significantly different gains, i.e. 3.2 and 1 respectively. Similar observations can be made for another dose of 1.81×10^{13} cm^{-2}, which, for the combination of N_p = 9.75×10^{16} cm^{-3} and d_p = 7.1 µm gives a gain of 19.5 whereas for the other combination, i.e. N_p = 1.025×10^{16} cm^{-3} and d_p = 6.8 µm gives a gain of only 2.8. It may be concluded that for the set of (N_p,d_p) values considered in this work, that low values of p-well doses are insufficient to provide gain, however, beyond a minimum dose, a combination of high d_p and low N_p is able to provide high gain. One may need to investigate this further by expanding the parameter space.

5.2.3 Effect of doping profile of n^+ implant

The variation of n^+ implant doping profile (N_n and d_n) also affects the n^+/p-well junction and region around it, and hence it affects the gain and the electric field distribution for a given p-well dose. An increase in d_n (for a given N_n) would shift the n^+/p-well junction slightly deeper where the p-well doping density would be lower. This leads to decrease in the electric field (and hence the gain) as shown in Fig.5.9. Similarly, an increase in the N_n (for a given d_n) would shift the n^+/p-well junction location deeper inside the silicon bulk where the p-well doping density is lower. This results in lower gain.

Fig. 5.10 show the net doping profile and electric field distribution respectively, for a fixed n^+ dose for two different combinations of N_n and d_n, i.e. (a) N_n = 9×10^{17} cm^{-3} and d_n =

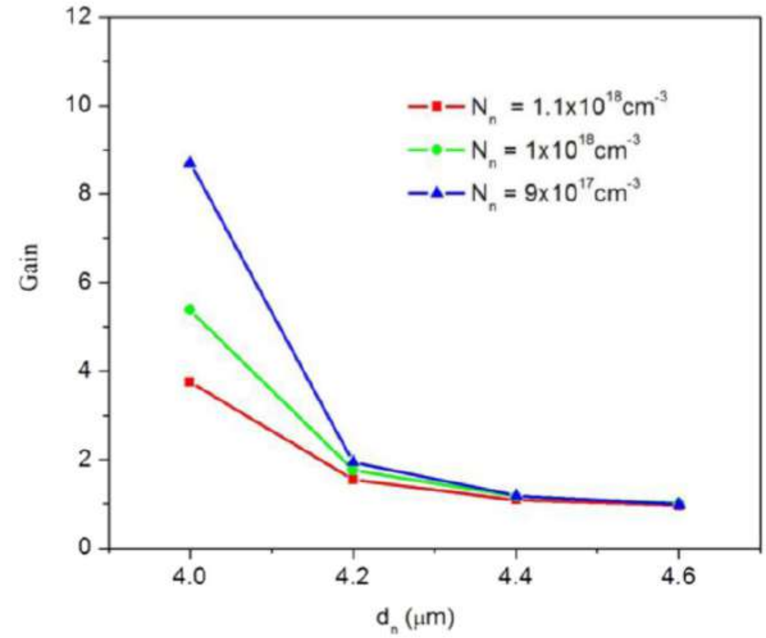

Figure 5.9: Gain vs. d_n for LGAD device for three different values of N_n.
Simulation parameters: $\mathbf{N_b}$ = $1{\times}10^{12}$ cm^{-3}; **d** = $300\,\mu m$; $\mathbf{N_{im}}$ = varied; $\mathbf{d_{im}}$ = varied; $\mathbf{N_p}$ = $9.75{\times}10^{16}$ cm^{-3}; $\mathbf{d_p}$ = $7\,\mu m$; **T** = 263 K; **V** = 200 V.

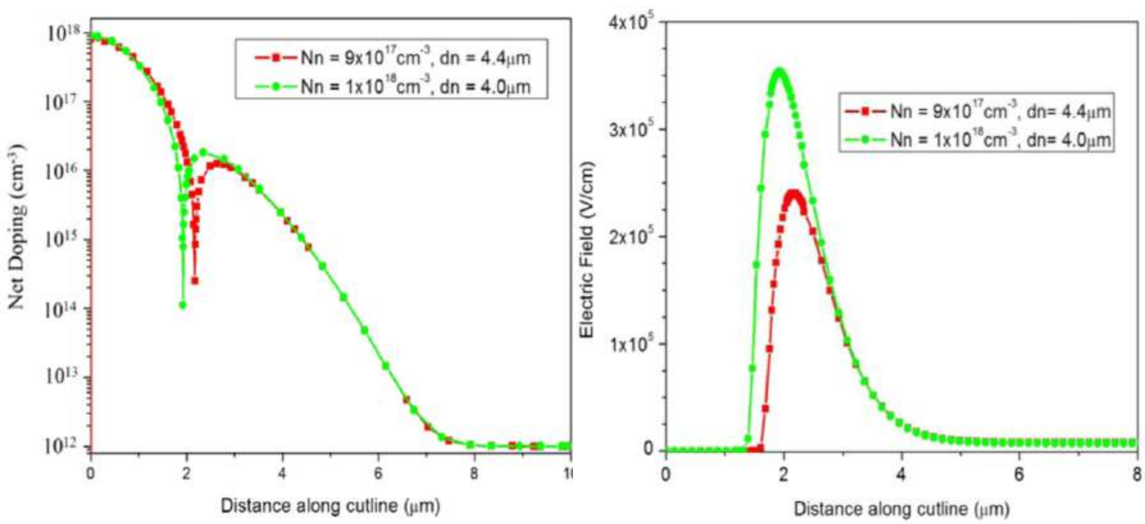

(a) (b)

Figure 5.10: (a) Doping profile and (b) Electric field along the depth near the p-well region.

$4.4\,\mu m$ and (b) N_n = $1{\times}10^{18}$ cm^{-3} and d_n = $4.0\,\mu m$. The former gives a gain of 1.0 while the latter gives a gain of 5.5. Thus, it may be concluded that, for the given set of (N_n, d_n)

values considered in this work, a judicious combination of the N_n and the d_n, as opposed to the total n^+ dose, would give an expected gain for the LGAD device.

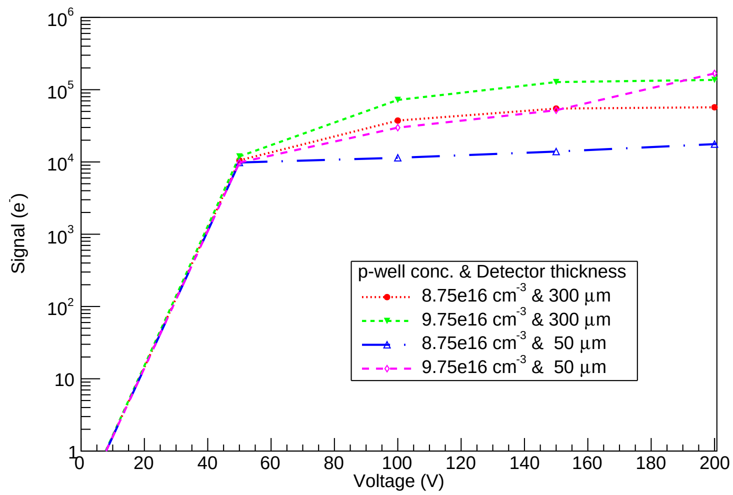

Figure 5.11: Charge collection as a function of bias voltage for a thick ($300\,\mu m$) and a thin ($50\,\mu m$) non-irradiated LGAD.
Simulation parameters: $\mathbf{N_b}$ = 1×10^{12} cm^{-3}; **d** = $300\,\mu m$, $50\,\mu m$; $\mathbf{N_{im}}$ = 1×10^{18} cm^{-3}; $\mathbf{d_{im}}$ = $4\,\mu m$; $\mathbf{N_p}$ = 8.75×10^{16} cm^{-3}, 9.75×10^{16} cm^{-3}; $\mathbf{d_p}$ = $7\,\mu m$; **T** = 253 K.

5.2.4 Effect of detector thickness

Figure 5.11 shows the comparison of the charge collection for LGADs of two thicknesses, $300\,\mu m$ and $50\,\mu m$, as a function of the bias voltage. These specific thicknesses are chosen deliberately to emphasize the comparison between the standard ($300\,\mu m$) and the thin ($50\,\mu m$) LGAD devices. Two different peak p-type doping for the p-well implant are considered: $N_{p,low}$ = 8.75 $\times10^{16}$ cm^{-3} and $N_{p,medium}$ = 9.75 $\times10^{16}$ cm^{-3}, corresponding to low and medium gain regimes [132] respectively of the LGAD detectors. It can be seen that a higher N_p results in a higher charge multiplication due to a stronger electric field around the n^+ and the p-well region. The CC for a thin detector with similar p-well characteristics as that of a thick detector is smaller due to reduced active volume and hence less primary charges generated from the interactions. Nevertheless, it is worth noting that the CC for the thin LGAD with medium gain $N_{p,medium}$ is comparable to the CC of the thick LGAD with low gain $N_{p,low}$, at a bias voltage of 150 V. The above results can be understood from Figures 5.12a and 5.12b, which show the peak electric field distributions for medium and low

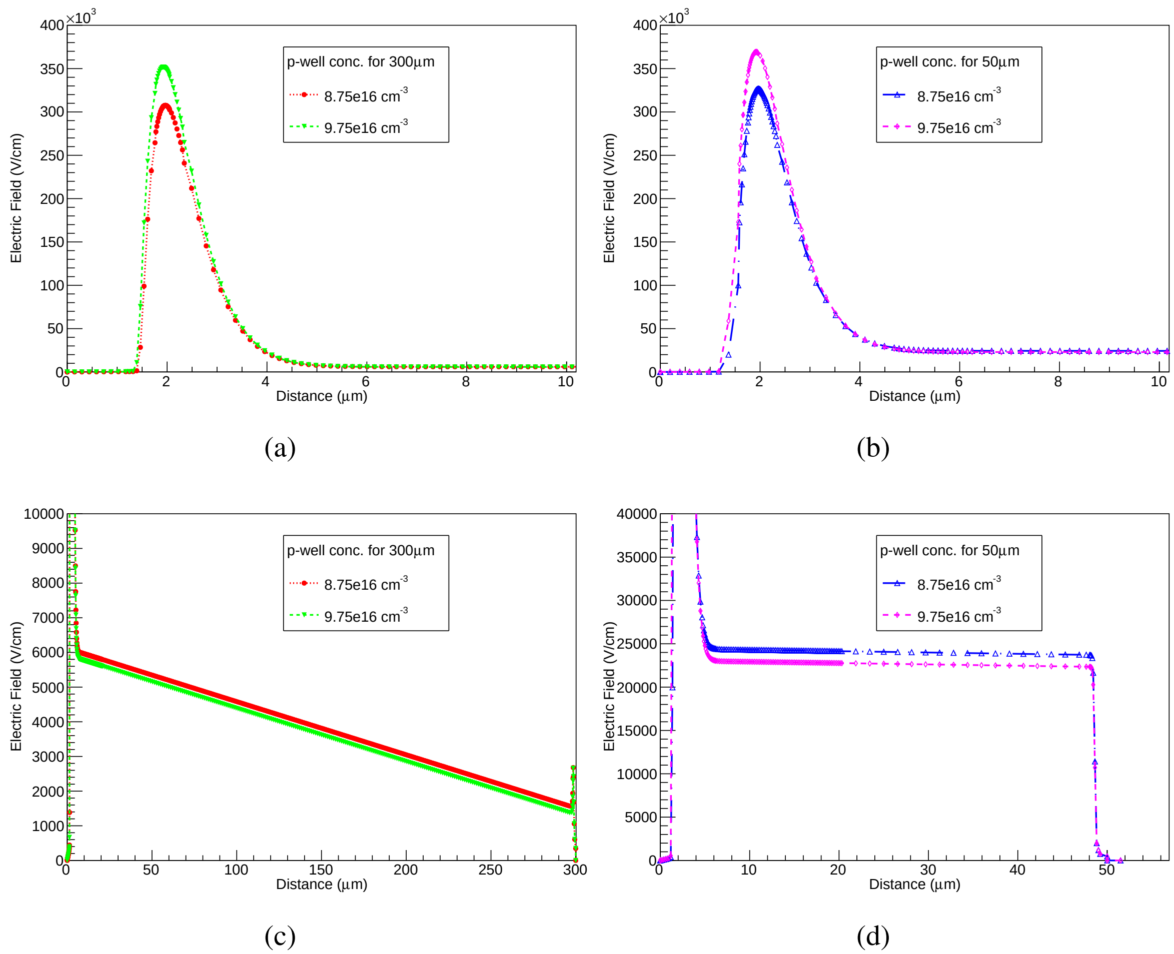

Figure 5.12: The peak electric fields (a and b) and the bulk electric fields (c and d) developed in the LGAD detector of thickness of 300 μm and 50 μm respectively, at a bias voltage of 150 V are shown.

gain in thick and thin detectors respectively. Figures 5.12c and 5.12d show how the electric field in the bulk region is almost five times higher for thin LGAD than for thick LGAD, resulting in efficient charge collection. Thus, it is the combination of both the peak and the bulk electric field distribution that play an important role in deciding the CC characteristic of the LGAD device.

In the LGAD devices, the electrons generated in the bulk move towards the n^+-p-well junction, get multiplied (e-h created), and the secondary holes move back towards the backside of the detector, for collection. For this reason, a fast collection of signal is seen for the thin detector compared to the thick detector, as the holes have to travel for a shorter distance.

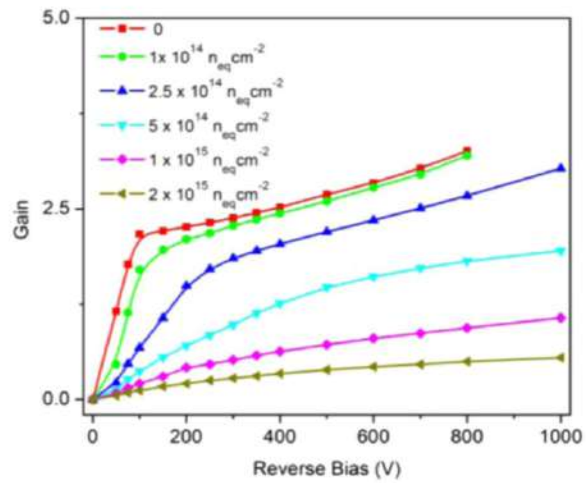

(a)

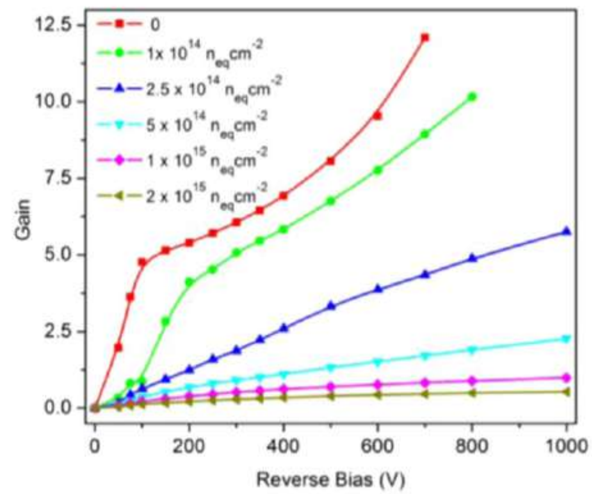

(b)

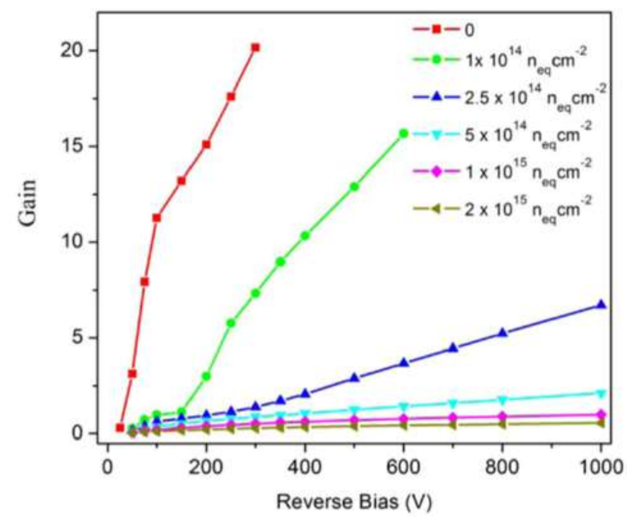

(c)

Figure 5.13: The gain vs. bias voltage for different fluence values for - (a) low multiplication (dose of 1.61×10^{13} cm^{-2}), (b) medium multiplication (dose of 1.78×10^{13} cm^{-2}), and (c) high multiplication (dose of 1.87×10^{13} cm^{-2}) at T = 253 K.

5.3 Effect of irradiation on LGAD

A plausible explanations to this loss of gain with irradiation is provided in Ref. [130] through experimental observations. However, a detailed investigation based on simulations, using the Silvaco tool [69] was performed describing the critical gain dependence of LGAD devices on the doping profiles of the p-well and the n^+ implant. As categorized earlier in Fig. 5.7, the effect of proton fluence is studied for the low gain, medium gain, and high gain LGAD devices. The variation of the gain with bias voltage for different fluence values is shown in Fig. 5.13 for low, medium and high N_p. The general trend of the plots for the irradiated devices is similar to that observed for the non-irradiated ones, but, it may be seen that the gain is reduced with an increase in fluence and it even decreases below that of the non-irradiated reference diode for higher fluence values. Moreover, the onset of plateau region also occurs at slightly higher applied bias.

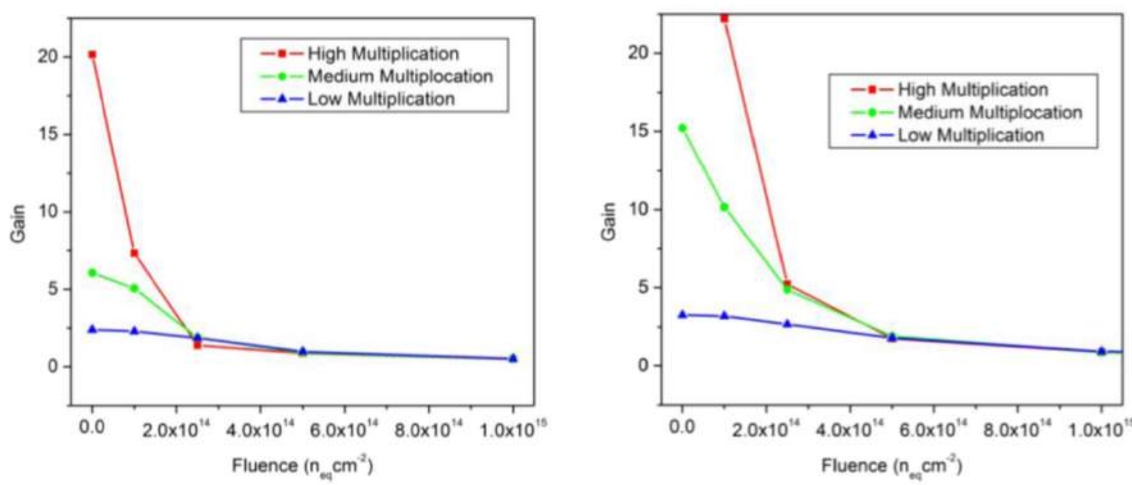

(a) (b)

Figure 5.14: The gain variation as a function of fluence for different gain scenarios at a reverse bias voltage of - (a) 300 V, and (b) 800 V at 253 K.

A comparison of the gain vs. fluence for all three cases at bias voltage of 300 V and 800 V are shown in Figs. 5.14a and 5.14b respectively. Although the initial value of the gain in the moderate and high gain for non-irradiated LGAD devices are higher but, it decreases sharply with irradiation and becomes comparable to the low gain LGAD devices for a fluence of about $5 \times 10^{14}\ n_{eq} \cdot cm^2$. This behaviour is consistent with the recent measurements of the LGAD devices, irradiated with charged hadrons [130].

The simulated leakage current variation with the fluence is shown in Figs. 5.15a and 5.15b for the low gain and the moderate gain LGAD structures respectively. These plots are

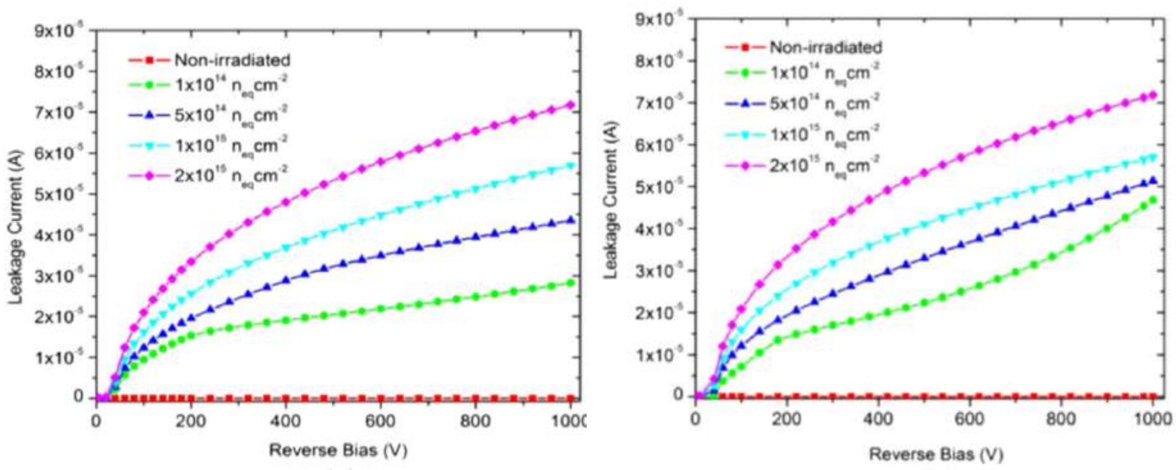

(a) (b)

Figure 5.15: The leakage current for the active area of 1 cm $\times$ 1 cm variation vs. fluence for - (a) low multiplication, and (b) moderate multiplication scenario at 253 K.

qualitatively similar to the measurements reported in Ref. [130]. It can be observed that, contrary to the reference diodes, leakage currents in LGAD structures are not linearly proportional to the fluence. Moreover, the leakage current of LGAD devices is about 1.5 to 5 times higher (depending on fluence) than that of the reference diodes. This implies that along with the usual charge carrier generation/recombination process due to the bulk traps (which creates leakage current linearly proportional to fluence), additional current is generated in the multiplication layer.

The effect of the proton irradiation on the gain for the different gain scenario can be understood in terms of irradiation effect on electric field profile inside the irradiated LGAD sensors. For the different values of fluence, the electric field variation inside the p-well region is shown in Fig. 5.16a while its variation into the sensor bulk is shown in Fig. 5.16b. The electric field profile is plotted for the moderate gain scenario at bias voltage of 500 V and T of 253 K. It can be observed from Fig. 5.16a that the peak value and the width of the electric field distribution inside the p-well region decrease with increase in fluence, which would affect the gain of the LGAD device. Moreover, the electric field near the p^+ backside grows with the increase in fluence due to the double junction effect [133–135], leaving lower values of the electric field inside the sensor bulk. Particularly, there is very low electric field region just below the p-well region, which leads to an inefficient transfer of electrons (for higher fluence values) to the multiplication region. Hence, lowering of the electric field around the n^+/p-well junction as well as in the bulk (below p-well) leads to very low or no gain for irradiated LGAD designs.

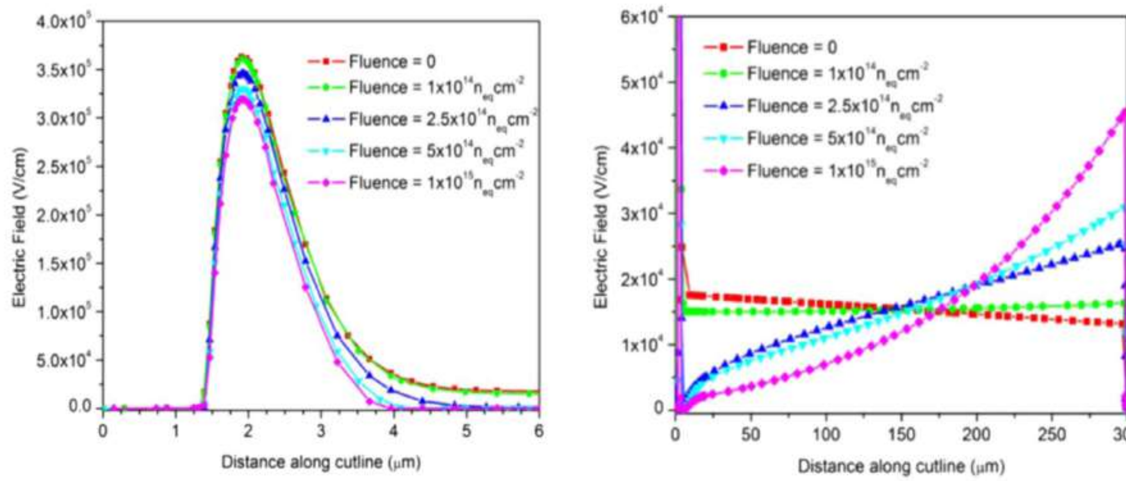

(a) (b)

Figure 5.16: The electric field for different irradiation fluence for a reverse bias voltage of 500 V - (a) around the multiplication region, and (b) inside the sensor volume; for N_p = 9.75×10^{16} cm^{-3} (moderate gain) at T = 253 K.

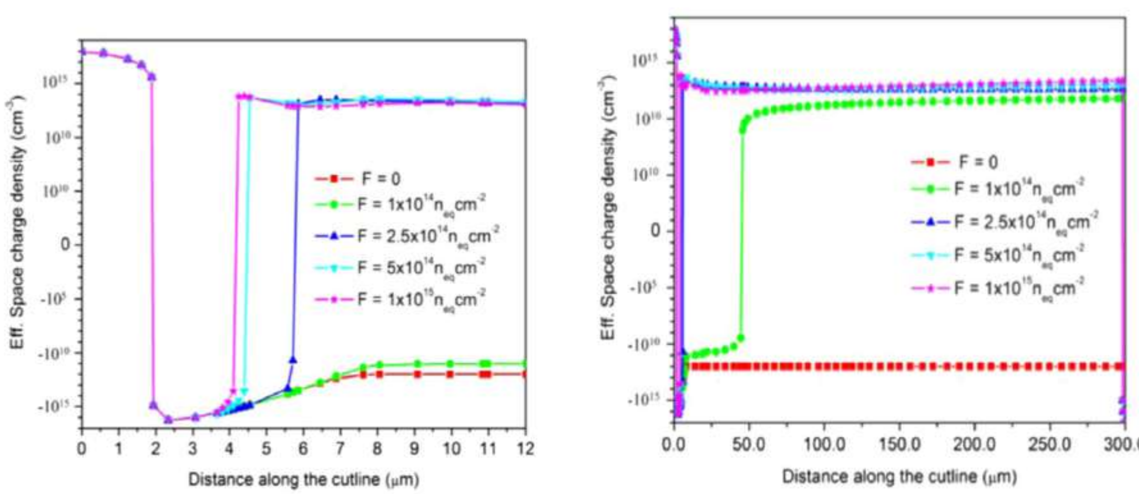

(a) (b)

Figure 5.17: The effective space charge density for different irradiation fluence values - (a) around the multiplication region, and (b) inside the sensor volume; for N_p = 9.75×10^{16} cm^{-3} (moderate gain) at T = 253 K for a bias voltage of 500 V.

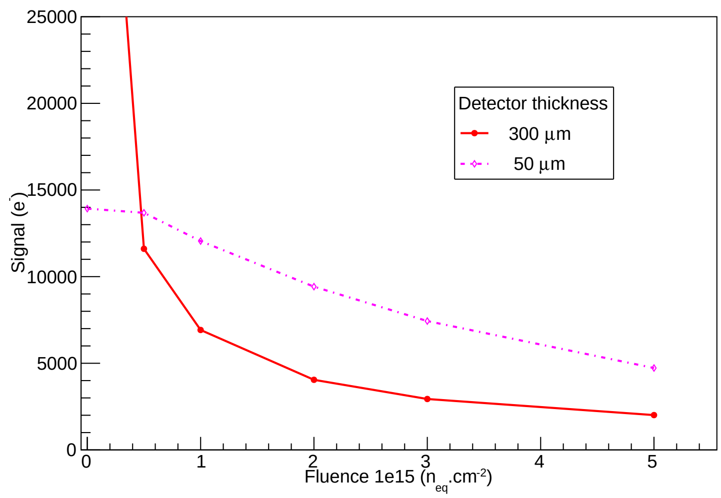

Figure 5.18: CC variation with fluence for two thicknesses of the LGAD detectors at a bias voltage of 150 V.

The effective space charge density inside the LGAD devices is strongly affected by the hadron irradiation. As shown in Fig. 5.15, the additional current component comes from the charge multiplication around the n^+/p-well junction after irradiation. Since the n^+/p-well junction is near the n electrode, the additional holes travel almost whole of the device bulk before getting collected at the p^+ electrode and thus would lead to predominately donor trap filling in the sensor bulk. The effective space charge density (n-type doping density ionized donor trap density p-type doping density - ionized acceptor trap density) for the moderate gain LGAD device is shown in Fig. 5.17. It can be seen that the sensor bulk becomes effectively donor type after irradiation [136] and the effective space charge density of the p-well is also affected. It may be noted that we have not used acceptor removal parametrization [130] in our simulation and the variation of the electric field, the leakage current, the effective space charge density and the gain with irradiation is only a manifestation of acceptor/donor traps effect.

The present simulation work is meant for the proton irradiated LGAD devices but neutron irradiation would also induce the similar gain lowering. Most of the traps due to the neutron and proton irradiation are quite similar [65] but the neutron irradiation induces fewer donor traps (particularly E(30K) trap) which would result in lower backside electric field [74] peak, near p-well. This would result in the slightly higher field towards the p-well side

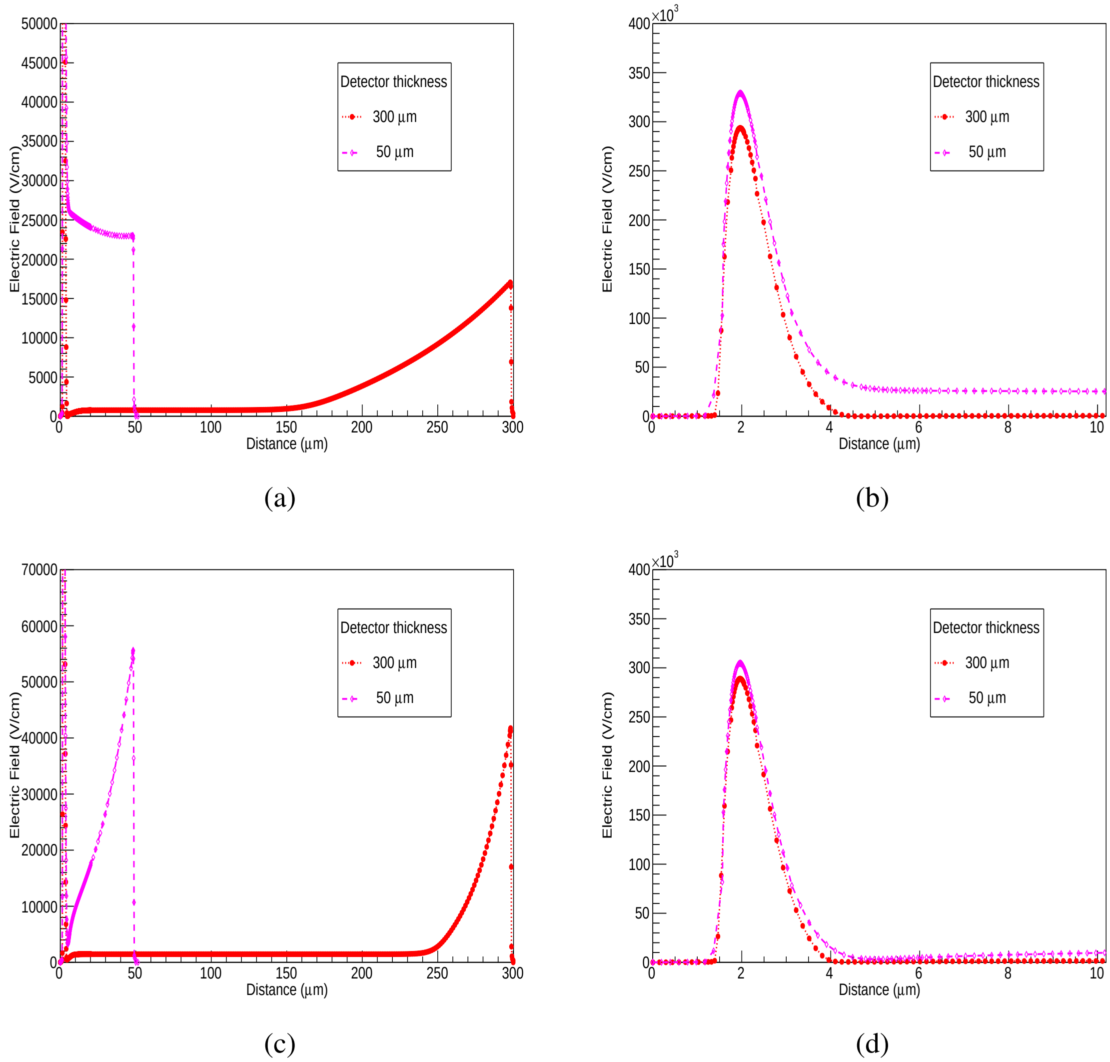

Figure 5.19: The bulk and the peak electric fields are shown for 2 fluence values - (a and b) 1×10^{15} and (c and d) 5×10^{15} $n_{eq} \cdot cm^{-2}$ respectively. With increasing fluence the shift in the electric field from the frontside of the detector to the backside of the detector is observed.

or slightly efficient electron collection for neutron irradiated sensors, resulting in a higher gain. This has been observed experimentally as well [130].

5.3.1 Effect of detector thickness

Fig. 5.18 shows the CC variation with proton fluence at a bias voltage of 150 V for two different detector thickness. Here, the low gain profile of the p-well has been chosen, i.e.,

$N_{p,low}$ = 8.75 $\times 10^{16}$ cm^{-3}, to simulate the scenario of thin LGADs in intense radiation environment. Even though thick LGADs show a higher CC at low fluences, the rate of decrease in CC is steeper in thick LGADs as compared to thin devices. In fact, at the highest fluence simulated, the $50\,\mu\mathrm{m}$ thin devices exhibit a better performance than $300\,\mu\mathrm{m}$ thick devices. To investigate this effect, we again checked the electric field distributions. At higher fluence, due to formation of the double junction, the peak electric field at the frontside of the detector decreases and there is a corresponding increase in the electric field at the backside. This determines a low electric field within the bulk of the thick detector and hence the generated charge carriers are incapable to traverse the length of the detector and get collected. On the other hand, for thin detectors there exists a sufficient electric field in the bulk for the same applied bias voltage for charge collection. The plots of the electric field in the bulk and at the n^+-p-well junction shown in Fig. 5.19 for two different fluences of 1×10^{15} n_{eq} $\cdot$ cm^{-2} and 5×10^{15} n_{eq} $\cdot$ cm^{-2}, at a constant bias voltage of 150 V, reveal this explanation.

This indicates that thin LGAD detectors can be operated at relatively lower voltages for recovering CC at high fluence.

5.4 Charge collection for thin LGADs

To further understand the CC for thin detectors, the variation of substrate doping concentration has been studied. Since the CC of the detector is a combined function of N_b and N_p, it is important to study the CC as a function of N_b as well. Fig. 5.20 shows the charge collection as a function of the N_p for two different values of N_b, for devices irradiated at 5×10^{15} n_{eq} $\cdot$ cm^{-2}. It appears that an increase in N_b will result in a stronger electric field for a constant value of N_p and hence a higher CC. However, for a constant N_b, the CC first increases and then decreases as N_p is increased. The initial increase is due to the higher electric field at the n^+-p-well junction. After a peak in CC is reached, a fall is observed because higher N_p would require a higher voltage to deplete the p-well layer, in order to establish the critical peak electric field for charge multiplication to occur. A similar behaviour is observed for all the values of N_b studied.

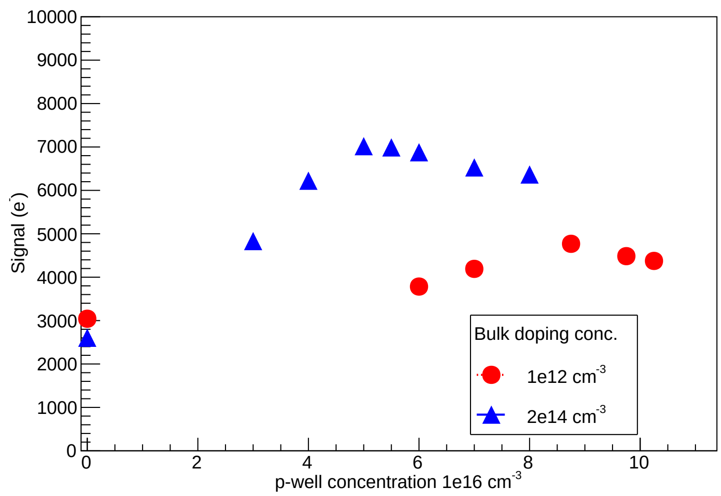

Figure 5.20: CC as a function of p-well concentration for two bulk doping concentrations of 1×10^{12} cm^{-3} and 2×10^{14} cm^{-3} at a constant voltage of 150 V.

5.5 Summary

The LGAD devices have received prominence in recent times due to their promising S/N ratio. However, it has been observed experimentally that their performance degrades with fluence. In this work, we have performed various simulations to study the effect of - (a) doping profile of p-well, (b) doping profile of n^{+} implant, and (c) detector thickness; on the charge collected in non-irradiated LGAD devices. These simulation results were used to understand the behaviour of irradiated LGAD devices and to look for an optimized radiation hard design. It has been found that the thin LGAD detectors exhibit a better charge collection performance over the thick LGAD detectors at high fluences. Further, it has been discovered that low resistivity LGAD substrates may survive longer in a heavy radiation environment. The work discussed in this chapter is reported in Refs. [132, 137].

Chapter 6

Radiation hard studies of pixel and low bulk resistivity sensors

This chapter contains simulation studies on various aspects of silicon sensors and are categorized under three broad categories.

- *The design optimization for pixel sensors for the HL-LHC upgrade* - The radiation hard simulation studies were carried out on pixel detectors under the CMS collaboration. In order to address the problems caused by the harsh radiation environment during the HL-LHC phase, all silicon tracking sensors (pixels and strips) in the CMS experiment will undergo an upgrade. And so to develop radiation hard pixel sensors, simulations have been performed using Silvaco, to obtain the design parameters. This work is done for the *Phase 2 Pixel Sensors* simulation group and all the design parameters for the simulation are provided by them. The effect of various design parameters are studied for the non-irradiated and the irradiated pixel sensors.

- *The determination of trapping time in a silicon sensor* - The simulation studies on trapping probability of irradiated sensors is also presented. This was done to test the radiation damage model developed by our group (Delhi radiation damage model). In this study, the effective trapping probability in a proton irradiated silicon pad sensor has been calculated using transient current simulations and ROOT software. The results are compared against the experimental results and are found to be in reasonable agreement.

- *The exploration of the radiation tolerance of low resistivity silicon sensors* - It is critical to develop the silicon sensor technology in order to maintain the performance in high radiation environment of future HEP experiments. Owing to better ability for higher CC efficiency and internal charge multiplication, there has been an increased interest for the relatively low bulk resistivity or, high bulk doping density (10^{13} - 10^{14} cm^{-3}) silicon sensors. In this chapter, a systematic TCAD simulation study for the effect of proton fluence (up to 3×10^{15} $n_{eq}.cm^{-2}$) on p-type silicon pad diodes of varied thicknesses is reported. The work was done under the *RD50 collaboration*.

6.1 Design for the pixel sensors

The silicon pixel sensors, because of their precise track reconstruction and accurate vertex identification in HEP experiments, are very closely placed to the interaction point. The instantaneous luminosity is expected to increase from 300 fb^{-1} to 3000 fb^{-1} in the HL-LHC upgrade (also mentioned in Chapter 1), thereby demanding radiation harder silicon pixel sensors than the existing ones [138]. Hence, a new radiation hard design for the pixel detectors has to be devised through careful optimization of different geometry parameters. In this work, a stepwise approach for identification of such a design, through 2D TCAD device simulations is described. Initially, a calibration of the simulations has also been performed with the Phase I pixel detector measurement data. Later, the effect of various design parameters like pixel size, pixel depth, implant width, metal overhang, p-stop concentration, p-stop depth and bulk doping density on the leakage current and critical electric field are studied for both non-irradiated as well as irradiated pixel sensors. These 2D simulation results of planar pixels are useful for providing insight into the behaviour of non-irradiated and irradiated silicon pixel sensors.

6.1.1 Pixel geometry and simulation structure

Simulations were carried out on two n-on-p planar pixel sensor geometries, $50 \times 50\,\mu m$ and $100 \times 25\,\mu m$, for two wafer thicknesses (d) of $150\,\mu m$ and $200\,\mu m$. Each geometry has two configurations, which are referred to as '*normal*' and '*wide*' having different implant widths as shown in Fig. 6.1, with various configurations of p-stop and p-spray isolation techniques. The detailed list of the parameters considered for the pixel geometries is given in Fig. 6.2. In simulations, a p-type silicon substrate with a uniform bulk doping N_b of 3×10^{12} cm^{-3} and n^+ implants with a Gaussian profile having a peak concentration of 1×10^{19} cm^{-3}

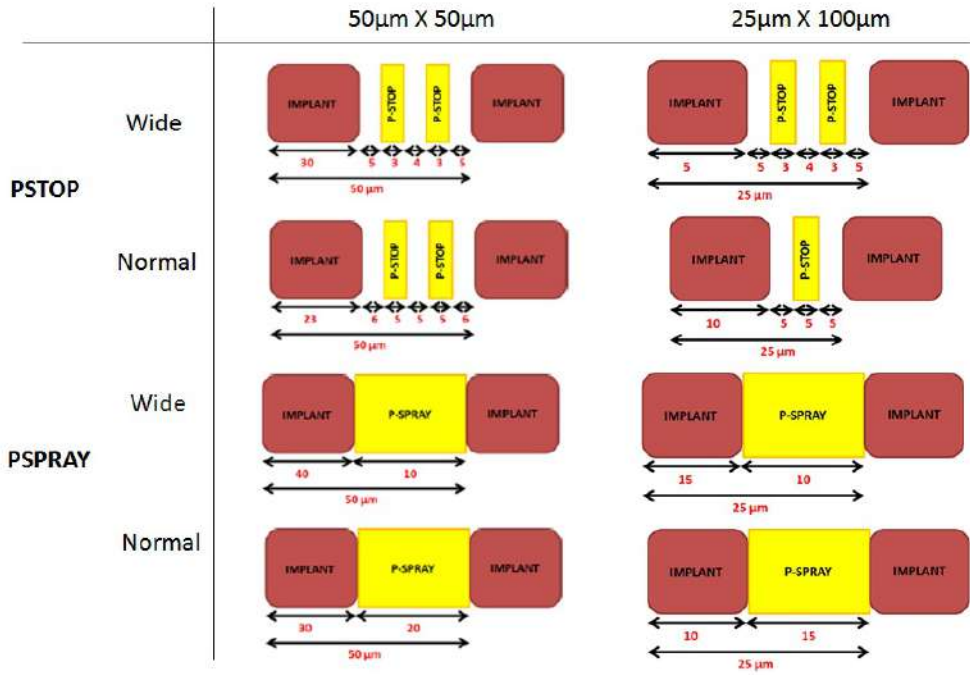

Figure 6.1: Schematics of the pixel geometries with different configurations.

	Structure No.	Pitch (p) (µm)	Im Width (w) (µm)	Metal Width (µm)	Ratio w/p	Iso Width (µm)	Iso1-Iso2 Separation (µm)	Im-Iso Separation (µm)
	1	25	10	10, 14	0.4	15	0	0
PSPRAY	2	25	15	15, 19	0.6	10	0	0
	3	50	30	30, 34	0.6	20	0	0
	4	50	40	40, 44	0.8	10	0	0
	5	25	5	5, 9	0.2	3	4	5
PSTOP	6	25	10	10, 14	0.4	5	0	0
	7	50	23	23, 27	0.46	5	5	6
	8	50	30	30, 34	0.6	3	4	5

Figure 6.2: The detailed parameters list of the considered pixel geometries. (Im is implant and Iso is isolation structure.)

and a junction depth equal to $1.5\,\mu\mathrm{m}$ are considered. A schematic of the simulated pstop isolation normal structure is shown in Fig. 6.3. While the simulation of non-irradiated pixel sensors is performed by incorporating a fixed N_{ox} of 1×10^{11} cm^{-2} and two interface traps at the Si/SiO_2 interface, with corresponding N_{it}; the irradiated pixel sensors are simulated by implementing two additional bulk trap levels along with appropriate values of N_{ox} and N_{it} for different fluences considering the level of radiation damage.

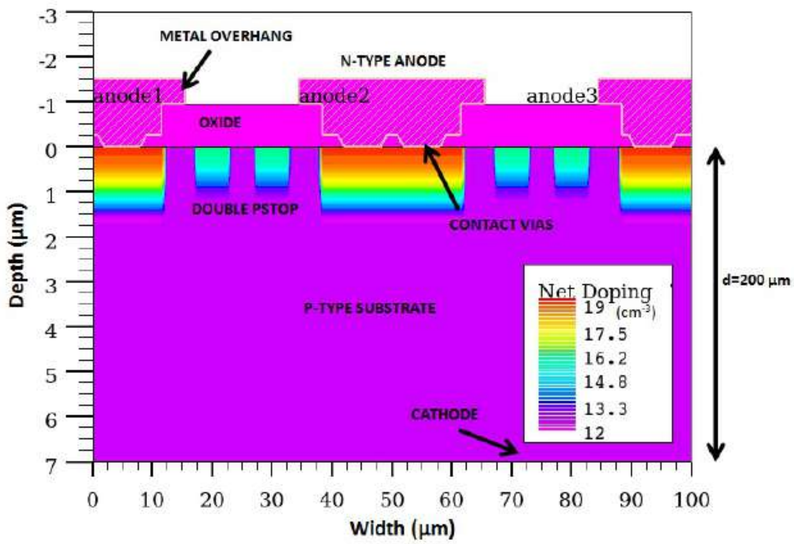

Figure 6.3: Device simulation structure for p-stop isolation studies.

6.1.2 Critical electric field regions

The electric field has been studied as a function of fluence for different design options, to compare the radiation hardness. The critical electric field is analyzed for different configurations and it is found that the maximum electric field is at $0.9\,\mu m$ below the Si/SiO_2 interface, near the implant curvature. The knowledge of the critical electric field is important because the geometry parameters are optimized looking at the operation stability against breakdown caused by the critical electric field in the sensor.

The 2D electric field contours

The pixel sensors of various configurations as described in Fig. 6.2, when irradiated, experience high electric field at three different regions - (i) at n^+ implant curvature due to high concentration of electron charge carriers, (ii) at p-stop curvature where electrons come in contact with the p-stop, and (iii) under MO due to attraction of electrons at MO edges. This can be seen in Fig. 6.4 for *P-stop Normal* configuration.

6.1.3 The 1D electric field plots along a horizontal cutline

The 1D electric field plots were drawn along various horizontal cutlines at a distance of - 0.1, 0.2, 0.5, 0.9, and $1.2\,\mu m$ below the oxide (see Fig. 6.5). It is noticed that the critical electric field region lies around $0.9\,\mu m$ horizontal cutline. Having identified the crit-

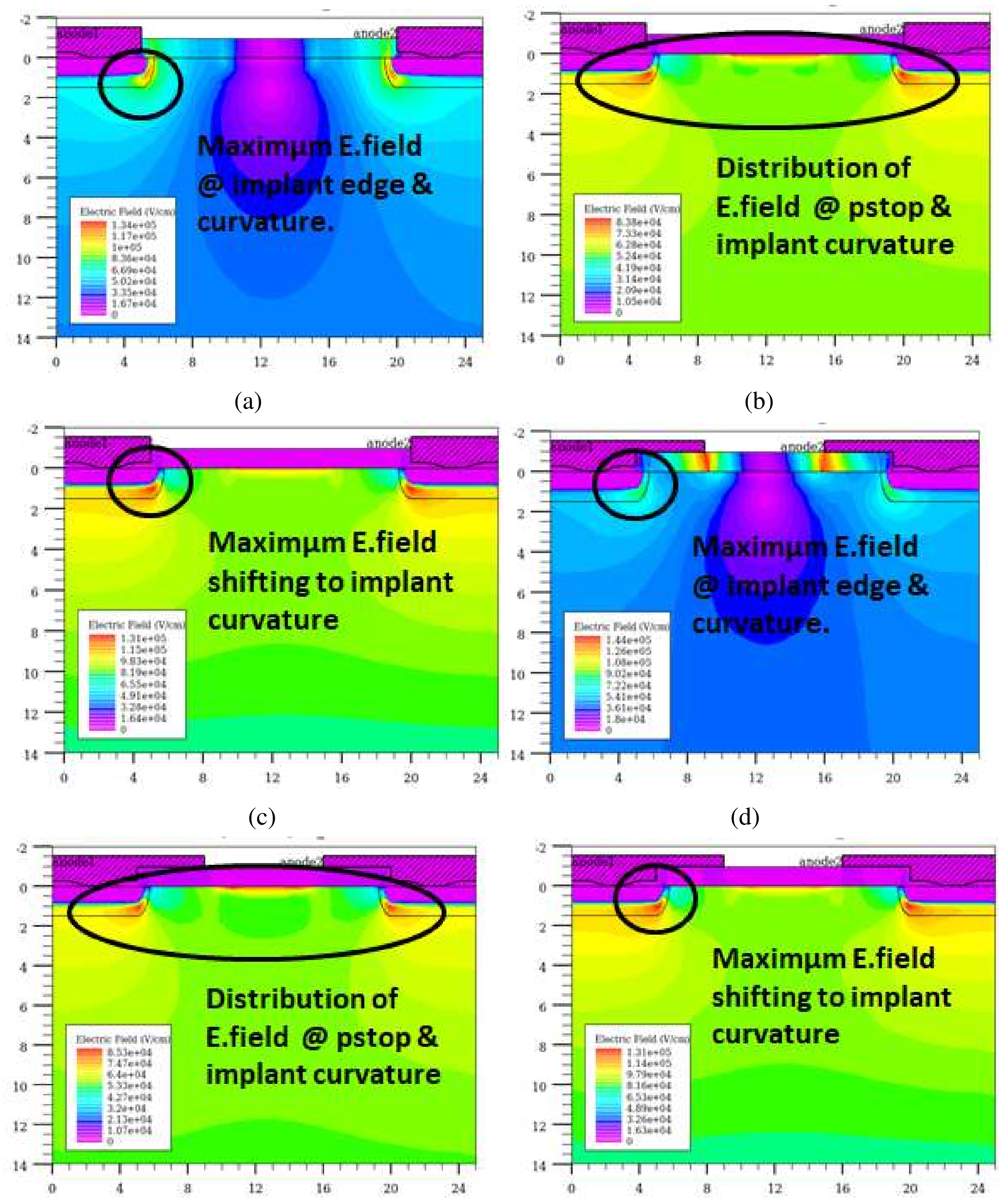

(a) (b) (c) (d) (e) (f)

Figure 6.4: The zoomed view of the 2D electric field contours generated within the detector bulk for fluence values of - (a,b) 0, (c,d) 1×10^{15}, and (e,f) 2×10^{15} $n_{eq} \cdot cm^{-2}$; at a reverse bias voltage of 500 V. The electric field is shown for 2 MO configurations - (a,c,e) 0 and (b,d,f) $4\,\mu m$.

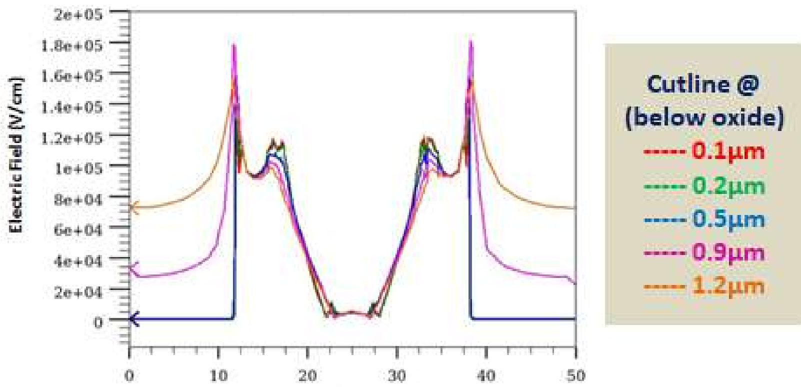

Figure 6.5: The 1D electric field lines at different horizontal cutlines.

ical electric field region, 1D electric field plots were generated at different fluence values by varying MO, p-stop peak doping concentration (N_{pst}), and depth of pstop (D_{pst}) (see Fig. 6.6). A visible shift of the peak electric field from the implant curvature to p-stop curvature and then back to the implant curvature is observed with increasing fluence. It is observed that a MO of $4\,\mu m$ is helpful in significantly reducing the high electric field regions for the non-irradiated pixel. However, it is redundant for irradiated pixels.

The 1D electric field plots along a vertical cutline

The 1D electric field profiles along a vertical cutline are shown in Fig.6.7 through - (a) the p-stop, and (b) the implant curvature. It may be noted that for the non-irradiated case, no electric field is present at the p-stop curvature and a uniform field develops inside the detector bulk. As soon as the pixel is irradiated, the electric field starts rising at both the implant curvature and the p-stop. However, the rise in the electric field at the implant curvature is faster than at the p-stop. In addition to this, the electric field at the backside also rises with increasing fluence. This results in decrease of the electric field in the detector bulk, thereby leading to loss of charge collection.

6.1.4 Identifying best pixel configuration

In Fig. 6.8, the maximum electric field is plotted as a function of fluence for all the 8 designs both with and without metal overhang (MO). It is found that of all the designs, p-stop normal configuration of pitch $25\,\mu m$ and p-spray wide configuration of pitch $50\,\mu m$, have the least increase in electric field with increasing fluence. For these configurations, the

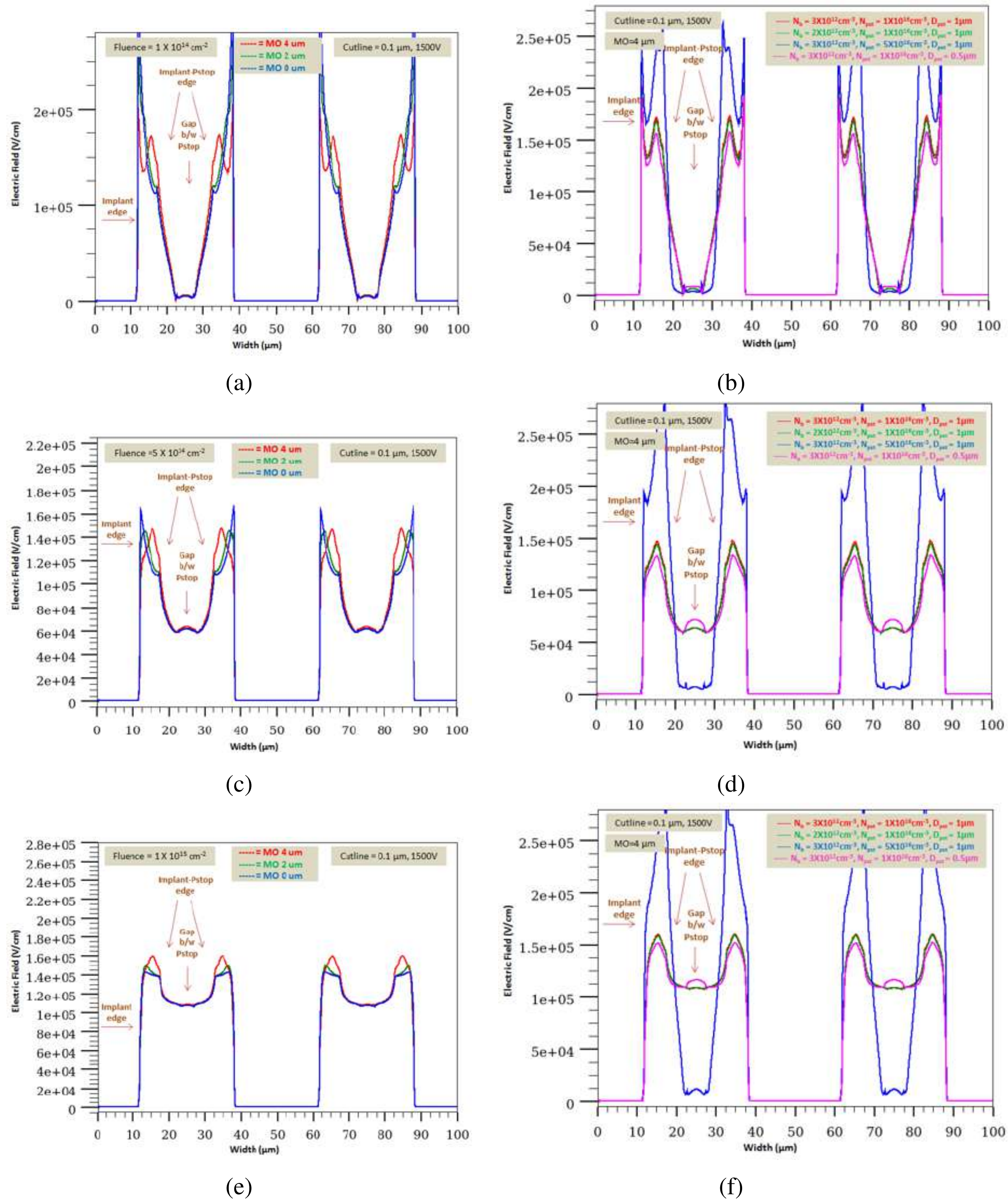

Figure 6.6: The 1D electric field profile through a horizontal cutline of $1.0\,\mu\mathrm{m}$ below the Si-SiO_2 interface is shown for *P-stop Normal* geometry at different fluence values of - (a,b) 1×10^{14} $n_{eq} \times cm^{-2}$, (c,d) 5×10^{14} , and (e,f) 1×10^{15} $n_{eq} \times cm^{-2}$. Additionally, the effect on the developed electric field can be seen as a function of - MO variation in (a,c,e) and N_b, p-stop peak doping concentration (N_{pst}), & depth of pstop (D_{pst}) in (b,d,f).

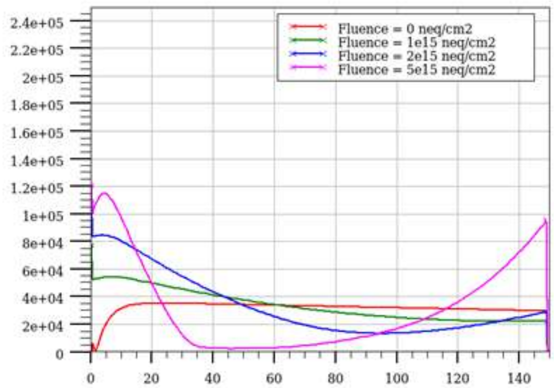

(a)

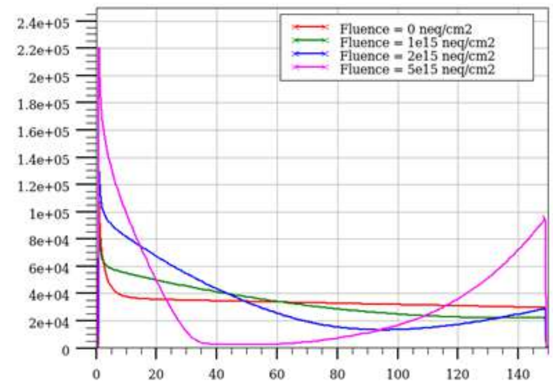

(b)

Figure 6.7: The 1D electric field profile along a vertical cutline into the detector bulk - (a) through p-stop, and (b) through implant curvature.

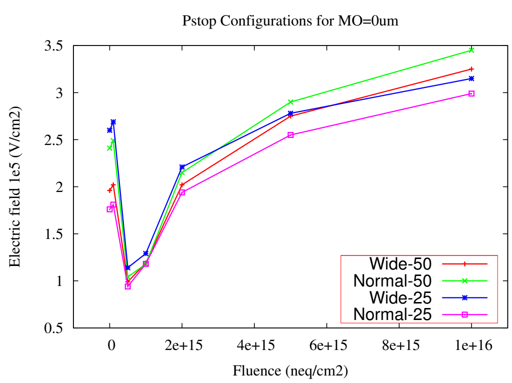

(a)

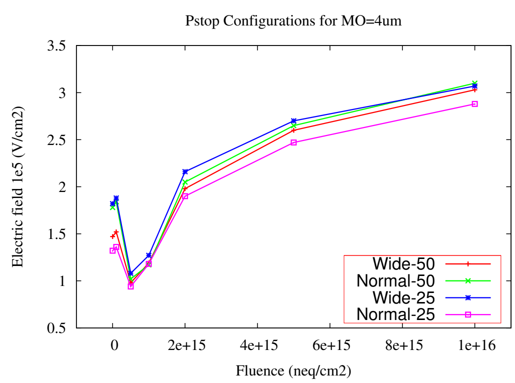

(b)

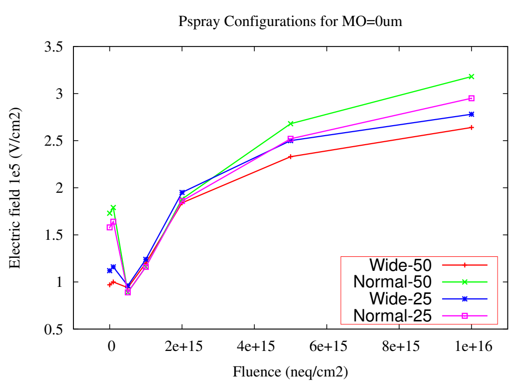

(c)

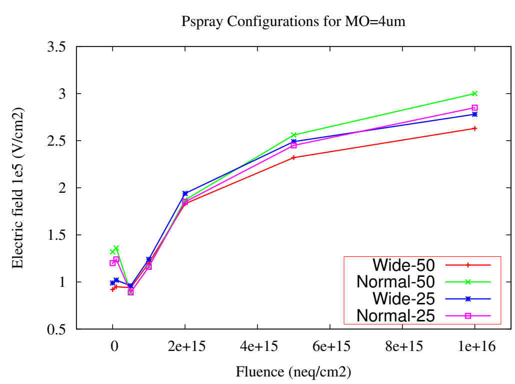

(d)

Figure 6.8: The maximum electric field is plotted as a function of fluence for all the 8 designs with sensor thickness of $200\,\mu m$ at a bias voltage of 1000 V.

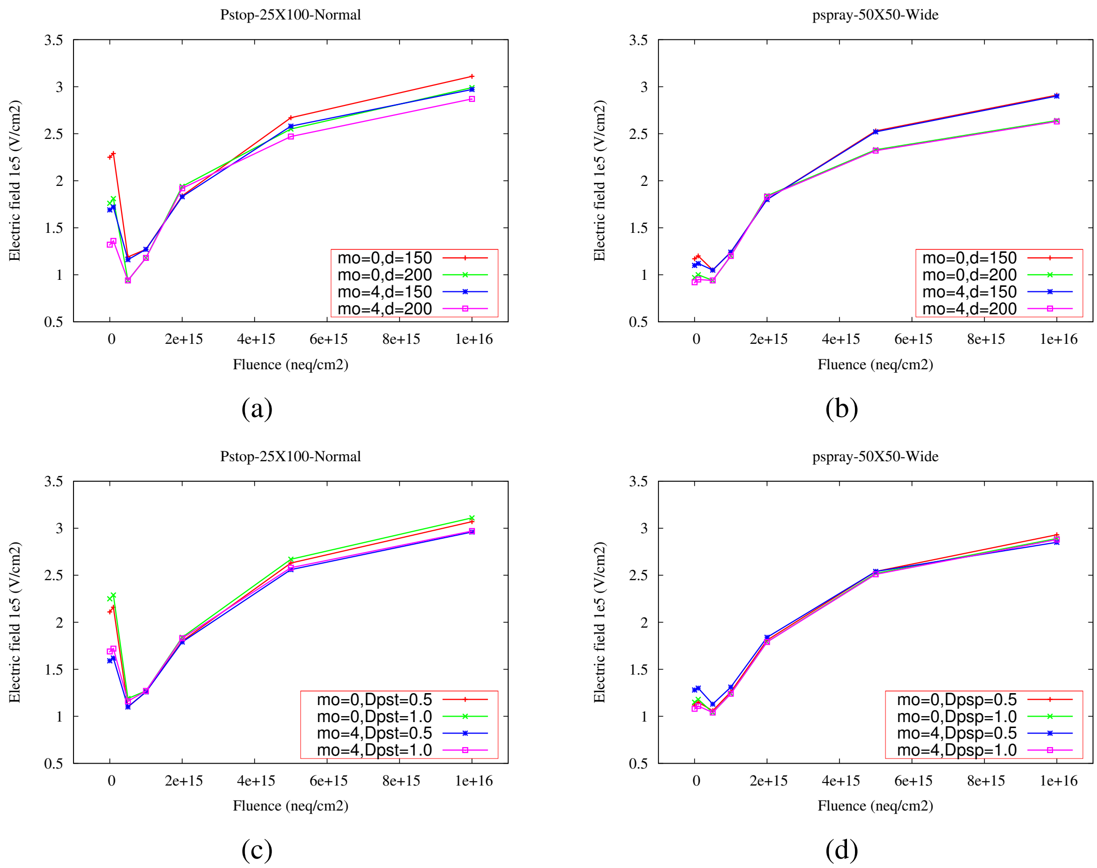

Figure 6.9: The effect of the variation of different geometry parameters is shown for the best p-stop and p-spray designs as concluded from Fig. 6.8. The sensor thickness is varied for constant p-stop/p-spray depth of 1 µm in top plots, whereas the p-stop/p-spray depth is varied for a fixed sensor thickness of 150 µm in bottom plots, with and without MO.

effect of sensor thickness (d) and p-stop/p-spray implant depth ($D_{\text{pst-psp}}$), for a constant p-stop/p-spray concentration ($N_{\text{pst-psp}}$) of 1×10^{16} / 1×10^{15} cm^{-3}, on the maximum electric field for different fluences for structures with and without MO is plotted in Fig. 6.9. It is seen that for p-stop normal configuration of pitch 25 µm the electric field reduces for larger sensor thickness and for the design with a MO of 4 µm. Also, the plot clearly shows that for the same configuration the effect of D_{pst} on the maximum electric field is negligible. On the other hand for the p-spray wide configuration of pitch 50 µm the electric field reduces for larger sensor thickness, but there is no effect of MO. Further, it may be noted that for this configuration the maximum electric field is insensitive to the variation in D_{psp}.

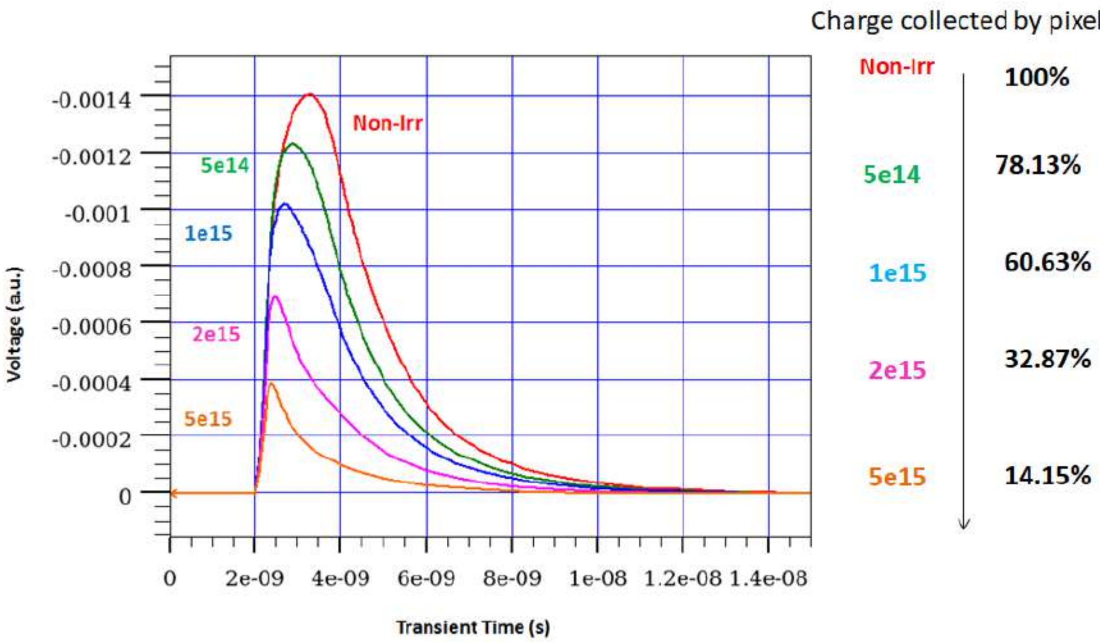

(a)

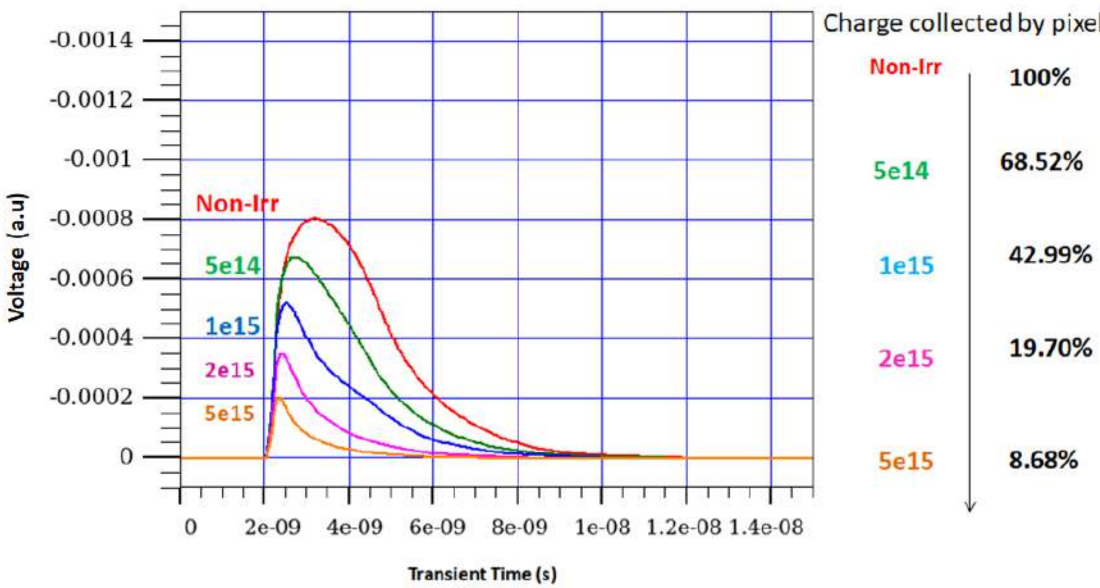

(b)

Figure 6.10: The transient signals generated when a laser is shone at the - (a) pixel centre, and (b) inter-pixel centre; on *P-stop Normal* configuration of detector depth of $150\,\mu\mathrm{m}$ at 500 V.

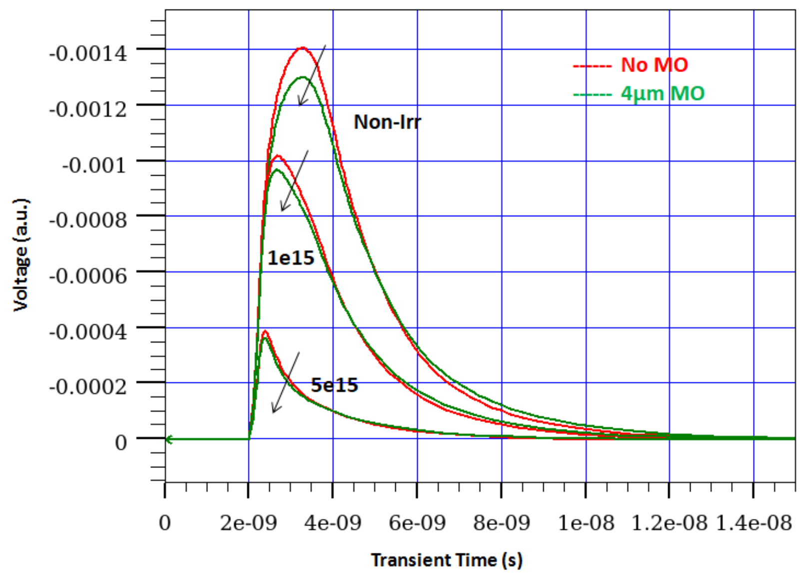

Figure 6.11: The slight decrease in the charge collection with the introduction of MO.

6.1.5 Charge collection

Figs. 6.10a and 6.10b show the developed transient signals in the *P-stop Normal* pixel configuration when infrared laser is shone at two positions - (a) at pixel centre, and (b) at inter-pixel centre. Assuming a 100% charge collection for the non-irradiated case, the CCE is calculated at higher fluences. It is found that while the CCE goes down to 33% when laser is shone at pixel centre, it is lowered to almost 20% when laser is shone at inter-pixel centre for a fluence of 2×10^{15} $n_{eq} \times cm^{-2}$. Further, an introduction of a $4\,\mu m$ MO, further decreases the CC slightly (shown in Fig. 6.11) for *p-stop Normal* configuration when laser is shone at the pixel centre. This is expected because the MO attracts electron charge carriers towards its edge.

6.1.6 3D simulations

In addition to 2D simulations, 3D simulations have also been initiated for the pixel sensors. The 3D pixel structure built in the simulator is shown in Fig. 6.12. On drawing a cutplane along the centre of the YZ plane (see Fig. 6.13, the critical electric field regions as identified in the 2D structure are visible. The leakage current characteristics as shown in Fig. 6.14, display onset of breakdown at a reverse bias voltage of 1500 V.

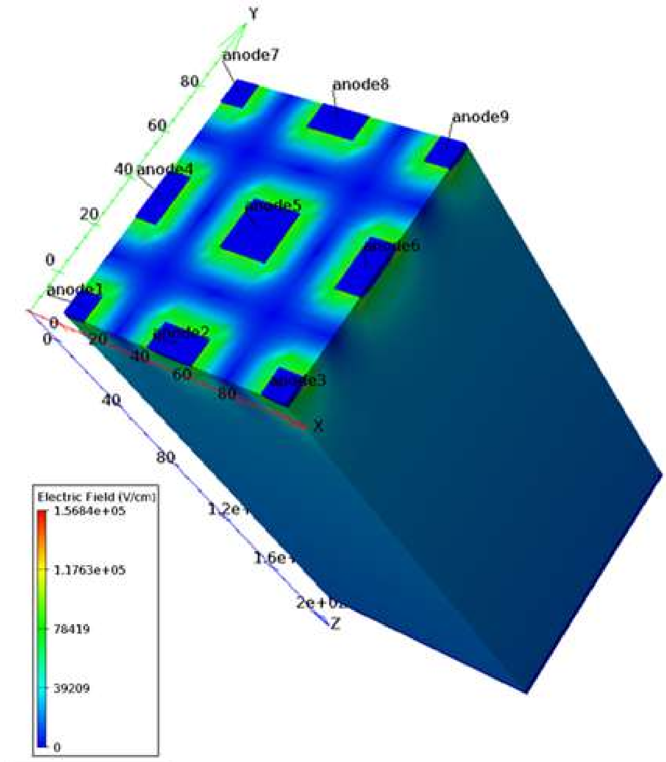

Figure 6.12: The pixel structure built in 3D simulator.

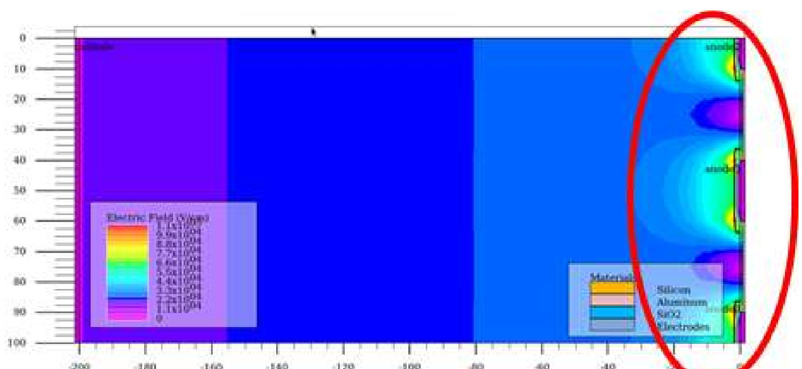

Figure 6.13: The electric field contours along the YZ cutplane.

6.1.7 Summary

2-D simulations have been performed to optimize the pixel sensor design for different configurations. Out of the 8 simulated designs, p-stop normal configuration with pitch $25\,\mu\mathrm{m}$ and p-spray wide configuration with pitch $50\,\mu\mathrm{m}$ are found to be the most radiation tolerant. The optimized set of parameters is : d = 200 μm with a p-stop/p-spray depth of 1 μm and

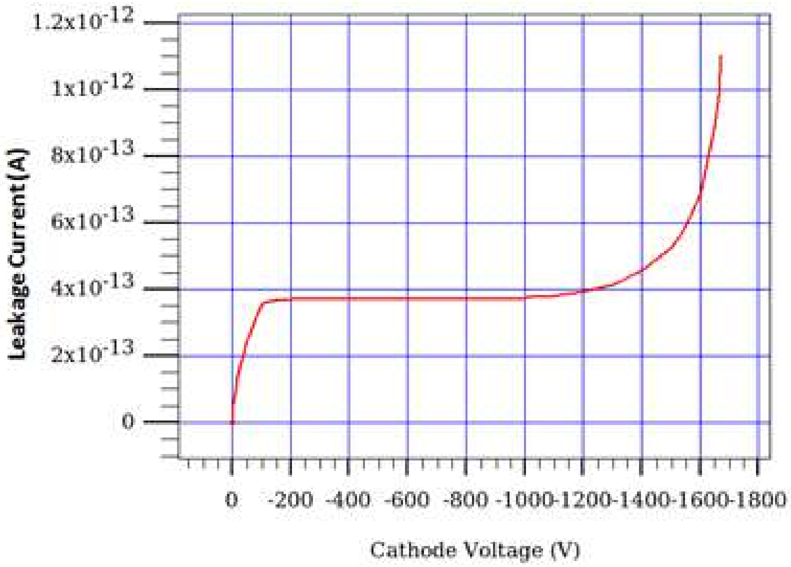

Figure 6.14: The non-irradiated leakage current characteristics for the 3D pixel structure.

a MO of 4 μm. A detailed measurement study on the charge collection efficiency is also needed to finalize the layout parameters.

6.2 Study of trapping probability

In HEP experiments, prolonged exposure to radiation flux leads to radiation damage in the silicon sensors. This causes increase in I_{tot}, change in V_{fd} and also charge carrier trapping, resulting in loss of CC and hindering particle detection operation [139]. The probability of a charge carrier to get trapped is given by the effective trapping probability, i.e., inverse of effective trapping time (τ_{eff}).

6.2.1 The method used

Since τ_{eff} is not a directly measurable quantity, it can be estimated using an exponential term method described in [140]. In this method, the laser based characterization technique - the TCT is used to generate a time evolved carrier signal, also called the TCT signal. The integration of the TCT signal within a certain time window gives CC. Due to the charge trapping, CC decreases by an exponential trapping term, exp(-t/τ_{eff}), with increasing fluence. To compensate for the trapping, the TCT signal is corrected by introducing an exponential term, exp(t/τ_{r}), where τ_{r} is trapping time. The value of τ_{r} is varied to determine

τ_{eff} as a function of bias voltage, such that for $\tau_r = \tau_{\text{eff}}$, CC is independent and becomes constant (after the full depletion voltage), for a particular fluence.

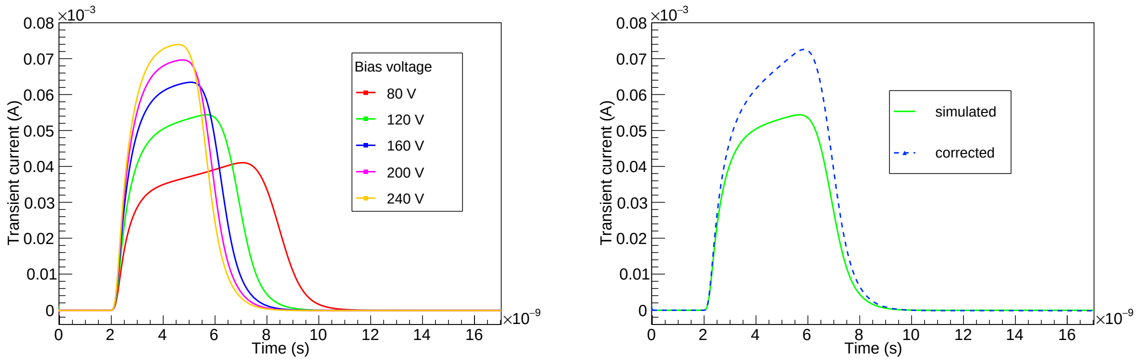

(a) (b)

Figure 6.15: TCT signal; (a) simulated at five different bias voltages, and (b) overlap of simulated and corrected for τ_r = 20ns, at 120V; for fluence = $3\times10^{13} n_{\text{eq}}\cdot\text{cm}^{-2}$.

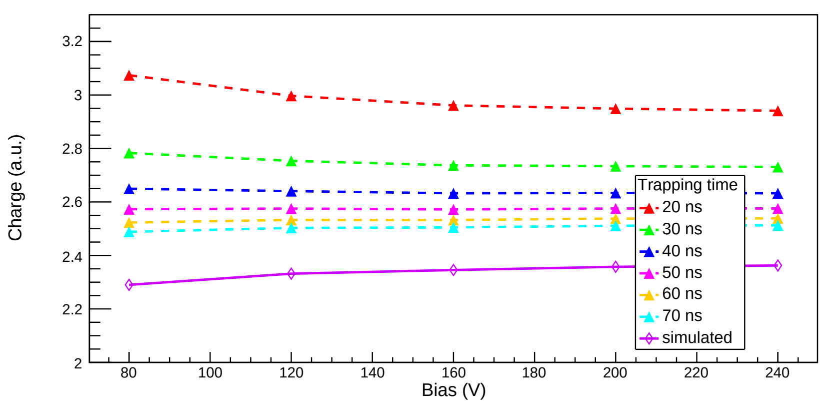

Figure 6.16: The simulated and corrected charge vs voltage plot for different values of τ_r for fluence of $3\times10^{13} n_{\text{eq}}\cdot\text{cm}^{-2}$.

6.2.2 Simulated and corrected TCT signals

A similar procedure as described in the above section was carried out using TCAD device simulation tool. The silvaco software was used to generate TCT simulations at different voltages on proton irradiated silicon pad detectors [141]. The pad detectors were chosen to be p-on-n type with $15\,\text{k}\Omega\cdot\text{cm}$ resistivity and $285\,\mu\text{m}$ thickness.

The TCT signal, at different bias voltages, is shown in Fig. 6.15a as a function of time, for fluence value of $3\times10^{13} n_{\rm eq}{\cdot}{\rm cm}^{-2}$. Similar TCT signals are generated at different fluence values. Next, by choosing different values of $\tau_{\rm r}$, corrected TCT signals are generated. An example of the corrected TCT signal at 120 V is shown in Fig. 6.15b, for a value of $\tau_{\rm r}$ equal to 20 ns.

6.2.3 Calculating trapping time probability

CC is plotted for various $\tau_{\rm r}$ as a function of bias voltage as shown in Fig. 6.16. It is observed that CC decreases for small $\tau_{\rm r}$ and increases for large $\tau_{\rm r}$, with increasing bias voltage. Accordingly three cases are envisaged - (i) if $\tau_{\rm r} < \tau_{\rm eff}$, this will cause incomplete correction of trapping; (ii) if $\tau_{\rm r} > \tau_{\rm eff}$, this will lead to more correction than what is required; and (iii) if $\tau_{\rm r} = \tau_{\rm eff}$, a complete and exact correction is accounted.

Hence, the slope of the linear fit for the plots is calculated. It is observed that the slope as a function of $\tau_{\rm r}$ changes polarity (shown in Fig. 6.17a) from negative to positive, according to the three cases as mentioned above. The value of $\tau_{\rm r}$ at which the curve intercepts the x-axis, i.e. when the slope goes to 0, is that value of $\tau_{\rm r}$ for which CC is independent and becomes constant as a function of bias voltage and hence equal to $\tau_{\rm eff}$, for that fluence.

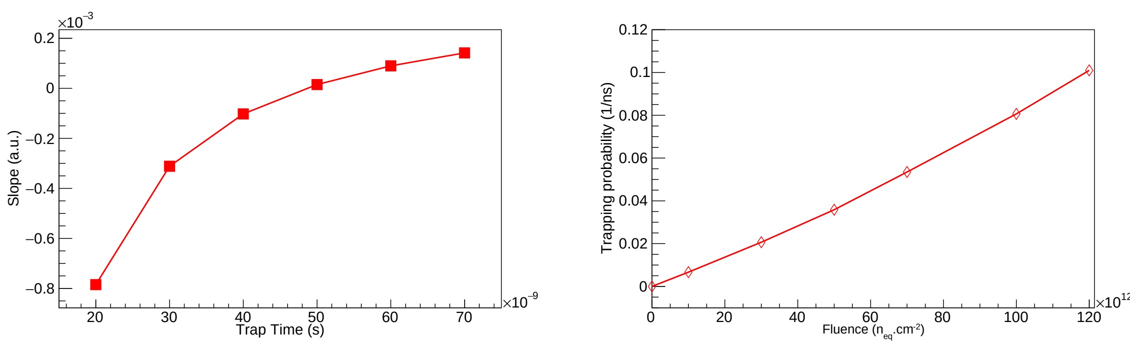

(a) (b)

Figure 6.17: (a) The slope of the linear fit to the corrected charge for the plot in Fig.2 as a function of $\tau_{\rm r}$. (b) The effective trapping probability as a function of fluence.

The above procedure is repeated for different values of the fluence to obtain $\tau_{\rm eff}$. Fig. 6.17b shows the effective trapping probability plot as a function of fluence. Using a linear fit of the form $1/\tau_{\text{eff}} = \beta \cdot \phi$, the value of β is found to be equal to $6.66\times10^{-16}\, n_{\text{eq}}^{-1}\cdot\text{cm}^2\cdot\text{ns}^{-1}$. This is close to the value $4.2\times10^{-16} n_{\text{eq}}^{-1}\cdot\text{cm}^2\cdot\text{ns}^{-1}$ as reported in the Ref. [140].

6.2.4 Future outlook

Further studies are envisaged at higher values of fluence, different detector depths, substrate resistivities, and also for p-type substrates. The effect of temperature on the effective trapping probabilities will also be investigated.

6.3 Low bulk resistivity silicon sensors

Silicon sensors owing to their better position resolution and robustness, are placed close to the collision point and hence are widely used as tracking and vertexing elements. However, it is observed that they suffer a drastic degradation in the charge collection efficiency with increase in fluence (see simulated result in Fig. 6.18) [142–145]. Even the thin detectors, with a less charge trapping probability are unable to survive. The future HEP experiments are expected to have even harsher radiation environment. Thus, it is mandatory to develop new silicon sensor technology, where the new design must be such that it can collect a reasonable charge even at higher fluences.

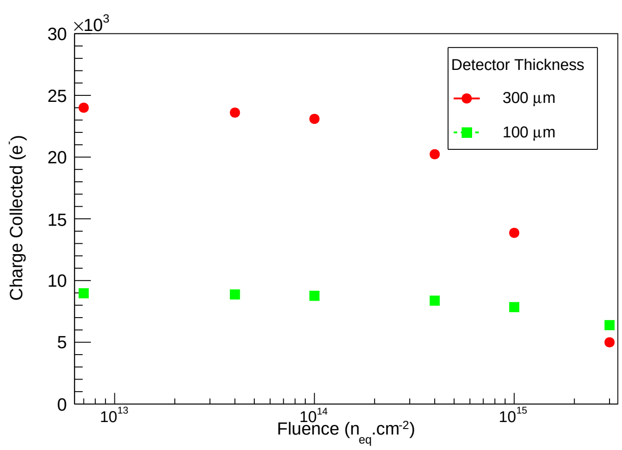

Figure 6.18: Charge collected in a traditional low bulk substrate doping concentration ($N_b = 1 \times 10^{12}$ cm^{-3}).

One of the possible candidates for such a requirement can be a 'low resistivity or high substrate bulk doping concentration (N_b) silicon sensors. When the sensor is biased to a sufficient voltage, it results in a localized high electric field due to the formation of a strong frontside pn junction. The charge carriers generated by the particle crossing the sensor are multiplied when they reach the high electric field region while moving towards the electrodes. Thus, a large CC is obtained as a result of multiplication.

6.3.1 Simulation study on low resistivity bulk

Silvaco is used to investigate the radiation hardness of thin and low resistivity bulk silicon detectors. The device is a n-on-p type in plane parallel diode configuration with a cross-section of $80\,\mu m^2$ with n^+ implant peak doping concentration of 1×10^{19} cm^{-3}. All simulations are performed at a temperature of 253 K. The radiation damage effect is incorporated using 2 trap proton damage model [74].

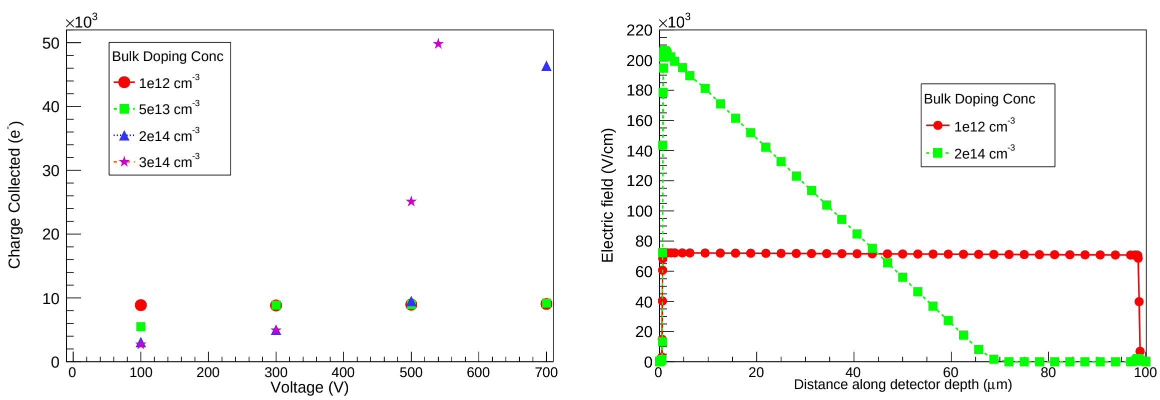

(a) (b)

Figure 6.19: (a) Charge collected as a function of bias voltage for varying N_b. (b) Electric field profile at a bias voltage of 500 V.

6.3.2 Charge collection of a non-irradiated detector

The behaviour of the charge collection as a function of bias voltage for a non-irradiated thin (100 μm) silicon detector with varying N_b is shown in Fig. 6.19a. It may be noticed that for small operating voltage, the high N_b substrates (2×10^{14} and 3×10^{14} cm^{-3}) hardly collect any charge. This is due to the negligible electric field in the detector bulk leading to non-transfer of the generated charge carriers. However, after a certain bias voltage, the frontside electric field peak, allows for charge multiplication to occur. Thus, a significant increase in the charge collection is observed. The electric field profiles can be seen in Fig. 6.19b).

6.3.3 Breakdown performance

The breakdown performance study has been performed for substrate with $N_b = 3 \times 10^{14}$ cm^{-3} as a function of increasing fluence to determine the operating voltage of the detector. It can be concluded from the IV characteristics depicted in Fig. 6.20 that the detector experiences an increase in the current beyond 550 V. So, a bias voltage of 500 V can be securely chosen as the operating voltage.

Premature breakdown is due to crowding of electric field lines. Hence, several peripheral structures (Guard ring GR and Junction Termination Extension JTE) were used to re-distribute the electric field lines so that the V_{BD} increases (see Fig. 6.21). The structure shown in Fig. 6.22 is used to simulate the breakdown characteristics. It may be noted that the structure is $100 \times 50 \times 1\,\mu m^3$ in dimensions. A half-implant distance (width) d_{IM} of $20\,\mu m$ and GR distance d_{GR} of $12.5\,\mu m$ is chosen. The GR is considered as the JTE when d_{GR} is taken to be zero.

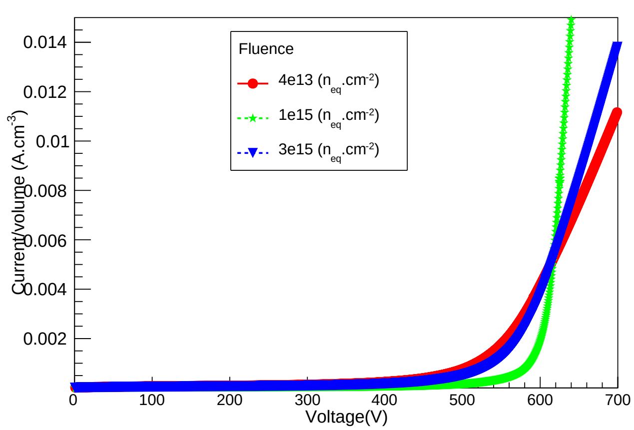

Figure 6.20: IV characteristics for silicon sensors with $N_b = 3 \times 10^{14}$ cm^{-3} at different fluence values.

The breakdown performance has been studied for depth and width variation of GR and JTE peripheral structures with respect to the unprotected low bulk resistivity substrate.

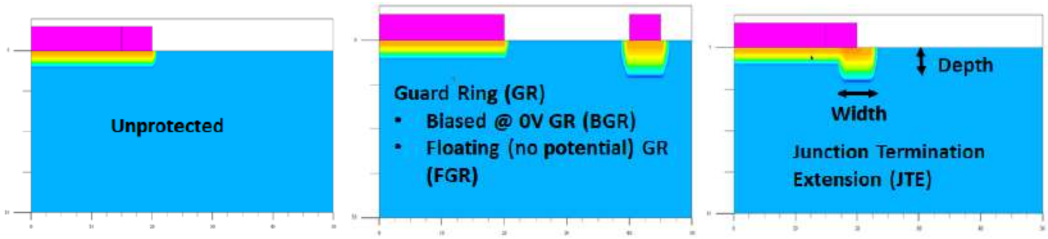

(a) (b) (c)

Figure 6.21: (a) No peripheral structure (unprotected), (b) Guard ring peripheral structure in two configurations - biased at 0 V (BGR) and floating, i.e. at no potential (FGR), and (c) Junction Termination extension structure (JTE).

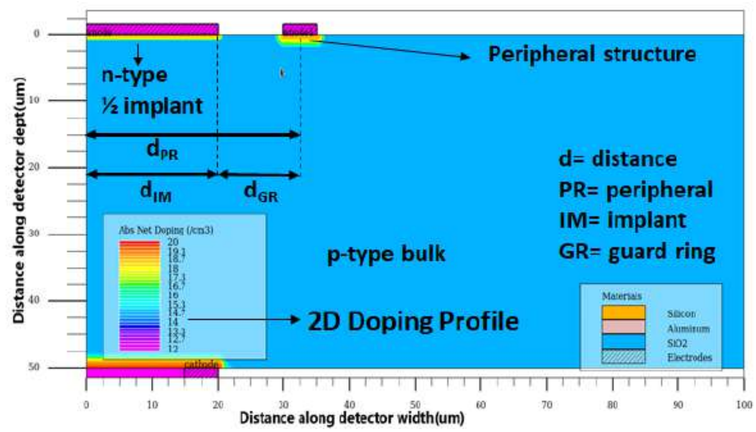

Figure 6.22: The structure used for simulating the breakdown performance.

- **Depth variation**: A depth variation of 2, 4 and 6 µm has been used to look at the IV characteristics for all the peripheral structures (see Fig. 6.23). It is found that V_{BD} increases with increase in the depth of all the three peripheral structures studies in comparison with an unprotected structure. Furthermore, the improvement in V_{BD} is maximum for FGR, followed by BGR and then JTE.

- **Width variation**: Since JTE shows the least benefit in increase of the V_{BD}, the width variation is performed for BGR and FGR to observe additional improvement if any (see Fig. 6.24). V_{BD} increases for increase in width for both BGR and FGR, with FGR displaying higher V_{BD}.

The better V_{BD} exhibited by the FGR can be understood by the electric field profile developed within the structure. Fig. 6.25 shows 1D electric field along the detector depth for an unprotected, BGR, and FGR structures. It is understood that the unprotected device breaks

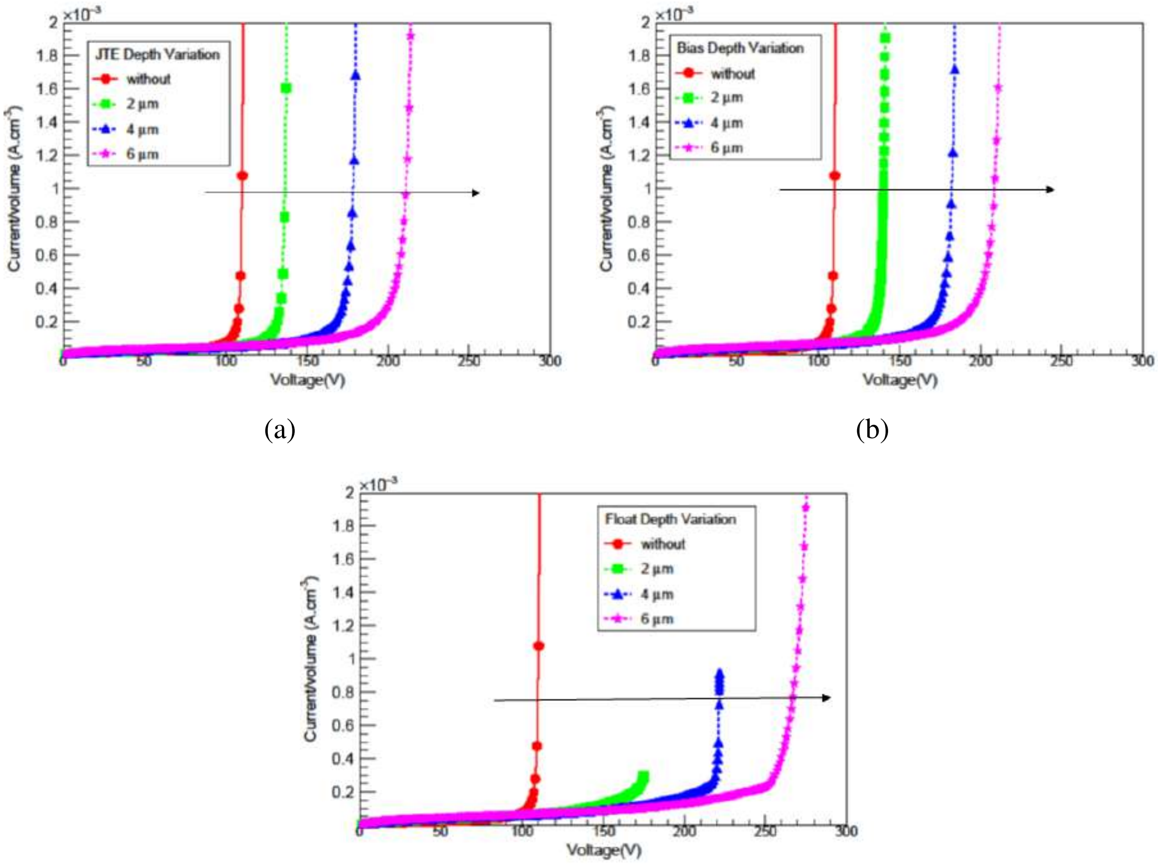

(c)

Figure 6.23: IV characteristics for - (a) JTE, (b) BGR, and (c) FGR, for a depth variation of the peripheral structures.

due to high electric field at its implant curvature. However, for the BGR, the breakdown occurs at the GR curvature. The reason for FGR showing the best breakdown performance is that the electric field lines extend towards the GR, thereby decreasing the crowding of lines at the implant curvature.

6.3.4 Charge collection

The charge collected is plotted as a function of fluence for silicon sensors with $N_b = 3 \times 10^{14}$ cm^{-3} for detectors of different thicknesses and is shown in Fig. 6.26. It is noticed that the collected charge decreases, then increases, before gradually decreasing, which is a typical characteristic of high N_b substrates [146]. The thin detector seems to be collecting

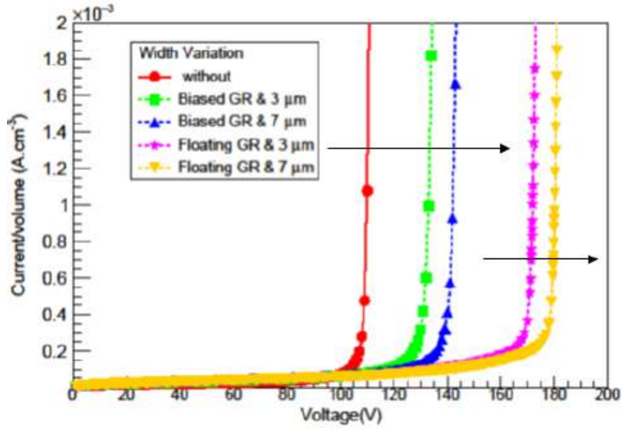

Figure 6.24: IV characteristics for BGR and FGR; for width variation of the peripheral structures.

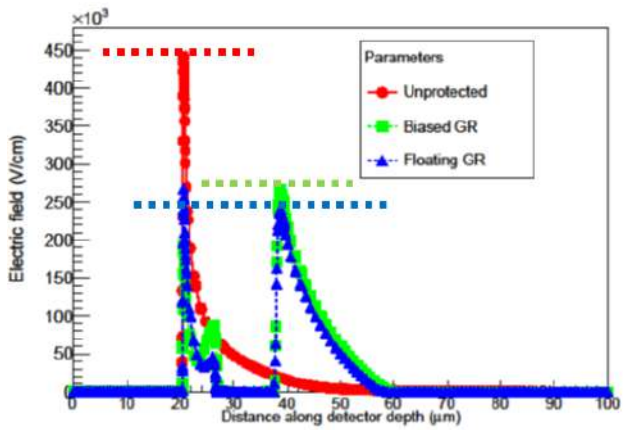

Figure 6.25: The electric field profile at a reverse bias voltage of 200 V.

higher charge over the thick detector. Thus, in this first performance comparison thin and high N_b substrates seem better candidates for radiation hardness than low N_b and thick detectors.

6.3.5 Summary

In this work, simulation studies of highly doped silicon detectors with respect to thickness and radiation hardness (for proton damage) are presented. The authors find that thin and highly doped substrates are more radiation hard than thicker or less doped substrates for the reported values of resistivities and bias voltage. It is important to investigate the results,

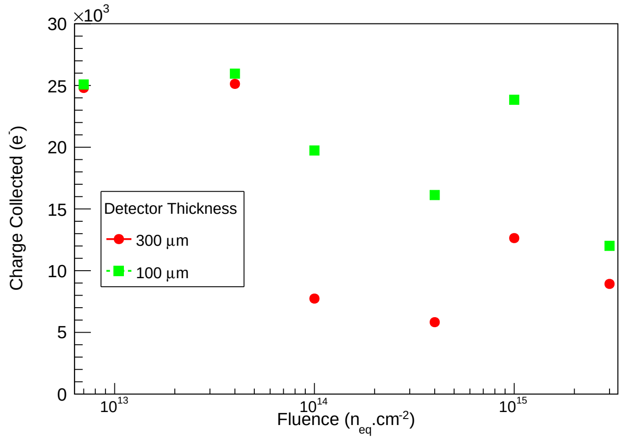

Figure 6.26: Charge collected in a thick and a thin high N_b irradiated detector.

in future, for different bias voltages, and for neutron damage.

6.4 Discussion

Radiation hard simulations have been performed on pixel detectors and low resistivity bulk silicon substrates using the proton radiation damage Delhi model. The radiation damage model has further been validated through calculation of the trapping probability and by comparison with the experimentally obtained value.

Chapter 7

Summary and Future Outlook

This thesis presents the results of the characterization studies performed on silicon strip sensors fabricated at BEL, Bangalore, development of silicon sensor hardware facility for sensor quality check and radiation hard study of novel sensor designs through Technological Computer Aided Design (TCAD) simulations. The 2D TCAD device simulations were performed using the Silvaco [69] simulator. The simulations were aimed at understanding and optimizing the designs of Low Gain Avalanche Detector (LGAD), pixel detectors, and low resistivity substrate silicon detectors. The parametrization of bulk and surface proton radiation damage model developed in Ref. [74] was used to simulate radiation damage.

7.1 Characterization of silicon strip sensors

An indigenous AC-coupled, poly-silicon biased, p-on-n, silicon strip sensor development was carried out at DU. The sensors were fabricated on 4-inch wafers at the BEL, and then characterized at DU and KIT facilities. A set of electrical measurements, consisting of both bulk and strip parameters, have been identified and performed on the fabricated non-irradiated and irradiated sensors.

It may be concluded from the non-irradiated characterization that the fabrication process shows good control of the parameters governing poly-silicon deposition, R_{int} and C_{int}. Although we observe some issues with the gradual increase of the I_{tot} beyond 300 V, the BEL fabricated sensors qualify most of the specifications as listed in Table 3.2. Further, a better control on the processing is desired to achieve < 1 % bad strips criterion. On the basis of pinholes, about 2-14 bad strips per sensor are found in the measurement.

The electrical characterization tests and CC studies on irradiated sensors show that increase in I_{tot} with fluence is consistent with literature. The strip scans of all the strip parameters demonstrate an excellent homogeneity over the sensors even after irradiation. The strip parameters - R_{poly}, C_{coup}, C_{int}, and I_{diel}, show only a moderate change with irradiation. As expected, a significant increase in I_{leak} and decrease in R_{int} is observed with increasing fluence. The CC falls to approximately 75 %, 64 %, and 50 % for fluence values of 1×10^{14}, 5×10^{14}, and 1×10^{15} $n_{eq}\cdot cm^{-2}$ respectively, assuming a 100 % CC for the non-irradiated case.

Although very high radiation tolerance is not achievable with this technology, overall the results are very encouraging and shows that AC-coupled silicon sensors developed on 4 inch wafers in India has laid a foundation for the technology and a path for sustainable development of radiation hard sensors in India.

Further, to improve the breakdown performance of strip sensors, measurements on diodes with different GR spacing were performed and a maximum breakdown voltage of 350 V is measured at an optimized GR spacing of $30\,\mu m$. Measurements on diodes having different number of GRs are also done and it is observed that on increasing the number of GRs, breakdown voltage increases. Also, MOS measurements reveal the value of N_{ox} equal to 0.97×10^{11} cm^{-2} approximately.

As for future outlook, n-in-n sensors have been sent for fabrication at BEL. These will be characterized using different isolation configurations and tested for radiation hard environment. Simulation studies have been carried out to determine the optimized parameters of the isolation structures [147].

7.2 Development of silicon sensor hardware facility

Several characterization setups were installed and commissioned to monitor the quality and behaviour of the fabricated silicon sensors. The hardware facility consists of a multi-strip characterization setup and a red laser transient current technique (TCT) setup.

The multi-strip characterization setup consists of a probe station, set of four electrical instruments (a high voltage SMU, a dual channel low voltage SMU, a LCR meter, and a switching matrix) and a compressed dry air (CDA) facility. The system is capable of performing 2 global and 6 strip parameter measurements, namely total leakage current (I_{tot}, backplane capacitance (C_{tot}), strip leakage current (I_{strip}), poly-silicon resistance (R_{poly}), interstrip capacitance (C_{int}), interstrip resistance (R_{int}), coupling capacitance (C_{coup}), and dielectric current (I_{diel}). The integration and installation of the system is discussed in detail in this thesis. The commissioning of the system at DU was carried out and cross-calibration of measurement results is performed with the measurements on KIT system. DU is actively participating in upgrades and commissioning of the CMS outer tracker detector. The upgrade work involves the sensor qualification of the 2S multi-strip sensors. After a formal certification, the DU probe characterization system will be utilized for this purpose. This development of a Sensor Qualification Centre (SQC) for the testing of the radiation hard silicon sensors is an indigenous effort by the experimental HEP group at DU and is for the first time in the country.

In addition to the static characterization system, a dynamic characterization system - the red laser TCT setup was also developed. The details of the operation of the setup, interfacing with the software, analysis techniques, etc. are reported in this thesis. TCT measurements performed on few silicon pad sensors are also shown.

7.3 Radiation hard design of LGADs

A LGAD device is a n-on-p silicon sensor, with an additional p-type implantation layer, called p-well, just below the n^+ implant and diffused into the p-type substrate. It is a suitable candidate for high fluence environment, considering its ability to cause local avalanche when operated in reverse bias mode. Since the avalanche is controlled, it leads to internal charge multiplication and thereby, a sufficiently high particle signal.

For the LGAD device, the simulation predictions provide a reasonable qualitative description of both the non-irradiated and the irradiated behaviour. It has been emphasized that the gain of the non-irradiated LGAD devices is strongly influenced by the overall doping profiles of the p-well and the n^+ implantations. The (N_p, d_p) parameter space of (8.75 -

10.25×10^{16} cm^3, 5.5 - 7.1 mm) and (N_n, d_n) parameter space of (0.9 - 1.1 $\times$ 10^{18} cm^3, 4.0 – 4.6 mm) was studied for the non-irradiated case. It has been found that within the parameter space studied, a minimum p-well dose is required to achieve the desired gain, however, beyond that dose, a combination of high implant diffusion depth and low peak doping concentration of the p-well provides higher gain. Additionally, the effect of detector thickness (thick = $300\,\mu m$) and thin = $50\,\mu m$) on the behaviour of gain was studied. The charge collection for a thin LGAD device with similar p-well characteristics as that of a thick LGAD device is smaller due to reduced active volume and hence less primary charges generated from the interactions. Nevertheless, it is worth noting that the charge collection for the thin LGAD device with medium gain (N_p = 9.75 $\times$ 10^{16} cm^3) is comparable to the charge collection of the thick LGAD with low gain (N_p = 8.75 $\times$ 10^{16} cm^3), at a bias voltage of 150 V.

The incorporated radiation damage model successfully explains the decrease in gain of the LGAD devices with an increase in proton fluence, as observed in measurements. It may be interesting to note that the gain simulation for irradiated LGAD structures is carried out without changing the acceptor concentration inside the p-well region. The gain variation with fluence seems to be due to the traps effect only, which is further corroborated using the electric field, leakage current and effective space charge density of the irradiated LGAD devices. It has been found that the space-charge density of the sensor bulk and the p-well regions change in a way such that the sensor bulk becomes effectively donor type after irradiation. Hence, these simulations provide another plausible explanation for the lowering of the gain as opposed to incorporation of only acceptor removal mechanism [130].

Although the thick irradiated LGADs also show a higher charge at low fluences, the rate of decrease in charge collection is steeper in thick LGADs as compared to thin LGADs. In fact, at the highest simulated fluence, the thin devices exhibit a better performance than thick devices.

Since the charge collection of the detector is a combined function of N_b and N_p, the charge collection as a function of N_b was also studied for the irradiated case. The study shows that an increase in N_b results in a stronger electric field for a constant value of N_p and hence a higher charge collection. However, for a constant N_b, the charge collection first increases and then decreases as N_p is increased. Thus, it may be concluded that a thin and a low resistivity LGAD substrate with an appropriate choice of p-well concentration can be made to achieve a reasonably large charge collection at a high fluence of upto 3.0 $\times$ 10^{15} $n_{eq} \cdot cm^{-2}$.

7.4 Studies on pixel and low bulk resistivity sensors

The radiation hard simulation studies were carried out on pixel detectors under the CMS collaboration. The effect of various design parameters are studied for the non-irradiated and the irradiated pixel sensors.

Radiation hard simulations were carried out on two n-on-p planar pixel sensor geometries, 50 $\times$ $50\,\mu m$ and 100 $\times$ $25\,\mu m$, for two wafer thicknesses (d) of $150\,\mu m$ and $200\,\mu m$. The effect of various design parameters like pixel size, pixel depth, implant width, metal overhang, p-stop concentration, p-stop depth and bulk doping density on the leakage current and critical electric field are studied for both non-irradiated as well as irradiated pixel sensors.

It was noticed that the MO is effective in improving the electric field profile at small fluence values only, after which the use of MO is redundant. The critical electric field regions were found to lie at the implant edges and its curvature, for small fluence values and at only implant curvature for high fluence values. The electric field at the implant edges decreases and the field between the 2 adjacent pixels starts growing, until they are at the same value with increase in fluence. With further increase in the fluence, they grow together. The *P-spray Wide* configuration shows the least increase in the electric fields at 1500 V for small fluence. At high fluence, all the configurations seem to be equivalent in terms of critical electric field regions. For all the configurations, while there is no effect in the electric field with the change in the bulk doping concentration, there is an increase in the critical electric field with increasing concentration of p-stop or p-spray. For the four p-spray configurations, there is no effect in the electric field with the change in the p-spray depth. However, for p-stop configurations, with decrease in the depth of p-stop, the electric field reduces slightly at the implant-p-stop edges and grows slightly between the p-stop gaps.

Owing to better ability for higher CC efficiency and internal charge multiplication, low bulk resistivity or, high bulk doping density (10^{13} - 10^{14} cm^{-3}) silicon sensors have been studied in this thesis. A systematic TCAD simulation study for the effect of proton fluence (up to 3×10^{15} $n_{eq}.cm^{-2}$) on p-type silicon pad diodes of varied thicknesses is reported.

The irradiated simulation study was performed on low bulk resistivity silicon sensors with respect to variation in thickness. It was observed, in the studied phase space, that thin and low bulk resistivity substrates are radiation harder than thick or high bulk resistivity substrates. Nevertheless, it is important to investigate the results, in future, for different bias voltages, and for neutron damage.

This work provides a useful insight into the working of devices - pixel detectors and low resistivity substrate silicon detectors. However, further simulation and experimental results are needed to understand and utilize the potential of these devices in the future high energy physics experiments.

7.5 Conclusion

The research work carried out on the development of the AC-coupled, poly-silicon biased silicon sensors and establishment of characterization laboratory at DU has laid a foundation for future advancements of the silicon sensor instrumentation technology in India. The radiation hardness simulation studies on LGAD, pixel, and low resistivity silicon sensors has provided useful inputs for the development of novel sensor technology for high luminosity HEP experiments.

Bibliography

[1] J. Dalton. *On the Absorption of Gases by Water and Other Liquids*, Memoirs of the Literary and Philosophical Society of Manchester (1803).

[2] J. J. Thomson. *On bodies smaller than atoms*, The Popular Science Monthly (1901) 323335.

[3] E. Rutherford. *The scattering of α and β particles by matter and the structure of the atom*, Philosophical Magazine (1911) 669688.

[4] J. Chadwick. *Nobel Lecture: The Neutron and Its Properties*, Nobel Foundation (1935).

[5] R. Oerter. *The Theory of Almost Everything: The Standard Model, the Unsung Triumph of Modern Physics*, Penguin Group **2** (2006).

[6] D. Griffiths. *Introduction to elementary particles*, Wiley-Vch Verlag GmbH & Co. KGaA, Weinheim (2004).

[7] J. Kemmer, et al. *Development of* $10\,\mu\mathrm{m}$ *resolution silicon counters for charm signature observation with the ACCMOR spectrometer*, Proceedings Silicon Detectors For High Energy Physics (1981) 195.

[8] J. T. Walker, et al. *Development of High Density Readout for Silicon Strip Detectors*, NIM A **226** (1984) 200.

[9] C. Adolphsen, et al. *The Mark-II silicon strip vertex detector*, NIM A **313** (1992) 63.

[10] SLAC National Accelerator Laboratory. https://www6.slac.stanford.edu/.

[11] N. Bingefors, et al. *The DELPHI microvertex detector*, NIM A **328** (1993) 447471.

[12] D. Creanze, et al. *The new ALEPH silicon vertex detector*, NIM A **409** (1998) 157160.

[13] S. Anderson, et al. *The extended OPAL silicon strip microvertex detector*, NIM A **403** (1998) 326350.

[14] M. Acciarri, et al. *The L3 silicon microvertex detector: Installation and results on 1993 performance*, NIM A **360** (1995) 103109.

[15] T. Altonenen, et al. *Operational experience, improvements, and performance of the CDF Run II silicon vertex detector*, NIM A **729** (2013) 143.

[16] J. Fast, et al. *The D0 silicon detector for run IIb at the Tevatron*, NIM B (2003) 352.

[17] D. Bortoletto. *How and why silicon sensors are becoming more and more intelligent?* JINST **10** (2015).

[18] CERN Homepage. http://public.web.cern.ch/public/en/about/abouten.html.

[19] T. S. Virdee. *The lhc project: The accelerator and the experiments*, NIM A 623 (2010) 110.

[20] L. Evans and B. Bryant (editors). *LHC Machine*, JINST **3** (2008) S08001.

[21] CERN Document Server (CDS), OPEN-PHO-ACCEL-2016-013. https://cds.cern.ch/record/2225847.

[22] The ALICE Collaboration. *The ALICE experiment at the CERN LHC*, JINST **3** (2008) S08002.

[23] The LHCb Collaboration. *The LHCb Detector at the LHC*, JINST **3** (2008) S08005.

[24] ATLAS Collaboration. *The ATLAS Experiment at the CERN Large Hadron Collider*, JINST **3** (2008) S08003.

[25] CMS Collaboration. *The CMS experiment at the CERN LHC*, JINST **3** (2008) S08004.

[26] ATLAS Collaboration. *Observation of a new particle in the search for the Standard Model Higgs boson with the ATLAS detector at the LHC*, Phys. Lett. B **716** (2012) 1.

[27] CMS Collaboration. *Observation of a new boson at a mass of 125 GeV with the CMS experiment at the LHC*, Phys. Lett. B **716** (2012) 30.

[28] CMS Collaboration. *Precise determination of the mass of the Higgs boson and tests of compatibility of its couplings with the standard model predictions using proton collisions at 7 and 8 TeV*, Eur. Phys. J. C **75** (2015) 212.

[29] W. Karpinski. `https://slideplayer.com/slide/8363727/`.

[30] F. Hartmann on behalf of the CMS Silicon Tracker Collaboration. *The CMS All-Silicon Tracker Strategies to ensure a high quality and radiation hard Silicon Detector*, NIM A **478** (2002) 285287.

[31] S. Tavernier. *Experimental Techniques in Nuclear and Particle Physics*, Springer (2010).

[32] G. Casse, et al. *New operation scenarios for severely irradiated silicon detectors*, PoS (Vertex) **008** (2009).

[33] M. Moll. *Development of Radiation Tolerant Silicon Sensors - A Status Report of the RD50 Collaboration*, PoS (Vertex) **026** (2013).

[34] G. Kramberger, et al. *Comparison of pad detectors produced on different silicon materials after irradiation with n, p & pions*, NIM A **612** (2010) 288-295.

[35] A. Affolder, et al. *Collected charge of planar silicon detectors after pion and proton irradiations up to 2.2 x 1016* $n_{eq} \cdot cm^{-2}$, NIM A **623** (2010) 177-179.

[36] V. A. J. van Lint, et al. *Mechanisms of radiation effects in electronic materials*, John Wiley & Sons (1980).

[37] J. H. Cahn. *Irradiation damage in germanium and silicon due to electrons and gamma rays*, J. Appl. Phys. **30** (1959) 1310.

[38] M. Moll. *Radiation Damage in Silicon Particle Detectors*, DESY-THESIS-1999-040.

[39] G. Casse and M. Moll. *Radiation hard semiconductors devices for very high luminosity colliders*, RD50 Status Report, LHCC (2017). https://indico.cern.ch/event/632309/contributions/2556473/attachments/1457030/2250199/170510-RD50-Status_2017-final.pdf.

[40] A. Hoecker. *Physics at the LHC Run-2 and Beyond*, CERN Yellow Reports: School Proceedings Archives **5** (2017).

[41] CMS Collaboration. *Technical Proposal for the Phase-II Upgrade of the CMS Detector*, CERN-LHCC-2015-010, LHCC-P-008, CMS-TDR-15-02 (2015).

[42] CMS Collaboration. *Updates on Performance of Physics Objects with the Upgraded CMS detector for High Luminosity LHC* CMS-DP-2016-065 (2016).

[43] CMS Collaboration. *Updates on Projections of Physics Reach with the Upgraded CMS Detector for High Luminosity LHC*, CMS-DP-2016-064 (2016).

[44] CMS Collaboration. *CMS Phase II Upgrade Scope Document*, Technical Report CERN-LHCC-2015-019, LHCC-G-165, CERN (2015).

[45] S. Mallows. BRIL webpage: https://twiki.cern.ch/twiki/bin/viewauth/CMSPublic/BRILRSelbaHGC.

[46] M. Guthoff. BRIL webpage: https://twiki.cern.ch/twiki/bin/view/CMSPublic/BRILRS1D1MeVneqAtTracker.

[47] CMS Collaboration. *The Phase-2 Upgrade of the CMS Tracker Technical Design Report*, CERN-LHCC-2017-009, CMS-TDR-17-001 (2017).

[48] P. Rose. *2S module CAD drawing* (2015). https://espace.cern.ch/Tracker-Upgrade/2S-Module/Shared.

[49] D. Ceresa, et al. *Macro Pixel ASIC (MPA): the readout ASIC for the pixelstrip (PS) module of the CMS outer tracker at HL-LHC*, JINST **9** (2014) C11012.

[50] S.M. Sze. *Physics of Semiconductor Devices*, John Wiley and Sons, New York **2** (1985).

[51] D. A. Neaman. *Semiconductor Physics and Devices, Basic Principles*, Mc Graw Hill, Avenue of the Americas, New York (2003).

[52] `http://wanda.fiu.edu/teaching/courses/Modern_lab_manual/pn_junction.html`

[53] C. Kittel. *Introduction to Solid State Physics*, New York:John Wiley **6** (1986).

[54] G. F. Knoll. *Radiation Detection and Measurement*, John Wiley & Sons **4** (2010).

[55] W. R. Leo. *Techniques for Nuclear and Particle Physics Experiments*, Springer, Berlin Heidelberg New York (1994).

[56] S. Ramo. *Current induced by electron motion*, Proc. of the I.R.E. **27** (1939) 584.

[57] W. Schokley. *Currents to conductors induced by a moving point charge*, J. Appl. Phys. **9** (1938) 635.

[58] J. P. Colinge and C. A. Colinge. *Physics of Semiconductor Devices*, Springer, Spring Street, New York (2006).

[59] G. Lutz. *Semiconductor Radiation Detectors*, Springer, Berlin (1999).

[60] J. A. Hoerni. *Method of Manufacturing Semiconductor Devices*, US3025589 A (1962).

[61] F. Hartmann. *Evolution of Sensor Technology in Particle Physics*, Springer, STMP 231 (2009) ISSN 0081-3869.

[62] J. Tauc. *Optical properties and electronic structure of amorphous Ge and Si*, Materials Research Bulletin **3** (1968) 3746.

[63] H. W. Kraner, et al. *The use of the signal current pulse shape to study the internal electric field profile and trapping effects in neutron damaged silicon detectors*, NIM A **326** (1993) 350-356.

[64] R. M. Hernandez. *A Portable Readout System for Microstrip Silicon Sensors (ALIBAVA)*, IEEE **56** (2009) 1642-1649.

[65] I. Pintilie et al. *Radiation-induced point- and cluster-related defects with strong impact on damage properties of silicon detectors*, NIM A **611** (2009) 52-68.

[66] M. Moll. *Development of radiation tolerant Silicon Sensors - A Status Report of the RD50 Collaboration*, PoS(Vertex) **026** (2013).

[67] A. Junkes. *Influence of radiation induced defect clusters on silicon particle detectors*, Ph.D. Thesis, University of Hamburg (2011).

[68] A. Dierlamm on behalf of the CMS Tracker Collaboration. *Characterisation of silicon sensor materials and designs for the CMS Tracker Upgrade*, PoS(Vertex) **016** (2012).

[69] ATLAS Silvaco. *Users manual*, Version 5.15.32.R Nov 2009, Silvaco webpage. `http://www.silvaco.com`

[70] Sentaurus TCAD. *Industry-Standard Process and Device Simulators*, Synopsys documentation. `http://www.synopsys.com`

[71] Cogenda: Genius Device Simulator. *User's guides*, Cogenda webpage. `http://www.cogenda.com`

[72] P. Antogneti and G. Massobrio. *Semiconductor Device Modeling With SPICE*. McGraw-Hill Book Company (1987).

[73] CMS Detector Note. *Simulation of Silicon Devices for the CMS Phase II Tracker Upgrade*, CMS DN-2014/016.

[74] R. Dalal, **G. Jain**, A. Bhardwaj, and K. Ranjan. *Simulation of Irradiated Si Detectors*, PoS(Vertex) **030** (2014).

[75] R. Dalal. *Performance Characteristics of Si Sensors at Collider Experiments*, Ph.D. Thesis, University of Delhi (2015).

[76] V. Eremin, E. Verbitskaya, and Z. Li. *The origin of double peak electric field distribution in heavily irradiated silicon detectors*, NIM A **476** (2002) 556-564.

[77] K. Ranjan. *Large p_T particle production in p-p collisions at LHC energies*, Ph.D. Thesis, University of Delhi (2004).

[78] A. Bhardwaj. *Some aspects of hadron-hadron collisions at the large hadron collider - CERN*, Ph.D. Thesis, University of Delhi (2004).

[79] A. Peisert and N. Zamiatin. *Silicon sensors for the CMS Preshower*, CMS NOTE 2000-061 (2000).

[80] P. Saxena, et al. *Development of multi-guard ring-equipped p+n Si microstrip detectors for the SiD detector at the ILC*, Semicond. Sci. Technol. **25** (2010) 105012.

[81] kLayout webpage. *Version 2.1.0*, User manual. www.klayout.de.

[82] T. Bergauer. *Process Quality Control of Silicon Strip Detectors for the CMS Tracker*, Diploma thesis, HEPHY (2004).

[83] T. Palviainen. *Minimizing guard ring dead space in silicon detectors with an n-type guard ring at the edge of the detector*, NIM A **573** (2007) 277-279.

[84] F. Hartmann. *Evolution of Silicon detector Technology in Particle Physics*, Springer, 2nd edition (2017).

[85] A. Furgeri. *Quality Assurance and Irradiation studies on CMS silicon strip sensors*. Diploma Thesis, Karlsruhe (2006).

[86] K. H. Hoffmann. *Development of new Sensor Designs and Investigations on Radiation Hard Silicon Strip Sensors for the CMS Tracker Upgrade at the High Luminosity Large Hadron Collider*, Ph.D. Thesis, Karlsruhe Institute of Technology (2013) IEKP-KA/2013-1.

[87] R. Eber. *Investigations of new Sensor Designs and Development of an effective Radiation Damage Model for the Simulation of highly irradiated Silicon Particle Detectors*, Dissertation Thesis, Karlsruhe Institute of Technology (2013).

[88] **G. Jain**, R. Dalal, K. Lalwani, A. Bhardwaj, and K. Ranjan. *Development and Characterization of ac-coupled Si strip detectors for Nuclear and High Energy Physics Applications*, DAE Symp. on Nucl. Phys. **59** (2014) 954-955.

[89] Alibava Systems. *Instruments for detection, Start-up guide and User's manual*, Alibava webpage. https://www.alibavasystems.com/.

[90] Beetle Manual. http://www.kip.uni-heidelberg.de/lhcb/Publications/BeetleRefManv13.pdf.

[91] S. Loechner. *Development, optimisation and characterisation of a radiation hard mixed-signal readout chip for LHCb*, Ph.D. thesis, Heidelberg University, (2006).

[92] Zyklotron AG. http://www.zyklotron-ag.de/en/.

[93] AIDA-2020 website. http://aida2020.web.cern.ch/.

[94] H. Bichsel. *Straggling in thin silicon detectors*, Rev. Mod. Phys. **60** (1988) 663-699.

[95] K. Lalwani, **G. Jain**, R. Dalal, A. Bhardwaj, K. Ranjan. *Design, Fabrication and Characterization of multi-guard-ring furnished p+n-n+ Silicon Strip*, NIM A **824** (2015) 428-431.

[96] MPI Corporation. *Probe station*. https://www.mpi-corporation.com/.

[97] The IMC group. *4000RHT Hanwell temperature and humidity monitoring Datasheet*.

[98] Tektronix. *Keithley 2657A Datasheet, Keithley Series 2657A High Power System SourceMeter*, SMU Instruments. https://www.tek.com/keithley-source-measure-units/keithley-smu-2650-series-high-power-sourcemeter.

[99] Tektronix. *Keithley 2636B Datasheet, Keithley Series 2600B System SourceMeter*, SMU Instruments. https://www.tek.com/keithley-source-measure-units/smu-2600b-series-sourcemeter.

[100] Keysight Technologies. *E4980A Precision LCR Meter Datasheet*. https://www.keysight.com/en/pd-715495-pn-E4980A/precision-lcr-meter-20-hz-to-2-mhz?cc=IN&lc=eng.

[101] Tektronix. *Keithley 707B Semiconductor Switch Matrix Mainframes Six-slot and Single-slot Versions Datasheet*. https://www.tek.com/semiconductor-test-systems/700-series-semiconductor-switching-systems-manual/models-707b-and-708b-se.

[102] Tektronix. *Keithley 7072 Semiconductor Matrix Card 8 × 12 Datasheet*. https://www.tek.com/default-accessory-series-manual/model-7072-semiconductor-matrix-card-instruction-manual-rev-c.

[103] Tektronix. *Keithley 7072-HV High Voltage Semiconductor Matrix Card 8 × 12 Datasheet*. https://www.tek.com/default-accessory-series-manual/model-7072-hv-high-voltage-semiconductor-matrix-card-instruction-man.

[104] Keithley. *Model 2657A-LIM-3 LO Interconnect Module*, User's Guide. https://www.tek.com/default-accessory-series-manual-29.

[105] Anest Iwata. *Compressed Dry Air, Zero oil, SLP series, Model 371E*. https://www.anest-iwata.co.jp/english/compressor/scroll/01.html.

[106] Tanco. *The PLT-261 series, Humidity and temperature control cabinet Datasheet*. http://www.tancolabproducts.com/humidity-and-temperature-cabinet.html.

[107] Tanco. *The PLT-153(B) series, Ultra low temperature cabinet Datasheet*. https://www.industrybuying.com/food-service-storage-and-transportation-tanco-FU.FO.1410174/.

[108] Keithley. *ACS software quick start guide*. https://www.tek.com/keithley-semiconductor-test-systems/automated-characterization-suite-acs-software-manual-1.

[109] Keithley. *ACS basic edition, Semiconductor parametric test software for component and discrete devices*. https://www.newark.com/keithley/acs-basic/acs-basic-edition-software-for/dp/59T4433.

[110] Keithley. *Datasheet*. https://www.testequity.com/products/4038/.

[111] Keithley. *Datasheet*. https://www.newark.com/keithley/2410/source-meter-dc-voltage-current/dp/19K4451.

[112] Keithley. *Datasheet*. https://www.tek.com/manual/model-590-cv-analyzer-instruction-manual-rev-d-197mb.

[113] PDL 828 SEPIA II multi channel Picosecond Quant Laser Controller. https://www.picoquant.com/products/category/picosecond-pulsed-driver/pdl-828-sepia-ii-computer-controlled-multichannel-picosecond-diode

[114] Keysight Technologies, Function Generator. https://www.keysight.com/en/pd-1871286-pn-33522A/

function-arbitrary-waveform-generator-30-mhz?&cc=IN&lc=eng.

[115] Picosecond PSPL5531 10 GHz Bias Tee. https://www.signaltestinc.com/product-p/pspl5531.htm.

[116] E3632A 120W Power Supply. https://www.keysight.com/en/pd-835964-pn-E3632A/120w-power-supply-15v-7a-or-30v-4a?cc=IN&lc=eng.

[117] DSO7104B Oscilloscope: 1 GHz, 4 Analog Channels. https://www.keysight.com/en/pdx-x201792-pn-DSO7104B/oscilloscope-1-ghz-4-analog-channels?cc=IN&lc=eng.

[118] ThorLabs. *Photodetector, Model DET02AFC*. https://www.thorlabs.com/thorproduct.cfm?partnumber=DET02AFC#ad-image-0.

[119] G. Casse, et al. *New operation scenarios for severely irradiated silicon detectors*, PoS(Vertex) **008** (2009).

[120] M. Moll. *Development of Radiation Tolerant Silicon Sensors - A Status Report of the RD50 Collaboration*, PoS(Vertex) **026** (2013).

[121] G. Kramberger, et al. *Comparison of pad detectors produced on different silicon materials after irradiation with neutrons protons and pions*, NIM A **612** (2010) 288-295.

[122] A. Affolder, et al. *Collected charge of planar silicon detectors after pion and proton irradiations up to 2.2* $\times 10^{16}$ $n_{eq} \cdot cm^{-2}$, NIM A **623** (2010) 177-179.

[123] N. Cartiglia, et al. *Beam test results of a 16 ps timing system based on ultra-fast silicon detectors*, NIM A **850** (2017) 83-88.

[124] H. F. W. Sadrozinski, et al. *Sensors for ultra-fast silicon detectors*, NIM A **765** (2014) 7-11.

[125] G. Pellegrini, et al. *Technology developments and first measurements of Low Gain Avalanche Detectors (LGAD) for high energy physics applications*, NIM A **765** (2014) 12-16.

[126] G. Kramberger. *Radiation hardness of Low Gain Amplification Detectors (LGAD)*, 24th RD50 Workshop, Bucharest, Romania (2014).

[127] G. D. Betta, et al. *Design and TCAD simulation of double-sided pixelated low gain avalanche detectors*, NIM A **796** (2015) 154-157.

[128] P. F. Martinez, et al. *Simulation of new p-type strip detectors with trench to enhance the charge multiplication effect in the n-type electrodes*, NIM A **658** (2011) 98-102.

[129] G. Pelligrini, et al. *Measurements of Low Gain Avalanche Detectors (LGAD) for high energy physics applications*, 9th International 'Hiroshima' Symposium (2013).

[130] G. Kramberger, et al. *Radiation effects in Low Gain Avalanche Detectors after hadron irradiations*, JINST **10** (2015) P0006 .

[131] C. Gallrapp, et. al. *TCT measurements on neutron and proton irradiated LGAD pad sensors*, 26th RD50 Workshop (2015).

[132] R. Dalal, **G. Jain**, A. Bhardwaj, and K. Ranjan. *TCAD simulations of Low Gain Avalanche Detectors*, NIM A **836** (2016) 113-121.

[133] Z. Li and H.W. Kraner. *Fast neutron radiation damage effects on high resistivity silicon junction detectors*, J. Electron. Mater. **21** (1992) 701.

[134] V. Eremin, Z. Li, and I. Iljashenko. *Trapping induced N_{eff} and electrical-field transformation at different temperatures in neutron-irradiated high-resistivity silicon detectors*, NIM A **360** (1995) 458.

[135] U. Biggeri, et al. *CV and hall effect analysis on neutron irradiated silicon detectors*, NIM A **338** (1997) 330-334.

[136] G. Kramberger, et al. *Initial acceptor removal in p-type silicon detectors*, 23rd RD50 Workshop (2013).

[137] **G. Jain**, R. Dalal, A. Bhardwaj, and K. Ranjan. *Dependence of charge multiplication on different design parameters of LGAD devices*, JINST **12** (2017) C03022.

[138] The CMS Collaboration. *The CMS experiment at the CERN LHC*, JINST **3**)2008) S08004.

[139] G. Lindstrom, M. Moll, and E. Fretwurst. *Radiation hardness of silicon detectors a challenge from high-energy physics*, NIM A **426** (1999) 1-15.

[140] G. Kramberger, et al. *Determination of effective trapping times for electrons and holes in irradiated silicon*, NIM A **476** (2002) 645-651.

[141] **G. Jain**, P. Kumari, K. Lalwani, R. Dalal, A. Bhardwaj, and K. Ranjan. *Development of Transient Current Technique Measurement setup at DU*, Workshop on Contemporary Trends in High-Energy Physics and Experimentation, Chandigarh (2014).

[142] G. Casse, et al. *New operation scenarios for severely irradiated silicon detectors*, PoS(Vertex) **008** (2009).

[143] M. Moll. *Development of Radiation Tolerant Silicon Sensors - A Status Report of the RD50 Collaboration*, PoS (Vertex) **026** (2013).

[144] G. Kramberger, et al. *Comparison of pad detectors produced on different silion materials after irradiation with neutron, proton and pion*, NIM A **612** (2010) 288-295.

[145] A. Affolder, et al. *Collected charge of planar silicon detectors after pion and proton irradiations up to* $2.2 \times 10^{16}\ n_{eq} \cdot cm^{-2}$, NIM A **3** (2010) 177-179.

[146] A. Affloder, et al. *CC studies in irradiated HV-CMOS particle detectors*, JINST **11** (2016) P04007.

[147] P. Saxena, et al. *Performance studies of the p-spray/p-stop implanted Si sensors for the SiD detector*, NIM A **658** (2011) 66-69.

Nuclear Inst. and Methods in Physics Research, A 913 (2019) 97–102

Contents lists available at ScienceDirect

Nuclear Inst. and Methods in Physics Research, A

journal homepage: www.elsevier.com/locate/nima

Radiation tolerance study on irradiated AC-coupled, poly-silicon biased, p-on-n silicon strip sensors developed in India

Geetika Jain [a], Chakresh Jain [a], Ashutosh Bhardwaj [a,*], Kirti Ranjan [a], Alexander Dierlamm [b], Frank Hartmann [b], Marcel Demarteau [c]

[a] Centre for Detector and Related Software Technology (CDRST), Department of Physics and Astrophysics, University of Delhi, Delhi 110007, India
[b] Karlsruhe Institute of Technology, Karlsruhe, Germany
[c] Argonne National Laboratory, IL, USA

ARTICLE INFO

Keywords:
Silicon sensors
AC-coupled
Characterization
Irradiation

ABSTRACT

The silicon sensors to be deployed in the next generation high energy physics experiments for operation in high luminosity scenarios, will require a high level of radiation tolerance. AC-coupled silicon strip sensors integrated with biasing poly-silicon resistors have been fabricated in collaboration with the Bharat Electronics Limited foundry using 4 inch n-type wafers in p-on-n configuration. Several sensors were irradiated with protons at different fluences at the Karlsruhe Cyclotron facility under the Advanced European Infrastructures for Detectors at Accelerators (AIDA) program. This paper reports on these radiation hardness study performed on the AC-coupled silicon sensors fabricated in India. The characterization comprises of electrical tests, including total current, voltage and strip scans and charge collection studies.

1. Introduction

Silicon strip sensors play a key role in High Energy Physics (HEP) experiments due to their superior performance in terms of radiation hardness resulting in robust and reliable charged particle tracks and vertex reconstruction. Owing to the placement of these sensors in a harsh radiation environment imposed by current and future HEP experiments, the radiation hardness study is invaluable both for optimizing the sensor design or developing new sensor configurations.

The HEP Group at the University of Delhi (DU) has developed and characterized AC-coupled, poly-silicon biased, p-on-n silicon strip sensors in collaboration with Bharat Electronics Limited (BEL), Fermi National Accelerator Laboratory (Fermilab), Argonne National Laboratory (ANL), and Karlsruhe Institute of Technology (KIT). The sensors were fabricated on 4-inch float-zone n-type wafers of crystal orientation (111), with an initial resistivity of 2–5 kΩ cm and of 320 μm active thickness. The sensors are AC-coupled through an oxide of 400 nm thickness and have poly-silicon bias resistors. The p-type strips have a strip width, pitch and length of 30 μm, 55 μm and 6 cm respectively. The non-irradiated sensors were subject to several tests defined in the characterization scheme for the quality assurance of the fabricated sensors. In Ref. [1], we described the details of the process steps involved in the fabrication cycle and the performance characteristics of the fabricated sensors. The measured data shows a good control of the process parameters governing the poly-silicon deposition and the quality and uniformity of the coupling oxide layer.

Next, the radiation tolerance was evaluated. The sensors were irradiated with a proton beam of 23 MeV energy at the compact cyclotron [2] operated in the ZAG Zyklotron AG, Karlsruhe, under the Advanced European Infrastructures for Detectors at Accelerators (AIDA) [3] programme. The results of the electrical characterization and the charge collection measurements of the irradiated sensors are described in the next sections of this paper. It is noted that this is the first radiation hardness study performed on AC-coupled sensors developed in India.

2. Irradiation campaign

A total of four sensors were irradiated at the ZAG facility to different values of fluence. The values of fluence are chosen to be 1×10^{14}, 5×10^{14}, 1×10^{15}, and 5×10^{15} n_{eq} cm^{-2}, which were selected to reflect the particle flux environment at which the silicon sensors are expected to be exposed to in future hadron colliders, particularly in the vertex and tracking regions. However, it may be noted that due to the large area of the sensors, the sensors may not have been irradiated uniformly.

As described in Ref. [1], the characterization tests are divided into two categories:

- **Passive electrical tests** - These are further sub-divided into global measurements and inter-strip parameter measurements (voltage scan at a fixed strip and strip scan at a fixed voltage).

* Corresponding author.
E-mail address: ashutosh.bhardwaj@cern.ch (A. Bhardwaj).

https://doi.org/10.1016/j.nima.2018.10.118
Received 17 April 2018; Received in revised form 15 October 2018; Accepted 16 October 2018
Available online xxxx

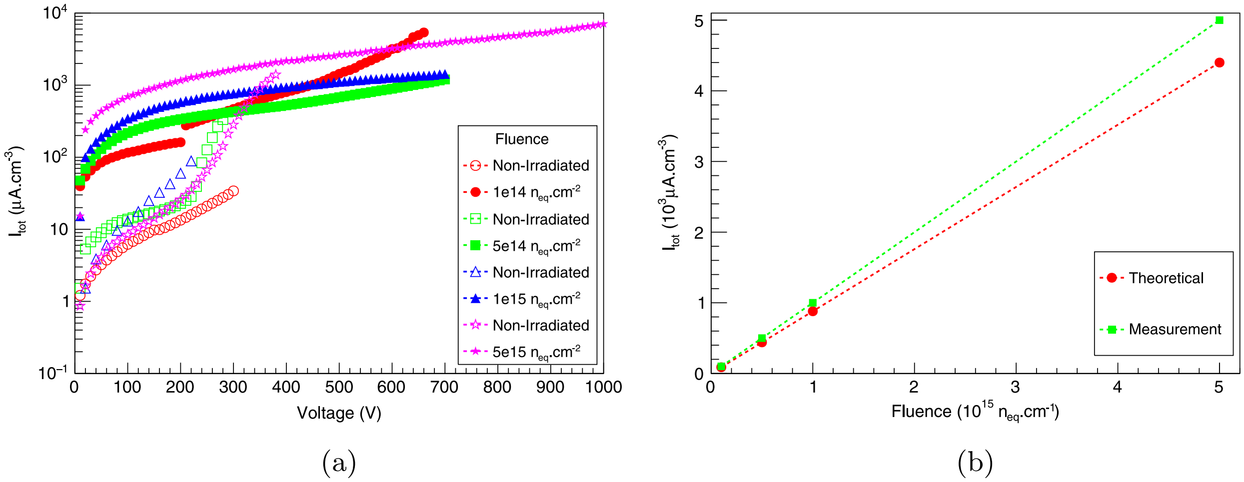

Fig. 1. (a) The behaviour of the total leakage current of the irradiated sensors as a function of reverse bias voltage measured at −20 °C. (b) The slope of the theoretical and measured current per unit volume as a function of fluence gives the corresponding alpha values.

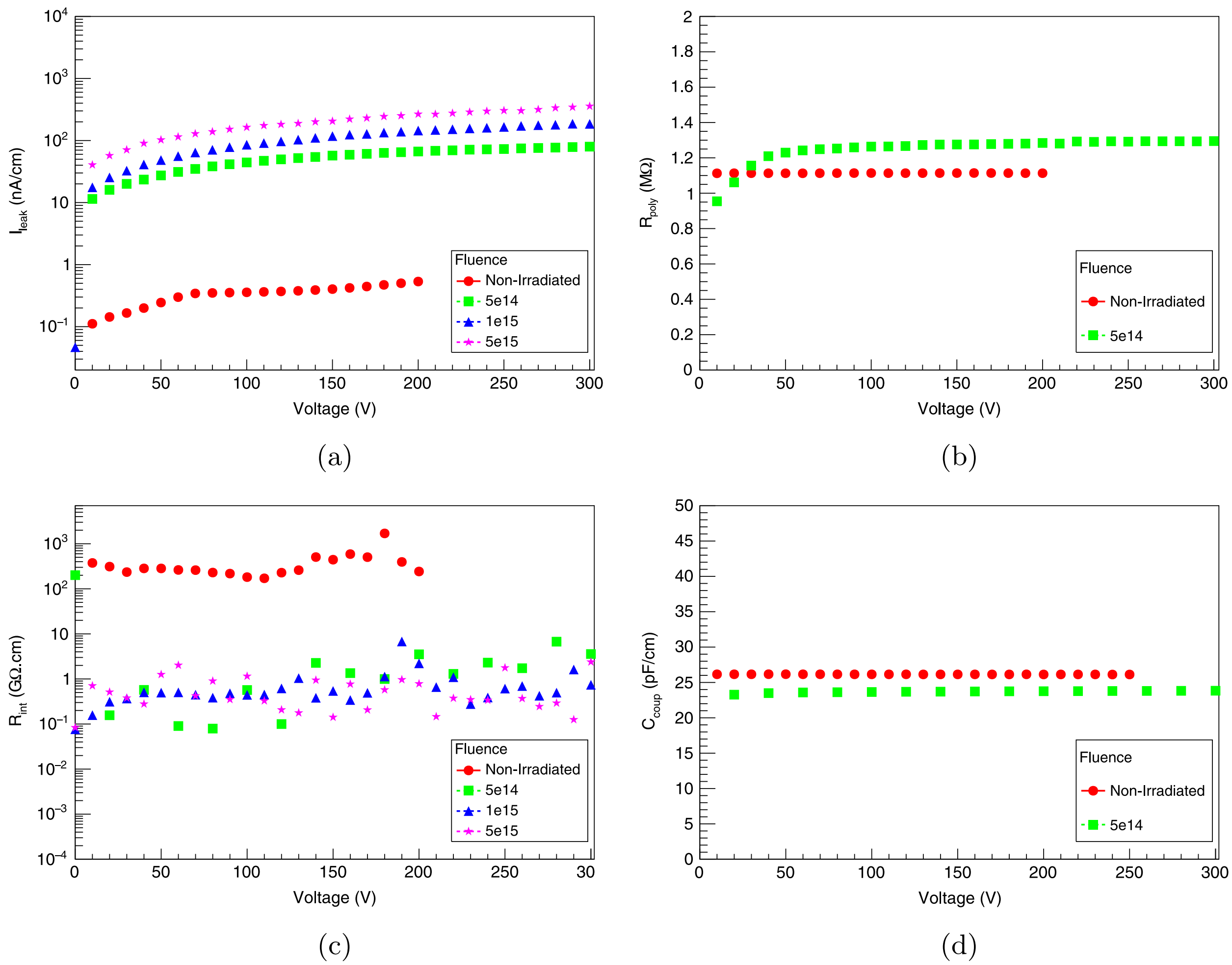

Fig. 2. The voltage scans of (a) strip leakage current, (b) poly-silicon resistance, (c) inter-strip resistance, and (d) coupling capacitance, before and after irradiation.

(a) Global parameters measurements: Total sensor leakage current (I_{tot}), and backplane capacitance (C_{tot})

(b) Inter-strip parameters measurements: Strip leakage current (I_{leak}), poly-silicon resistance (R_{poly}), inter-strip resistance (R_{int}), coupling capacitance (C_{coup}), inter-strip capacitance (C_{int}), and dielectric current (I_{diel})

- **Charge Collection (CC) measurements**

The tests are carried out at KIT, using a set of electrical equipments and an automatic probe station able to operate at cold temperatures. The ^{90}Sr source based ALiBaVa analogue read-out setup [4] is used to carry out the CC measurements. The details regarding the characterization setups are given in Ref. [1].

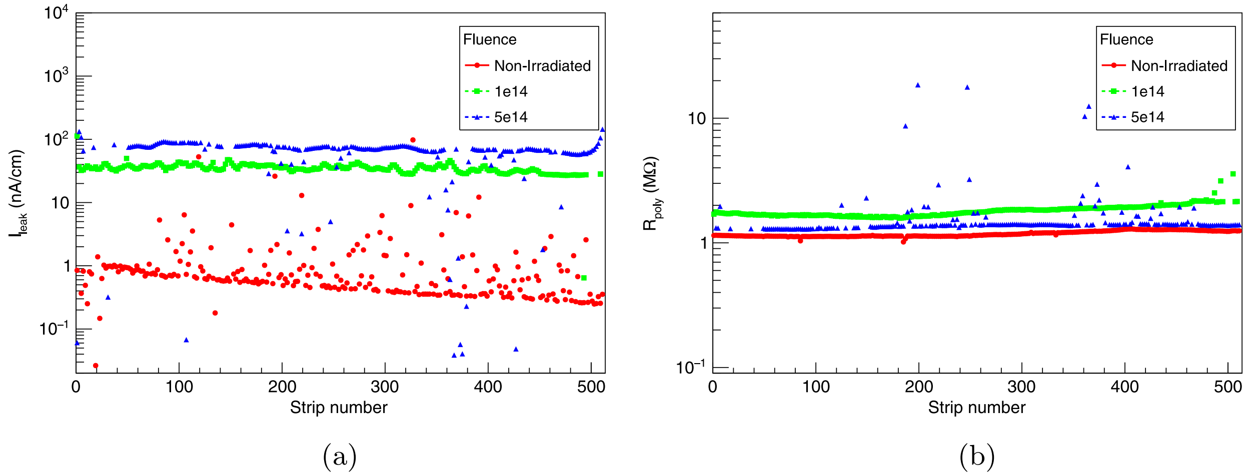

Fig. 3. The strip scans at a constant voltage of 200 V for - (a) strip leakage current, and (b) poly-silicon resistance, before and after irradiation.

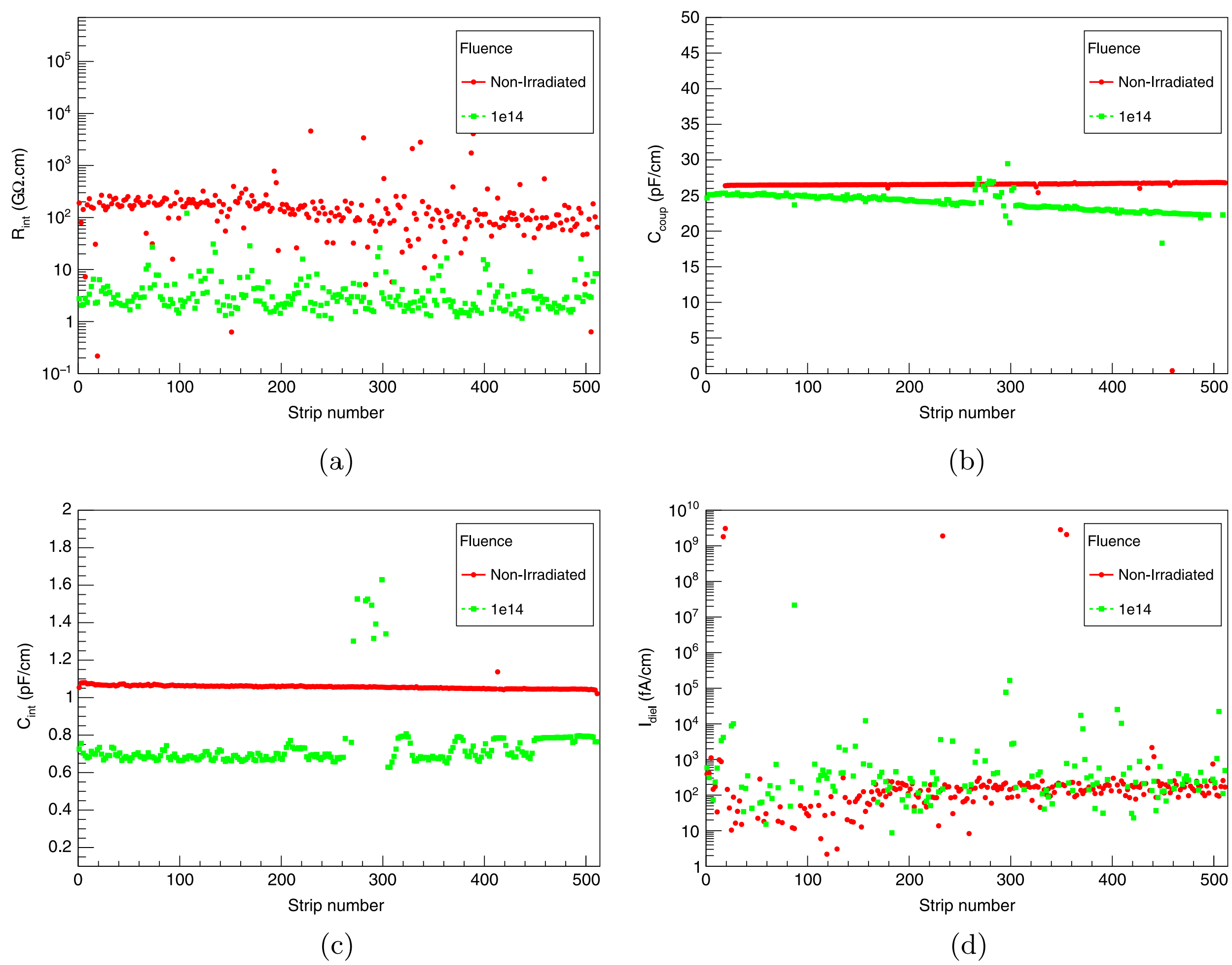

Fig. 4. The strip scans at a constant voltage of 200 V for - (a) inter-strip resistance, (b) coupling capacitance, (c) inter-strip capacitance, and (d) dielectric current, before and after irradiation.

The measurements on the irradiated sensors are carried out in a clean room having a controlled low humidity (RH < 10%) and at a base temperature of −20 °C. A typical behaviour of the non-irradiated sensor (measurement performed at room temperature) is also shown for comparison. It may be noted that the results of certain parameters could not be measured for a few irradiation steps due to hardware issues and hence are missing. Nevertheless, the measured data is sufficient to draw conclusions on the radiation tolerance of the sensors.

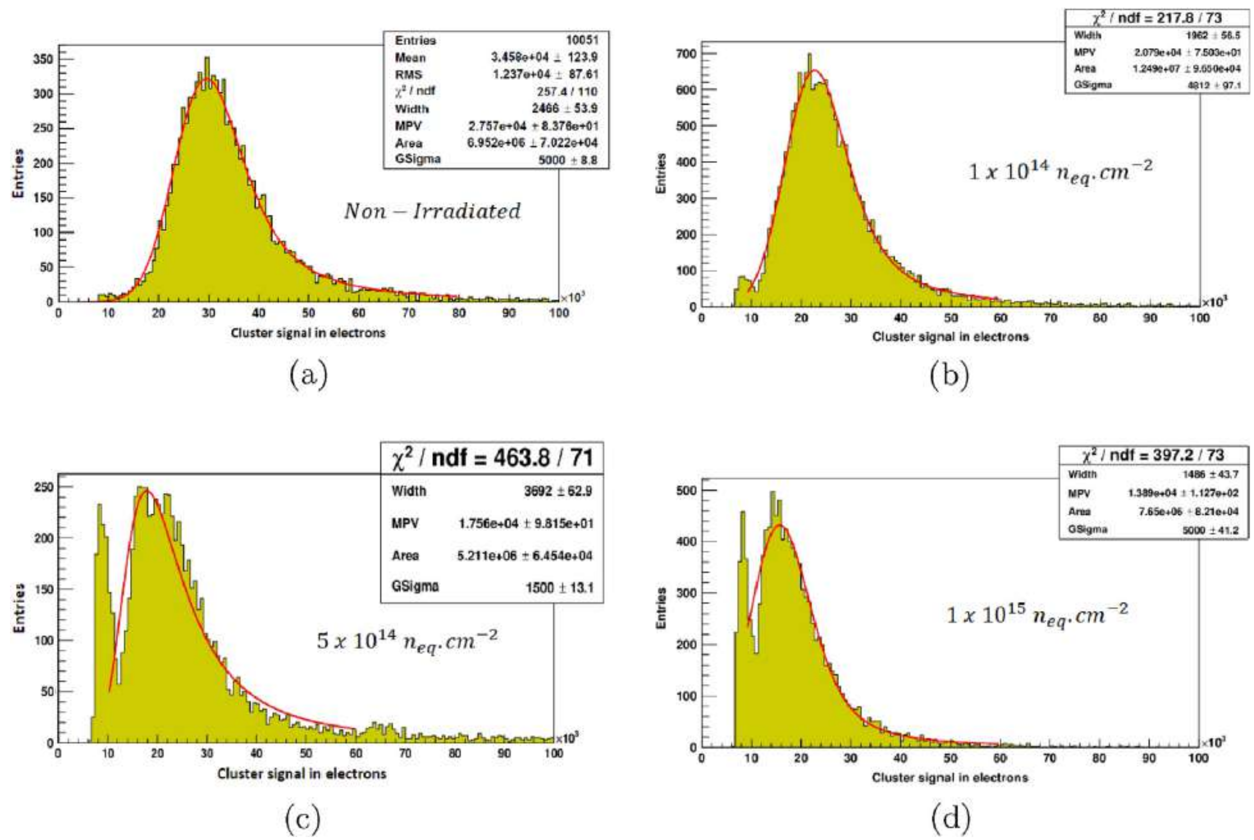

Fig. 5. The charge collection distribution — entries (number of events) vs cluster signal in electrons (number of electrons collected in a cluster) for the (a) non-irradiated sensor at a bias voltage of 150 V, and sensors irradiated to a fluence of (b)1×10^{14}, (c) 5×10^{14}, and (d) 1×10^{15} n_{eq} cm^{-2}, at a bias voltage of 350, 600, and 900 V respectively.

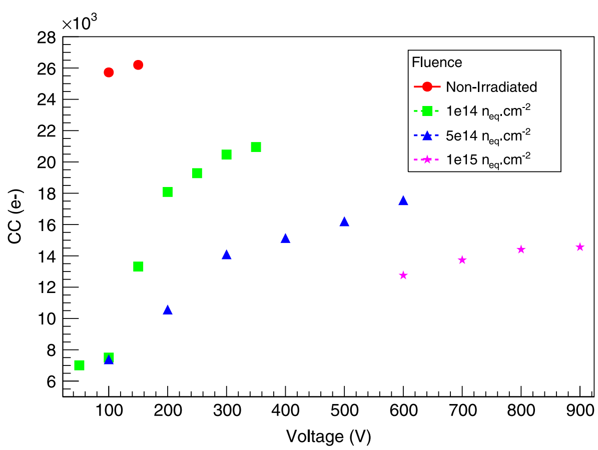

Fig. 6. The charge collected for the non-irradiated and the irradiated sensors.

3. Passive electrical tests

3.1. Global parameter

The DC characteristics of the sensors as a function of bias voltage are measured before irradiation and after irradiation and are shown in Fig. 1a. As expected, the irradiated sensors show a significant increase in the current compared to their non-irradiated counterpart. The soft breakdown observed for (a) the non-irradiated scenario and (b) the higher currents at a lower fluence of 1×10^{14} n_{eq} cm^{-2} at large voltages (>200 V) is attributed to local discharges. This behaviour is no longer observed at higher fluence.

We have considered all four values of fluence for estimating the leakage current damage constant, $\alpha(T)$, where T is temperature. The total current is noted for fluence values of 1×10^{14}, 5×10^{14}, 1×10^{15}, and 5×10^{15} n_{eq} cm^{-2} at bias voltages of 200, 500, 700, and 1000 V respectively. The $\alpha(T)$, as estimated from this work, is found to be 1.00×10^{-18} A cm^{-1} after annealing for 80 min at 60 °C for the strip sensors, which is in reasonable agreement with the theoretically calculated value of 8.80×10^{-19} A cm^{-1} at a temperature of −20 °C [5] (see Fig. 1b).

3.2. Individual strip & inter-strip parameters

The strip parameters are evaluated through two measurement schemes - (a) voltage scan at only one fixed strip, and (b) strip scan at a constant voltage. The plots for voltage and strip scans for the strip parameters are illustrated in Figs. 2–4 respectively. While the voltage scans depict the behaviour of the strip parameters as a function of increasing voltage, the strip scans show the values of the strip parameters at a fixed bias voltage of 200 V. The strip scan results are available for fluence = 1×10^{14} n_{eq} cm^{-2} and partially for fluence = 5×10^{14} n_{eq} cm^{-2}.

It is observed from Figs. 2a and 3a that I_{leak} remains around 1 μA (or, approximately 200 nA/cm) after irradiation. For R_{poly} (Figs. 2b and 3b), a small change with fluence is observed. Figs. 2c and 4a show that the value of R_{int} decreases significantly from about 100 GΩ cm to 0.01–1 GΩ cm. For a suitable sensor operation, R_{poly} should be lower than R_{int} while maintaining uniformity over the strips of the sensor even after irradiation [6]. The measured R_{poly} values for fluence = 1×10^{14} and 5×10^{14} n_{eq} cm^{-2} lie in the range of 1–2.5 MΩ which is at least an order of magnitude less than the R_{int} values and also displays a reasonable uniformity. No change in C_{coup} (Figs. 2d and 4b) is observed within the measurement accuracy. Fig. 4c shows a decrease in the value of C_{int} for

Table 1
The mean values of the strip parameters at a reverse bias voltage of 200 V.

Strip parameter	Non-irradiated	Irradiated	Irradiated	Irradiated	Irradiated
Fluence (n_{eq} cm^{-2})	0	1×10^{14}	5×10^{14}	1×10^{15}	5×10^{15}
Temperature	20 °C	−20 °C	−20 °C	−20 °C	−20 °C
Strip leakage current (I_{leak})	0.2–2 nA/cm	20–50 nA/cm	60–100 nA/cm	≈150 nA/cm	≈200 nA/cm
Poly-silicon resistance (R_{poly})	1–2 MΩ	1–2 MΩ	>2 MΩ for few strips	–	–
Inter-strip resistance (R_{int})	>100 GΩ cm	>2.5 GΩ cm	≈2.5 GΩ cm	≈2 GΩ cm	≈0.7 GΩ cm
Coupling capacitance (C_{coup})	26 pF/cm	22–25 pF/cm	≈23 pF/cm	–	–
Inter-strip capacitance (C_{int})	1–1.2 pF/cm	0.6–0.8 pF/cm	–	–	–
Dielectric current (I_{diel})	<10^5 fA/cm at 10 V	<10^5 fA/cm at 10 V	–	–	–

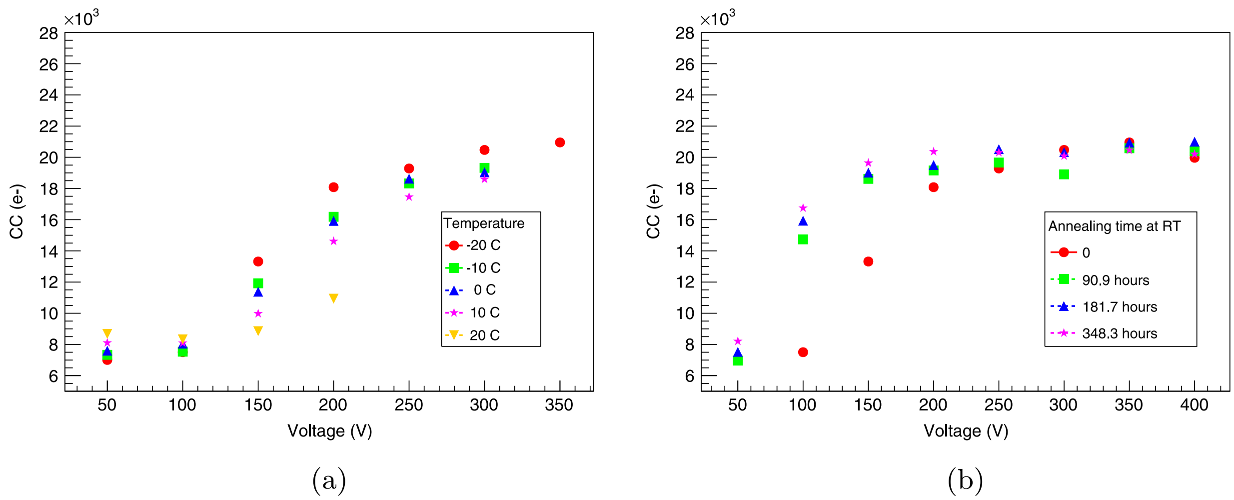

Fig. 7. The charge collection as a function of bias voltage for the sensor irradiated to a fluence = 1×10^{14} n_{eq} cm^{-2} for (a) varying measurement temperature annealed for 1 h at RT on the sensor; and (b) increasing annealing at constant measurement temperature of −20 ° C. The legend lists the normalization to RT based on the parametrization given in Ref. [5]. The annealing is performed in steps of - (i) 60 °C for 20 min (or, equal to 90.9 h at RT), (ii) followed by an additional 60 °C for 20 min (or, equal to 181.7 h at RT), and (iii) additional 60 °C for 40 min (or, equal to 348.3 h at RT).

fluence = 1×10^{14} n_{eq} cm^{-2}. The current through the dielectric, I_{diel} does not change as shown in Fig. 4d and only a few pinholes are observed, which demonstrates a good control over pinholes after irradiation. The measurement of the strip parameters shows excellent uniformity across the sensor, even after irradiation.

Table 1 summarizes the mean strip parameters of the measured voltage and strip scans, before and after irradiation at a bias voltage of 200 V. In general, full depletion voltage increases with increasing fluence and so a better comparison of the results would have been made by measuring the sensors at different bias voltages for different fluences.

4. Charge collection studies

One of the crucial sensor properties is the charge collection efficiency, which, degrades with increasing fluence. The increase in fluence severely affects the CC performance of the sensor [7] due to the following reasons -

- An introduction of trapping centres in the sensor bulk
- A change in the full depletion voltage
- A change in the electric field distribution due to surface damage leading to poor isolation between strips.

However, the CC can be increased by operating at higher bias voltages. The CC distribution of the number of electrons is recorded for the sensors with respect to increasing bias voltage in small voltage steps at −20 °C. The CC measurement used the strip with a signal three times larger than the threshold as the 'seed'. Signals from neighbouring strips with a signal at least two times larger than the threshold were added to form a 'cluster signal' (More details can be found in Ref. [1]). These clusters were recorded for approximately 10 thousand events with a sampling time of 25 ns. The recorded CC distribution is then fitted with a convolution of a Landau and a Gaussian distribution and the most probable value (MPV) of the fit gives the CC for the sensor. The CC distribution at the maximum measured bias voltage for all the fluence values along with the fit is shown in Fig. 5 and the response of CC as a function of bias voltage is represented in Fig. 6. It is observed that the non-irradiated sensor of 320 μm thickness has a MPV charge of 27k electrons at 150 V with a signal to noise ratio (SNR) of 17. However, as the fluence is increased to 1×10^{14}, 5×10^{14}, and 1×10^{15} n_{eq} cm^{-2}, the corresponding MPV charge decreases to 21k (SNR = 12), 17k (SNR = 9), and 14k (SNR = 8) electrons, respectively at bias voltages of 350, 600, and 900 V. It is observed that for the sensor irradiated to the maximum fluence of 5×10^{15} n_{eq} cm^{-2}, the signal could not be distinguished from noise even at a maximum bias of 1100 V and hence is not reported here.

Besides fluence, other parameters like measurement temperature and annealing may also affect the CC of a sensor. Thus the CC is investigated as a function of voltage for two cases - (a) with varying measurement temperature with 1 h at RT annealing and (b) by performing several annealing steps and measuring at a temperature of −20 °C. The corresponding plots are shown in Figs. 7a and 7b respectively. It is observed from Fig. 7a that beyond full depletion, CC decreases with increase in temperature. Fig. 7b shows a notable increase in CC with increasing annealing for low bias voltages. Further, at higher bias voltages, CC tends to attain a constant value irrespective of the annealing.

5. Summary

This paper presents an irradiation study of AC-coupled, poly-silicon biased p-on-n silicon sensors of 320 μm thickness, fabricated in India. The electrical characterization tests and CC studies were performed on the sensors irradiated to a fluence of 1×10^{14} and 5×10^{14} n_{eq} cm^{-2}. Additionally, selective results are shown at high fluences of 1×10^{15} and 5×10^{15} n_{eq} cm^{-2}, which are not within the scope of this sensor technology. It is observed that the increase in I_{tot} with fluence is consistent with the literature. The strip parameters - R_{poly}, C_{coup}, C_{int}, and I_{diel}, show only a moderate change for fluence values of 1×10^{14} and 5×10^{14} n_{eq} cm^{-2}. As expected, a significant increase in I_{leak} and decrease in R_{int} is observed with increasing fluence. The CC efficiency falls to approximately 75%, 64%, and 50% for fluence values of 1×10^{14}, 5×10^{14}, and 1×10^{15} n_{eq} cm^{-2} respectively, assuming a 100% CC for the non-irradiated case. It is also observed that for a fluence of 1×10^{14} n_{eq} cm^{-2}, CC becomes independent of the measurement temperature and annealing at high voltages. Although the results presented are statistically limited and restricted to a few values of fluences, the present work on the development of the AC-coupled, poly-silicon biased silicon sensors lays a foundation and provides useful inputs for future advancements of the detector technology at BEL.

BEL had provided single-sided, DC-coupled silicon sensors to the CMS Preshower and the reported work was aimed to explore its capabilities for the fabrication of AC-coupled sensors. Now, BEL is in the process of upgrading its fabrication line from 4-inch to 6-inch. This will provide the opportunity to explore the 6-inch sensor technology. In the meantime, to further explore its fabrication capability, we have communicated the design for n-in-n sensors to BEL, with different isolation configurations. The batch of sensors will be delivered soon. Additionally, at Delhi, we are also in the process of commissioning an automated and programmable micro-strip characterization setup. The setup will be used to carry out electrical characterization on the fabricated n-in-n sensors.

Acknowledgements

The authors would like to thank Mr. Y. P. Prabhakara Rao and Ms. Rejeena Rani from BEL for the fabrication of the sensors. We are also thankful to the irradiation team at ZAG, Karlsruhe for the irradiations of the sensors. This project has received funding from the European Union's Horizon AIDA 2020 Research and Innovation programme under Grant Agreement no. 654168. Additionally we would like to acknowledge DST, India (ref. no. SR/MF/PS-02/2014-DUA (C) and SR/MF/PS-02/2014-DUA (G)), R&D grant University of Delhi, India, CSIR, India and UGC, India (ref. no. Schs/SRF/AA/139/F-203/2013-14) for financial support.

References

[1] G. Jain, R. Dalal, A. Bhardwaj, K. Ranjan, Development of AC-coupled, poly-silicon biased, p-on-n silicon strip detectors in india for HEP experiments, NIM A 882 (2018) 1–10.
[2] AG. Zyklotron, http://www.zyklotron-ag.de/en/.
[3] AIDA-2020 website http://aida2020.web.cern.ch/.
[4] Alibava Systems, Instruments for detection, Start-up guide and User's manual. Alibava webpage https://www.alibavasystems.com/.
[5] G. Lindstrom, et al., Radiation hard silicon detectors - developments by the RD48 (ROSE) collaboration, NIM A 466 (2001) 308–326.
[6] A. Dierlamm on behalf of the CMS Tracker Collaboration, Silicon sensor developments for the CMS Tracker upgrade, JINST 7 (2012) C01110.
[7] G. Kramberger, et al., Comparison of pad detectors produced on different silicon materials after irradiation with neutrons, protons and pions, NIM A 612 (2010) 288–295.

Nuclear Inst. and Methods in Physics Research, A 882 (2018) 1–10

Contents lists available at ScienceDirect

Nuclear Inst. and Methods in Physics Research, A

journal homepage: www.elsevier.com/locate/nima

Development of AC-coupled, poly-silicon biased, p-on-n silicon strip detectors in India for HEP experiments

Geetika Jain [a], Ranjeet Dalal [a], Ashutosh Bhardwaj [a,*], Kirti Ranjan [a], Alexander Dierlamm [b], Frank Hartmann [b], Robert Eber [b], Marcel Demarteau [c]

[a] Centre for Detector and Related Software Technology (CDRST), Department of Physics and Astrophysics, University of Delhi, Delhi-110007, India
[b] Karlsruhe Institute of Technology, Karlsruhe, Germany
[c] Argonne National Laboratory, IL, USA

ARTICLE INFO

Keywords:
Silicon detectors
AC-coupled
Characterization

ABSTRACT

P-on-n silicon strip sensors having multiple guard-ring structures have been developed for High Energy Physics applications. The study constitutes the optimization of the sensor design, and fabrication of AC-coupled, poly-silicon biased sensors of strip width of 30 μm and strip pitch of 55 μm. The silicon wafers used for the fabrication are of 4 inch n-type, having an average resistivity of 2–5 kΩ cm, with a thickness of 300 μm. The electrical characterization of these detectors comprises of: (a) global measurements of total leakage current, and backplane capacitance; (b) strip and voltage scans of strip leakage current, poly-silicon resistance, interstrip capacitance, interstrip resistance, coupling capacitance, and dielectric current; and (c) charge collection measurements using ALiBaVa setup. The results of the same are reported here.

1. Introduction

Silicon is an excellent material for particle tracking systems, energy measurements, vertexing, heavy quark tagging, etc., owing to its efficient particle detection performance, precise position measurement and reasonable sustainability in the radiation environment [1]. However, for the future high energy physics (HEP) experiments and the upgrades of the existing HEP experiments like the High Luminosity Large Hadron Collider (HL-LHC), the vertex and the tracker sub-detectors will have to face a larger flux of particles in the long term operation. The intense radiation environment will deteriorate the surface and the bulk electrical properties of the silicon sensors, thereby severely affecting their performance.

The HEP group at University of Delhi (DU), India, participated in the design, fabrication and characterization of the silicon sensors for the Preshower Detector of the CMS Experiment [2,3], which were DC-coupled, and with a strip width and strip pitch of the order of 2 mm [4]. The work was done in collaboration with the Bhabha Atomic Research Centre (BARC), Mumbai, India and the sensors were fabricated and tested at Bharat Electronics Limited (BEL), Bengaluru, India. The HEP experiments typically employ AC-coupled silicon strip sensors having a strip width (s_w) and strip pitch (s_p) of about 15–80 μm and 80–180 μm, respectively. Thus, an R&D effort was initiated to develop silicon sensors for the tracker (and other relevant sub-detectors) of the future HEP experiments indigenously. This work is done in collaboration with Fermi National Accelerator Laboratory (Fermilab) and Argonne National Laboratory (ANL), US and Karlsruhe Institute of Technology (KIT), Germany. The initial design was chosen after reviewing the detector designs used at earlier experiments, mainly D0 at Fermilab. The design of the single sided AC-coupled silicon sensors was optimized [5] using Silvaco, a Technological Computer Aided Design (TCAD) device simulator [6]. This is discussed briefly in Section 2.1. The layout of the strip sensor and the various test structures is described in Section 2.2. The AC-coupled silicon sensors with s_w and s_p of 30 and 55 μm, respectively were fabricated at BEL on 4-inch float-zone n-type wafers, with 2–5 kΩ · cm initial resistivity. The planar fabrication process [7] and the eight photolithography masks used for the fabrication are described in Section 2.3. Considering that this work reports the first batch produced by the foundry, this development is in the early stages. The characterization of the silicon sensors was carried out at DU and KIT as discussed in Section 3. The global and strip parameters were measured and the results are reported in Section 4. The charge collection response for the sensors is recorded using the ALiBaVa system [8] and is reported in Section 4.4.

* Corresponding author.
E-mail address: ashutosh.bhardwaj@cern.ch (A. Bhardwaj).

https://doi.org/10.1016/j.nima.2017.10.010
Received 5 April 2017; Received in revised form 6 October 2017; Accepted 6 October 2017
Available online 10 November 2017
0168-9002/

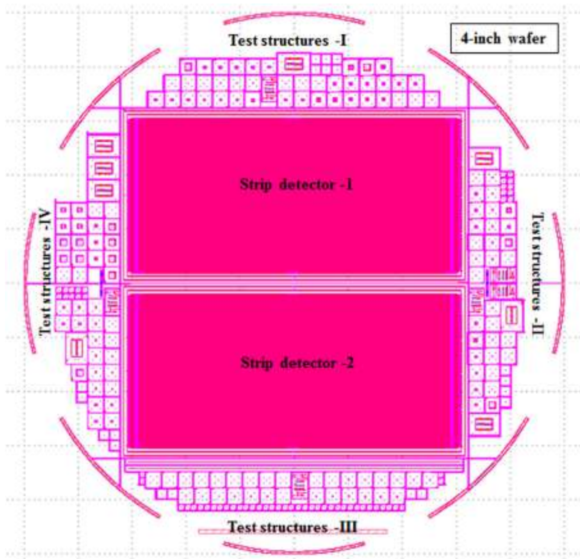

Fig. 1. The layout of the wafer consists of two silicon strip detectors and several test structures on the periphery of the wafer. This layout is built in the kLayout [9] software.

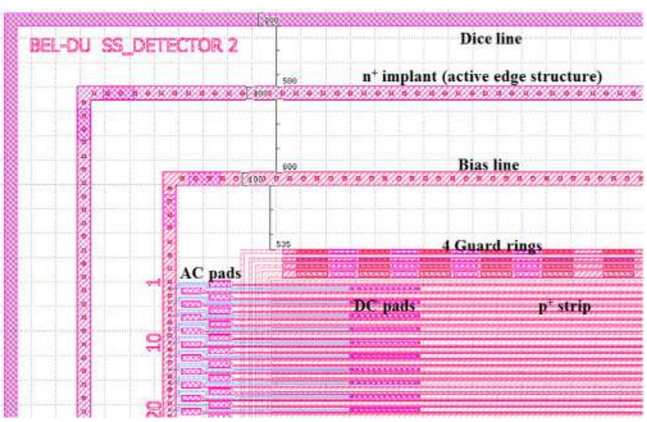

Fig. 2. The enlarged view of the strips, the guard ring structures, the bias line and the dice line, can be seen.

2. Overview of design, layout and fabrication of the detectors

The main purpose of this project was to fabricate AC-coupled, poly-silicon biased sensors with the desired strip width and strip pitch and then test the capabilities of these sensors to meet the desired tolerances for the HEP experiments. This successful development will pave the path to challenging detector technology in India and would allow us to develop radiation hard detectors for future Nuclear and HEP experiments.

2.1. Optimization of the design using simulation

The AC-coupled silicon sensors used in the tracker of the HEP experiments impose stringent specifications like low leakage current, low full depletion voltage, high junction breakdown voltage, choice of appropriate s_w and s_p for low interstrip capacitance and high interstrip resistance, and appropriate oxide thickness and quality for adequate coupling capacitance, etc. The metal overhangs and guard ring designs were optimized to meet the requirements in terms of breakdown voltage. Therefore, before the fabrication of the sensors, an extensive study for the optimization of the design parameters was performed using Silvaco TCAD tool. The study included an analysis of the parameters for the sensor layouts with various design guard ring parameters, like spacing between two consecutive guard rings, guard ring width, number of guard rings, and metal overhang parameters, like inward extension, outward extension, etc. to ensure reliable characteristics. The detailed work is reported in Ref. [5].

Table 1
Design specifications chosen for the AC-coupled, poly-silicon biased, *p*-on-*n* silicon strip detectors.

Parameters	Value
Detector geometry	6.43 cm × 3.25 cm
Resistivity	2–5 kΩ · cm
Number of strips	512
Strip width	30 μm
Strip pitch	55 μm
Strip length	6 cm
Detector thickness	300 ± 20 μm
Metal overhang	5 μm on both sides of the strip
Number of guard rings	4
Width of guard rings	50 μm for innermost, 25 μm for others
Spacing between strip and guard ring	25 μm
Spacing between guard rings	25, 30,40 μm
Aluminium contacts	DC and AC pads

2.2. Layout of the detectors

The wafer layout, which is shown in Fig. 1, includes two strip detectors along with several test structures,[1] like MOS capacitors, pad diodes with different configurations, mini-strip detectors, etc. placed at the periphery of the wafer (referred to as "Test Structures I–IV").

Each of the strip detectors has a surface area of 6.43 cm (length) × 3.25 cm (width), processed on a 4-inch, 300 μm thick silicon wafer. Each detector has 512 strips of s_w of 30 μm and s_p of 55 μm surrounded by four guard rings having different spacing. The first guard ring is 50 μm wide followed by three guard rings, each of equal width of 25 μm. A distance of 535 μm from the last guard ring separates the 100 μm wide p^+ doped bias line. Further, a 100 μm n^+ implant active edge structure separated by a distance of 600 μm from the bias line edge is provided. This has been implemented to minimize the dead space at the edge of the sensor. Usually under the effect of bias, the depletion region grows from the anode to the cathode, but having an implant of the same type as that of the cathode leads to the extension of the depletion region sideways also. This enhances the efficiency of the detector as the dead space is only the area under the guard ring in this case [12]. Another 100 μm n^+ implant is provided at a distance of 500 μm for dicing the detectors. The DC readout pads, placed alternately on left and right end of the strips and inside the bias line structure perimeter, have been included to provide electrical contacts to the *p*-implants for the characterization. The staggered AC pads are provided at both ends of the strips and serve as wire-bonding points for the connection to the readout. The design specifications are listed in Table 1 and the enlarged view of the layout is shown in Fig. 2, depicting the design aspects.

2.3. Fabrication

N-type, 4-inch diameter silicon wafers with crystal orientation of $\langle 111 \rangle$ having a nominal thickness of 300 ± 20 μm and average resistivity of 2–5 kΩ · cm, have been used to fabricate the sensors. The mask set used for the fabrication includes eight different levels, each one associated to a different photolithography step.

A sacrificial oxidation layer is grown on the bare high resistivity n-type wafer. The back side of the wafer is stripped off the oxide for the purpose of gettering,[2] followed by the stripping of the front side oxide.

[1] Designs built on ideas described in Refs. [10] and [11].

[2] Gettering is the process of introduction of a getter (Argon, in our case) that absorbs impurities, if any.

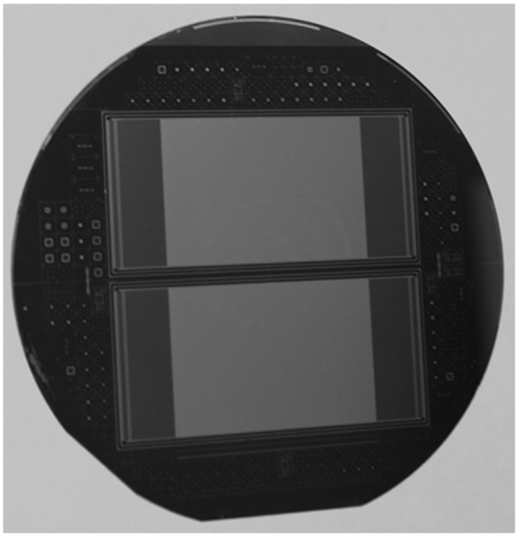

Fig. 3. The fabricated wafer consisting of two silicon detectors along with several test structures.

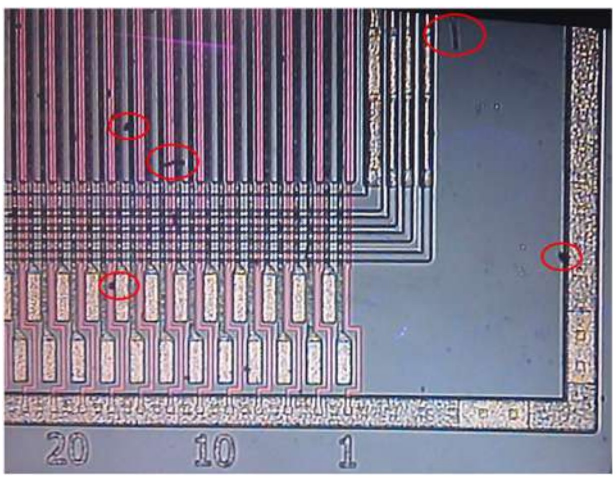

Fig. 4. A small region of the detector seen through a microscope for optical inspection. The red circles in the figure possibly show the dust particles on the detector. The detector has to be cleaned before placing it in the probe station for measurement.

Table 2
Specifications for a typical sensor qualification of HEP experiments.

Specifications	Tolerance limit
Total leakage current (I_{tot})	<2 nA/mm^3 at 500 V
Junction breakdown (V_{bd})	>700 V
Full depletion voltage (V_{fd})	<100 V
Strip leakage current (I_{leak})	<2 nA/cm at 500 V
Poly-silicon resistance (R_{poly})	1.5 ± 0.3 MΩ
Interstrip capacitance (C_{int})	<1 pF/cm
Interstrip resistance (R_{int})	>10 GΩ·cm
Coupling capacitance (C_{coup})	>1 pF/cm· μm
Dielectric current (I_{diel})	<1 nA at 10 V
No. of bad strips	<1% per detector

Next, an initial oxide is grown, being subsequently etched at appropriate places, making windows for the p^+ strip implantations (512 strips, 4 different guard rings,[3] and 1 bias line[4]) by the photolithographic process using *mask 1*. A thin oxide is regrown in the windows to prevent implantation damage. After a boron implantation of dose 9×10^{13} cm^{-2} at an energy of 80 keV, the dopant activation and drive-in diffusion was performed by employing the drive-in cycles at a temperature of 1373 K, to reach a depth of 3.5–4.0 μm. Subsequently, the n^+ implant (active edge structure) on the front side was lithographically defined by *mask 2* and phosphorus implantation was performed first on the front side and then on the back side, followed by the drive-in cycle to form the n^+ implants on the front p-side and ohmic contact on the back side.

The coupling capacitors (*mask 3*) were then lithographically defined on the front side followed by a step employing the dry–wet–dry ambient regime, resulting in a thickness of 400 nm. Further, using *mask 4*, oxide openings over strip implants were defined to provide contact of the poly-silicon with the under-lying strip implant regions. After lithographic patterning using *mask 5*, the poly-silicon was deposited and boron implantation was performed to form poly-silicon resistors.

Mask 6 was used for the contact lithography to open windows through the oxide for making contact with aluminium, i.e. contact between active n^+ edge, bias ring, and guard rings to their respective upper aluminium coverage. The various electrical contacts were defined using *mask 7* by patterning the metal layer, followed by phosphosilicate glass and silicon dioxide passivation step. The last lithography step (*mask 8*) on the front surface resulted in opening to the metal bond pads for connection to the read-out electronics and biasing. An aluminium metallization was finally carried out over the back surface.

The fabricated strip detectors and the test structures on the periphery of the wafer are shown in Fig. 3.

3. Measurement setup

The electrical characterization of the detector can be broadly divided into four categories: (a) Optical inspection; (b) Global measurements — total detector leakage current (I_{tot}) and backplane capacitance (C_{tot}); (c) Strip measurements — strip leakage current (I_{leak}), poly-silicon resistance (R_{poly}), interstrip capacitance (C_{int}), interstrip resistance (R_{int}), coupling capacitance (C_{coup}), and dielectric current (I_{diel}); and (d) Charge Collection (CC) measurements. The measurements are important to check the over-all performance of the detector.

The optical inspection provides a quick and immediate inspection of any damage to the structure of the detector, like dust particles, scratches, etc. during the fabrication. The I_{tot} determines the overall quality of the detector. It is a source of shot noise in a readout system thereby affecting the total power consumption. The most significant contribution to the total noise comes from the load capacitance, which comprises of C_{tot} and C_{int}. The full charge collection of a detector is ensured by operating it beyond the full depletion voltage (V_{fd}), which in turn is determined from the C_{tot} vs. applied reverse bias (V) plot. Besides contributing to the noise, C_{int} also plays a significant role in charge sharing between two adjacent strips. The signal of the read-out electronics is directly proportional to the C_{coup}, which depends on the quality of the dielectric layer between the implant and the readout aluminium strip. To reduce the parallel thermal noise in a detector, a high value of R_{poly}, together with its uniformity among the strips, is desired. A high value of R_{int} is important to accomplish the isolation of individual strips, and should be of the order of GΩ. Shorts between the aluminium readout and the strip implant (pinholes) can be determined by the measurement of I_{diel}. The measured parameters should qualify certain acceptance criterion that are listed in Table 2, the values of most of which are listed in Ref. [10]. In addition to this, the CC response of the detector is determined using beta particles from the Strontium source (^{90}Sr) using the ALiBaVa system [13]. The effect of these parameters has been discussed in detail in [14,15].

To carry out these tests, the measurement facilities at DU and KIT were used for the electrical characterization of the detectors. KIT was a Sensor Qualification Centre (SQC) for the initial construction of the phase-0 CMS tracker [16] and has two semi-automatic probe stations

3 Each of the guard rings are provided with an option of biasing. This helps in shaping the field inside the sensitive area by minimizing the edge effects, thereby reducing the leakage current.

4 To reverse bias the detector.

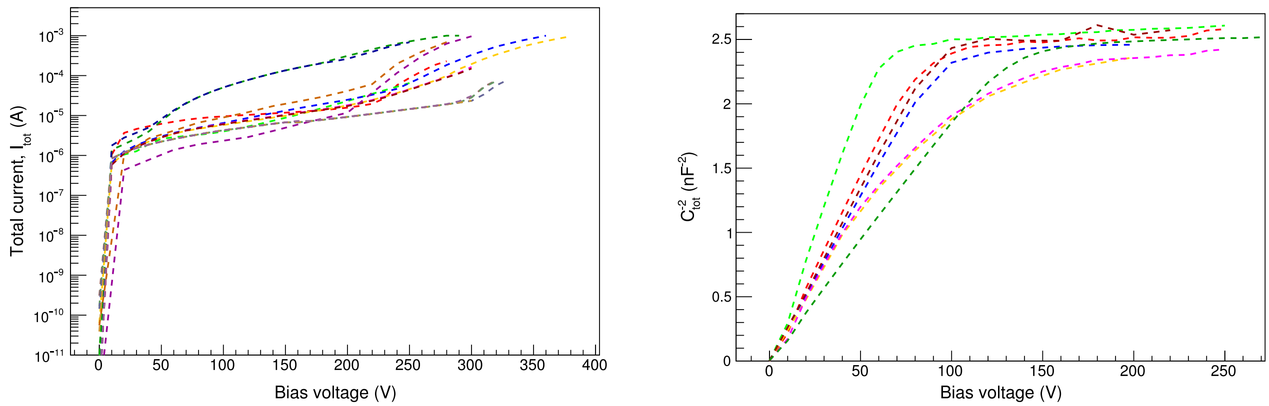

(a) (b)

Fig. 5. The measurement results of (a) the total leakage current, and (b) the inverse square of the backplane capacitance, measured as a function of reverse bias voltage.

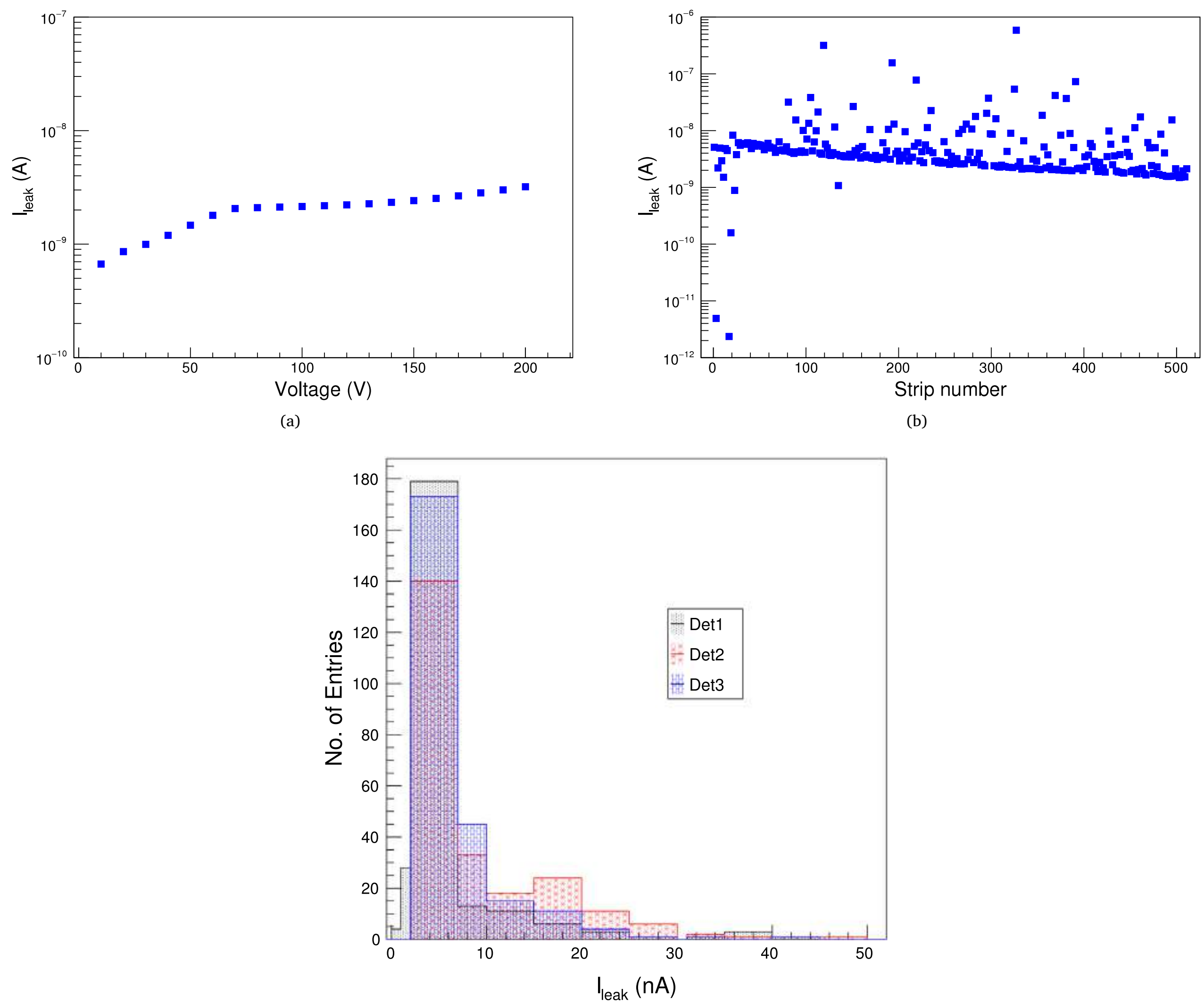

(a) (b) (c)

Fig. 6. The measurement results of (a) voltage scan, and (b) strip scan, of I_{leak} at 200 V, for one detector. (c) The histogram of strip scans of I_{leak} for 3 detectors at 200 V.

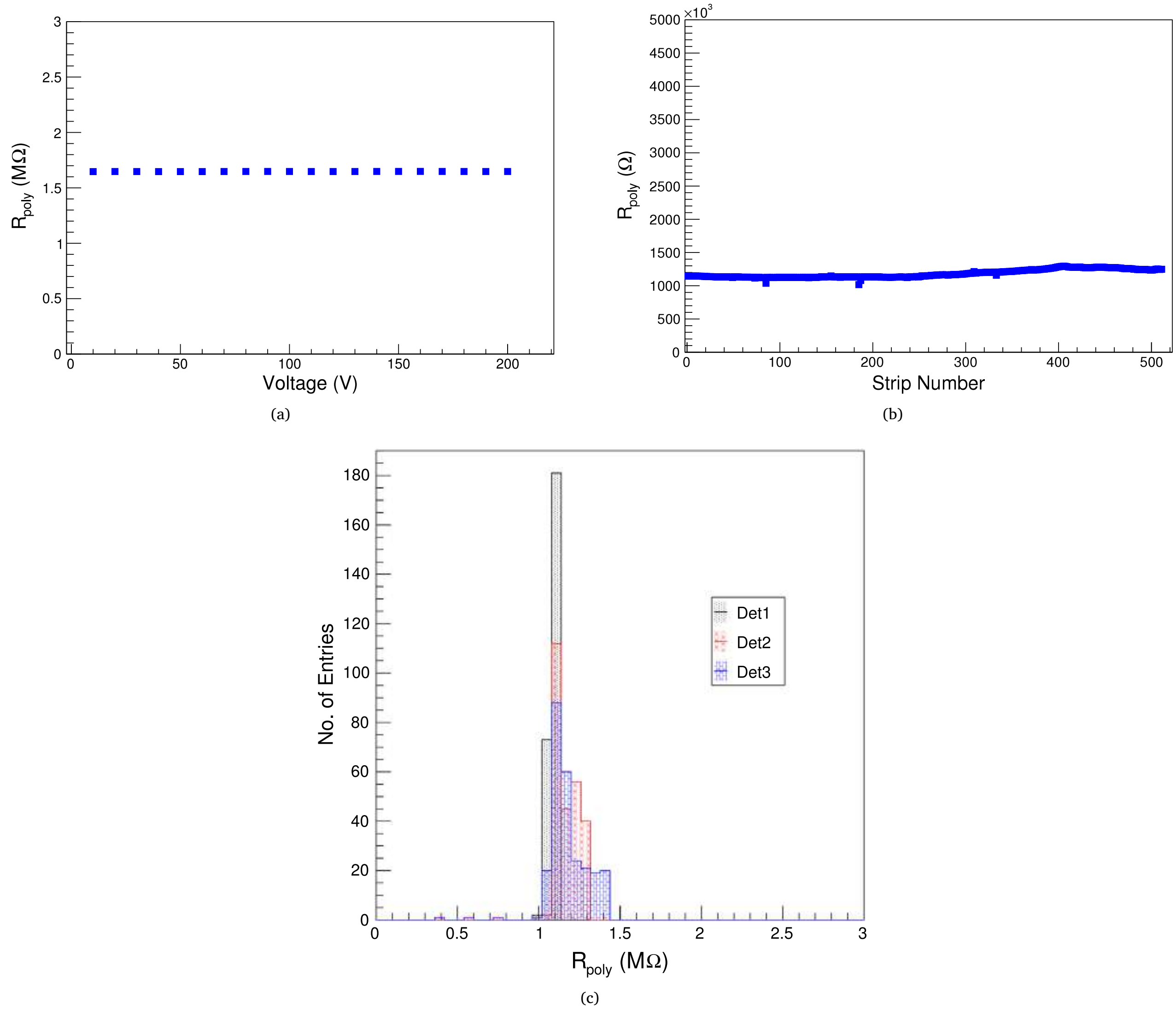

Fig. 7. Electrical measurements of poly-silicon resistance for (a) voltage scan at one strip and (b) strip scan at 200 V, for one of the detector. (c) The distribution plot of strip scan of poly-silicon resistance at 200 V for 3 detectors.

and electrical instruments, connected to a computer through a Data Acquisition (DAQ) system of General Purpose Interface Buses (GPIBs). These are controlled through a dedicated LabView program. Each of the probe stations is equipped with a microscope-monitor system, a chuck plate with an extended platform, micro-positioners, microprobe needles, and a relay network. The system is placed on a heavy metal table to minimize mechanical vibration. Since the initial detector orientation has to be done manually before automated measurements, these probe stations are termed as semi-automatic. The silicon strip detector is placed on an automated and programmable stepping stage, with translation in all three coordinates ((XYZ) stage). The detector is then aligned for automated measurements. The electrical equipment's involve two source measuring units (SMU) — Keithley 2410 and Agilent 6614C, a pico-ampere meter — Keithley 6485, and a capacitance voltage measuring unit — Hewlett Packard 4284A. These instruments are connected to the micro-positioners of the probe station through a relay switching matrix, the connections of which are activated through LabView program, to perform the eight measurements as mentioned above, except for optical inspection and CC measurements, sequentially. The full detector and the strip parameter measurements (for alternate strips) were carried out. The schematics and details of the measurement tests can be found in Ref. [17].

DU also has a semi-automated probe station (Cascade), and the instruments can be controlled through a LabView program. However, the relay network is not yet implemented in the setup and therefore only the I_{tot} and C_{tot} measurements could be carried out with the setup. This is reported in [18].

For the CC measurements, the ALiBaVa setup [19] consists of a table, a board to mount the strip detector, a daughter-board, a source and a scintillation detector, placed inside, and a mother-board placed outside of an electromagnetic shielded box. The mother-board and the daughter-board are the components of the ALiBaVa readout system, which use two Beetle chips [20,21]. The Beetle chip has a system clock with a time period of 25 ns clock as the other LHC strip read-out chips.

All the measurements were carried out in a controlled low humidity (RH < 40%–50%) and clean environment and at a room temperature.

4. Measurement results

4.1. Optical inspection

At a first glance, the detector is seen through the microscope for any dust particles, scratches, short-circuited implants, uneven edges, non-uniform strips, etc. Fig. 4 shows a photograph of one of the strip

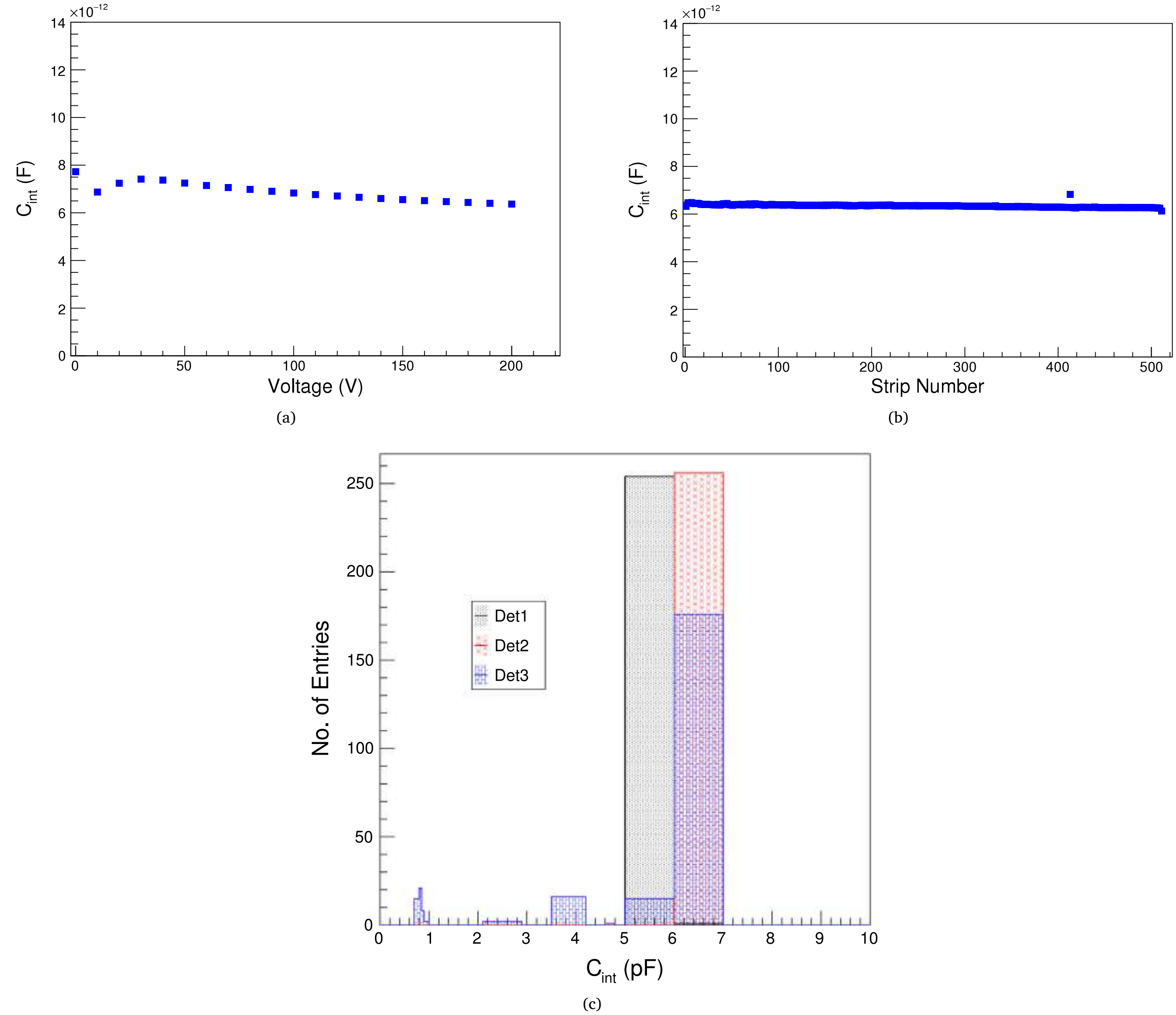

Fig. 8. The interstrip capacitance measurements for (a) the voltage scan at one strip and (b) the strip scan at 200 V, for one detector, and (c) the distribution plot of strip scan at 200 V for 3 detectors.

detectors inspected under a microscope. Most of the detectors were qualified under the inspection; a very few showing the possibility of having dust particles on it.

4.2. Global measurements

The voltage scans of the global parameters of the detector are carried out.

4.2.1. Leakage current, I_{tot}

Fig. 5(a) shows a plot of the I_{tot} as a function of V, keeping all the four guard rings floating. Except for two detectors, the I_{tot} for all the detectors lie in the range of 9 μA to 40 μA at 200 V. The onset of the gradual increase in the leakage current in the detectors lies between 230 V to 300 V.

4.2.2. Backplane capacitance (C_{tot})

Fig. 5(b) shows a plot of C_{tot}^{-2} vs V. The C_{tot} is measured from 0 V to 200 V in a step size of 10 V under reverse bias mode, keeping the guard rings floating and at a frequency of 1 kHz. Using the linear intersection method, V_{fd} was extracted and is found to lie in 60 V–120 V range, for different detectors. Using the value of the V_{fd} and C_{tot}, the detector thickness and bulk resistivity values are calculated to be around 320 μm and 2–5 kΩ · cm respectively, which are consistent with their design values.

4.3. Strip measurements

The voltage and strip scans are performed for the strips detectors. The scan of the strip parameter as a function of voltage, at any one strip, is defined as the voltage scan. The strip scan is the measurement of the strip parameter at a constant V, on all the strips of the detector. For the measurements reported in this paper, a random strip from the centre of one of the three (randomly chosen) detector was used to carry out the voltage scan. A strip scan was performed for the same detector at a constant voltage of 200 V. A histogram distribution of the strip scans for 3 detectors is also shown.

4.3.1. Strip leakage current (I_{leak})

Fig. 6(a) shows the voltage scan of I_{leak} for one of the representative detector. The plot shows the expected increase in I_{leak} with V, with the current remaining below 10 nA at 200 V. The strip scan plot, shown in Fig. 6(b), depicts the uniformity of I_{leak} as I_{leak} lies in the range of 1 nA to 10 nA at 200 V, for most of the strips. Very few low current outliers

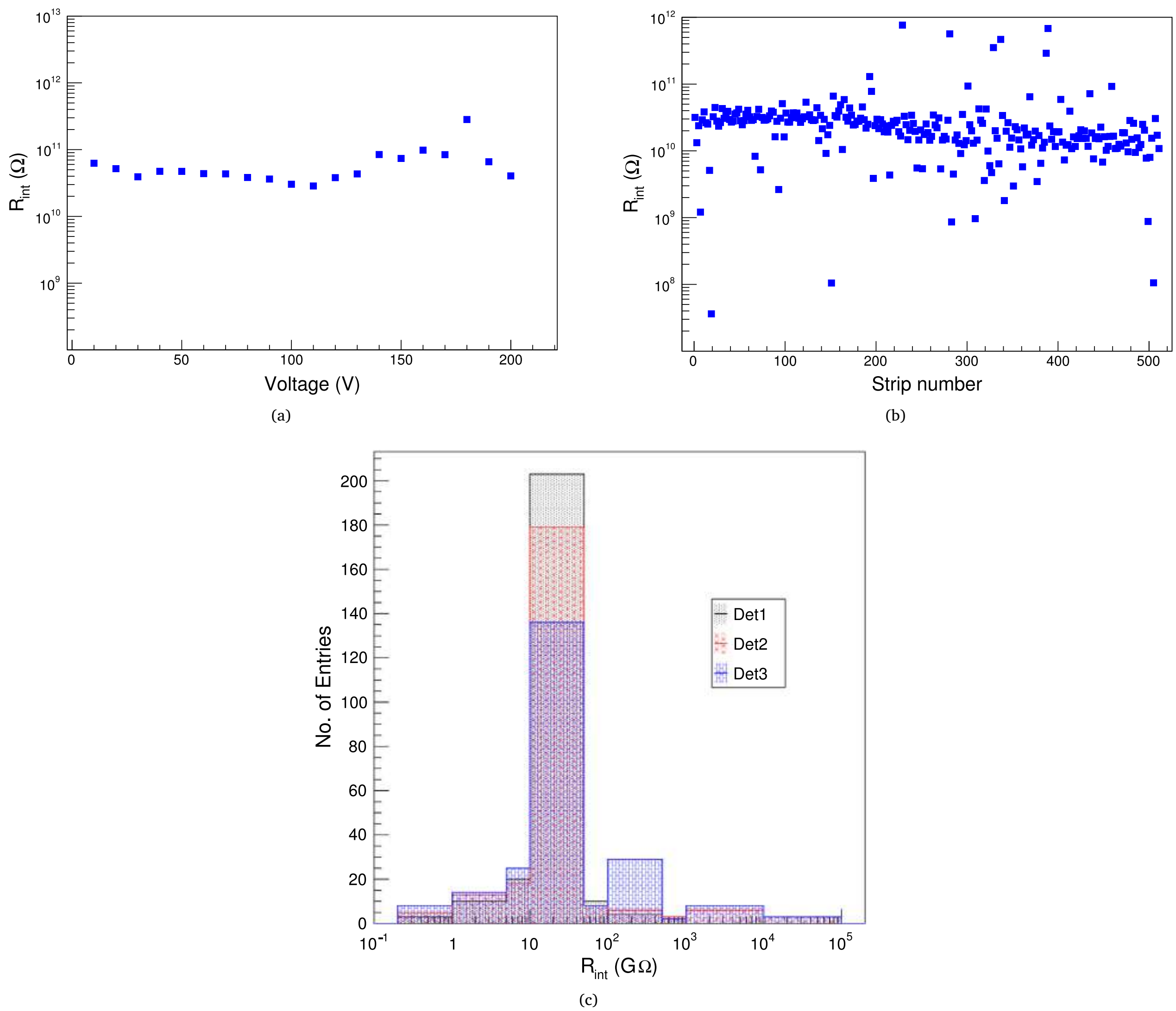

Fig. 9. The interstrip resistance measurements for (a) voltage scan at one strip and (b) strip scan at 200 V, for one detector. (c) The distribution plot of strip scan of interstrip resistance at 200 V for 3 detectors.

are observed in the plot, which can be attributed to loss of connection between the probe needle and the detector pad during the measurement. Fig. 6(c), showing the histogram representation of the strip scan of three detectors, illustrates that on an average, less than 3% of the strips in a detector have $I_{leak} > 30$ nA.

4.3.2. *Poly-silicon resistance (R_{poly})*

For the R_{poly} measurement, a fixed DC voltage of 2 V is applied on the DC contact of a particular strip and the difference in the current of that strip(i.e. with DC voltage of 2 V) with respect to the original current in that strip (i.e. without DC voltage of 2 V) is calculated. The ratio of the voltage (2 V) and this difference in the current gives the Rpoly value. The voltage and the strip scans of R_{poly} are shown in Figs. 7(a) and 7(b). It can be concluded from the plots that the value of the R_{poly} remains uniform throughout at around a value of 1.1–1.2 MΩ value for majority of the strips, which is consistent with the acceptance criterion. In addition to this, the R_{poly} is fairly uniform for the other detectors as well, and its value lies between 0.9–2.0 MΩ. This can be seen from Fig. 7(c), which is the histogram plot of the strip scans.

4.3.3. *Interstrip capacitance (C_{int})*

The C_{int} is measured, between a DC strip and one of its immediate neighbouring DC strip. First an open calibration is performed by the internal calibration procedure of the LCR meter. This calibration is then applied for each subsequent C_{int} measurement. The measurement is performed at an AC frequency of 1 MHz. The C_{int} increases with V and then saturates at approximately 6–7 pF, which is close to the value of 7 pF in the acceptance criterion. This can be seen in Fig. 8(a). Further, Figs. 8(b) and 8(c) show that the measured value of C_{int} is quite uniform throughout the detector, indicating the good quality of the fabrication process.

4.3.4. *Interstrip resistance (R_{int})*

Similar to the R_{poly} measurement, for the R_{int} measurement, a voltage ramp is applied on the DC contact of a strip and the current is measured from one of its immediate neighbouring strip. And then, voltage vs current plot is used to derive the R_{int} value. The variation of R_{int} with voltage is shown in Fig. 9(a). The Fig. 9(b) illustrates that for most of the strips on a detector, the R_{int} is consistent with the acceptance criterion. Also, a histogram representation of the strip scan for three detectors, in Fig. 9(c), emphasizes the consistency in the R_{int}.

4.3.5. *Coupling capacitance (C_{coup})*

The voltage and the strip scans for the C_{coup} are shown in Figs. 10(a) and 10(b). The measurement was performed at an AC frequency of 100 Hz, with an open calibration, followed by C_{coup} measurements.

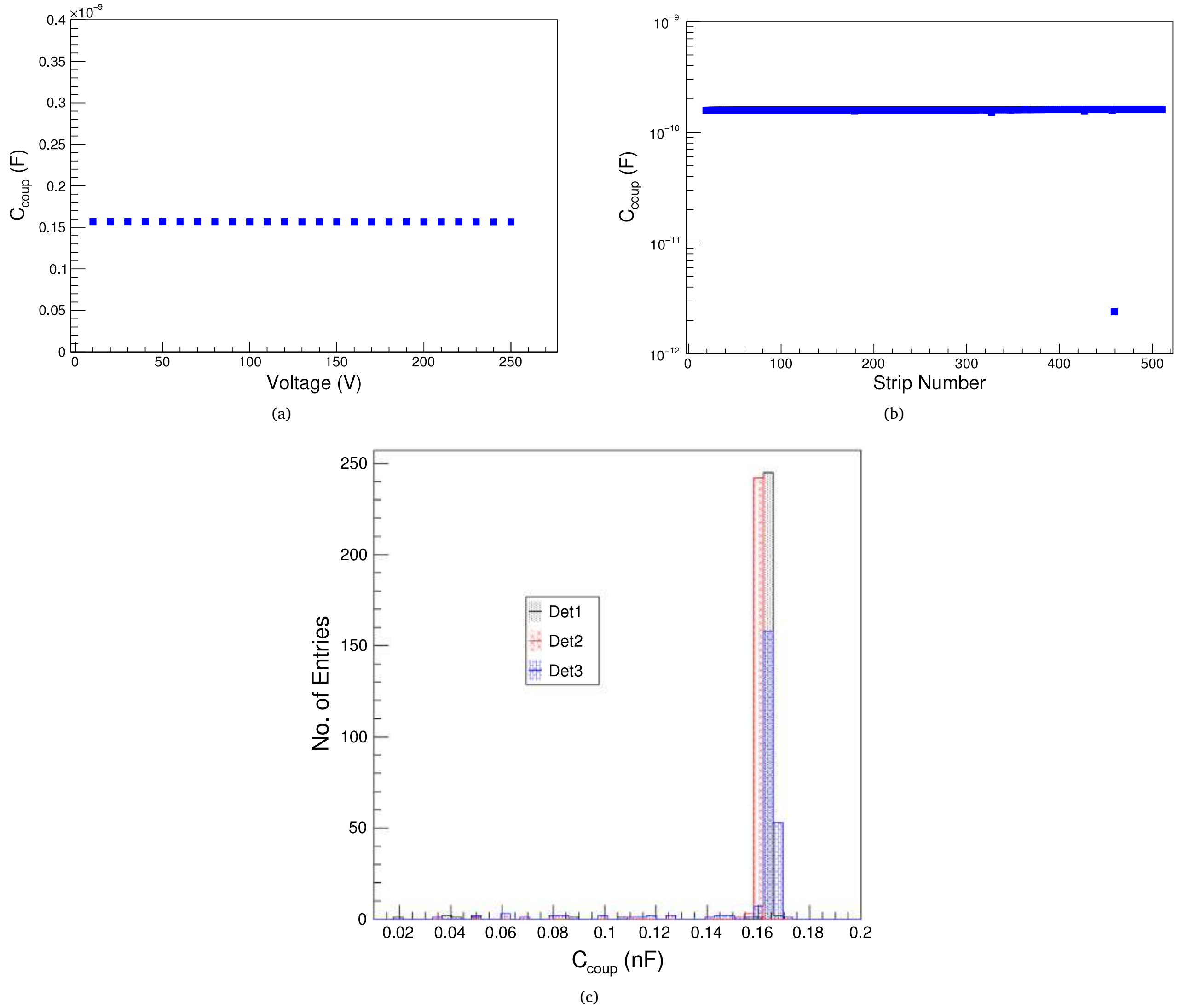

Fig. 10. The measurements of coupling capacitance for (a) voltage scan at one strip and (b) strip scan at 200 V, for one detector. (c) The distribution plot of strip scan of coupling capacitance at 200 V for 3 detectors.

From the plots, it can be deduced that the mean value of the coupling capacitance is approximately 0.16 nF (0.88 pF/cm-μ m). This is consistent with the specifications given in the acceptance criterion. The histogram of the strip scan distribution, illustrated in Fig. 10(c), shows a small spread from the average coupling capacitance value, which highlights the uniformity of the oxide layer, indicating a good quality control in the fabrication process.

4.3.6. *Dielectric current (I_{diel})*

A DC voltage of 10 V is applied on the DC contact of one of the strips of the detector, and the current through its corresponding AC contact is recorded. If there is a presence of a pinhole in the oxide layer (short connection between the DC and the AC contacts), an excessive current is seen at the read-out electronics. If this I_{diel} exceeds 1 nA, at 10 V, the strip is defined as defective and is rejected for connection to the readout. The voltage and the strip scans for the I_{diel} are illustrated in Figs. 11(a) and 11(b). The presence of spikes at a few strips can be attributed to the presence of pinholes on those strips of the detector. A distribution plot of the strip scan of the I_{diel} on three detectors (Fig. 11(c)), highlights the average number of detected pinholes in the detector batch. One of the detectors show less than 1% of the strips having excessive current, whereas one detector shows 2% and the other shows 5% of such strips.

4.4. *Charge collection*

For the CC measurement using the ALiBaVa measurement setup, a ^{90}Sr source, emitting β^- particles, and having a mean energy of 939 keV, is placed on top, at a certain distance from the detector. A small section of the detector strips (about 45 strips) is wire bonded to Beetle chip channels (1 Beetle chip consists of 128 readout channels) (hereafter 'strip' will be referred as 'channel') through the pitch adaptors, which is in turn connected to the other readout electronics. The detector is biased to 150 V and is kept at a temperature of 293 K.

There are three kinds of runs — pedestal run, radioactive source (RS) run, and calibration run. During the 'pedestal run', the readout is taken from all the channels in the absence of the source. The plot for the ADC counts recorded by 256 channels for 1 event is shown in Fig. 12(a). The unbonded channels and the channels with ADC counts greater than 7 ADCs are masked (shown in solid red line), i.e. not used in further analysis. The correction for the electronic readout fluctuations over different events (called the 'common mode') is applied. The 'threshold signal' for each channel is then defined as the standard deviation of the pedestal after correcting for each event for the common mode. For the 'RS run', the hit map, i.e number of events a channel for which the strip is hit in the presence of ^{90}Sr source, can be viewed in Fig. 12(b).

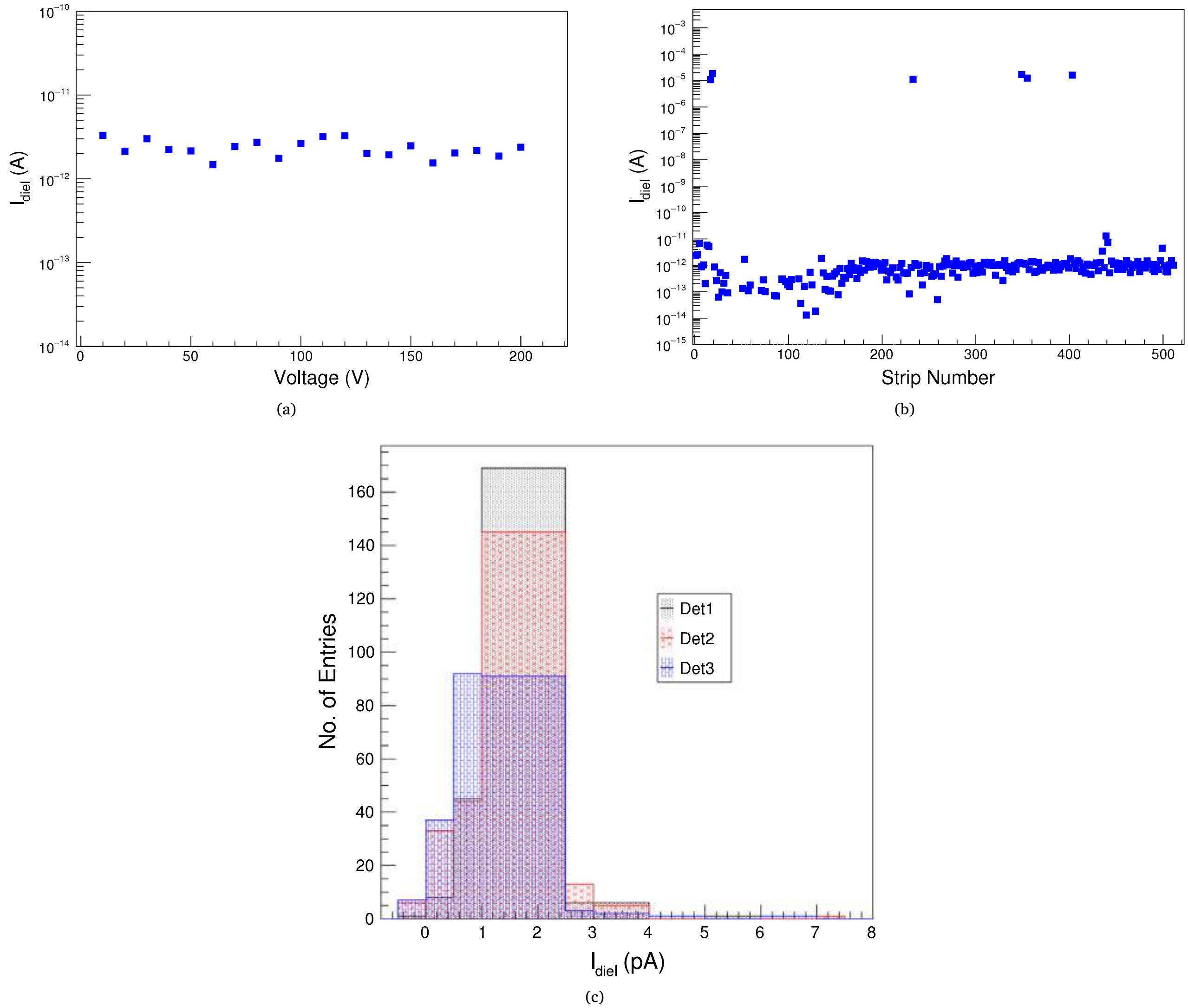

Fig. 11. The measurement results of (a) voltage scan at one strip and (b) strip scan at 200 V, for one detector, of dielectric current. (c) The distribution plot of strip scan of dielectric current at 200 V for 3 detectors.

A total of 10 015 events were recorded with a sampling time of 25 ns. The channel having a signal three times larger than the threshold signal is considered as the ‘seed signal’ and the neighbouring channels with signal higher than two times the threshold signal are added to the seed signal to form a ‘cluster signal’. Finally, a ‘calibration run’ is performed where the system injects a known quantity of charge into the Beetle readout channels. The corresponding ADC counts recorded are said to be equivalent to the number of electrons injected, in each channel. The plot for this is shown in Fig. 12(c). The charge collection distribution of the number of electrons collected for 10 051 events, shown in Fig. 12(d), is fitted with a convolution of a Landau and a Gaussian distribution. It can be seen that the most probable value (MPV) of the cluster signal is approximately 27 570 electrons, or 86 electrons per μm for a 320 μm thick detector. Since the internal gain calibration has an uncertainty of ∼10% (spread of capacitance in chip) and in addition there is a ∼2–3% higher signal due to low energetic electrons from ^{90}Sr; the observed MPV is close to the expected 79 electrons per μm [22].

5. Summary

An indigenous AC-coupled, poly-silicon biased, p-on-n, silicon strip detector development has been carried out at DU. The detectors were fabricated on 4-inch wafers at the BEL, and then characterized at DU and KIT facilities. A set of electrical measurements, consisting of both bulk and strip parameters, have been identified and performed on the fabricated detectors. The fabrication process shows good control of the parameters governing poly-silicon deposition, interstrip resistance and capacitance. Although we observe some issues with the gradual increase of the I_{tot} beyond 300 V, the BEL fabricated detectors qualify most of the specifications as listed in Table 2. Further, a better control on the processing is desired to achieve < 1% bad strips criterion. On the basis of pinholes, about 2–14 bad strips per detector are found in the measurement. Overall the results are very encouraging for the future advances of poly-silicon biased, AC-coupled silicon detectors with the desired width and pitch in the country.

Further, we are in the process of fabricating n-in-n sensors for radiation hard environment, with different isolation configurations. Simulation studies have been carried out to determine the optimized parameters of the isolation structures [23].

Acknowledgements

We would like to acknowledge DST (ref. no. SR/MF/PS-02/2014-DUA (C) and SR/MF/PS-02/2014-DUA (G)), R&D grant University of Delhi, CSIR and UGC (ref. no. Schs/SRF/AA/139/F-203/2013-14) for financial support. We are thankful to Mr. Y. P. Prabhakara Rao and Ms. Rejeena Rani from BEL for the detector fabrication.

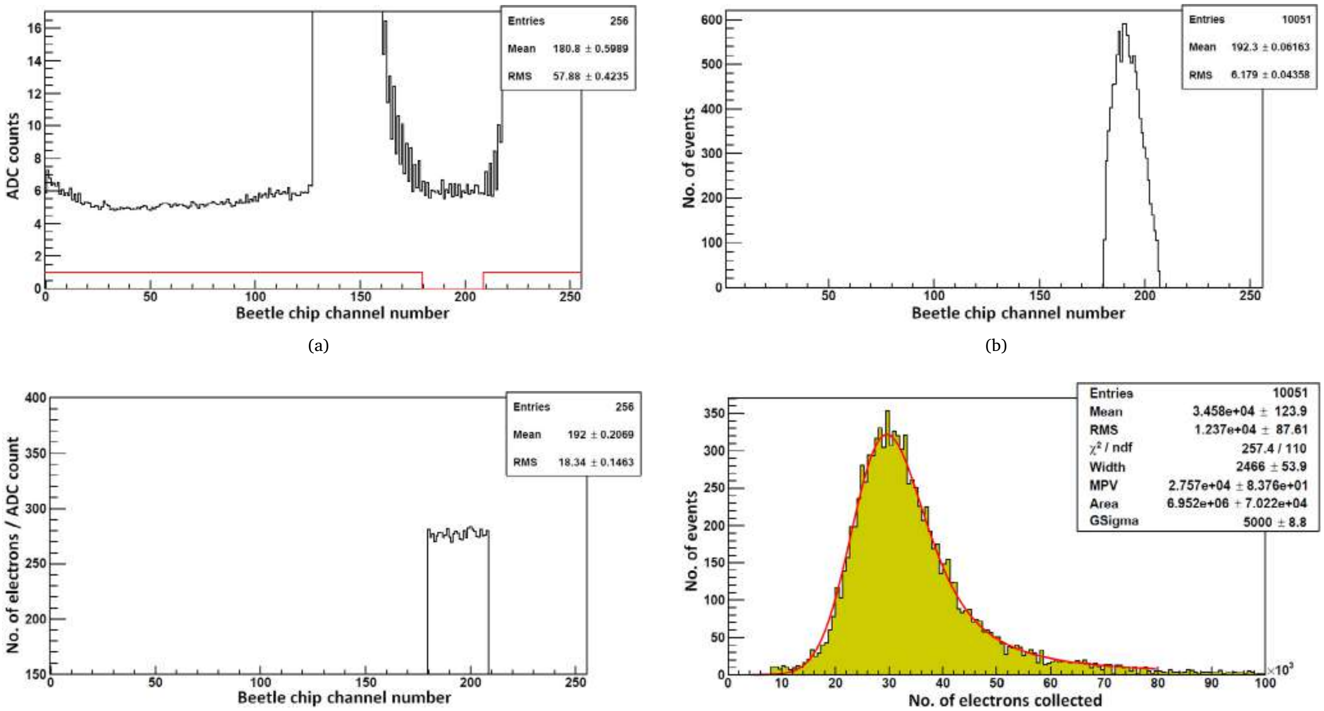

(a) (b) (c) (d)

Fig. 12. The recorded (a) pedestal scan, (b) hit map (c) calibration run, and (d) charge collection distribution, for one of the detectors.

References

[1] F. Hartmann, Silicon tracking detectors in high energy physics, Nucl. Instrum. Methods A 666 (2012) 25–46.

[2] K. Ranjan, Large p_T particle production in p–p collisions at LHC energies (Ph.D. thesis), University of Delhi, 2004.

[3] A. Bhardwaj, Some aspects of hadron–hadron collisions at the large hadron collider — CERN (Ph.D. thesis), University of Delhi, 2004.

[4] A. Peisert, N. Zamiatin, Silicon sensors for the CMS Preshower, CMS NOTE 2000-061, 2000.

[5] P. Saxena, et al., Development of multi-guard ring-equipped $p+$–n Si microstrip detectors for the SiD detector at the ILC, Semicond. Sci. Technol. 25 (2010) 105012.

[6] ATLAS Silvaco version 51532R Nov 2009, Users manual. Silvaco webpage http://www.silvaco.com.

[7] J.A. Hoerni, Method of Manufacturing Semiconductor Devices, US3025589 A, 1962.

[8] R. Marco-Hernandez, A portable readout system for microstrip silicon sensors (ALIBAVA), IEEE Trans. Nucl. Sci. 56 (2009) 1642–1649.

[9] kLayout version 210, User manual. kLayout webpage www.klayout.de.

[10] F. Hartmann, Evolution of Silicon Detector Technology in Particle Physics, Springer, 2009.

[11] T. Bergauer, Process Quality Control of Silicon Strip Detectors for the CMS Tracker (Diploma thesis), 2004.

[12] T. Palviainen, Minimizing guard ring dead space in silicon detectors with an n-type guard ring at the edge of the detector, Nucl. Instrum. Methods A 573 (2007) 277–279.

[13] A. Dierlamm, Studies on the Radiation Hardness of Silicon Sensors (Ph.D. thesis), IEKP-KA/2003-23, 2003.

[14] P. Ghosh, Systematic characterization and quality assurance of silicon micro-strip detectors for the silicon tracking system of the CBM experiment, J. Instrum. C 07001 (2014) 9.

[15] J. Hacker, et al., Development of an automatic characterisation system for silicon detectors, Nucl. Instrum. Methods A 485 (2002) 61–66.

[16] F. Hartmann, The CMS all-silicon tracker strategies to ensure a high quality and radiation hard silicon detector, Nucl. Instrum. Methods A 478 (2002) 285, Proceedings of the Ninth Vienna Conference on Instrumentation.

[17] A. Furgeri, Quality Assurance and Irradiation Studies on CMS Silicon Strip Sensors (Diploma thesis), Karlsruhe, 2006.

[18] G. Jain, et al., Development and characterization of ac-coupled Si strip detectors for nuclear and high energy physics applications, in: DAE Symp. on Nucl. Phys., Dec. 08–12, 2014, 59, 2014, pp. 954–955.

[19] Alibava Systems, Instruments for detection, Start-up guide and User's manual. Alibava webpage https://www.alibavasystems.com/.

[20] See Beetle manual. http://www.kip.uni-heidelberg.de/lhcb/Publications/BeetleRefManv13.pdf.

[21] S. Loechner, Development, optimisation and characterisation of a radiation hard mixed-signal readout chip for LHCb (Ph.D. thesis), Heidelberg University, 2006 (see Table 6.11 in CERN-THESIS-2006-061).

[22] H. Bichsel, Straggling in thin silicon detectors, Rev. Modern Phys. 60 (1988) 663–699.

[23] P. Saxena, et al., Performance studies of the p-spray/p-stop implanted Si sensors for the SiD detector, Nucl. Instrum. Methods A 658 (2011) 66–69.

Nuclear Instruments and Methods in Physics Research A 836 (2016) 113–121

Contents lists available at ScienceDirect

Nuclear Instruments and Methods in Physics Research A

journal homepage: www.elsevier.com/locate/nima

TCAD simulation of Low Gain Avalanche Detectors

Ranjeet Dalal, Geetika Jain, Ashutosh Bhardwaj*, Kirti Ranjan

Center for Detector & Related Software Technology (CDRST), Department of Physics and Astrophysics, University of Delhi, India

A R T I C L E I N F O

Article history:
Received 9 December 2015
Received in revised form
28 July 2016
Accepted 24 August 2016
Available online 26 August 2016

Keywords:
Detector modeling and simulations
Radiation hard detectors
Low Gain Avalanche Detector

A B S T R A C T

In the present work, detailed simulation using Technology Computer Aided Design (TCAD) tool, Silvaco for non-irradiated and irradiated LGAD (Low Gain Avalanche Detector) devices has been carried out. The effects of different design parameters and proton irradiation on LGAD operation are discussed in detail. An already published effective two trap bulk damage model is used to simulate the radiation damage without implementing any acceptor removal term. The TCAD simulation for irradiated LGAD devices produce decreasing gain with increasing fluence, similar to the measurement results. The space charge density and electric field distribution are used to illustrate the possible reasons for the degradation of gain of the irradiated LGAD devices.

1. Introduction

Recently proposed Low Gain Avalanche Detector (LGAD) designs have been the subject of increasing interest within the silicon (Si) sensor community [1–5]. The possibility of controlled avalanche in these devices would allow the fabrication of thinner Si sensors, thus reducing the material budget and the operating voltage for future applications [1,2]. The LGAD devices fabricated by CNM (Barcelona) have shown promising characteristics before irradiation [2]. But, after hadron irradiation, a significant degradation of gain (charge multiplication) has been observed in these devices. These results have not been explained by earlier simulations and are attributed to the possible acceptor removal with irradiation [1]. The charge multiplication process in these devices can be useful in designing the thinner Si sensors with output signals similar to the standard thicker sensors. Moreover, these devices can be considered as ideal candidates for ultrafast sensors [2]. The signal gain (charge multiplication) in these devices is due to the very high electric field region created by depositing moderate doping density of boron layer or p-well, under the n^+ implant in n-on-p Si sensors (resulting in so-called n^{++}-p^+-p configuration). The basic charge multiplication mechanism in these devices is similar to the principle of the avalanche photodiodes [6,7]. The presence of a high electric field in the multiplication region results in higher gain but it can affect the breakdown voltage adversely. Thus, the gain in LGAD devices is strongly influenced by the n^+ and p-well doping profiles and hence these doping profiles must be carefully tuned to obtain a required gain with a sufficiently high breakdown voltage (>1000 V). A few TCAD simulation works have already investigated the effect of the p-well dose on gain and breakdown of non-irradiated LGAD devices [1,6].

In Section 3, we will investigate the gain as a function of the exact p-well profile, not just the peak doping density. In addition, the effect of the n-well doping profile will be considered.

If the LGAD devices qualify to be used in the tracker of high luminosity collider experiments, these detectors will be exposed to extremely harsh radiation scenario and face both neutral (mainly neutrons) and charged (protons and pions) hadron environment. It has been observed that the gain of 300 μm thick devices decreases sharply with fluence [1,3,8] and becomes very low (or almost negligible) for fluence greater than $5 \times 10^{14}\ n_{eq}\ cm^{-2}$. This performance has not been properly understood. It may be interesting to note that earlier simulation studies have indicated that the electric field inside the p-trench region (or p-well) would remain almost same with fluence and hence gain would not be affected by the irradiation [1,6], contradicting the experimental data. Recently, the acceptor removal mechanism has been suggested as a possible explanation for the lowering of gain with fluence in LGAD devices [1,3,8], however, it is not yet successfully implemented in any TCAD simulation framework. In Section 2.2, we will introduce realistic radiation damage model and investigate the effect of proton radiation on the gain of LGAD devices.

* Corresponding author.
E-mail address: ashutosh.bhardwaj@cern.ch (A. Bhardwaj).

http://dx.doi.org/10.1016/j.nima.2016.08.053
0168-9002/

2. Simulation structures and bulk damage model

2.1. Simulation structure

The TCAD simulations are performed on a p-type Si substrate with a uniform bulk doping concentration of $1 \times 10^{12}\ cm^{-3}$. The gain of the LGAD devices are simulated using a plane parallel 2-D structure with a width of 80 μm and a thickness of 300 μm. The Gaussian profile is used for n^+ implantation and p-well implantation (on the top side). If not otherwise specified, the peak doping density for the n^+ (N_n) is kept at $1 \times 10^{18}\ cm^{-3}$ with an implant diffusion depth (d_n) of 4 μm (having 1 Gaussian $\sigma = 0.76$ μm) , while the peak doping density for p-well (N_p) is kept at $9.75 \times 10^{16}\ cm^{-3}$ with an implant diffusion depth (dp) of 7 μm (which corresponds to a p-well dose of 1.78 × 1013 cm-2 and $\sigma = 1.46$ μm). For a given implant diffusion depth ($d_{n,p}$) and peak doping density ($N_{n,p}$), Gaussian σ can be estimated by the relation given below:

$$\sigma = \frac{d_{n.p}}{\sqrt{-2.\ \ln\left(\frac{R}{N_{n,p}}\right)}},$$

where R denotes the reference or bulk doping density of the device. For all the doping profiles used in the present work, a table is provided in the Appendix A listing the values of Gaussian σ for corresponding values of implant diffusion depth and peak doping density of the device. It may be noted from the implant profile shown in Fig. 1(b) that the n^+/p-well junction depth is a function of both n^+ and p-well doping profiles and is less than the value of d_n. The backside p^+ contact is implemented using the peak doping concentration of $1 \times 10^{18}\ cm^{-3}$ and implant diffusion depth of 2 μm ($\sigma = 0.38$ μm) with the gaussian profile. A zoomed view of the n^+ and p-well region of the simulation structure is shown in Fig. 1(a). Fig. 1(b) shows the doping profile along the depth of the detector (near the multiplication region). The gain simulation for these devices is carried out using a 1 μm wide front side infrared laser pulse of wavelength 1060 nm. The laser power density of $1\ W\ cm^{-2}$ and 100 ps duration is used. A device area factor of 2×10^5 is used in the simulation which acts as a multiplicative factor in the signal output for transient simulations. Metal contacts are removed from the entry and exit points of the laser to avoid reflection. Signal simulation is carried out using mix-mode simulation in which external circuit elements of a bias-tee are implemented. The bias-tee resistance of 3.1 kΩ and capacitance of 2.2 nF are used to extract the transient signal through 50 Ω resistance. The LGAD gain is defined as the ratio of the collected charge (calculated by integrating TCT signal pulse) for a LGAD device and that of the reference diode (without the p-well). All the design parameters of the reference diode, including the doping of n^+ and its implant diffusion depth, are kept similar to the LGAD devices for comparison purposes. The breakdown voltage is simulated by keeping the width of the p-well (58 μm) less than the width of the n^+ implant (80 μm) and by including an additional junction termination extension (JTE) structure.

Silvaco TCAD solves the continuity and Poisson's equation for the charge carriers. The default parameters were used for the concentration-dependent lifetime, Shockley-Read-Hall (SRH) recombination and for concentration and field dependent mobility models. The Selberherr impact ionization model is included in the simulation. The simulations are performed using a triangular grid generated by the DevEdit (Silvaco). Reflecting Neumann conditions are imposed at the outer edges of the structure and also on the top of SiO_2.

2.2. Radiation damage model

In order to explain the measurements and predict the behavior of 300 μm thick LGAD devices in the challenging radiation scenario, it is important to include an appropriate radiation damage model within the simulation software. In our previous work, it has been shown that the various effects of proton irradiation can be explained in terms of acceptor and donor trap generation due to irradiation [9,10]. The effective trap model [10] reproduces the correct leakage current, the full depletion voltage and the charge collection efficiency of the Si sensors (reference devices without additional p-well layer) irradiated with the proton fluence up to $2 \times 10^{15}\ n_{eq}\ cm^{-2}$. This simulation model incorporates one acceptor and one donor trap. For both the traps, an uniform trap distribution is assumed inside the sensor bulk. The trap parameters, like the trap energy levels with respect to the conduction or valance bands (for the acceptor and donor traps respectively), introduction rates (g_{int}) for proton fluence and electron/hole capture cross sections (σ_e/σ_h) are listed in Table 1. All the fluence and introduction rates are normalized to 1 MeV neutron equivalent fluence following the NIEL (Non Ionizing Energy Loss) hypothesis. The surface damage is implemented using appropriate oxide charge density and interface trap densities as described in Ref. [10]

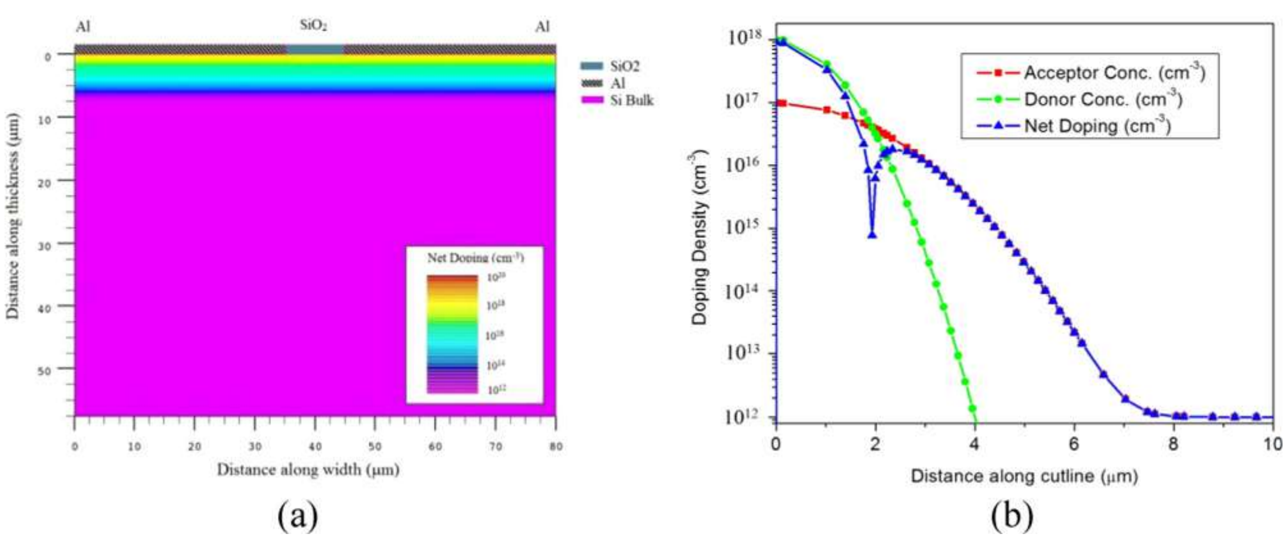

Fig. 1. (a) 2-D zoomed-in net doping profile around the n^+/p-well region of the simulated LGAD structure having width 80 μm. A 10 μm wide SiO_2 window is used for infrared laser TCT simulation. (b) 1-D doping profile of the n^+ implant, p-well and net doping along the vertical cut line through the depth of the device.

Table 1
Two trap level model parameters [10].

No.	Trap	Energy Level	g_{int} (cm^{-1})	σ_e (cm^2)	σ_h (cm^2)
1.	Acceptor	$E_c-0.51$ eV	4	2×10^{-14}	3.8×10^{-15}
2.	Donor	$E_v+0.48$ eV	3	2×10^{-15}	2×10^{-15}

for simulating the breakdown voltage for the irradiated devices. However, for simulating the gain of the LGAD devices the surface damage is not important since the gain is due to the localized high electric field in the bulk near the p+ well region.

3. Performance of non-irradiated LGAD devices

Fig. 2(a) shows the signal generated in the LGAD device for an applied bias (V_{bias}) of 200 V when the laser (infrared) is shone on the top surface. The total charge is calculated by integrating the signal over a time period of 25 ns. The device gain is defined as the ratio of the charge collected by the LGAD device to that collected by the reference diode (same device without p-well). Fig. 2 (b) shows the representative plot of the gain as a function of V_{bias} considering different p-well doses by varying the N_p while keeping other parameters constant. On the basis of the achieved gain, these LGAD devices are labeled as low gain (~2.5 at 200 V for a dose of 1.61×10^{13} cm^{-2}), moderate gain (~5 at 200 V for a dose of 1.78×10^{13} cm^{-2}) and high gain (~15 at 200 V for a dose of 1.87×10^{13} cm^{-2}). For the low and moderate gain devices, there are two visibly distinct regions: steep increment with V_{bias} before full depletion, and a gradually increasing plateau region for higher biases. However, for the high gain structure, the plateau region no longer remains constant and its slope increases sharply with increase in gain. The simulated moderate gain variation with V_{bias} is similar to the ones reported in earlier work [1,3,8], whereas that of the low gain is similar to the measurements shown in Ref. [8,12]. Fig. 3 shows the typical IV characteristics of the representative LGAD device. For comparison purposes, a plot of the reference diode is also shown. The breakdown voltage (V_{BD}) is defined by a sharp increase in the leakage current.

As mentioned above, the characteristics of the LGAD devices are strongly dependent on the doping profiles of n^+ implant and p-well. A careful tuning of both the profiles is imperative to

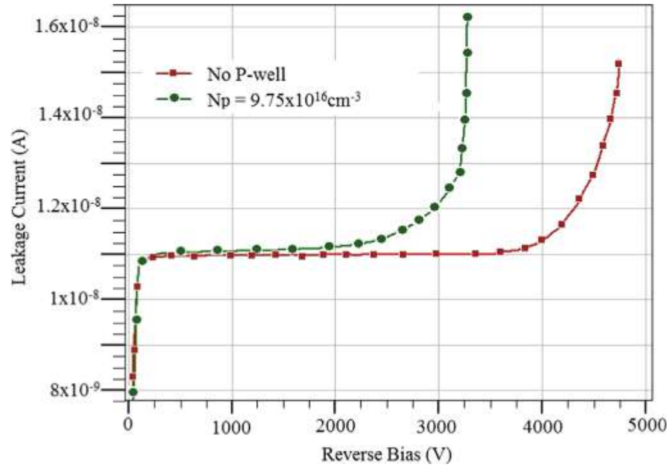

Fig. 3. The IV characteristics of reference diode and LGAD structure (moderate gain) at T=263 K.

achieve the desired performance. A systematic study of the variation of these profiles on the gain and V_{BD} is provided in following sub-sections. It may be noted that the actual V_{BD} and its location are sensitive to the layout of the JTE structure. The V_{BD} study of the LGAD diodes, which strongly depends on the JTE structure, is beyond the scope of this article. Hence, the results concerning the V_{BD} in this work should be considered more as a qualitative indication than a truly quantitative estimate.

3.1. Effect of p-well doping profile

As mentioned earlier, the p-well dose can be varied by changing either N_p (keeping d_p fixed) or d_p (while keeping N_p fixed) or both. We have studied several possible cases for both the variations. Fig. 4(a) shows a plot of the gain and the V_{BD} vs. N_p (or dose) while keeping the d_p fixed. It can be seen that the gain remains almost unity up to N_p of 7.6×10^{16} cm^{-3} and increases sharply with increase in N_p, reaching to a value of 15 for N_p value equal to 1.025×10^{17} cm^{-3}. The increase in the gain with the p-well dose is attributed to an increase in the electric field around the n^+/p-well junction, as shown in Fig. 4(b). The overall sensor gain depends on the magnitude of the electric field as well as the width of the high field region [7] around the n^+/p-well junction. Since the width of

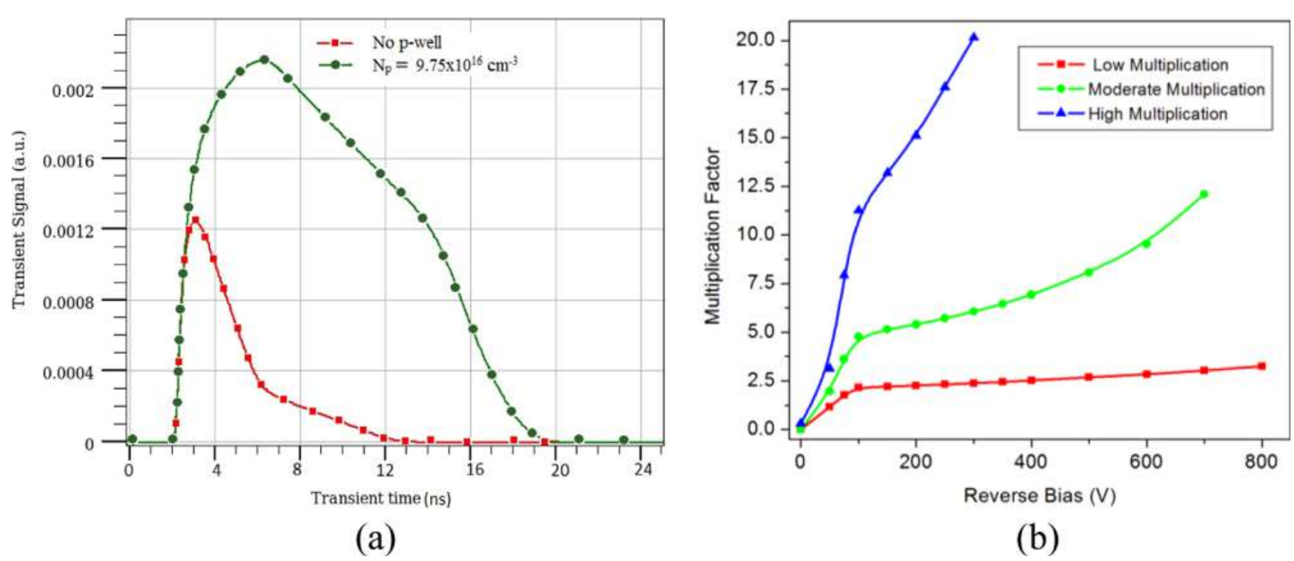

Fig. 2. (a) The transient signal output for reference diode and LGAD structure with $N_p=9.75\times10^{16}$ cm^{-3} (or dose of 1.78×10^{13} cm^{-2}) at V_{bias}=200 V. (b) Gain vs. V_{bias} for three different values of doses using d_p=7 μm.

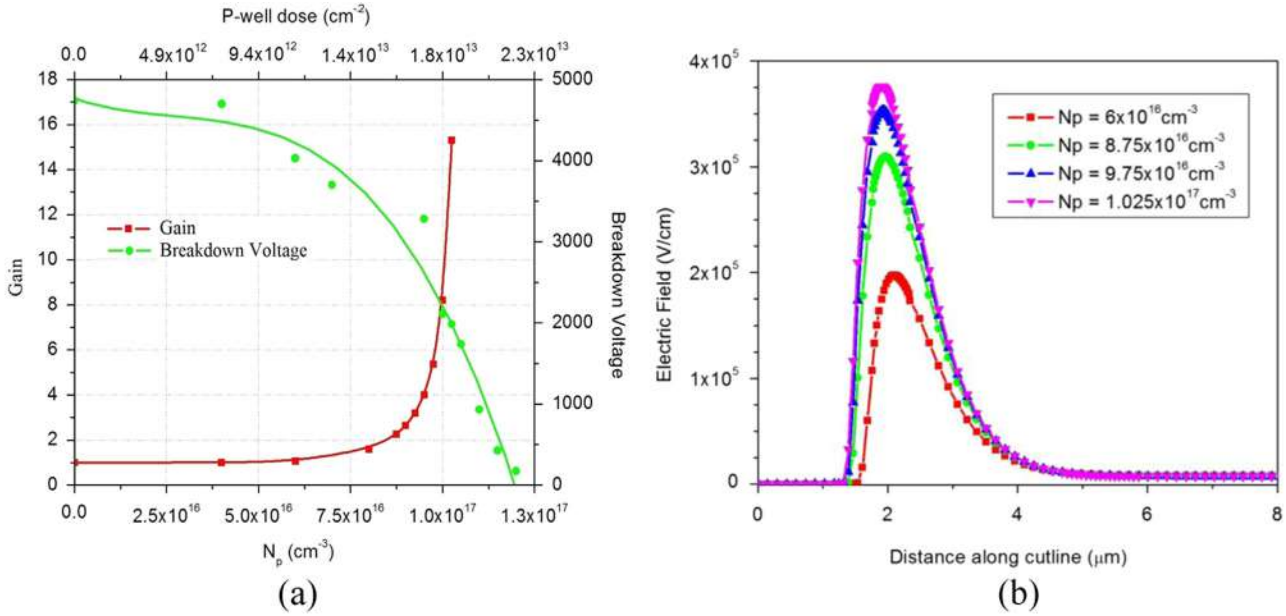

Fig. 4. (a) Gain at V_{bias}=200 V and V_{BD} variation vs. N_p. (b) Simulated electric field near the p-well region for different N_p at V_{bias}=200 V. Following parameters are used for these simulations: d_p=7 μm, $N_n = 1 \times 10^{18}$ cm^{-3}, d_n=4 μm and T=263 K.

the high field region is only few micron for LGAD devices, the peak electric field should be around 3×10^5 V/cm or more for a significant gain. It can be seen from Fig. 4(b) that the peak electric field in the multiplication region is about 3×10^5 V/cm for the low multiplication case and reaches about 3.6×10^5 V/cm for the high gain scenario. The higher gain achieved in LGAD devices, however, is at the expense of the reduced V_{BD}, as shown in Fig. 4(a). It may be noted that the V_{BD} of 2000 V is achieved for the N_p of $\sim 1.025 \times 10^{17}$ cm^{-3} (corresponding to the gain of 15).

Further, similar variation was studied for different values of d_p. Fig. 5(a) shows the plot of gain vs. d_p for different values of N_p. It can be seen that the gain of LGAD device is also affected by varying d_p, while keeping the N_p constant. For these N_p values, the gain remains constant for a minimum d_p, beyond which it increases sharply. Increase in the d_p (for a given N_p) results in higher acceptor density and hence leads to the higher electric field around the n^+/p-well junction (Fig. 5(b)), leading to the increase in gain. For a given d_p, the gain increases with increase in N_p beyond a minimum d_p.

To illustrate the relevance of doping profile (as opposed to total p-well dose only) in tailoring the gain of the LGAD devices, Table 2 lists the gain (in parentheses) and p-well dose values for different combinations of N_p and d_p. It may be noted from this Table that a dose of about 1.6×10^{13} cm^{-2} can be attained using (a) $N_p = 8.75 \times 10^{16}$ cm^{-3} with d_p=7.1 μm or (b) $N_p = 1.025 \times 10^{17}$ cm^{-3} with d_p=6 μm. However, these two combinations (for the same p-well dose) give significantly different gains, i.e. 3.2 and 1 respectively. Similar observations can be made for another dose of 1.81×10^{13} cm^{-2}, which, for the combination of $N_p = 9.75 \times 10^{16}$ cm^{-3} and d_p=7.1 μm gives a gain of 19.5 whereas

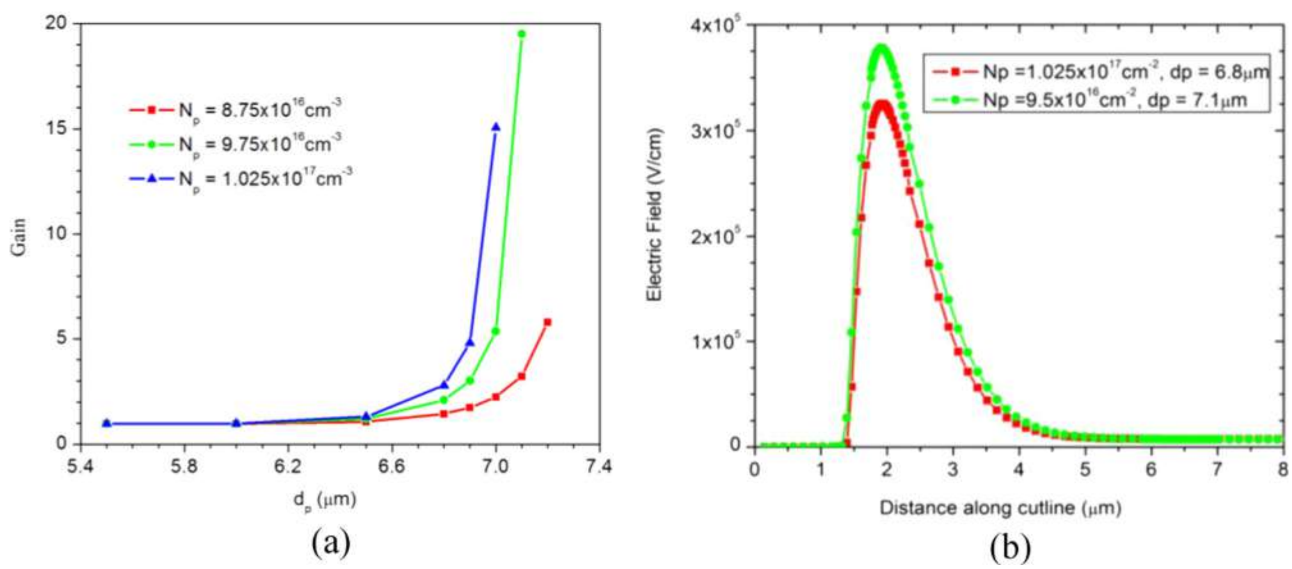

Fig. 5. (a) Variation of the gain vs. d_p for the different values of N_p, and (b) electric field variation around n^+/p-well junction for two different p-well profiles. Following parameters are used for these simulations: $N_n = 1 \times 10^{18}$ cm^{-3}, d_n=4 μm, V_{bias}=200 V and T=263 K.

Table 2
Dose values and gain (in parentheses) for different values of N_p and d_p. Following parameters are used for these simulations: $N_n=1\times10^{18}$ cm^{-3}, $d_n=4$ μm, $V_{bias}=200$ V and T=263 K.

N_p (cm^{-3})	p-well dose in cm^{-2} (gain)				
	$d_p=5.5$ μm	$d_p=6$ μm	$d_p=6.5$ μm	$d_p=6.8$ μm	$d_p=7.1$ μm
8.75×10^{16}	1.26×10^{13} (1.0)	1.38×10^{13} (1.0)	1.49×10^{13} (1.1)	1.56×10^{13} (1.4)	1.63×10^{13} (3.2)
9.75×10^{16}	1.40×10^{13} (1.0)	1.53×10^{13} (1.0)	1.66×10^{13} (1.2)	1.73×10^{13} (2.1)	1.81×10^{13} (19.5)
1.025×10^{17}	1.47×10^{13} (1.0)	1.60×10^{13} (1.0)	1.74×10^{13} (1.3)	1.82×10^{13} (2.8)	1.90×10^{13} (-)

for the other combination, i.e. $N_p=1.025\times10^{17}$ cm^{-3} and $d_p=6.8$ μm gives a gain of only 2.8.

It may be concluded that for the set of (N_p, d_p) values considered in this work, low values of p-well doses are insufficient to provide the gain, however, beyond a minimum dose, a combination of high d_p and low N_p provides higher gain. One may need to investigate this further by expanding the parameter space.

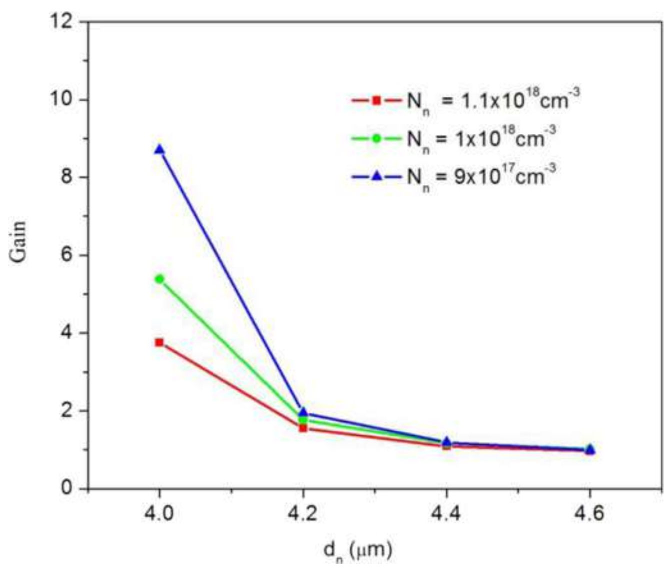

Fig. 6. Gain vs. d_n for LGAD structures for three different values of N_n. Following parameters are used for these simulations: $N_p=9.75\times10^{16}$ cm^{-3}, $d_p=7$ μm, $V_{bias}=200$ V and T=263 K.

3.2. Effect of n^+ doping profile

The variation of n^+ doping profile (N_n and d_n) also affects the n^+/p-well junction and region around it, and hence it affects the gain and electric field distribution for a given p-well dose. An increase in d_n (for a given N_n) would shift the n^+/p-well junction slightly deeper where the p-well doping density would be lower. This leads to decrease in the electric field (and hence the gain) as shown in Fig. 6. Similarly, an increase in the N_n (for a given d_n) would shift the n^+/p-well junction location deeper inside the Si bulk where the p-well doping density is lower. This results in lower gain as shown in Fig. 6.

Figs. 7(a) and (b) show the net doping profile and electric field distribution respectively, for a fixed n^+ dose for two different combinations of N_n and d_n, i.e. (a) $N_n=9\times10^{17}$ cm^{-3} and $d_n=4.4$ μm and (b) $N_n=1\times10^{18}$ cm^{-3} and $d_n=4.0$ μm. The former gives a gain of 1.0 while the latter gives a gain of 5.5. Thus, it may be concluded that, for the given set of (N_n, d_n) values considered in this work, a judicious combination of the N_n and the d_n, as opposed to the total n^+ dose, would give an expected gain for the LGAD device.

4. Effect of irradiation on LGAD devices

A systematic analysis of the proton irradiation effect on the LGAD devices is carried out using our bulk damage model [10] within Silvaco framework [11]. As categorized earlier in Fig. 3, the effect of proton fluence is studied for the low gain, medium gain, and high gain LGAD devices. The variation of the gain with V_{bias} for different fluence values is shown in Fig. 8(a), (b) and (c) for

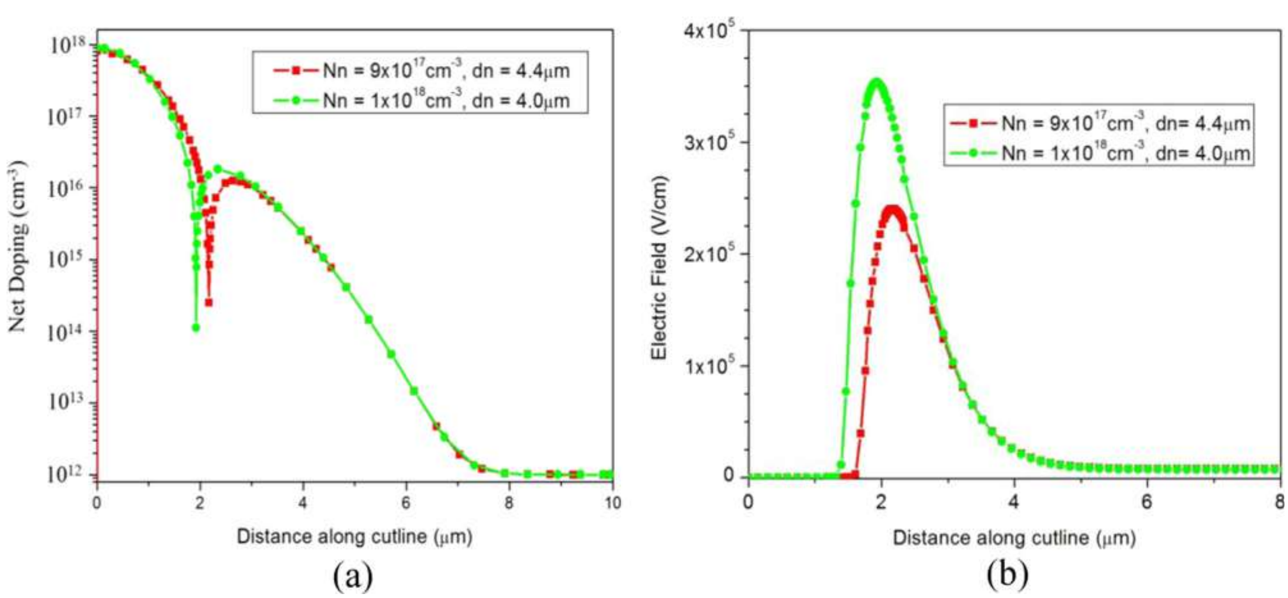

Fig. 7. (a) Doping profile and (b) Electric field along the depth near the p-well region. Following parameters are used for these simulations: $N_p=9.75\times10^{16}$ cm^{-3}, $d_p=7$ μm, $V_{bias}=200$ V and T=263 K.

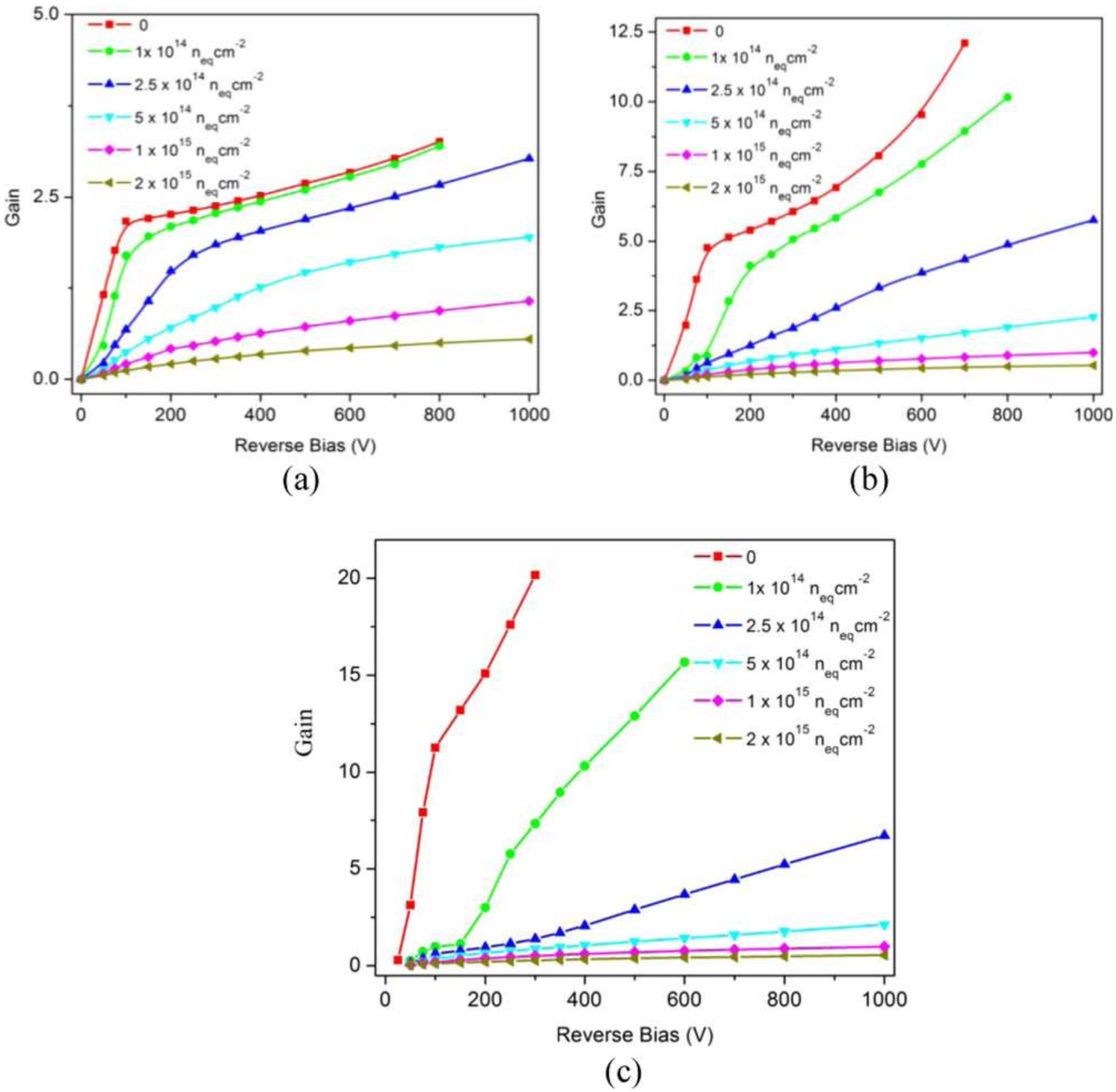

Fig. 8. The gain vs. V_{bias} for different fluence values for (a) low gain (dose of 1.61×10^{13} cm^{-2}), (b) moderate gain (dose of 1.78×10^{13} cm^{-2}), and (c) high gain (dose of 1.87×10^{13} cm^{-2}) at T=253 K.

different categories. The general trend of the plots for the irradiated devices is similar to that observed for the non-irradiated ones, but, it may be seen that the gain is reduced with an increase in fluence and it even decreases below that of the non-irradiated reference diode for higher fluence values. Moreover, the onset of plateau region also occurs at slightly higher applied bias.

A comparison of the gain vs. fluence for all three cases at V_{bias}=300 V and 800 V are shown in Fig. 9(a) and (b) respectively. Although the initial value of the gain in the moderate and high gain for non-irradiated LGAD devices are higher but, it decreases sharply with irradiation and becomes comparable to the low gain LGAD devices for a fluence of about 5×10^{14} n_{eq} cm^{-2}. This behavior is consistent with the recent measurements of the LGAD devices, irradiated with charged hadrons [8].

The simulated leakage current variation with the fluence is shown in Fig. 10(a) and (b) for the low gain and the moderate gain LGAD structures respectively. These plots are qualitatively similar to the measurements reported in Ref. [8]. It can be observed that, contrary to the reference diodes, leakage currents in LGAD structures are not linearly proportional to the fluence. Moreover, the leakage current of LGAD devices is about 1.5–5 times higher (depending on fluence) than that of the reference diodes. This implies that along with the usual charge carrier generation/recombination process due to the bulk traps (which creates leakage current linearly proportional to fluence), additional current is generated in the multiplication layer.

The effect of the proton irradiation on the gain for the different gain scenario can be understood in terms of irradiation effect on electric field profile inside the irradiated LGAD sensors. For the different values of fluence, the electric field variation inside the p-well region is shown in Fig. 11(a) while its variation into the sensor bulk is shown in Fig. 11(b). The electric field profile is plotted for the moderate gain scenario at V_{bias}=500 V and T=253 K. It can be observed from Fig. 11(a) that the peak value and the width of the electric field distribution inside the p-well region decrease with increase in fluence, which would affect the

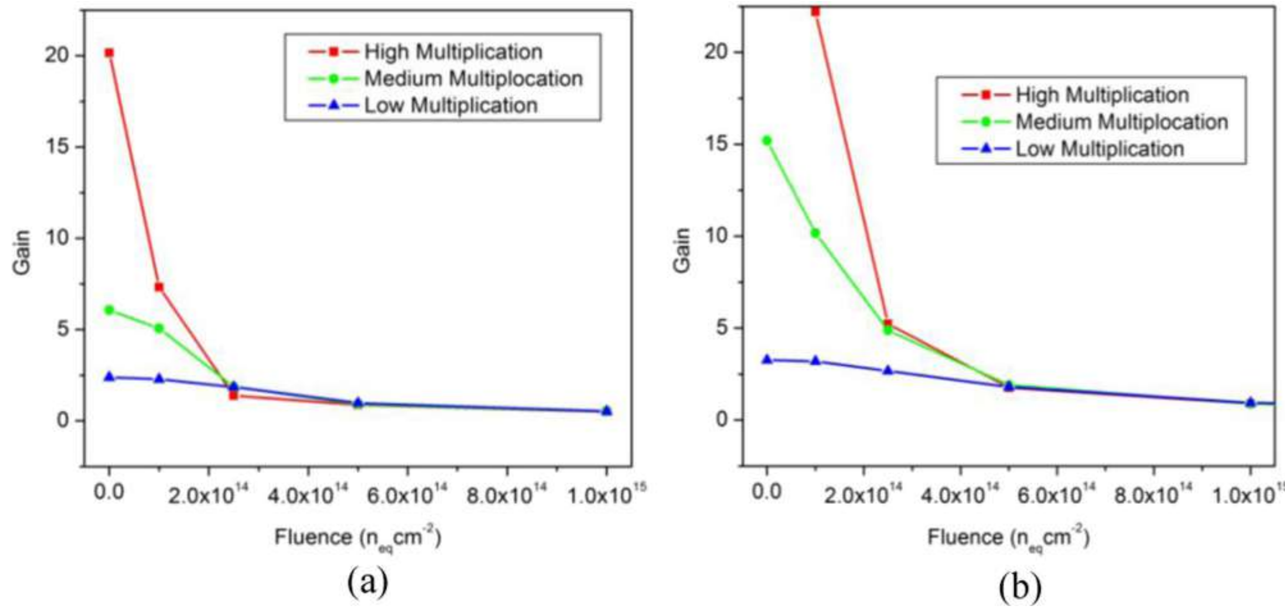

Fig. 9. The gain variation vs. fluence for the different gain scenario at the reverse bias voltage (a) of 300 V, and (b) of 800 V at 253 K.

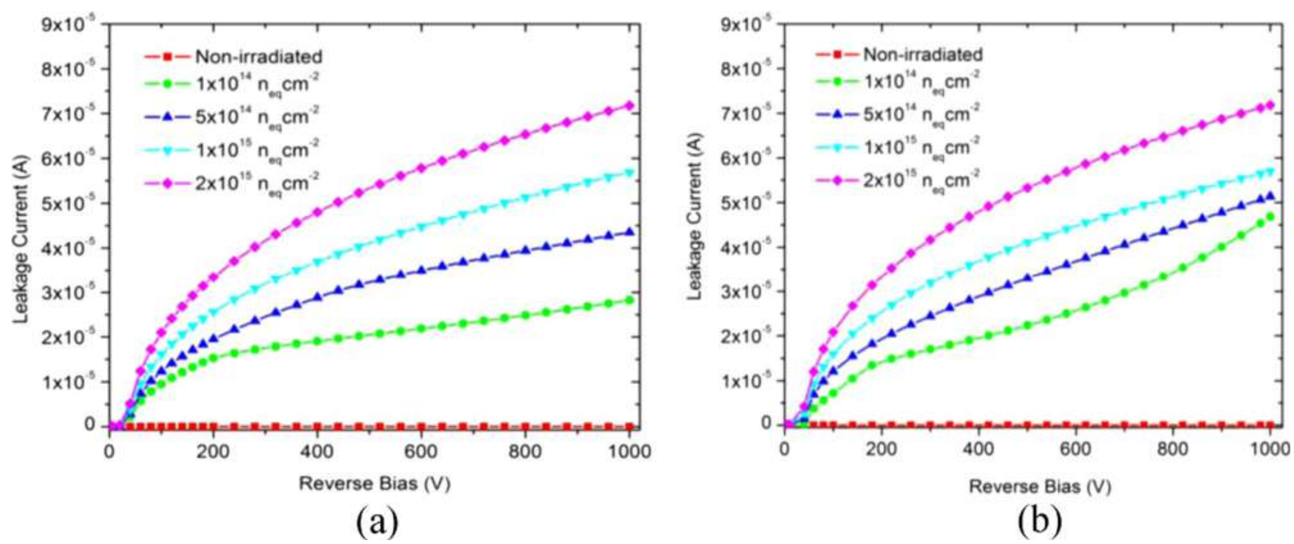

Fig. 10. The leakage current (for the active area of 1 cm × 1 cm) variation vs. fluence (a) for the low gain and (b) for the moderate gain scenario at 253 K.

gain of the LGAD device. Moreover, the electric field near the p^+ backside grows with the increase in fluence due to the double junction effect [13–15], leaving lower values of the electric field inside the sensor bulk. Particularly, there is very low electric field region just below the p-well region, which leads to an inefficient transfer of electrons (for higher fluence values) to the multiplication region. Hence, lowering of the electric field around the n^+/p-well junction as well as in the bulk (below p-well) leads to very low or no gain for irradiated LGAD designs.

The effective space charge density inside the LGAD devices is strongly affected by the hadron irradiation. As shown in Fig. 10, the additional current component comes from the charge multiplication around the n+/p-well junction after irradiation. Since the n+/p-well junction is near the n+ electrode, the additional holes travel almost whole of the device bulk before getting collected at the p+ electrode and thus would lead to predominately donor trap filling in the sensor bulk. The effective space charge density (n-type doping density+ionized donor trap density – p-type doping density - ionized acceptor trap density) for the moderate gain LGAD device is shown in Fig. 12(a) and (b). It can be seen that the sensor bulk becomes effectively donor type after irradiation [16] and the effective space charge density of the p-well is also affected. It may be noted that we have not used acceptor removal parameterization [8] in our simulation and the variation of the electric field, the leakage current, the effective space charge density and the gain with irradiation is only a manifestation of acceptor/donor traps effect.

The present simulation work is meant for the proton irradiated LGAD devices but neutron irradiation would also induce the similar gain lowering. Most of the traps due to the neutron and proton irradiation are quite similar [17] but the neutron irradiation induces fewer donor traps (particularly E30 trap) which would result in lower backside electric field [10] peak, near p+. This would result in the slightly higher field towards the p-well side or slightly efficient electron collection for neutron irradiated sensors, resulting in a higher gain. This has been observed experimentally as well [8].

5. Summary

We have presented simulation results for the LGAD devices. The simulation predictions provide a reasonable qualitative description

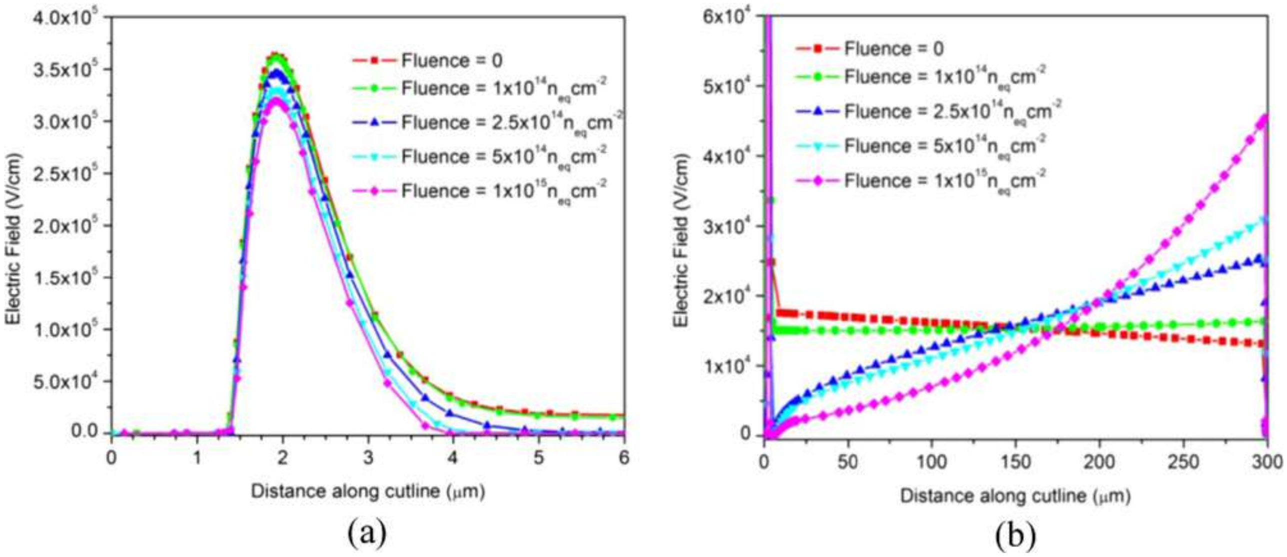

Fig. 11. The electric field for different irradiation fluence (a) for $V_{bias}=500$ V around the multiplication region, and (b) inside the sensor volume for $N_p=9.75\times10^{16}$ cm^{-3} (moderate gain case) at T=253 K.

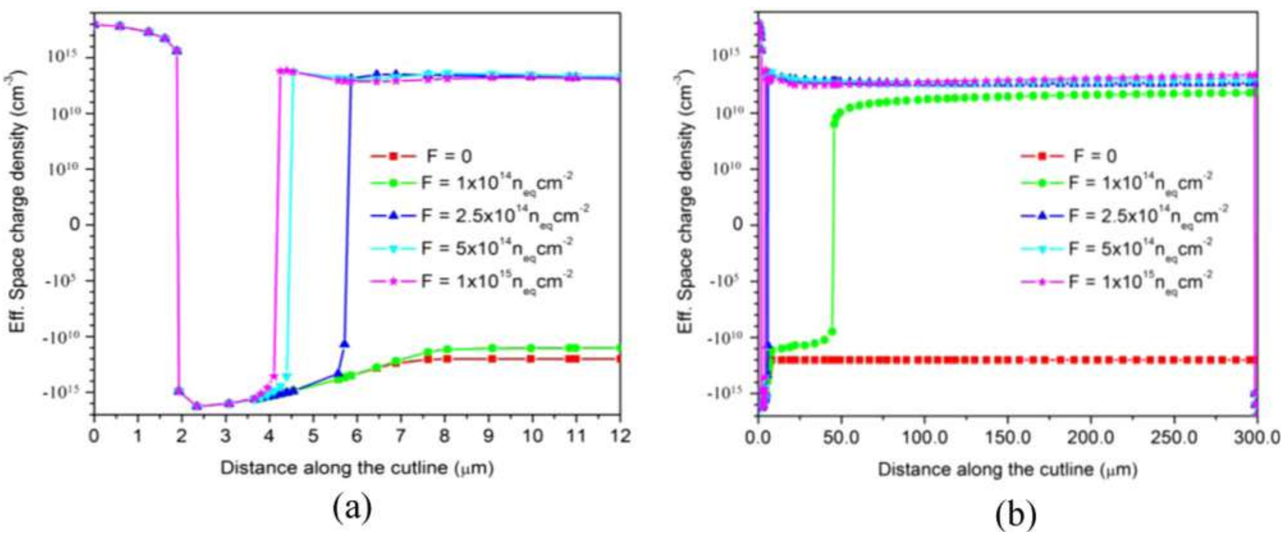

Fig. 12. The effective space charge density for different irradiation fluence (a) around the multiplication region, and (b) inside the sensor volume for $N_p=9.75\times10^{16}$ cm^{-3} (moderate gain case) at T=253 K for $V_{bias}=500$ V.

of both the non-irradiated and irradiated LGAD device behavior. It has been emphasized that the gain of the non-irradiated LGAD devices is strongly influenced by the overall doping profiles of the p-well and n^+ implantations. We have studied the (N_p, d_p) parameter space of (8.75–10.25 × 10^{16} cm^{-3}, 5.5–7.1 μm) and (N_n, d_n) parameter space of (0.9–1.1 × 10^{18} cm^{-3}, 4.0–4.6 μm). It has been found that within the parameter space studied, a minimum p-well dose is required to achieve the desired gain, however, beyond that dose, a combination of high implant diffusion depth and low peak doping concentration of the p-well provides higher gain.

An effective two trap bulk damage model is used to simulate the radiation damage. The incorporated radiation damage model successfully explains the decrease in gain of the LGAD devices with an increase in proton fluence, as observed in measurements. It may be interesting to observe that the gain simulation for irradiated LGAD structures is carried out without changing the acceptor concentration inside the p-well region. The gain variation with fluence seems to be due to the traps effect only, which is further corroborated using the electric field, leakage current and effective space charge density of the irradiated LGAD devices. It has been found that the space-charge density of the sensor bulk and the p-well regions change in a way such that the sensor bulk becomes effectively donor type after irradiation. Hence, these simulations provide another plausible explanation for the lowering of the gain as opposed to incorporation of only acceptor removal mechanism [8]. Authors would like to emphasize that this work provides a useful insight into the working of LGAD devices, however, further simulation and experimental results are needed to understand and utilize the potential of LGAD devices in the future high energy physics experiments.

Acknowledgments

Authors would like to thank University of Delhi and Department of Science & Technology (DST, India) for providing financial assistance. The work was partly performed in the framework of the RD50 collaboration. RD and GJ would also like to thank UGC for providing financial assistance.

Appendix A

See Table A1.

Table A1
The RMS of the Gaussian implant diffusion profile (σ) for the corresponding values of implant diffusion depth and peak doping density of the device.

$d_{n,p}$ (μm)	$N_{n,p}$ (cm^{-3})	σ (μm)
4	1×10^{18}	0.7610
7	9.75×10^{16}	1.4604
2	1×10^{18}	0.3805
7	7.6×10^{16}	1.4765
7	1.025×10^{17}	1.4572
6.8	1.025×10^{17}	1.4156
7.1	9.5×10^{16}	1.4829
5.5	8.75×10^{16}	1.1529
5.5	9.75×10^{16}	1.1474
5.5	1.025×10^{17}	1.1450
6	8.75×10^{16}	1.2577
6	9.75×10^{16}	1.2518
6	1.025×10^{17}	1.2490
6.5	8.75×10^{16}	1.3625
6.5	9.75×10^{16}	1.3561
6.5	1.025×10^{17}	1.3531
6.8	8.75×10^{16}	1.4254
6.8	9.75×10^{16}	1.4187
7.1	8.75×10^{16}	1.4883
7.1	9.75×10^{16}	1.4812
7.1	1.025×10^{17}	1.4780

References

[1] G. Pellegrini, et al., Nucl. Instrum. Methods Phys. Res. A 765 (2014) 12–16.
[2] H.F.W. Sadrozinski, et al., Nucl. Instrum. Methods Phys. Res. A 765 (2014) 7–11.
[3] G. Kramberger, et al., 24th RD50 Workshop, Bucharest, Romania, 11–13 June 2014.
[4] G. Dalla Betta, et al., Nucl. Instrum. Methods Phys. Res. A 796 (2015) 154–157.
[5] I. Vila, et. al., ALCW-2015 workshop, KEK Tsukuba, Japan, 20–24 April 2015.
[6] P. Fernández-Martínez, et al., Nucl. Instrum. Methods Phys. Res. A 658 (2011) 98–102.
[7] S.M. Sze, K.K. Ng, Physics of Semiconductor Devices, 3rd ed., John Wiley & Sons, Inc, Hoboken, NJ, USA, 2007.
[8] G. Kramberger et. al., 2015 JINST 10 P0006.
[9] R. Dalal et al., Simulations of hadron irradiation effects for Si sensors using effective bulk damage model, in: Proceedings of the 24th RD50 Workshop, Bucharest, Romania, 11–13 June 2014.
[10] R. Dalal et al., Simulation of irradiated Si detectors, in: Proceedings of the 23rd International Workshop on Vertex Detectors, PoS (Vertex2014)030, 2014.
[11] ATLAS Silvaco version 5.15.32.R Nov, 2009, Users manual ⟨http://www.silvaco.com⟩.
[12] C. Gallrapp et. al., TCT measurements on neutron and proton irradiated LGAD pad sensors, in: Proceedings of the 26th RD50 Workshop, June 2015.
[13] Z. Li, et al., J. Electron. Mater. 21 (7) (1992) 701.
[14] V. Eremin, et al., Nucl. Instrum. Methods Phys. Res. A 360 (1995) 458.
[15] U. Biggeri, et al., Nucl. Instrum. Methods Phys. Res. A 338 (1997) 330.
[16] G. Kramberger et al., Initial acceptor removal in p-type silicon detectors, Presented at 23rd RD50 Workshop, CERN, Nov. 2013.
[17] I. Pintilie, et al., Nucl. Instrum. Methods Phys. Res. A 611 (2009) 52–68.